A MULTI-PHYSICS STUDY ON GAS DIFFUSION AND CHEMICAL REACTIONS IN CEMENT MATERIAL WITH CO_2 SORPTION

by

Peng Wang

A dissertation submitted to the faculty of
The University of North Carolina at Charlotte
in partial fulfillment of the requirements
for the degree of Doctor of Philosophy in
Infrastructure and Environmental Systems

Charlotte

2015

Approved by:

____
Dr. Shen-En Chen

____
Dr. Jy Wu

____
Dr. Andy Bobyarchick

____
Dr. Thomas Nicholas

____
Prof. Xianbiao Mao

ABSTRACT

PENG WANG. A multi-physics study on gas diffusion and chemical reactions in cement material with CO_2 sorption. (Under the direction of DR. SHEN-EN CHEN)

Emission control and storage of carbon dioxide (CO_2) from fossil fuel combustion is an emerging and frontier research area to counter likely global climate changes. Although the carbon dioxide separation techniques are quite mature, there is still an issue of excessive carbon dioxide being emitted into the atmosphere. Carbon sequestration as mineral carbonates is an attractive and novel method with the potential to be implemented with acceptable economics to dispose carbon dioxide in large scale. This study suggests innovative research in using building materials (cement and concrete) for CO_2 storage and presents two new tools for the development of this technology. The tools are developed so that a quantitative measure of the sorption potential of the futuristic building material can be determined.

The Constant Temperature Pressurized Reaction Chamber (CTPRC) testing technique is a cylindrical structure that allows mineral sequestration and embedment of CO_2 within a highly porous, calcium rich material. The material allows high diffusion and maximizes chemical sorption.

Test setup involves the measurement of the amount of CO_2 being absorbed using the ideal gas law. Because of the porosity, the actual sorption process engages multi-physical processes including complex diffusion behavior, elastic material deformation under pressure and over seven chemical reactions. Environmental scanning electron microscopy (ESEM) and X-ray powder diffraction (XRD) were used to validate the forming of carbonates with the test specimens. A numerical model is developed to help understand the sorption process, which over seven stoichiometric equations have been derived.

This dissertation summarized the hazards of carbon dioxide to the environment and society, the source of carbon dioxide in atmosphere and the current control technologies in the world. Laboratory experiments were conducted to demonstrate the CTPRC testing technique and the sorption potential. The theory behind the mineral carbonation mechanism is investigated including the complicated dynamic behavior about porous material deformation, carbon dioxide gas diffusion and chemical reactions. The coupled system involved in the laboratory study is then simulated with the multi-physical model. The main contributions and results are as follows:

(1) An experimental technique, CTPRC (Constant Temperature Pressurized Reaction Chamber) is developed to quantify the carbon dioxide mineral carbonation and a series of six experiments were reported to determine critical factors involved in the sorption process including initial gas pressure, initial sample porosity and initial sample water-binder ratio. These factors influenced the rate of carbonation reaction.

(2) The hydration and carbonation reactions involved in the cement based porous material were reasonably simplified in the numerical simulation and each component quantity changes were analyzed. According to mass conservation involved in the process of chemical reaction and diffusion, the reaction rate equations were established and were summarized into seven reaction rates. Ten kinds of component concentration field and CO_2 gas diffusion velocity field with different water-binder ratios, initial CO_2 pressure and initial sample porosities were simulated by the numerical modeling. The impact of the three factors on the component concentration field was investigated.

(3) The results involving the carbon dioxide sorption process using both physical and chemical sorption of the porous cement material conclusively indicate a hopeful sequester of a maximum 50% of the injected CO_2 within initial 48 hours.

This research work reported can be the foundation for future works that may involve further optimization of sorption potential of the cementitious material. Additional studies involved the utilization of fly ash have also been performed, which add further values to the futuristic material development enabling a sustainable environment that can be free of wastes of gas, liquid and solid forms.

ACKNOWLEDGMENTS

First and foremost I want to thank my advisor Dr.Shen-En Chen. It has been an honor to be his Ph.D student. I appreciate all his contributions of time, ideas, and funding to make my Ph.D experience productive and stimulating. I am thankful for the excellent example he has provided me as a successful engineer and professor. I also thank the other members of my thesis committee: Dr. Jy Wu, Dr. Andy Bobyarchick, Dr. Thomas Nicholas and Professor Xianbiao Mao for their time, interest, and helpful comments.

I had the pleasure of being educated by amazing faculty members in the Department of Civil and Environmental Engieering at UNC Charlotte. Dr. Rajaram Janardhanam and Dr. Jy Wu proved themselves to be fantastic teachers and mentors. Not only did they provide me with in-depth guidance about how to think and critique, but they also took time to talk to me about my ideas, my concerns, and my career goals. They were reliable, consistent sources of support for me. I always knew I could turn to them for guidance about intellectual or professional endeavors, and they would give me honest, helpful feedbacks. Furthermore, Dr. Wu's participation as a committee member on this dissertation was essential to my success. In regards to my experimental setup, I thank Dr. Youngjin Park for helping me in setting up my experiments.

I would also like to acknowledge the State Key Laboratory for Geo-mechanics & Deep Underground Engineering at China University of Mining and Technology (CUMT), where I did my ESEM and XRD tests. For developing the CTPRC experimental system, Dr. Qianlin Zhu and Professor Qiyan Feng from Low Carbon Research Institute at CUMT made significant contributions. I am especially grateful for the supports from

Professors Xianbiao Mao and Zhanqing Chen from CUMT, as we strive to construct the numerical simulation model presented in the dissertation.

I gratefully acknowledge the funding sources that made my Ph.D work possible. I was funded by the U.S. Department of Energy (Project Numer: DE-FC26-06NT43029) for my fisrt 3 years, with the rest of my studies supported by China National Science Foundation (Project Award Number: 51304207-E0402) and the open fund from the State Key Laboratory for Geo-mechanics & Deep Underground Engineering at CUMT.

I was fortunate to develop friendship during graduate school with Benjamin Smith. He was a wonderful friend throughout graduate school. Not only did he provide me with intellectual stimulation, but he also kept me entertained and encouraged along the way.

Lastly, I would like to thank my family for all their love and encouragement. For my parents who raised me with a love of science and supported me in all my pursuits. I consider Professor Xiexing Miao a dear uncle, who introduced me to Dr.Chen and provided this wonderful opportunity to study at UNC Charlotte. And most of all for my loving, supportive, encouraging, and patient wife, Wen Jiang, whose faithful support during the final stage of this Ph.D is so appreciated. Thank you.

Peng Wang
University of North Carolina at Charlotte
November 2015

TABLE OF CONTENTS

CHAPTER 1: INTRODUCTION

1.1 Introduction

Carbon Capture and Storage (CCS), is defined as a systematic process that integrates three stages: CO_2 capture, transport and geologic storage. It is regarded as an important option for the global greenhouse gas (GHG) mitigation. CCS is viewed as the bridging technology during the transition from conventional fossil fuel-based energy society to an alternative energy future. It offers a tangible means to deal with large volumes of CO_2 emissions by using technologies already in-hand (Karayannis, Charalampides, and Lakioti 2014, Ming et al. 2014, Nataly Echevarria Huaman and Xiu Jun 2014, Ping et al. 2014, Zhu, Duan, and Fan 2015).

Geological storage is key to CCS, but is also the most difficult and risky part in the whole CCS process. Geological storage of CO_2 has been a natural process in the Earth's upper curst for hundreds of millions of years. The engineered injection of CO_2 into subsurface geological formations was first attempted in Texas, USA, in the early 1970s and was for the purpose of enhanced oil recovery (EOR). Similar projects have been ongoing and at many other locations ever since (Warwick et al. 2014). If CO_2 geological storage is to make a significant contribution to emission reduction, it will have to be carried out on a very large scale, safely and economically. Geological storage of anthropogenic CO_2 as a greenhouses gas mitigation option was first proposed in the

1970s, but little research was done until early 1990s (Finley et al. 2011, Warwick et al. 2014, Zhang and Song 2014).

International Energy Agency (IEA) has reported that CCS could account for about 19% of the 50% of the energy-related CO_2 emission reductions, which are required to establish the atmospheric CO_2 concentration of 450ppm (Figure1.1), in order to be consistent with the limiting projected temperature rises to 20℃ by 2050 (Taylor 2010). Between 2025 and 2030, there needs to be a rapid increase in CCS technology deployment while energy efficiency and renewable technologies are being pursued and CCS becomes more economically competitive. The Intergovernmental Panel on Climate Change (IPCC) suggested that until 2100, CCS should provide 15% to 55% of the cumulative green house gas (GHG) mitigation effort (Taylor 2010). Without CCS, the overall cost to achieve a 50% reduction in CO_2 emissions by 2050 will increase by 70% (Pires et al. 2011, Rackley 2009).

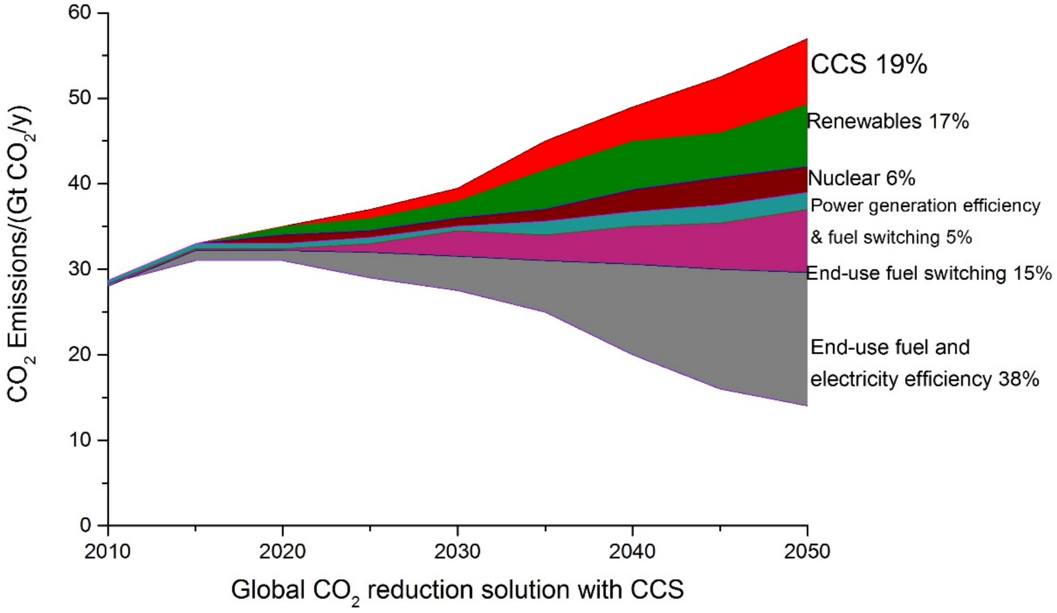

Figure 1.1: Global CO_2 reduction soltion with CCS

Before 2010 there has been little report of geological storage of CO_2, except for the Sleipner (Rubin 2008, Zakkour and Haines 2007). There are several suggestions to the geological formation setting for CO_2 injection. In Salah Andosnohvit projects is the only commercial project involved the injection of CO_2 into a geologic formation to enhance oil recovery. Other fossil fields such as shale gas and coal beads are also possible. However, saline formations are the most promising long-term storage reservoir, with the largest storage capacity. Current estimated capacity of geological storage is listed in Table 1.1 and Table 1.2 (Blunt, Fayers, and Orr 1993, Kovscek and Cakici 2005, Shaw and Bachu 2002).

Table 1.1: Geological storage capacity estimated by IPCC

Reservoir	Lower estimate of storage capacity (Gt CO_2)	Upper estimate of storage capacity (Gt CO_2)
Oil and gas fields	675	900
Unminable coal seams	3~15	200
Deep Saline Formations	1000	Uncertain, but possible 10^4
Data source: (Taylor 2010)		

Table 1.2: Global geological storage potential by estimate by IEA

Region	Theoretical storage Capacity (Gt CO_2)	Total CO_2 stored 2020 (Mt)	Total CO_2 stored 2050 (Mt)
OECD	2170~4650	520	38100
OECD Europe	120~940	170	15600
OECD Pacific	800~900	130	14300
China & India	1520~3020	170	37500
Other Non-OECD	3480~5990	250	39100
World	8090~15500	1240	144600
Data source: (Taylor 2010)			

To reduce green house gas emission by 50%, IEA proposed to target a cumulative CO_2 storage of 145Gt from 2010 to 2050. This requires globally more than 3400 CO_2 geological storage projects by 2050. Although there are potentially many areas considered as highly suitable for storage, there are still many geological unknowns, uncertainties and risks associated with these areas. In the following section, a review of the geological storage technology is presented and offers an argument for alternative storage technology.

1.2 Mechanism of Geological Storage of CO_2

A complete geological storage project is likely to have four distinct phases: (1) site selection and development (approximately 3~10 years); (2) operation (over decades); (3) closure (over years) and (4) post-closure maintenance and monitoring. Once the CO_2 is safely injected into the ground, it is expected to remain there for an extended geological period of time (Benson and Cole 2008, Gale et al. 2001, Thomas and Benson 2015). Hence, although the storage capacity is huge, the preparation and operation times are quite long.

To geologically store CO_2, the gas must first be compressed, usually into a dense fluid state known as supercritical (Figure 1.2). The density of CO_2 will increase with injection depth until at about 800 m or greater, the injected CO_2 then will be in a dense supercritical state. Supercritical CO_2 fills the pores with the density of a liquid but some of the physical properties of a gas. If a 1000 m^3 CO_2 gas at ground surface were injected, the volume would be dramatically reduced to only 2.7m^3 at 2,000 meters depth (Figure 1.2). This is one of the factors that make the geological storage of large quantities of CO_2 so attractive (Bachu 2000, Carcione et al. 2006, Fischedick 2007).

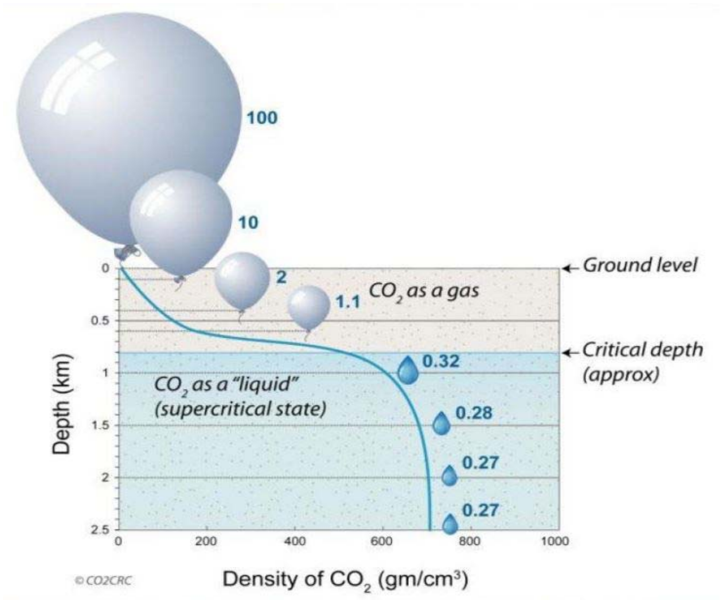

Figure 1.2: Change of CO_2 density with the injection depth (Bachu 2000)

The density of the injected CO_2 depends greatly on the geothermal gradient and hydrostatic pressure within the rock formation: Recent work has shown that in basins with a high geothermal gradient, CO_2 may start to enter the supercritical state at around 200kg/m^3 (Benson et al. 2012, Mead et al. 2013).

The definition of the pore volume available for containment depends primarily on five parameters: formation thickness; area of storage site; rock porosity (percent of voids per bulk volume); CO_2 density; and permeability (the ability of fluids to flow through a formation). Porosity values greater than around 10% in carbonate formations or 15% in classic formations are generally desirable (Okwen, Stewart, and Cunningham 2010, Shtepani 2006). Porous rocks have a wide range of permeability, between around 0.1 mili-Darcy (for very tight rocks) to several Darcies (for very permeable formations). Ideally, CO_2 storage requires high permeabilities (>100mD) for economic injection.

Potential CO_2 storage reservoirs must fulfill stringent geological criteria of which the essential ones being:

(1) Sufficient container with high injectivity and capacity;

(2) Safe cap rock, which is the overlying impermeable rock layer, to prevent the CO_2 from migrating upwards (Figure 1.3);

(3) Location deeper than 800m, where pressures and temperatures are high enough to enable the storage of CO_2 in a dense fluid-like phase (Gozalpour, Ren, and Tohidi 2005, Kovscek 2002, Rubin 2006, Rutqvist and Tsang 2002).

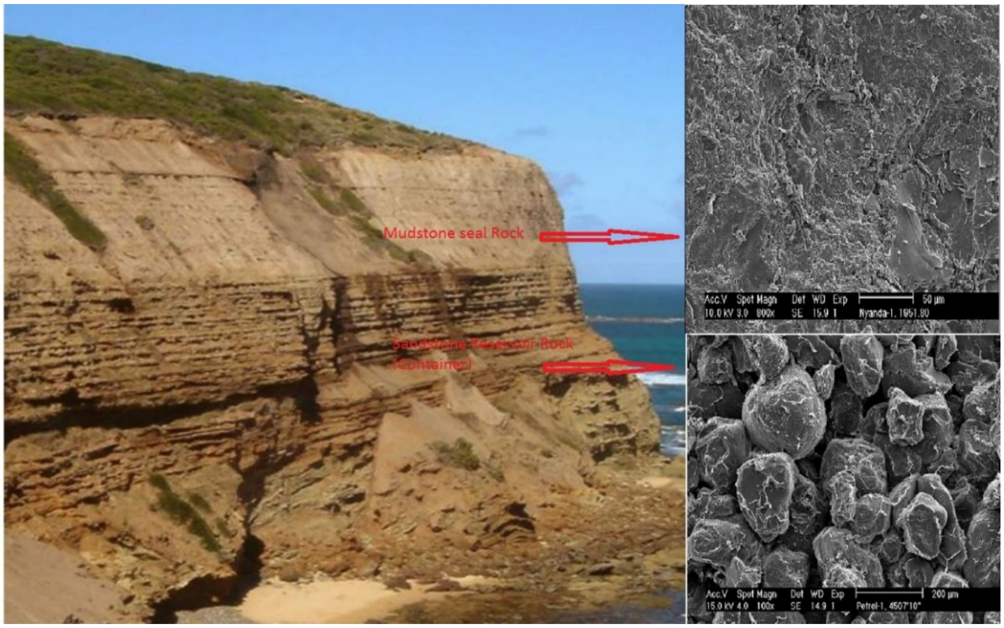

Figure 1.3: Illustration for the container and lid layer in geological storage

Suitable formations for geologically storage of CO_2 can be classified into 4 categories, where depleted reservoirs are the most readily available storage solutions. (Figure 1.4 (Rubin 2006))

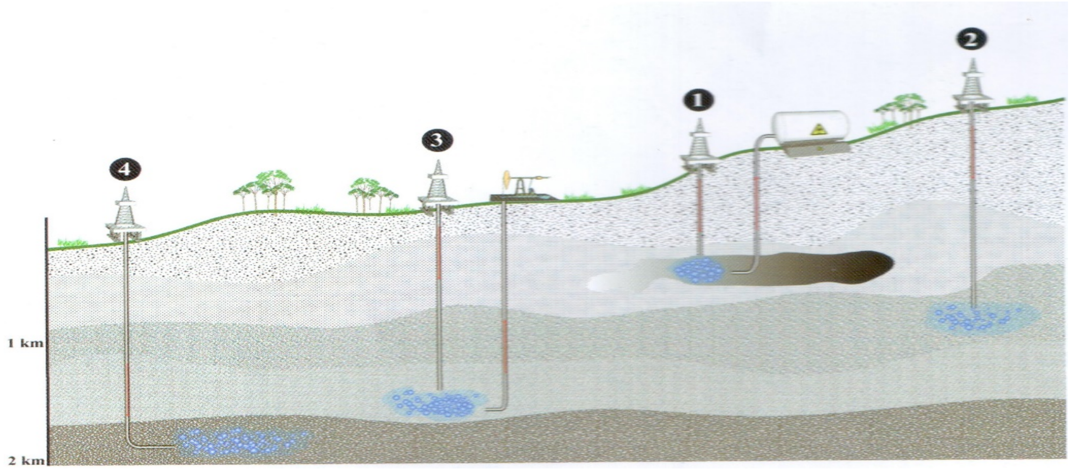

Figure 1.4: Modes of CO_2 storage formation (1. CO_2-ECBM; 2. deplete oil, gas and coal reservoir, 3. CO_2-EOR, 4. deep saline formation)

This is mainly because most of these reservoirs have been thoroughly characterized with a large amount of data available that can be directly applied to the understanding of the dynamics of CO_2 storage. These depleted reservoirs offer suitable pressure regimes and with existing wells allow immediate access to the reservoir. Enhanced oil recovery (EOR) and CO_2-EGR (Enhanced Gas Recovery) through CO_2 flooding are the most economically viable geologically based GHG mitigation technology at the present. This is because carbon dioxide has been used for EOR can achieve an incremental oil recovery of 7%~23% of the original oil in place (Kovscek 2002, Rutqvist and Tsang 2002).

In EOR, the oil displaced by injected CO_2 relies on the phase behavior of the CO_2 and crude oil mixtures. More than 50%, and up to 67% of the injected CO_2, may return with the produced oil and is usually separated and re-injected into the reservoir. Most of the CO_2 is eventually retained within the reservoir, although it may take a number of cycles of injection, production, capture and re-injection before this occurs.

Coal seams are unique in the sense that injected CO_2 is to a large extent adsorbed into the coal matrix, preferentially replacing methane molecules. It is argued that if coal seams have held methane for millions of years, it will probably retain CO_2 for similar timescales. However, there are still several aspects to be studied on the interaction between CO_2 and coal seams, especially the chemical reactions and physical processes which could occur during CO_2 injection, and their impacts on the integrity of the coal seams (Reeves 2001, 2003).

Deep saline formations with good storage potential generally present in the same basins as oil and gas reservoirs. The site characterization methods are essentially similar (White et al. 2003).

Once CO_2 is injected into the reservoir, four kinds of trapping mechanisms will help retain the injected CO_2, namely structural and stratigraphic trapping, residual trapping, solubility trapping and mineral trapping (Figure 1.5) (Damen, Faaij, and Turkenburg 2006, Johnson, Nitao, and Knauss 2004). Over time, the physical process of residual CO_2 trapping decreases and mineral geochemical process of solubility trapping and mineral trapping would increase.

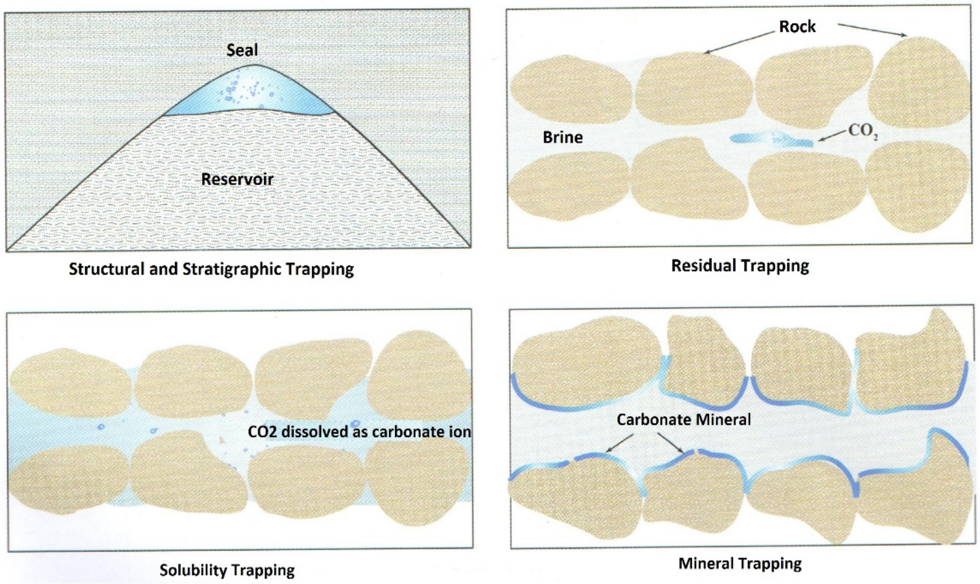

Figure 1.5: Trapping mechanism

(1) Structural and Stratigraphic Trapping: When injected into a reservoir, the CO_2 fills the rock's pore spaces. The supercritical CO_2 will rise up due to buoyancy which may stop when an impermeable rock layer is encountered. Commonly composed of clay or salt, this cap rock acts as a vertical barrier, preventing the CO_2 from rising any further (Szulczewski, Hesse, and Juanes 2013).

(2) Residual Trapping: Residual trapping occurs when the pore spaces in the reservoir rock are so narrow that the CO_2 can no longer move upwards (trapped by capillary force), despite the difference in density with the surrounding water. The overall effect of residual trapping is that of a migrating volume of CO_2 will leave behind a considerable amount of CO_2 trapped in the recesses of pores and on mineral surfaces (Juanes et al. 2006, Krevor et al. 2011).

(3) Solubility Trapping: CO_2 is highly soluble in water and also may dissolve in oil. The primary benefit of solubility trapping is that once CO_2 is dissolved, it no longer exists as a separate phase, thereby eliminating the buoyant force that drives it upwards. A consequence of dissolution is that the water with dissolved CO_2 is heavier than the water without, and it tends to move downwards to the bottom of the reservoir. Rough estimates at the Sleipner project for example indicates that about 15% of the injected CO_2 is dissolved within formation waters after 10 years of injection (Gunter, Bachu, and Benson 2004, MacMinn, Szulczewski, and Juanes 2011, Suekane et al. 2008).

(4) Mineral Trapping: Dissolved CO_2 can react with the minerals comprising the storage formation. Some reaction maybe leads to stable carbonate minerals. Mineral trapping is believed to be comparatively slow and may potentially take a thousand years or longer. Xu, Apps, and Pruess (2003) estimated that over 5000 years, all the CO_2 injected into the

Weyburn Oil Field will dissolve or be converted to carbonated minerals.

1.3 Alternative Storage Strategy: Cement CO_2 Mineral Sequestration

For reasons described in previous section, this study investigates an alternative carbon storage strategy which focuses on near earth surface carbon sequestration potentials. Through extensive literature reviews, the predominant mechanism that constitutes most research in alternative CCS technologies is mineral carbonation. Hence, this section we offer an examination of the carbonation process. The focus will be placed on the use of cementitious materials in building technology.

Carbonation is a natural phenomenon affecting commonly used cementitious materials, which can have detrimental effects on structural concrete. On the other hand, carbonation has been demonstrated to act positively in the immobilization of heavy metal-contaminated soils and other residues (Macias, Kindness, and Glasser 1997, Valls and Vazquez 2001, Venhuis and Reardon 2001, Walton et al. 1997). In one patented application (Hills 1999, Hills and Macleod 2001), the use of carbonation has been used to overcome the inhibiting effects of complex waste materials on the hydraulic and pozzolanic reactions responsible for effective solidification. The solid mixture is carbonated under a gaseous, carbon dioxide (CO_2) rich environment, which promotes rapid stiffening of the green product into a structural medium within minutes (Lange 1997). In addition, the binding of toxic metals may occur as the carbonating product rapidly solidifies. The consequent significant improvement in the chemical and physical properties of the CO_2 treated materials can facilitate re-use in a variety of construction applications. The accelerated carbonation of hazardous wastes is an example of controlled version of the otherwise naturally occurring process. Thus the following sections differentiate what is natural carbonation and what is accelerated carbonation.

(a) Natural Carbonation

The utilization of natural carbonation for the formation of carbonated cementitious systems is not new. Alkaline earth hydroxide cements and mortars, which harden due to their reaction with atmospheric CO_2, have been used in construction for thousands of years. However, the development of strength in these calcareous cements is slow and uneven due to the low partial pressure of CO_2 in the atmosphere (which is only0.03–0.06% v/v), and the slow rate of diffusion of CO_2 into the cement matrix (Bukowski and Berger 1979).

In service, ordinary Portland cement based materials are usually exposed to percolating ground water or infiltrated rainwater and, therefore, subjected to corrosion. If the water contains CO_2, the effect is that carbonic acid neutralizes alkalizes in the pore water. The calcium silicate hydrate (C–S–H) gel, which is the dominant hydration product resulting from normal hydration of Portland cement, is dissolved by the acidic environment, consequently affecting the leachability characteristics and the durability of cementitious products over time. As acid attack proceeds, a considerable amount of dissolution of primary cementitious phase and the precipitation of secondary phase results. The main secondary mineral, $CaCO_3$, is formed by the combination of moist CO_2 with Ca^{2+}, which is mobilized via the dissolution of calcium hydroxide (Portlandite), and from the decalcification of the gel phase, C–S–H (Bonen and Sarkar 1995, Chen et al. 2009).

(b) Accelerated Carbonation of Cementitious Materials

When applied to compacted systems, such as mortars, carbonation takes place mainly in the outer portions of the monoliths. The initial reaction upon the exposure to CO_2 appears to be an accelerated hydration of the silicates to form a C–S–H-like gel and calcite. After 3 minutes of carbonation, the amount of C_3S reacted is similar to that after 12 hours of hydration (Shao, Mirza, and Wu 2006, Young, Berger, and Breese 1974). The stoichiometry of the initially formed C–S–H gel is similar to that found in conventional hydration. Further reaction results in progressive carbonation of the gel with the consequent decrease in its calcium content. However, the strength development in the compacted mortar exposed to CO_2 is much more rapid than during normal hydration (Sorochkin, Shchurov, and Safonov 1975), and experiments have shown that approximately 1000 kg/cm^2 is obtained within 15 minutes in carbonated Portland cement paste, confirming the potential of carbonation to accelerate the hardening of thin-walled materials (Verbeck 1958).

1.4 Research Objectives

In the grand scheme of atmospheric anthropogenic carbon emission containment, recent studies indicated that there are potentially huge quantities of fossil fuel remains underground. Atmospheric CO_2 saturation may reach before the depletion of fossil fuel. Therefore, there is a need for diverse storage options.

This research will focus on the unconventional CCS technique, especially, in the use of storage capacity of the most common building material, namely, cement.

This research uses gas diffusion coupled chemical reactions phenomena in cement based porous material as its research starting point. The research goal is to understand carbon dioxide gas diffusion and its mineral carbonation in porous cement material. This understanding will help in the design of the carbon sequestering material. These research methods will be based on experimental works, theoretical analysis and numerical simulation. The major research will focus on the processes include CO_2 gas diffusion behavior in porous material, mineral carbonation effect on diffusion coefficient and the coupling system kinetic behavior in gas diffusion and chemical reaction. The following are the research objects:

(1) To establish an experimental method to study CO_2 gas diffusion and chemical reaction in cement based porous material

Based on the principle of volumetric sorption method, a constant temperature pressurized chemical reaction chamber (CTPRC) is developed to study the sorption process. By measuring CO_2 pressure variation in CTPRC system, we could calculate how much CO_2 is consumed in the system according to the gas state and equilibrium equations. The changing characteristics of the mineral carbonation with different initial conditions such as water-binder ratio, CO_2 pressure and sample porosity, can then be investigated.

(2) To establish evidence of carbonation using microcosmic-test on carbonated cement based porous material

In this part, Environment Scanning Electron Microscope (ESEM) is used to study samples' microstructure, the distribution of pores and carbonate crystallization degree which those samples were made with different initial conditions. In addition, X-ray Diffraction (XRD) method is used to analysis the mineral composition which could help us understand CO_2 diffusion and chemical reaction in cement based porous material.

(3) To develop an algorithm to study CO_2 diffusion and chemical reaction in cement based porous material

Cement hydration reaction and mineral carbonation reaction in cement based porous material were reasonably simplified, and chemical reaction kinetics theory is introduced to analysis the mass concentration variation for each chemical component. According to mass conservation of cement chemical components in the process of chemical reaction and gas diffusion, reaction rate equations were established, which contain seven reaction rate and ten kinds of chemical component mass concentration. A numerical method is developed to determine the effects of chemical component concentration field, reaction rate field, diffusion rate field, diffusion coefficient field and sample porosity.

(4) To develop a coupled system dynamics model about CO_2 gas diffusion, hydration reaction, carbonation reaction and sample deformation system response computation method was designed and a response calculation code was programmed. The system responses were calculated with different initial and boundary conditions, and comparatively analyzed to determine the distribution of stress, strain, displacement, components mass concentration and reaction rate with different water-binder ratios, initial gas pressure and sample porosities.

1.5 Research Methodology and Scope of Work

According to the research objective outlined, this research would explain carbon dioxide gas diffusion and its mineral carbonation in porous cement material on the basis of experimental method, theoretical analysis and numerical method. The research methodology is conceptualized in Figure 1.6. Please note that an experimental design (CTPRC) has been developed during this study. CTPRC is used to generate the base line data that are compared to the numerical analysis results. Several experiments have been performed in this study, but only six different experiment types will be used to validate the multi-physical sorption model and the numerical scheme developed.

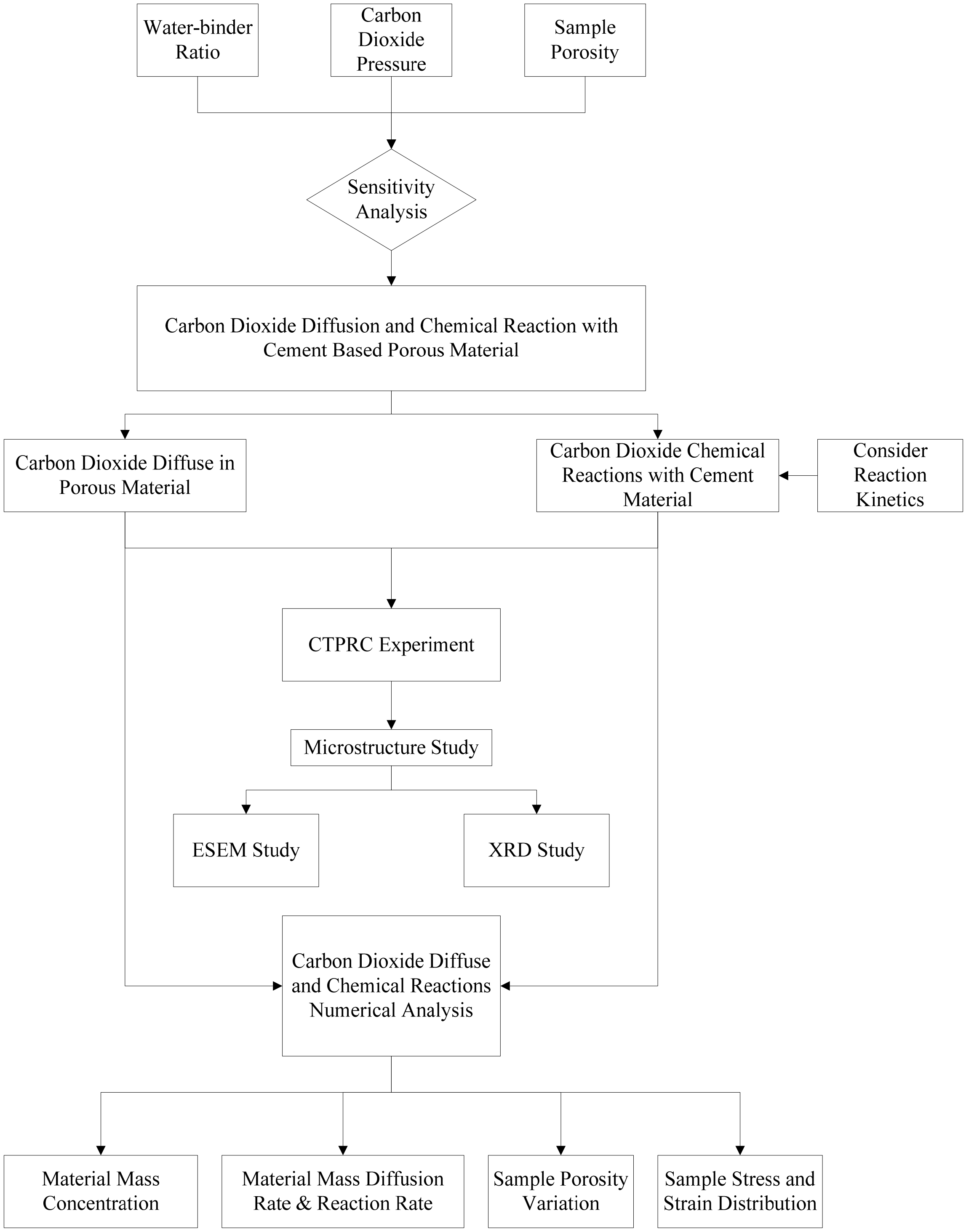

Figure 1.6: Research courses

1.6 Outline of Dissertation

Chapter 1 of this dissertation introduced the subject of study and the research objectives. Chapter 2 described the fundamental theory that describes the gas diffusion process and the participating chemical reactions involved in the CO_2 sorption process of the porous cementitious material. Chapter 3 of this dissertation described the experimental design of the CTPRC test and the results; Chapter 4 outlined the numerical code that computes the sorption outcomes based on a simplified version of the fundamental multi-physical model (chapter 2). Chapter 5 shows examples of simulation results which were used in a comparative study presented in chapter 6. Finally chapter 7 concludes current study and outlines future study plans.

CHAPTER 2: FUNDAMENTAL THEORY OF GAS DIFFUSION AND CHEMICAL REACTION KINETICS IN PORE MEDIUM

2.1 Introduction

Chapter 1 of this dissertation laid out a call for investigation of a cement material that can rapidly receive CO_2 into itself and, thus, demand an understanding of how cement materials are formed and how CO_2 can be trapped within the material matrix. As a man-made material, cement (whatever composition it maybe) is typically calcium-rich and formed in initial gel-like state and gradually hardened to form the solid building block. Hence, study cement material mineral carbonation, especially during the fresh cement mortar stage, when the material is still wet and transiting from gel to solid state, we need to understand the CO_2 diffusion and chemical reaction process involved in the material forming stage.

During the procedure of cement material solidification, CO_2 is diffusing through the pore structure in the sample; meanwhile, it involved a series of chemical reactions with the components of the cement solidification material. Some solid matter will be generated due to water and gas being consumed during the chemical reaction involved in the hydration process. From a physical science perspective, this phenomenon will result in a variety of porosities and diffusion coefficients, which will bring about changes of CO_2 diffusion velocities and concentration ratios. In return, the variety of CO_2 concentration ratios and diffusion velocities will cause changes in the concentration of the reaction products. Therefore, there is a coupling effect exist between the gas diffusion and chemical reactions. Figure 2.1 shows the critical elements dictating the coupling effect between gas diffusion and chemical reaction which are influenced by porosity, diffusion, CO_2 mass concentration and other chemical component concentrations involved in the reactions, respectively

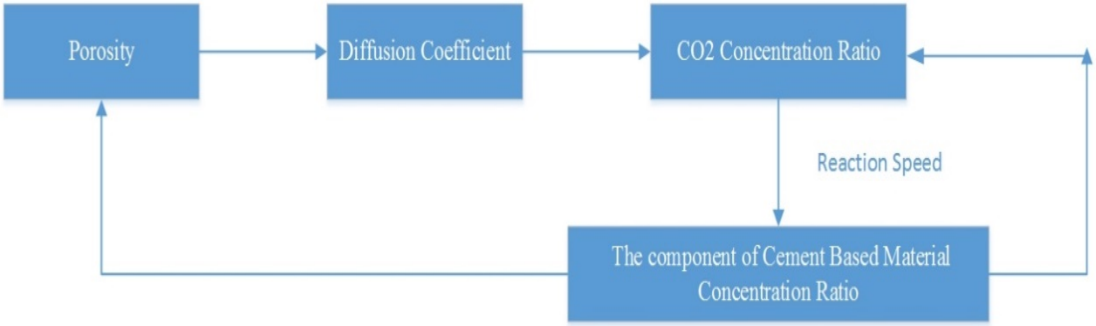

Figure 2.1: Coupling relationships between the gas diffusion and chemical reaction

This chapter will present a basic theory frame of the coupling relationship between gas diffusion and chemical reaction which is based on the fundamental theories of gas diffusion law and chemical reaction kinetics.

2.2 Gas Diffusion in Porous Medium

There is a noteworthy difference between the gas diffusion in porous material and cavity space: Consider the size of pore passage, the shape of the pore structure and fluid pressure, there are three kinds of gas diffusion in porous material, namely, molecular diffusion, Knudsen diffusion and transition zone diffusion (Kärger and Valiullin 2011, Millington 1959).

When the capillary channel diameter, d_p, is much larger than the molecular average free path, l: ($\frac{l}{d_p} \le \frac{1}{100}$), the proportion of the impact between the gas molecules and capillary channel is very small. So the diffusion mechanism is quite similar to molecular diffusion. When the molecular average free path, l, is much larger than the capillary channel diameter d_p ($\frac{l}{d_p} \geq 10$), the proportion of the impact between the gas molecules and capillary wall is larger than the molecular collisions (Evans III, Watson, and Mason 1961). This kind of diffusion is called Knudsen diffusion. The transition zone diffusion is between the molecular diffusion and Knudsen diffusion.

All those three diffusions are complying with the Ficks law with the only difference is their diffusion coefficients (Jaynes and Rogowski 1983, Webb and Pruess 2003). To derive the diffusion equation, we start by building a space coordinate (shown in Figure 2.2) in the porous medium ($O - x_1, x_2, x_3$), where the base vector is e_i $(i = 1,2,3)$. For the steady state diffusion, the relationship between the diffusion velocity $\vec{J}$ and mass concentration ρ can be assumed to be proportionate:

$$\vec{J} = -D\vec{\nabla}\rho \tag{2.1}$$

where, $\vec{\nabla} = \vec{e}_i \frac{\partial}{\partial x_i}$ is the Hamilton operator and D is the effective diffusion coefficient; the negative sign means the gas is diffused from high concentration to low concentration. The above equation is the vector form of Fick’s first law of diffusion.

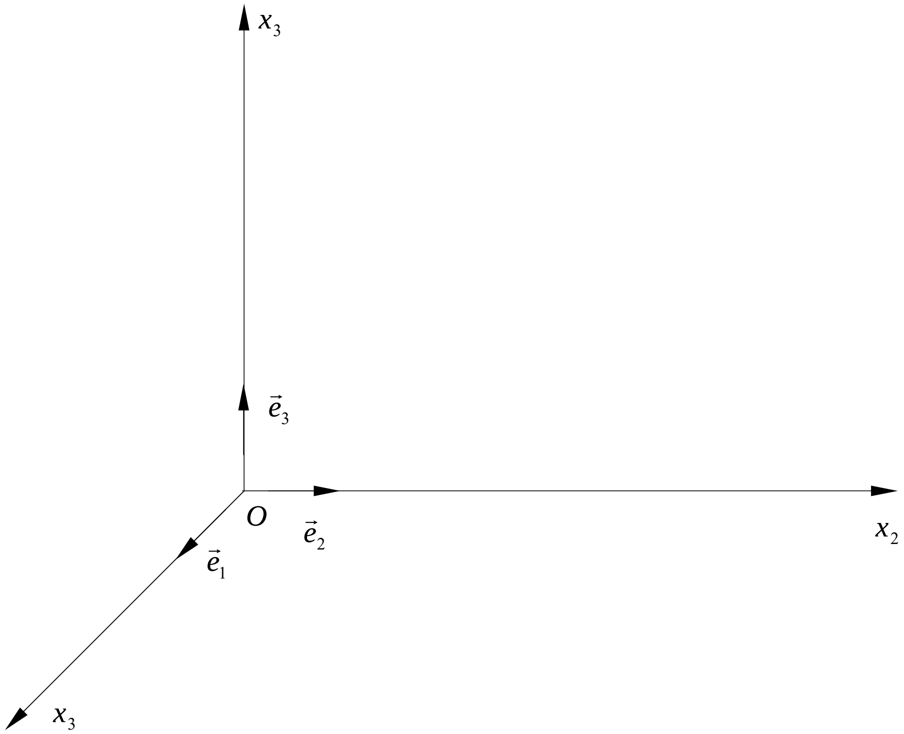

Figure 2.2: Space coordinates and base vector

For the unsteady state diffusion, the relationship between the gradient of the concentration and the divergence of the diffusion flux is also proportional.

$$\frac{\partial \rho}{\partial t} = -\vec{\nabla} \cdot \vec{J} \tag{2.2}$$

Substitute equation (2.2) into equation (2.1), we can get

$$\frac{\partial \rho}{\partial t} = \vec{\nabla} \cdot (D\vec{\nabla}\rho) \tag{2.3}$$

Equation (2.3) implied mass conservation during the diffusion process, and can be further shown that:

$$\vec{\nabla} \cdot (D\vec{\nabla}\rho) = \left(\vec{\nabla}D\right) \cdot \vec{\nabla}\rho + D\left(\vec{\nabla} \cdot \vec{\nabla}\right)\rho \tag{2.4}$$

For a homogeneous medium, $\vec{\nabla}D = \vec{0}$, the equation (2.4) can be simplified as:

$$\frac{\partial \rho}{\partial t} = D\Delta\rho \tag{2.5}$$

where $\Delta = \vec{\nabla} \cdot \vec{\nabla} = \frac{\partial^2}{\partial x_i \, \partial x_i}$ is the Laplace operator.

In reality, porosity and effective coefficient are both heterogeneous. So the component form of equation (2.3) can be shown to be:

$$\frac{\partial \rho}{\partial t} = \frac{\partial}{\partial x_i}\left(D \frac{\partial \rho}{\partial x_i} \right) \tag{2.6}$$

The effective diffusion coefficient is dependant on the porosity, the coefficient of tortuosity and temperature. We can derive the effective diffusion equation which is based on capillary model and thermodynamic theory for bulk diffusion, Knudsen diffusion and transition zone diffusion. However, because the complexity and time-dependent nature of the pore structure, there is a potential danger of generating errors if we use directly the equation. Instead, we will use an empirically derived effective diffusion coefficient equation directly from lab experiments.

GaO et al. (2012) showed that the relationship between the chloride ion effective diffusion coefficient (D) and porosity in cement based material can be defined as:

$$D = a_0 + a_2 \phi^2 \tag{2.7}$$

Li and Liu (1999) established that an empirical relationship between the tortuosity factor (β) and porosity:

$$\beta = \left(2 - \phi\right)^{1.5} \phi^{0.5} \tag{2.8}$$

For this study, we adopt the empirical form and define the relationship between the effective diffusion coefficient and porosity as:

$$D = \left(2 - \phi\right)^{-1.5} \phi^{0.5} \tag{2.9}$$

Due to $\phi << 2$， so

$$\left(2-\phi\right)^{-1.5}=\frac{1+0.75\phi}{2\sqrt{2}} \tag{2.10}$$

Substitute equation (2.10) into equation (2.9), we get:

$$D=\frac{\sqrt{2}}{4}\left(1+0.75\phi\right)\phi^{0.5} \tag{2.11}$$

Consider the correlation between diffusion coefficient and porosity, we could use power function to represent the relationship between porosity and diffusion coefficient.

$$D=D_r\left(\frac{\phi}{\phi_r}\right)^{p_d} \tag{2.12}$$

where, ϕ_r is the reference value of porosity, superscript p_d is the power exponent， D_r is diffusion coefficient corresponding to the reference porosity ϕ_r .

2.3 Reaction Rate Equation

During the process of CO_2 gas penetrating into the sample, the gas will have a series of chemical reactions with the components of the cement based material. The combined action of gas diffusion and chemical reaction will cause changes to the porosity, CO_2 gas concentration and the component concentration within the sample. Unfortunately, stoichiometric equations can only describe the mass scale in reactants and resultants; therefore, reaction kinetics is needed to describe the changing processes of gas concentration. We will introduce the reaction order, the reaction rate and the rate coefficient that contribute to the reaction rate equation (Connors 1990, Levenspiel 1999).

Chemical thermodynamic successfully forecasts the spontaneous direction of chemical reaction and defined the limitation of chemical reaction. Many chemical reactions are instantaneous, for instance, blasting of explosives and acid-base neutralization, etc. On the other hand, some chemical reactions are too slow to visualize. For example, at temperature 298K, hydrogen and oxygen gas would react to generate water, the chemical reaction is spontaneous. However, the same reaction does not seem to occur in normal pressure and temperature (NPT) condition. And like steel rusting and rock weathering, the reaction is too slow to observe. The rate of chemical reaction is controlled by chemical reaction kinetics. The chemical reaction kinetics is the science to study the reaction rate and mechanism during the chemical reaction. There are several parameters that affect the reaction rate, including the concentration of reactant, environment pressure, and temperature.

During the chemical reaction process, the reactant concentration and reaction rate will decrease as time increases (Connors 1990, Levenspiel 1999). In chemical reaction kinetics, for A and B reactions, reaction rate is described as the concentration variation in unit time. The reaction rate can be expressed either as the reactant consumption rate or resultant formation rate:

$$\mathrm{aA+bB} \rightarrow \mathrm{dD+eE} \tag{2.13}$$

The consumption rates are $v(\mathrm{A}) = -\Delta c(\mathrm{A})/\Delta t,\ v(\mathrm{B}) = -\Delta \mathrm{c}(\mathrm{B})/\Delta t$, the formation rates of resultants D, E are $v(\mathrm{D}) = \Delta c(\mathrm{D})/\Delta t,\ v(\mathrm{E}) = \Delta c(\mathrm{E})/\Delta t$. We can rewrite the equation as:

$$v = \frac{1}{a}v(\mathrm{A}) = \frac{1}{b}v(\mathrm{B}) = \frac{1}{d}v(\mathrm{D}) = \frac{1}{e}v(E) \tag{2.14}$$

where v is the consumption rates, a, b, d and e are stoichiometric coefficients. The unit of the reaction rate is $\mathrm{mol/(dm^3 \cdot s)}$.

2.3.1 Elementary Reaction

We defined the following elementary reaction,

$$m_1 A_1 + m_2 A_2 + m_3 A_3 = m_4 A_4 + m_5 A_5 + m_6 A_6 \tag{2.15}$$

Assuming the molecular weight is $\mu_i \ (i = 1, 2, \cdots, 6)$ for material $A_i \ (i = 1, 2, \cdots, 6)$, so the relationship between the reactant consumption amount $M_i \ (i = 1, 2, 3)$ and the resultant formation amount $M_i \ (i = 4, 5, 6)$ is given as:

$$M_1 : M_2 : M_3 : M_4 : M_5 : M_6 = m_1 \mu_1 : m_2 \mu_2 : m_3 \mu_3 : m_4 \mu_4 : m_5 \mu_5 : m_6 \mu_6 \tag{2.16}$$

where m_i is a proportional coefficient. In elementary reaction, the reactant consumption rate can be varied, and the resultant formation rate can also be varied and both can be expressed as:

$$\xi = \pm \frac{1}{m_i \mu_i} \frac{\partial \rho_i}{\partial t} \tag{2.17}$$

For the reactant reaction $(i = 1,2,3)$, the right hand side of the above equation is set as negative. For resultant $(i = 4,5,6)$, the right hand side of the equation is set as positive. Now we can define the stoichiometric coefficient as:

$$c^i = \begin{cases} -m_i \ , i = 1, 2, 3 \\ m_i \ , i = 4, 5, 6 \end{cases} \tag{2.18}$$

where superscript i is the material type. Equation (2.17) is then rewritten as:

$$\xi = \frac{1}{c^i \mu_i} \frac{\partial \rho_i}{\partial t} \tag{2.19}$$

The mass concentration $\rho_i \ (i = 1, 2, \cdots, 6)$ satisfies the following:

$$\rho_1 : \rho_2 : \rho_3 : \rho_4 : \rho_5 : \rho_6 = m_1 \mu_1 : m_2 \mu_2 : m_3 \mu_3 : m_4 \mu_4 : m_5 \mu_5 : m_6 \mu_6 \tag{2.20}$$

After the reaction is finished, if the mass of the reactant $A_i\ (i=1,2,3)$ is zero, we call this kind of reaction as a complete reaction (Kondrat'Ev 2013). Its mass fraction can is given as:

$$Y_i = \frac{\rho_i}{\rho_1 + \rho_2 + \rho_3} (i=1,2,3) \tag{2.21}$$

The reactant mass fraction in a stoichiometry equation is given as:

$$Y_i^{\mathrm{stoi}} = \frac{m_i \mu_i}{m_1 \mu_1 + m_2 \mu_2 + m_3 \mu_3} (i=1,2,3) \tag{2.22}$$

Equate (2.21) to equation (2.22), we get:

$$Y_i = \frac{\rho_i}{\rho_1 + \rho_2 + \rho_3} (i=1,2,3) = Y_i^{\mathrm{stoi}} = \frac{m_i \mu_i}{m_1 \mu_1 + m_2 \mu_2 + m_3 \mu_3} (i=1,2,3) \tag{2.23}$$

In general, the masses of reactant and resultant usually do not meet the above condition. For this reason, we introduce the following coefficient to describe the shortage and overage of the reactant.

$$\zeta_i = \frac{Y_i}{Y_i^{\mathrm{stoi}}} (i=1,2,3) \tag{2.24}$$

And $\zeta_i > 1$ means the reactant is overage, $\zeta_i < 1$ means the reactant is shortage. Equation (2.24) can be rewritten as:

$$\zeta_i = \min\left\{\zeta_1, \zeta_2, \zeta_3\right\} \tag{2.25}$$

The reaction rate is determined by the concentration of the reactant.

$$\xi = k \rho_1^{\lambda_1} \rho_2^{\lambda_2} \rho_3^{\lambda_3} \tag{2.26}$$

where, k represents the reaction rate coefficient, $\lambda_i \ (i=1,2,3)$ represents the reaction order of the reactant $A_i \ (i=1,2,3)$, and $\lambda = \sum_{i=1}^{3} \lambda_i$ represents the total reaction order.

The reaction rate coefficient and reaction order are obtained from the experiments. In order to simplify the calculation and analysis of dynamic process, we could pre-set the reaction order as a first order reaction (Gillespie 2007), and consider using time-dependent ρ_{i^*} to determine the reaction rate. Thus, the reaction rate equation becomes:

$$\xi = k\rho_{i^*} \tag{2.27}$$

Therefore, the reaction order of reactant $A_i \ (i=1,2,3)$ can be simplified as:

$$\lambda_i = \begin{cases} 1, & \text{if } i = i^* \\ 0, & \text{if } i \neq i^* \end{cases} \tag{2.28}$$

Substitute equation (2.26) to equation (2.19), and modify slightly the equation, we get:

$$\frac{\partial \rho_i}{\partial t} = kc^i \mu_i \rho_1^{\lambda_1} \rho_2^{\lambda_2} \rho_3^{\lambda_3} \ (i = 1, 2, \cdots, 6) \tag{2.29}$$

This is the reaction rate equation, which be further expanded into:

$$\begin{cases} \frac{\partial \rho_1}{\partial t} = -m_1 \mu_1 \xi = -m_1 \mu_1 k \rho_1^{\lambda_1} \rho_2^{\lambda_2} \rho_3^{\lambda_3} \\ \frac{\partial \rho_2}{\partial t} = -m_2 \mu_2 \xi = -m_2 \mu_2 k \rho_1^{\lambda_1} \rho_2^{\lambda_2} \rho_3^{\lambda_3} \\ \frac{\partial \rho_3}{\partial t} = -m_3 \mu_3 \xi = -m_3 \mu_3 k \rho_1^{\lambda_1} \rho_2^{\lambda_2} \rho_3^{\lambda_3} \\ \frac{\partial \rho_4}{\partial t} = m_4 \mu_4 \xi = m_4 \mu_4 k \rho_1^{\lambda_1} \rho_2^{\lambda_2} \rho_3^{\lambda_3} \\ \frac{\partial \rho_5}{\partial t} = m_5 \mu_5 \xi = m_5 \mu_5 k \rho_1^{\lambda_1} \rho_2^{\lambda_2} \rho_3^{\lambda_3} \\ \frac{\partial \rho_6}{\partial t} = m_6 \mu_6 \xi = m_6 \mu_6 k \rho_1^{\lambda_1} \rho_2^{\lambda_2} \rho_3^{\lambda_3} \end{cases} \tag{2.30}$$

As explained previously, the reaction rate equations actually describe the mass conservation relationship.

2.3.2 Chain Reaction

In practical engineering problems, the causality of an outcome is typically resulted from a series of chemical reactions. Thus, a set of chain reaction rate equations can be established to solve the gas diffusion problem (Bamford and Tipper 1973, Semenov 1935):

$$\sum_{j=1}^{N_2} c_s^{ij} A_j = 0, (i = 1, 2, \cdots, N_1) \tag{2.31}$$

where, N_1 represent the number of reactions, and N_2 represent the number of reactant components. Stoichiometric coefficients, C_s^{ij} $(i = 1, 2, \cdots, N_1; j = 1, 2, \cdots, N_2)$, is represented by two dimensional array. Assume the molecular weight $\mu_j (j = 1, 2, N_2)$ of material $A_j (j = 1, 2, N_2)$ and concentration $\rho_j (j = 1, 2, N_2)$, equation (2.31) becomes (Cussler 2009, Loitsyanskiy and Nunn 1995):

$$\frac{\partial \rho_j}{\partial t} = \sum_{i=1}^{N_1} c_s^{ij} \mu_j \xi_i \ , \ (i = 1, 2, \cdots, N_1 \ , \ j = 1, 2, \cdots, N_2) \tag{2.32}$$

the reaction rate can be given as:

$$\xi_i = k \rho_1^{\lambda_1^i} \rho_2^{\lambda_2^i} \cdots \rho_{N_2}^{\lambda_{N_2}^i} \ , \ (i = 1, 2, \cdots, N_1) \tag{2.33}$$

where, λ_j^i represents the reaction order in i reaction equation with j material $(i = 1, 2, \cdots, N_1 \, ; \, j = 1, 2, \cdots, N_2)$.

2.4 Mass Conservation in Gas diffusion and Chemical Reaction Procedure

Considering the chain reaction in pore medium, the reaction rate equation can be given as equation(2.32). Let j_g represents the gas reactant material, and the gas not only has the chemical reaction with other components, but also diffuses through the pore structure, we can assume gas diffusion coefficient as D. The mass conservation equation for the gas reactant can then be written as:

$$\frac{\partial \rho_{j_g}}{\partial t} = \sum_{i=1}^{N_1} c^{ij_g} \mu_{j_g} \xi_i + \vec{\nabla} \cdot \left(D \vec{\nabla} \rho_{j_g} \right) \tag{2.34}$$

For other components, the mass conservation equation will be:

$$\frac{\partial \rho_j}{\partial t} = \sum_{i=1}^{N_1} c^{ij} \mu_j \xi_i \ , \ (j = 1, 2, \cdots, j_g - 1, j_g + 1, \cdots, N_2) \tag{2.35}$$

2.5 Gas Diffusion and Chemical Reaction Coupled with Pore Medium Deformation Dynamics

The gas diffusion and chemical reaction have an effect on pore medium deformation which includes different variations on porosity, strength, and Young's modulus and Poisson's ratio. Figure 2.3 shows the impacts from different parameters on the deformation, diffusion and reaction processes.

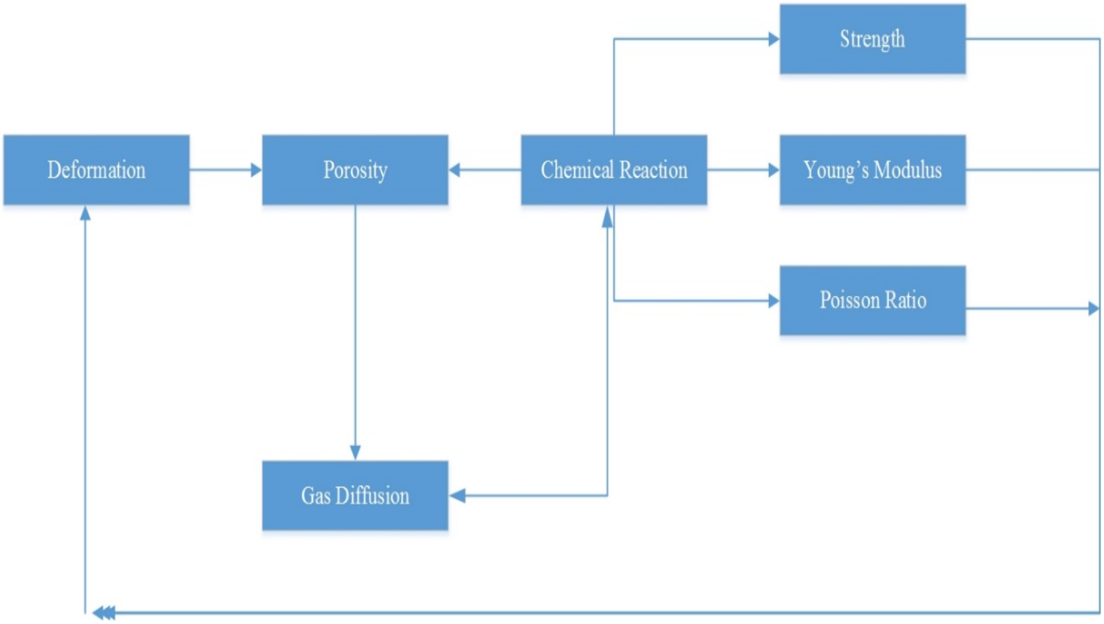

Figure 2.3: Impact among the deformation, diffusion and chemical reaction

2.5.1 Fundamental Equation of Pore Medium Deformation

To establish the deformation equation, Figure 2.4 shows the line segment unit $\delta\vec{x}$, which takes the position AB at a t moment, and the velocity at A point is $\vec{v}$. Due to the continuity within the deformed state, the velocity at point B will be $\vec{v}+\frac{\partial\vec{v}}{\partial\vec{x}}\cdot\delta\vec{x}$. When the time goes through dt, the position will become $A'B'$, so the substantial derivative can be given as:

$$\frac{D}{Dt}\left(\delta\vec{x}\right)=\frac{\delta\vec{x}\big|_{t+dt}-\delta\vec{x}\big|_{t}}{dt}=\frac{\overrightarrow{A'B'}-\overrightarrow{AB}}{dt}=\frac{\overrightarrow{BB'}-\overrightarrow{AA'}}{dt}=\frac{\partial\vec{v}}{\partial\vec{x}}\cdot\delta\vec{x} \qquad (2.36)$$

Based on Helmholtz decomposition theorem (Fujiwara and Morimoto 1977, Nield and Bejan 2013), the motion can be divided in three parts which include translation motion, rotation motion and deformation motion. Deformation motion and rotation motion are controlled by deformation rate tensor $\vec{B}$ and rotation tensor $\vec{Z}$. Assume the base vector $\vec{e}_i\ (i=1,2,3)$ is in the $O-x_1x_2x_3$ coordinates, so that the deformation rate tensor and rotation tensor can be given as:

$$\vec{\vec{B}}=\frac{1}{2}\left[\left(\frac{\partial\vec{v}}{\partial\vec{x}}\right)+\left(\frac{\partial\vec{v}}{\partial\vec{x}}\right)^T\right]=\frac{1}{2}\left(\frac{\partial v_i}{\partial x_j}+\frac{\partial v_j}{\partial x_i}\right)\vec{e}_i\,\vec{e}_j \tag{2.37}$$

$$\vec{\vec{Z}}=\frac{1}{2}\left[\left(\frac{\partial\vec{v}}{\partial\vec{x}}\right)-\left(\frac{\partial\vec{v}}{\partial\vec{x}}\right)^T\right]=\frac{1}{2}\left(\frac{\partial v_i}{\partial x_j}-\frac{\partial v_j}{\partial x_i}\right)\vec{e}_i\,\vec{e}_j \tag{2.38}$$

Then, introducing the permutation symbol,

$$\varepsilon_{ijk}=\vec{e}_i\cdot\left(\vec{e}_j\times\vec{e}_k\right) \tag{2.39}$$

The rotation tensor can then be given as:

$$\vec{\omega}=\frac{1}{2}\vec{\nabla}\times\vec{v}=\frac{1}{2}\vec{e}_k\varepsilon_{kij}\frac{\partial v_j}{\partial x_i} \tag{2.40}$$

For any nonzero vector $\vec{u}$, the following relation always hold:

$$\vec{\vec{Z}}\cdot\vec{u}=\vec{\omega}\times\vec{v} \tag{2.41}$$

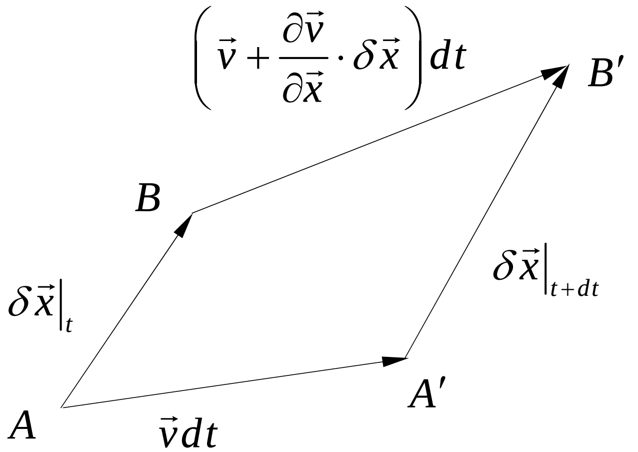

Figure 2.4: Line segment units

The relationship among displacement, velocity and acceleration can be given as:

$$\frac{\partial\vec{u}}{\partial t}=\vec{v} \tag{2.42}$$

$$\frac{\partial \vec{v}}{\partial t} = \vec{a} \tag{2.43}$$

The relationship between strain $\overleftrightarrow{S}$ and the deformation rate $\overleftrightarrow{B}$ can be given as:

$$\frac{\partial \overleftrightarrow{S}}{\partial t} = \overleftrightarrow{B} \tag{2.44}$$

The relationship between stain and displacement can be written as:

$$\overleftrightarrow{S} = \frac{1}{2}\left[\left(\frac{\partial \vec{u}}{\partial \vec{x}}\right) + \left(\frac{\partial \vec{u}}{\partial \vec{x}}\right)^{T}\right] = \frac{1}{2}\left(\frac{\partial u_i}{\partial x_j} + \frac{\partial u_j}{\partial x_i}\right)\vec{e}_i\,\vec{e}_j \tag{2.45}$$

Assume the body force $\vec{b}$ on the solid particle in the pore medium, the effective stress tensor is $\overleftrightarrow{T}^{\text{eff}}$, the pore pressure is p, the equivalent pore pressure coefficient is α, the mass density is m_s. So the momentum conservation can be written as:

$$m_s \frac{\partial \vec{v}}{\partial t} = \vec{\nabla} \cdot \left(\overleftrightarrow{T}^{\text{eff}} - \alpha p \overleftrightarrow{E}\right) + \vec{b} \tag{2.46}$$

In the above equation, $\overleftrightarrow{E} = \delta_{ij}\vec{e}_i\,\vec{e}_j$ represents Young's modulus as the second-order unit tensor, and ν is Poisson's ratio. During the gas diffusion and chemical reaction process, the concentration of the reactant components is changed over time. The variation potential of component concentration will cause changes in Young's modulus ($\overleftrightarrow{E}$) and Poisson's ratio (ν). Gas diffusion and chemical reaction happen very slow in the carbonation process, so we can assume the effective stress component and strain component still comply with the generalized Hooke law (Boresi, Schmidt, and Sidebottom 1993, Nur and Byerlee 1971):

$$\overleftrightarrow{T}^{\text{eff}} = \lambda\left(\vec{\nabla} \cdot \vec{u}\right)\overleftrightarrow{E} + 2G\overleftrightarrow{S} \tag{2.47}$$

Here, Lame's coefficients are representing as:

$$\lambda = \frac{E\nu}{(1+\nu)(1-2\nu)}, \; G = \frac{E}{2(1+\nu)} \tag{2.48}$$

where E represents Young's modulus, ν represents the Poisson's ratio. Then, we can get the effective stress as:

$$\vec{\Sigma}^{\text{eff}} = \lambda\left(\vec{\nabla}\cdot\vec{u}\right)\vec{E} + G\left[\left(\frac{\partial\vec{u}}{\partial\vec{x}}\right) + \left(\frac{\partial\vec{u}}{\partial\vec{x}}\right)^T\right] \tag{2.49}$$

the component of equation (2.49) can be written either as:

$$\sigma_{ij}^{\text{eff}} = \lambda\varepsilon_{kk}\delta_{ij} + 2G\varepsilon_{ij} \tag{2.50}$$

or

$$\sigma_{ij}^{\text{eff}} = \lambda\frac{\partial u_k}{\partial x_k}\delta_{ij} + G\left(\frac{\partial u_i}{\partial x_j} + \frac{\partial u_j}{\partial x_i}\right) \tag{2.51}$$

2.5.2 Mass Conservation Relationship amongst Pore Medium Deformation, Gas Diffusion and Chemical Reaction

The volume on a unit element is defined as $\delta\Omega_0$ and $\delta\Omega$ at $t=0$. Based on the continuum mechanics theory, we have:

$$\delta\Omega = J\delta\Omega_0 \tag{2.52}$$

where,

$$J = \left|\delta_{ij} + \frac{\partial u_i}{\partial x_j}\right| \tag{2.53}$$

and,

$$\frac{DJ}{Dt} = J\vec{\nabla}\cdot\vec{v} \tag{2.54}$$

Let the initial porosity and mass density be m_s^0 and ϕ_0. ϕ and m_s represent the porosity and mass density at current moment. The initial solid skeleton volume and current moment solid skeleton volume can be written as $\phi_0 \delta\Omega_0$, and $\phi\delta\Omega$. The mass can be represented as $m_s^0(1-\phi_0)\delta\Omega_0$ and $m_s(1-\phi)\delta\Omega$. Due to the fact that the gas will react with the solid skeleton component; the solid skeleton mass will change in the unit element. The substantial derivative can be given as:

$$\frac{D}{Dt}\left(m_s(1-\phi)\delta\Omega\right)=\frac{Dm_s}{Dt}\left(1-\phi\right)\delta\Omega-m_s\frac{D\phi}{Dt}\delta\Omega+m_s\left(1-\phi\right)\frac{D}{Dt}\left(\delta\Omega\right) \qquad (2.55)$$

According to the theory of continuum mechanics, the substantial derivative on the unit element is given as:

$$\frac{D}{Dt}\left(\delta\Omega\right)=\left(\vec{\nabla}\cdot\vec{v}\right)\delta\Omega_0 \qquad (2.56)$$

Substitute both equations (2.52) and (2.56) to equation (2.55), we get:

$$\frac{D}{Dt}\left(m_s(1-\phi)\delta\Omega\right)=\frac{Dm_s}{Dt}\left(1-\phi\right)J\delta\Omega_0-m_s\frac{D\phi}{Dt}J\delta\Omega_0+m_s\left(1-\phi\right)\left(\vec{\nabla}\cdot\vec{v}\right)\delta\Omega_0 \quad (2.57)$$

For a small deformation problem, we have $J=1+\frac{\partial u_k}{\partial x_k}$. So equation (2.57) can be simplified as:

$$\begin{aligned}&\frac{D}{Dt}\left(m_s(1-\phi)\delta\Omega\right)\\&=\left[\frac{Dm_s}{Dt}\left(1-\phi\right)\left(1+\frac{\partial u_k}{\partial x_k}\right)-m_s\frac{D\phi}{Dt}\left(1+\frac{\partial v_k}{\partial x_k}\right)+m_s\left(1-\phi\right)\left(\vec{\nabla}\cdot\vec{v}\right)\right]\delta\Omega_0\end{aligned} \qquad (2.58)$$

Gas diffusion will not change the solid skeleton mass. However, it will cause the solid skeleton component concentration to vary. Then, the mass variation rate can be shown as:

$$\frac{D}{Dt}\left(m_s(1-\phi)\delta\Omega\right)=\sum_{\substack{i=1\\i\neq j_g}}^{N_2}\frac{\partial\rho_i}{\partial t}\left(1-\phi\right)\delta\Omega=\sum_{\substack{i=1\\i\neq j_g}}^{N_2}\frac{\partial\rho_i}{\partial t}\left(1-\phi\right)J\delta\Omega_0 \qquad (2.59)$$

Substitute equation (2.59) into equation (2.58), we get

$$\begin{aligned}&\frac{Dm_s}{Dt}(1-\phi)\left(1+\frac{\partial u_k}{\partial x_k}\right)-m_s\frac{D\phi}{Dt}\left(1+\frac{\partial v_k}{\partial x_k}\right)+m_s(1-\phi)\left(\vec{\nabla}\cdot\vec{v}\right)\\&=\sum_{\substack{i=1\\ i\neq j_g}}^{N_2}\frac{\partial\rho_i}{\partial t}(1-\phi)J\end{aligned}\tag{2.60}$$

This is the mass conservation equation under the combined effects of solid skeleton deformation, gas diffusion and chemical reaction. If $\frac{Dm_c}{Dt}$ is very small, then, $\phi << 1$, $\frac{\partial u_k}{\partial x_k} << 1$, and equation (2.60) can be simplified as:

$$\frac{D\phi}{Dt}=\frac{\partial v_k}{\partial x_k}-\frac{1}{m_s}\sum_{\substack{i=1\\ i\neq j_g}}^{N_2}\frac{\partial\rho_i}{\partial t}\tag{2.61}$$

Then, we could get:

$$\frac{D\phi}{Dt}=\frac{\partial v_k}{\partial x_k}-\frac{1}{m_s}\vec{\nabla}\cdot\left(D\vec{\nabla}\rho_{j_g}\right)\tag{2.62}$$

2.6 Summary

In this chapter, first we discussed the gas diffusion behavior in porous material. Then we explained the mass concentration will cause the characteristics of the chemical components under the interaction of gas diffusion and chemical reaction. We then get the law of conservation of mass， law of conservation of momentum and deformation kinetics for the solid skeleton under the joint interaction of gas diffusion, chemical reaction and solid skeleton deformation. Thus, a theoretical framework for the design and analysis of the kinetic model of CO_2 gas diffusion and chemical reaction in cement based porous material is established. The following are assumptions made in the formulation:

(1) We assumed that the molecular diffusion is a gas diffusion type in porous material. The law of conservation of mass during gas diffusion is described by Fick's law. By considering the relationship between gas diffusion coefficient and permeability, we can express the gas diffusion coefficient as the exponential function of the porosity.

(2) During the chain chemical reaction, only gas material is involved in both gas diffusion and chemical reaction. Other chemical compounds just take part in the chemical reaction. Each of the chemical reaction should be recognized as a first order reaction, which means the sum of the reaction order in the certain reaction equation should be one.

(3) The variation of material mass concentration brings on porosity changes, and then causes the diffusion coefficient change. Hence, the change of diffusion coefficient acts back to the change of material mass concentration. Meanwhile, the gas reacts with other chemical components, and its mass concentration would also have the corresponding changes. This is the coupling mechanism between gas diffusion and chemical reaction.

(4) Both of the skeleton deformation and material mass concentration variations would cause the change in porosity. And the change of porosity would effect on gas diffusion coefficient and the effective stress of the solid skeleton. The gas diffusion coefficient would cause differences in the chemical material mass concentration, and the skeleton effective stress brings on the change of skeleton displacement. This is the coupling mechanism among gas diffusion, chemical reaction and solid deformation.

CHAPTER 3: CO_2 MINERAL CARBONATION IN CEMENT BASED POROUS MATERIAL EXPERIMENTAL STUDY

3.1 Experimental Design Principle

Carbon always presents in CO_2 and other carbonated compounds as a highly-charged element where upon these carbon-containing compounds are relatively stable. However, CO_2 is not the most stable compound with carbon. As shown in Figure 3.1, the standard Gibbs free energy of carbonated compounds are lower than $60 \sim 180\text{kJ} \cdot \text{mol}^{-1}$ from the standard Gibbs free energy of CO_2 (Kondrat'Ev 2013). Hence, the most stable existence for carbon element should be carbonated compounds. Therefore, the most security and energy efficient way to sequestrate CO_2 is to turn CO_2 into carbonated compounds.

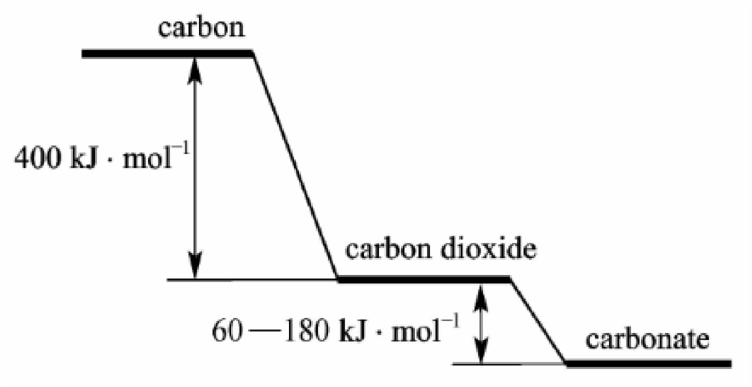

Figure 3.1: Gibbs energy state of carbon

3.1.1 Theoretical Basis for Carbonation Measurement

For most mineral sequestration techniques, the core reaction is the carbonation process. For a solid to be suitable for accelerated carbonation, it must have the right kind of chemical and physical properties. Hence, we first describe the carbonation mechanism.

Ionised carbon dioxide induced solvation of calcium ions from the solid phases, which then re-precipitated in the pore space of the mixtures as $CaCO_3$, forming a solidified product. The entire process is strongly exothermic and is diffusion-controlled. The gas diffused into the solid resulting in a growing front of carbonated materials surrounding an inner zone of non-carbonated material. The conceptual model for the reaction of carbon dioxide is presented in Figure 3.2 (Huijgen and Comans 2003, Metz et al. 2005, O'Connor et al. 2002, Oelkers, Gislason, and Matter 2008).

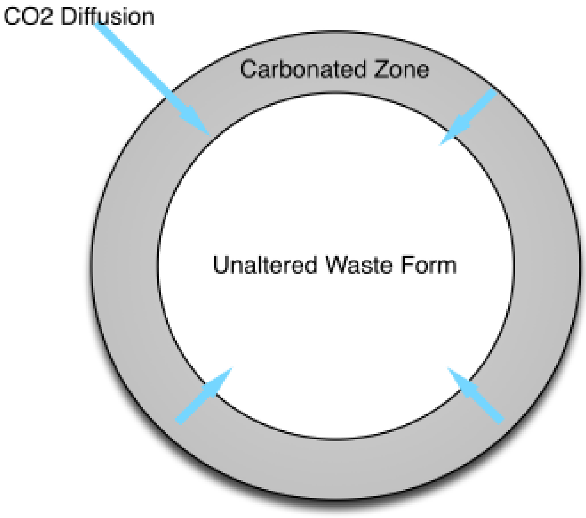

Figure 3.2: Schematic of carbonation process

The carbonation process for cementitious materials is a little more complicated and involves the following sequential mechanisms as illustrated in Figure 3.3, which shows the steps are:

(1) Diffusion of CO_2 in air space.

(2) Permeation of CO_2 through the gel mixture.

(3) Solvation of $CO_{2(g)}$ (CO2 gas) to $CO_{2(aq)}$ (aqueous carbon dioxide – a dissolved gas). Throughout the process, boundary layer transfer is favoured by a high internal surface area of solid.

(4) Hydration of $CO_{2(aq)}$ to H^+, HCO_3^- and CO_3^{2-}. This occurs almost instantaneously, making the pH fall by approximately 3 units (typically from 11 to 8).

(5) Dissolution of cementitious elements, C_3S and C_2S. Portland cement is a heterogeneous, fine grained material consists of four main solid elements, namely tricalcium silicate (C_3S), dicalcium silicate (C_2S), calcium silicate hydrate (C-S-H) gel and calcium hydroxide ($Ca(OH)_2$). During the hydration, calcium silicate hydrate (C-S-H) gel and calcium hydroxide ($Ca(OH)_2$) are formed from the silicates C-S-H, which is a major hydration product representing the main strength forming phase in the cement paste. $Ca(OH)_2$ is a crystalline, isotropic structural element with natural mineral Portlandite. The cement hydration reactions are:

$$2(CaO\cdot SiO_2)+6H_2O\rightarrow 3CaO\cdot 2SiO_2\cdot 3H_2O+3Ca(OH)_2 \tag{3.1}$$

$$2(2CaO\cdot SiO_2)+4H_2O\rightarrow 3CaO\cdot 2SiO_2\cdot 3H_2O+Ca(OH)_2 \tag{3.2}$$

Because this process is cyclic, this step is rapid and extensive, and generates considerable amounts of heat (exothermal). The calcium silicate grains are covered by a loose layer of calcium silicate hydrate gel, which is quickly dissolved, releasing Ca^{2+} and SiO_4^{4-} ions.

(6) Nucleation of $CaCO_3$ into C-S-H. The nucleation is favoured by slightly high temperatures and the presence of finely divided material, which acts like a heterogeneous nuclei:

$$Ca(OH)_2 + CO_2 \rightarrow CaCO_3 + H_2O \tag{3.3}$$

Note the production of water at this stage, which is essential to the cyclic carbonation process.

(7) Precipitation of solids. At the beginning, vaterite and aragonite can found, but these polymorphs of $CaCO_3$ ultimately revert to calcite. Amorphous calcium carbonate can be found in the final product of the following process.

$$3CaO \cdot 2SiO_2 \cdot H_2O + 3CO_2 \rightarrow 3CaCO_3 \cdot 2SiO_2 \cdot 3H_2O \tag{3.4}$$

(8) Secondary carbonation. C-S-H gel forms and is progressively decalcified, converting ultimately to S-H and $CaCO_3$ through the following reactions,

$$C_3S + 3CO_2 + \gamma H_2O \rightarrow SiO_2 \cdot \gamma H_2O + 3CaCO_3 \tag{3.5}$$

$$C_2S + 2CO_2 + \gamma H_2O \rightarrow SiO_2 \cdot \gamma H_2O + 2CaCO_3 \tag{3.6}$$

It is important to recognize that regular cement is used in the experiments conducted throughout this study, which consists of many complex chemical elements. The above processes described are key elements that dictate the experimental outcomes and also considered in the later numerical simulation described in Chapter 5.

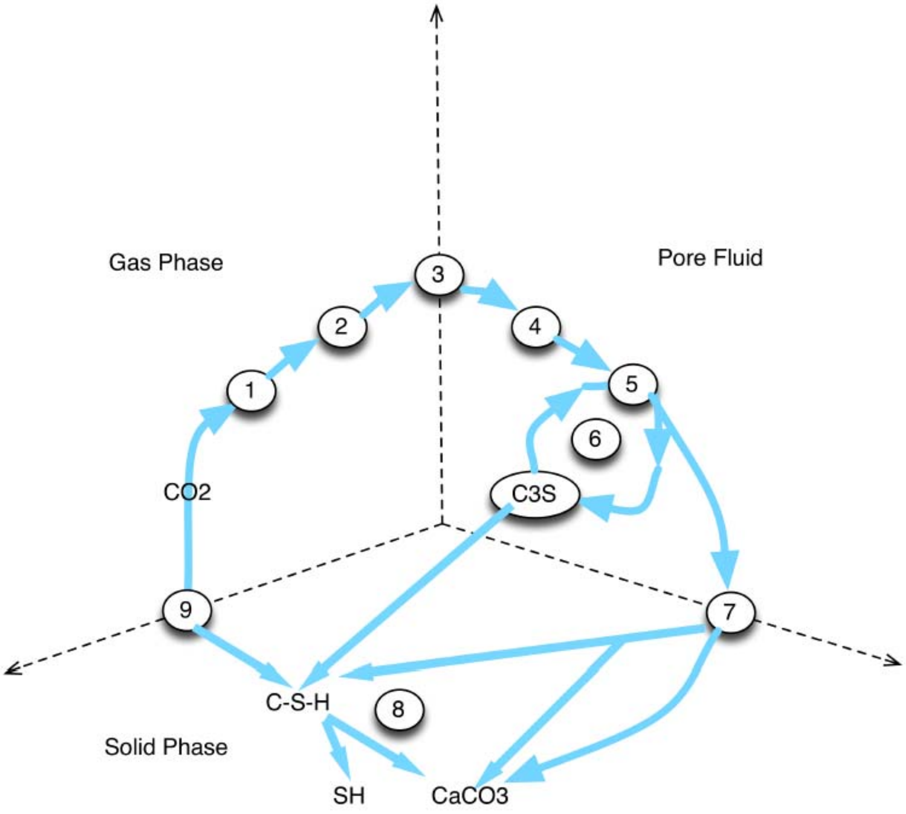

Figure 3.3: Proposed mechanisms for cement based material accelerated carbonation

3.1.2 Experiment Methodology Review

In this section, we first review different gas sorption measurement techniques and our own experimental design will be introduced in section 3.2.

3.1.2.1 Manometric Method

The manometric method is commonly used for measuring gas physisorption capacities on coal sample (Gensterblum et al. 2010, Keller and Staudt 2005, Krooss et al. 2002, Nodzeński 1998, O'Connor et al. 2002, Romanov, Soong, and Schroeder 2006, Siemons and Busch 2007). The experimental setups are either custom made or designed in-house and match standard calibrated reference and sample cells. Pressure and temperature sensors are either connected to the sample cell (reference) only or to both cells. To analyze physisorption from methane (CH_4), the composition of the mixed gas is set to be measured by using gas chromatographic equipment. Either sample or reference cells or both are connected to the GC through a sampling valve. A basic schematic of this setup is provided in Figure 3.4.

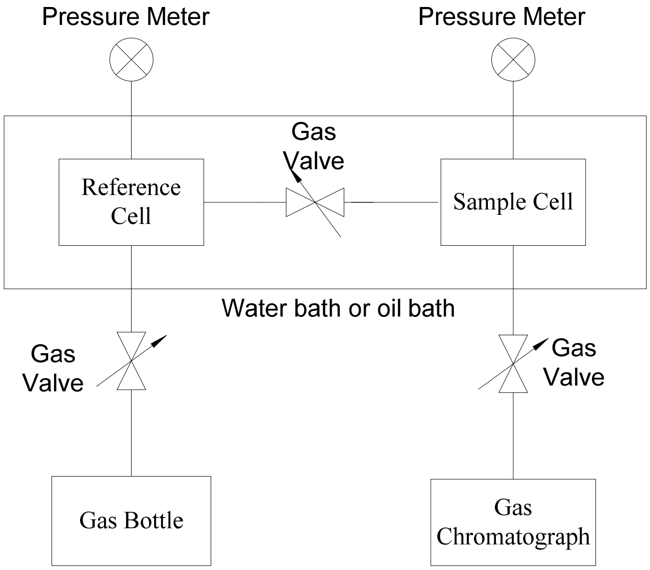

Figure 3.4: Schematic diagram of manometric gas sorption device

In the manometric procedure, defined amounts of gas are successively transferred from a calibrated reference volume into the sample cell containing the sample. Prior to the sorption experiment, the void volume ($\mathrm{V}^0_{\mathrm{void}}$) of the sample cell is determined by expansion of a "non-sorbing" gas, which is typically helium. Helium densities are calculated using the equation of state (EOS) by McCarty and Arp (1990) or using the van-der Walls equation with the "a" and "b" parameters reported by Michels, Wouters, and De Boer (1936). This procedure also provides the skeletal volume ($\mathrm{V}^0_{\mathrm{sample}}$) and the skeletal density (ρ^0_{sample}) of the sample.

For gas sorption isotherms, the void volume multiplied by the density of the gas phase ($\mathrm{V}^0_{\mathrm{void}} \cdot \rho^{\mathrm{CO_2}}\left(\mathrm{T,p}\right)$), yields the "non-sorption" reference mass. Densities are calculated using the corresponding EOS for CO_2, CH_4, N_2 or their binary and ternary mixtures (Kunz et al. 2006, Peng and Robinson 1976, Setzmann and Wagner 1991). The excess sorption mass ($m_{excess}^{CO_2}$) is the difference between the mass of gas that has been transferred into the measuring cell up to a given pressure step and a "non-sorption" reference mass:

$$m_{excess}^{gas} = m_{transferred}^{gas} - V_{void}^{0} \cdot \rho^{gas}\left(T,p\right) \tag{3.7}$$

The mass transferred from the reference cell into the measuring cell during N successive pressure steps is given by:

$$m_{transferred}^{gas} = \sum_{i=1}^{N} V_{ref} \cdot \left(\rho_i^{gas}\left(p_{i,}T\right) - \rho_{i-1}^{gas}\left(p_{i-1},T\right)\right) \tag{3.8}$$

3.1.2.2 Volumetric Method

The volumetric method is similar to the manometric method and the results have frequently been published by several researchers (Fitzgerald et al. 2005, Gasem et al. 2002, Ozdemir, Morsi, and Schroeder 2003, Reeves et al. 2005). A simplified scheme of the experimental apparatus is shown in Figure 3.5. The reference and sample cell sections of the apparatus are maintained in two constant temperature water baths. Similar to the manometric method, the sample is placed in the sample cell, the volume of which is determined using helium as non-sorbing gas. The isotherm is determined by continuously decreasing the volume in the piston pump and thus increasing the gas pressure. The amount of gas injected is determined by an accurate reading of the volume changes of the pump. By adjusting the piston pump volume, sorption quantities can be determined at defined pressures while for the manometric method (with fixed reference and void volumes) the equilibrium pressure depends on the reference to sample cell volume, ratio and the pressure change in the reference cell. The amount of gas injected, $m_{gas}^{injected}$, can be determined from the pump position as it moves forward:

$$m_{gas}^{adsorbed} = m_{gas}^{injected} - m_{gas}^{unadsorbed} \tag{3.9}$$

$$m_{gas}^{injected} = \left(\frac{p \Delta V M}{ZRT} \right)_{pump} \tag{3.10}$$

$$M_{gas}^{unadsorbed} = \left(\frac{p V_{void} M}{ZRT} \right)_{sample\ cell} \tag{3.11}$$

where m denotes the mass of gas, p is pressure, T is temperature, M is the molar mass of the gas species, Z is the compressibility coefficient of the pure gas species and R is the universal gas constant. ΔV is the volume change in the pump and V_{void} is the volume of the free gas in the sample cell.

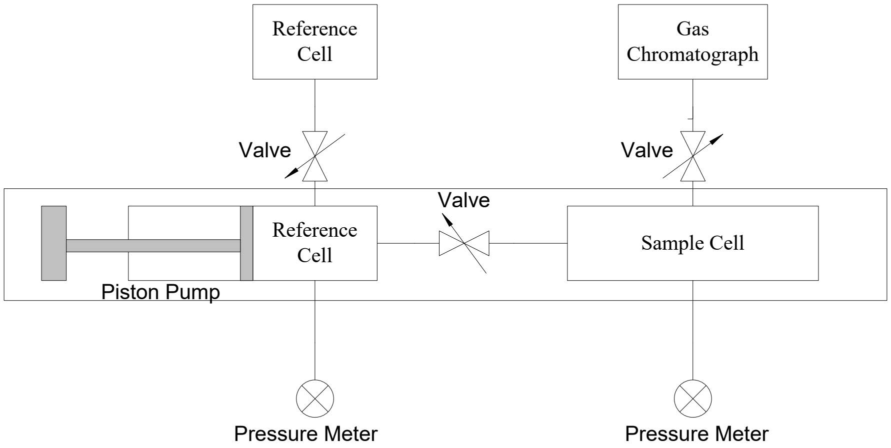

Figure 3.5: Schematic diagram of volumetric gas sorption device

3.1.2.3 Helium as Reference Gas

The gravimetric and the manometric/ volumetric methods use helium (sometimes argon is used) as reference gas to determine the void volume of the sample cell. By definition and experimental practice, they represent differential methods with respect to helium.

Helium is commonly considered as non-sorbing. A small degree of helium sorption (which cannot be excluded but also not quantified) will lead to an underestimation of the sample volume for both methods. Thommes (2010) proposed a method to correct sorption data for helium sorption. Helium sorption, in turn, would result in an error of the excess sorption capacity. As noted by Day, Fry, and Sakurovs (2012), helium sorption, if present, will be in the μmol/g range as compared to CH_4 or CO_2 sorption capacity on cement, which is usually in the mmol/g range and hence can be neglected. Another potential problem in using helium as reference gas is related to the accessibility of the pore space. It is commonly assumed that the same pore volume is accessed by helium as by CO_2 or CH_4. An overview on the state of discussion is provided by Day, Fry, and Sakurovs (2012) and Siemons and Busch (2007).

3.2 Experiment System Design

The following discussion intends to describe a testing technique to determine the CO_2 storage through carbonation of cement based porous material. This cement based porous material is proposed as part of the mineral sequestration approaches to address the issue of anthropogenic CO_2 capture and storage and other waste reductions.

Cement based material would provide the alkaline environment through calcium carbonation to chemically fixate CO_2. To increase CO_2 storage capacity, aluminum powder is added to the mixture to cause percolation, which can increase the void space. The void space would not only give more physical space to store CO_2 gas, but also can provide more gas-solid contact surface for the chemical procedure.

The resulting material is a highly porous cementitious material intended to accelerate sequestration of CO_2 and can be designed to maximize the CO_2 storage capacity through increase of the pore spaces. By injecting CO_2 into cement based porous material, two major processes may be activated for CO_2 storage: chemical absorption and physical adsorption.

The carbonation mechanism is often described as a process comprised of at least two steps that includes a prior CO_2 absorption in water followed by the actual carbonation reaction in aqueous medium. The primary reaction is known to be the $Ca(OH)_2$ carbonation in aqueous medium, which corresponds to:

$$\mathrm{CaO{+}H_2O} \rightarrow \mathrm{Ca\left(OH\right)_2} \tag{3.12}$$

$$\mathrm{Ca\left(OH\right)_2} + \mathrm{CO_2} \rightarrow \mathrm{CaCO_3} + \mathrm{H_2O} \tag{3.13}$$

Physical adsorption occurs when CO_2 saturates the pore space and adheres to the matrix surface. The strength of this material is inversely correlated to the pore space and the CO_2 storage capacity. Thus, this new material can be designed to have competitive sequestration, which means we can increase either chemical absorption or physical adsorption by altering its pore space and calcium contents.

The biggest challenge in this research is to quantify how much and how fast CO_2 can actually be sequestered in this material. Since this material is a man-made material and goes through a process of maturation, traditional sorption tests (manometric/volumetric method) cannot address the multi-phase change. Also during the CO_2 injection process, compressed air (CO_2) may be involved and the porous material may swell due to the air void expansion. Hence, to accurately quantify the CO_2 absorption process and to characterize the manufactured material, a new testing technique is proposed: the CTPRC (constant temperature, pressurized reaction chamber) test.

The CTPRC testing technique isolates temperature effects and can measure the gas absorption volume through pressure change measurements. Figure 3.6, Figure 3.7 and Figure 3.8 show the CTPRC experimental setup and schematics, which involves:

(1) The stainless reaction chamber that can be filled with CO_2 or flue gas and the reaction specimen;

(2) Water bath used in temperature control during physical sorption and chemical reaction procedure;

(3) Instrumental setup showing automated pressure measurements.

Contrast to most gas absorption studies using milligram specimens, CTPRC uses specimens in the gram range, hence, can quantify both chemical and physical absorptions involving sufficiently large volume material.

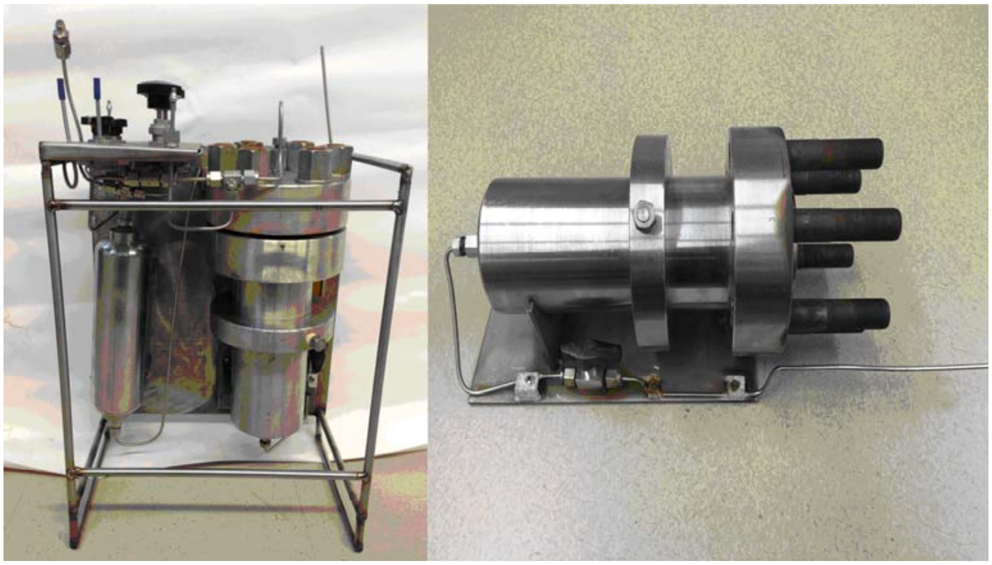

Figure 3.6: Reference cell and reaction cell

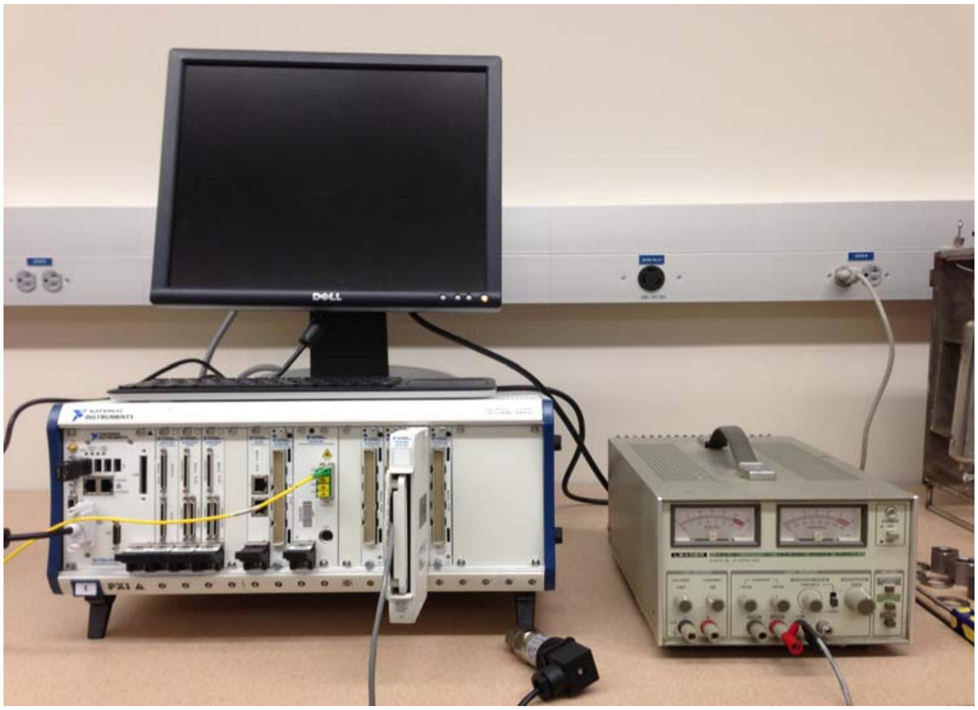

Figure 3.7: Data recording system

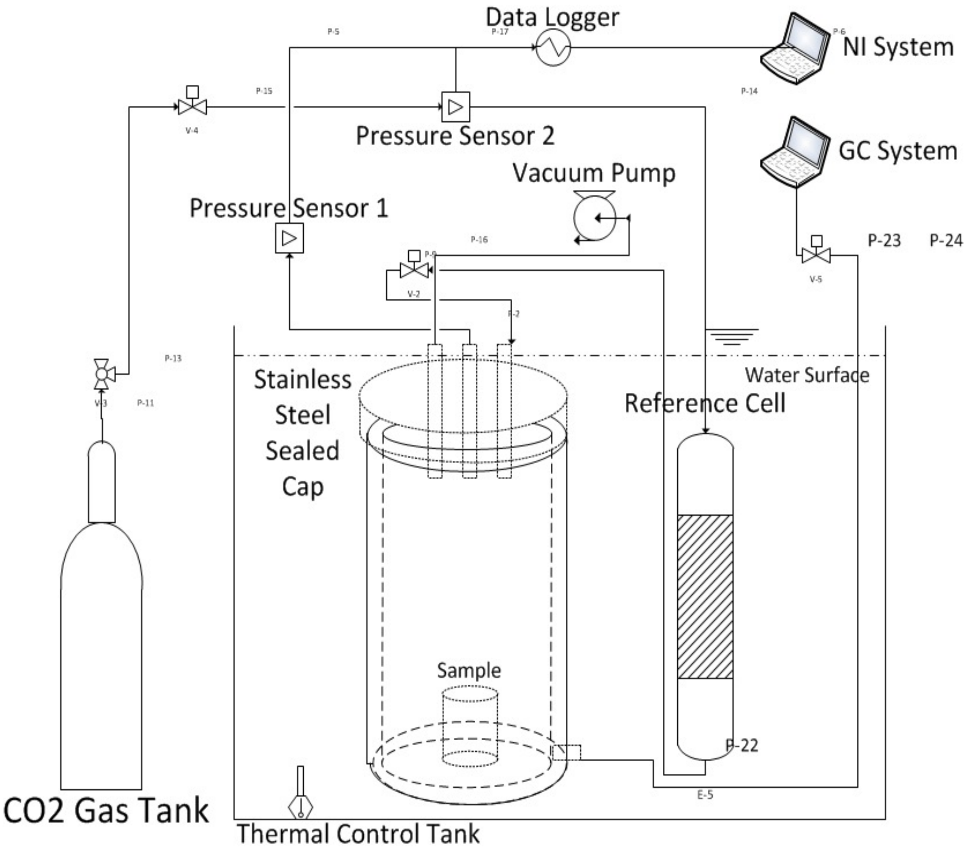

Figure3.8: Schematic diagram of CTPRC device

3.3 Experimental Procedure

The total free volume is the key parameter to calculate the total carbon dioxide sorption value. In the experimental setup, the total free space in the sample cell includes four major parts:

(1) The void space between the sample particles;
(2) The micro-porous in the sample;
(3) The free space left in the sample cell after loading the sample;
(4) The free space in connecting tubes and valves.

In general, there are two methods to measure the total free volume in this experimental setup:

1. Straight-forward method
2. Indirect method

What is called a straight-forward method is using the volume of reference gas to indicate the total void space in the sample cell. First, the unabsorbed gas (helium) will be injected into the sample cell under specified temperature and a specified pressure. And then based on gas expansion effect to calculate the total void volume by ideal gas law.

The indirect method is the use of the total volume in sample cell to subtract the sample volume to get the total void volume. However, this method has some limitations for non-homogeneous porous materials. Not only is the sample structure in this study duo-porous, but the porous distribution will not be homogeneous. So, the true density for the sample cannot be measured by indirect method. That explains why most of the sorption experimental setups choose straight-forward method to determine the void volume.

In this experiment, we will use pure helium gas expansion effect to measure the total void space in the sample cell. First, the air tightness of the experimental system must be tested. We put the sample in the reaction cell, open all the valves in the system, then vacuum the air in the reference cell and sample cell and seal all the valves in the experimental system and maintain the status for 6 hours. During that time, the pressure sensors will record the pressure data for each cell. If the pressure in both cells keeps the same level as the initial status, then it indicates that the experimental system is well sealed. Then we can pump the helium gas into the reference cell and record the pressure P_1 . After this step, the balance valve between the reference cell and sample cell can be reopened. The helium gas will expand into the sample cell. The pressure P_2 will be recorded after the pressure is balanced in both cells. The gas balance equation is then used to calculate the total free space in the experimental system:

$$V_0 = V_r \left(\frac{P_1 T \; Z_2 - P_2 T_1 Z_1}{P_3 T_1 Z_1 - P_1 T_3 Z_3} \right) \tag{3.14}$$

where, P_1 represents the pressure status after the pressure balanced procedure; P_2 represents the initial pressure in the reference cell; P_3 represents the initial pressure in the sample cell; V_r represents the volume of reference cell; V_0 represents the total free volume in the sample cell; T_1 represents the temperature after the pressure balanced procedure; T_2 represents the initial temperature in the reference cell; Z_1 represents the gas compressibility factor under equilibrium condition; Z_2 represents the initial gas compressibility factor in reference cell; Z_3 represents the initial gas compressibility in sample cell.

Before the testing, we have to do a leakage test. Assume the experimental system will require 150psi pressurized CO_2 gas. So, the system will be injected with 150psi CO_2 under constant temperature condition. The data recording system will monitor the system pressure change in 6 hours. If the pressure data from pressure sensor shows that there is no variation in the system, then the experiment can continue.

First, the sample cell and reference cell will be vacuumed and the constant temperature condition will be set up. The CO_2 tank pressure valve and the reference cell valve are then opened the gas will pump from the high pressure CO_2 container to the reference cell. The value on the reference cell is then closed for 5 minutes. The pressure value (P_1^0) is then recorded. After that, open the balance valve between the reference cell and sample cell is then opened and CO_2 in the reference cell will expand from the reference cell into the sample cell. The total amount of CO_2 pumped into the reference cell can be calculated as:

$$n_1^0 = \frac{P_1^0 \cdot V_r}{Z_1^0 \cdot R \cdot T} = \frac{P_1^0 \cdot V_r}{Z_1^0} \cdot \frac{1}{8.375 \cdot (273.15 + t)} \tag{3.15}$$

Where, n_0^1 represents total amount of CO_2 injected into the reference cell; t represents the environmental temperature in CTPRC system; P_1^0 represents the balanced pressure; Z_1^0 represents CO_2 gas compressibility factor under P_1^0 condition.

Keep the system for 48 hours, when the pressure is balanced and record the pressure value (P_1). The remaining CO_2 in the system is then calculated as:

$$n_1 = \frac{P_1 \cdot (V_r + V_0)}{Z_1 \cdot R \cdot T} = \frac{P_1^0 \cdot (V_r + V_0)}{Z_1} \cdot \frac{1}{8.735 \cdot (273.15 + t)} \tag{3.16}$$

where, n_1 represents the left amount of CO_2; P_1 represents the final CO_2 pressure; Z_1 represents the CO_2 compressibility factor at pressure P_1 .

Equation (3.15) is subtracted from Equation (3.16) to calculate how much CO_2 has been consumed:

$$n_1^0 - n_1 = \frac{P_1^0 \cdot V_r}{Z_1^0} \cdot \frac{1}{8.735 \cdot (273.15 + t)} - \frac{P_1^0 \cdot (V_r + V_0)}{Z_1} \cdot \frac{1}{8.735 \cdot (273.15 + t)} \tag{3.17}$$

3.4 Sample Preparation and Experiment Plan

3.4.1 Sample Material and Experiment Plan

The cement used in the experiments is the regular Portland cement. The general chemical and mineral contents can be found in Table 3.1 and 3.2, respectively.

Table 3.1: Chemical composition of Portland cement

Oxide Formula	Shorthand Notation	Percentage by Mass in Cement
CaO	C	65%
SiO_2	S	27%
Al_2O_3	A	5%
Fe_2O_3	F	2%
MgO	M	1%
Source: (Bye 1999)		

Table 3.2: Typical mineralogical composition of modern Portland cement

Chemical Formula	Oxide Formula	Shorthand Notation	Description	Typical Percentage
Ca_3SiO_5	$(CaO)_3 SiO_2$	C_3S	Tricalcium silicate	50-70
Ca_2SiO_4	$(CaO)_2 SiO_2$	C_2S	Dicalcium silicate	10-30
$Ca_3Al_2O_6$	$(CaO)_3 Al_2O_3$	C_3A	Tricalcium aluminate	3-13
$Ca_4Al_2Fe_2O_{10}$	$(CaO)_4 Al_2O_3Fe_2O_3$	C_4AF	Tetracalcium aluminoferrite	5-15
Source:(Bye 1999)				

In the experiment, the cement will mix with water and aluminum powder first, and then the sample placed into the reaction chamber. The mass percentage in Table 3.2 is used to set up the material initial value in numerical simulation (Chapter 5).

There are three key parameters that impact on the carbonation of the cement based porous material: initial sample porosity, initial CO_2 injection pressure and initial water-binder ratio. The experiments conducted here will determine the effects of these three parameters. The experiment plan for each parameter can be found in Figure 3.9, Figure 3.10 and Figure 3.11.

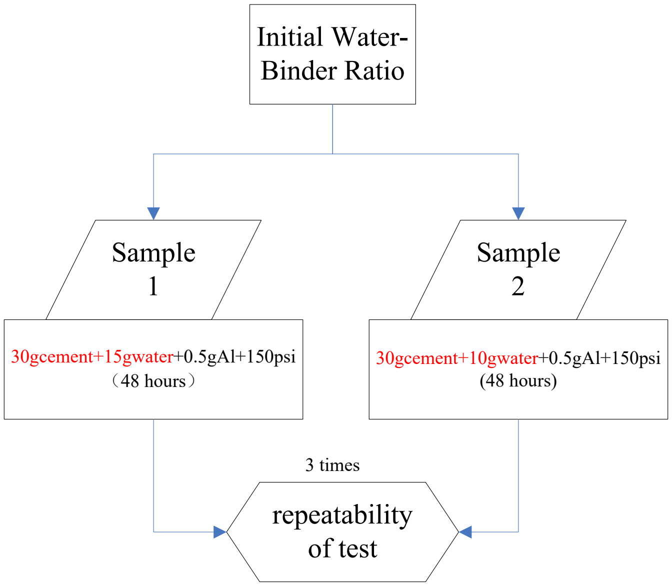

Figure 3.9: Experiment plan for different initial water-binder ratios

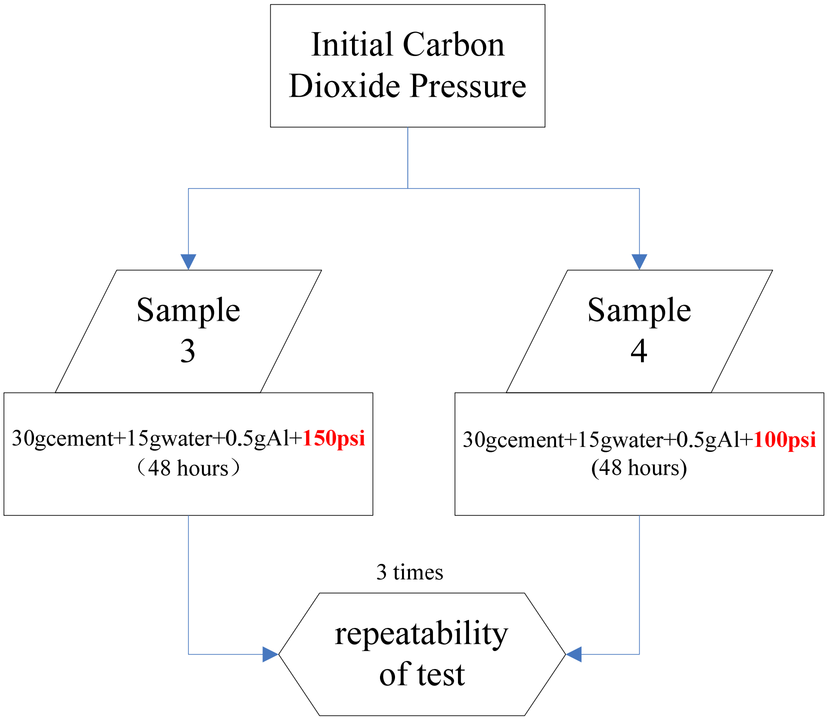

Figure 3.10: Experiment plan for different initial CO_2 injection pressures

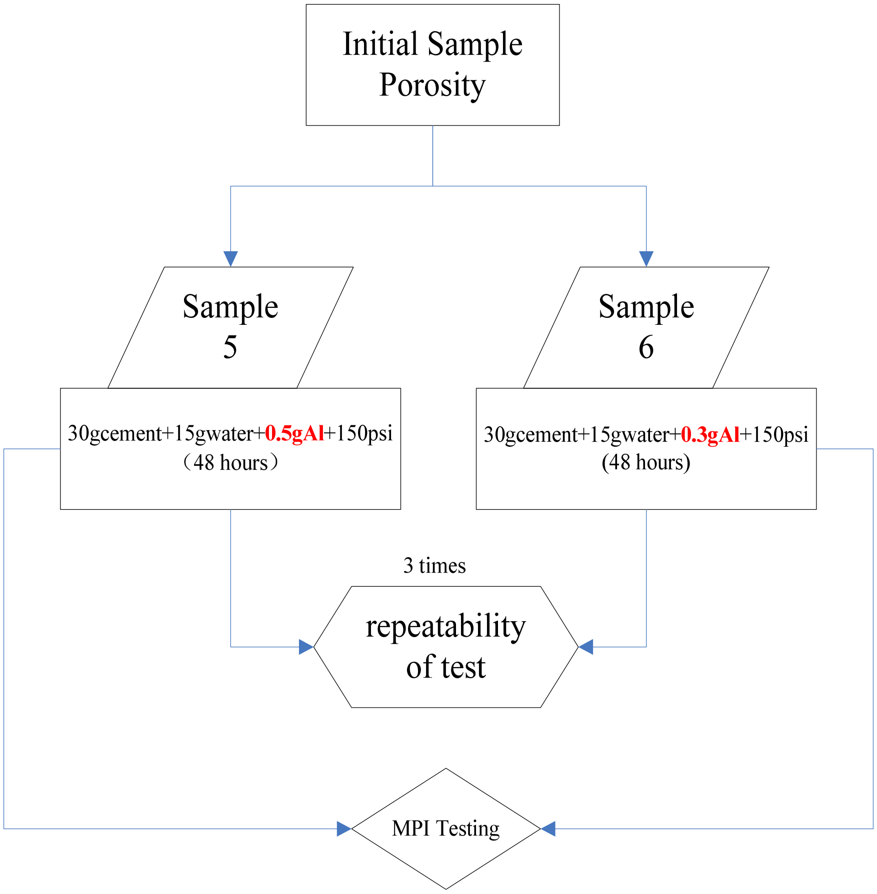

Figure 3.11: Experiment plan for different initial porosities

3.4.2 Sample Post-Analysis Methods

This section explains the quantitative methods need in this study on the samples after each test. The specimens are packed and sampled carefully for each of the testing methods described below:

(1) ESEM micro-structural analysis method

Electronic microscope becomes a powerful tool for studying the mechanism of cement hydration. There are three types of electronic microscope for microstructure research: the transmission electon microscopy (TEM), the high voltage transmission electon microscopy (HVTEM) and the scanning transmission electron microscopy (STEM).

TEM and SEM are the dominant methods for the microstructure research. However, the sample preparation is very complicated for the above methods. For instance, the sample for TEM has to be cut thin enough to get sufficient electronic conductivity, which would cause microscopic damages in the sample. The sample for SEM has to be kept dry and the sample surface has to be coated with an electronic conducting layer. The coating procedure may lose some fine structures. Furthermore, during TEM and SEM testing, the sample needs to be placed in high vacuum environment, which could cause some damages to the sample. For the above reasons, TEM and SEM methods are deemed not suitable for the cement based porous material microstructure study.

Environmental scanning electron microscopy (ESEM) has some unique design like multi-stage vacuum system, etc. Sample preparation is also relatively easy. Furthermore, the sample does not need coating procedure, and monitoring condition needs only low vacuum environment (Ye et al. 2002).

For future comparison and analysis, ESEM pictures will be used to determine $CaCO_3$ and C_3S in the samples. (Figure 3.12 and Figure 3.13)

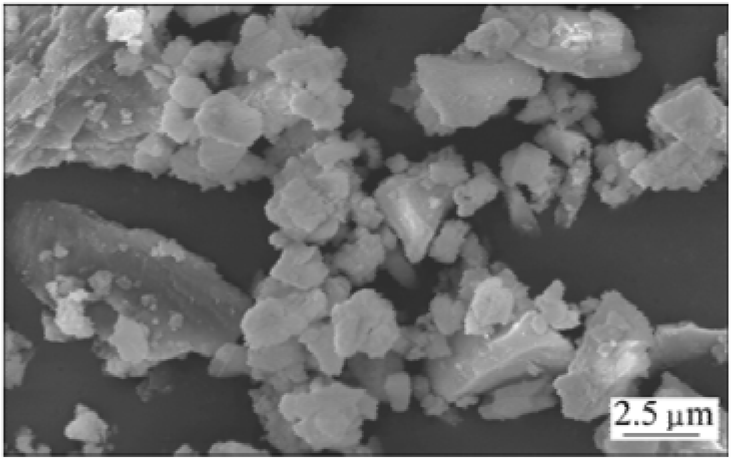

Figure 3.12: Pure C_3S microstructure

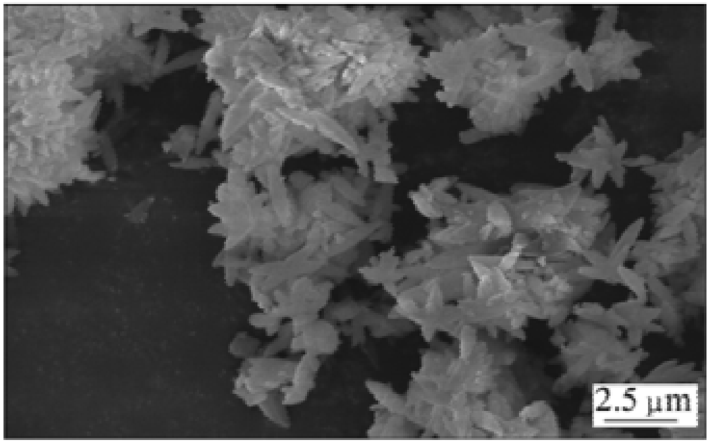

Figure 3.13: Pure $CaCO_3$ microstructure

As shown in Figure 3.12, C_3S crystal has irregular geometry with angular shape and has non-consistent sizes. In Figure 3.13, $CaCO_3$ particle has thin layer shape. Most of the crystals have oblong shapes and pile up into clumps.

(2) X-ray powder diffraction qualitative analysis method

X-ray powder diffraction (XRD) is a rapid analytical technique primarily used for phase identification of a crystalline material and can provide information on unit cell dimensions. The analyzed material is finely grounded, homogenized, and average bulk composition is determined.

Max von Laue, in 1912, discovered that crystalline substances acted as three-dimensional diffraction gratings for X-ray wavelengths similar to the spacing of planes in a crystal lattice. X-ray diffraction (Figure 3.14) is now a common technique for the study of crystal structures and atomic spacing.

X-ray diffraction is based on constructive interference of monochromatic X-rays in a crystalline sample. The X-rays are generated by a cathode ray tube, filtered to produce monochromatic radiation, collimated to concentrate, and directed toward the sample. The interaction of the incident rays with the sample produces constructive interference (and a diffracted ray) when conditions satisfy the Bragg's Law ($n\lambda = 2d\sin\theta$), which relates the wavelength of electromagnetic radiation to the diffraction angle and the lattice spacing in a crystalline sample (Warren 1969). These diffracted X-rays are then detected, processed and counted. By scanning the sample through a range of 2θ angles, all possible diffraction directions of the lattice can be attained due to the random orientation of the powdered material. Conversion of the diffraction peaks to d-spacings allows identification of the minerals, because each mineral has a set of unique d-spacings. Typically, this is achieved by comparison of d-spacings with standard reference patterns (James 2014).

X-ray powder diffraction is most widely used for the identification of unknown crystalline materials (e.g. minerals, inorganic compounds). Determination of unknown solids is critical to studies in geology, environmental science, material science, engineering and biology. Other applications include:

(1) characterization of crystalline materials;

(2) identification of fine-grained minerals such as clays and mixed layer clays that are difficult to determine optically;

(3) determination of unit cell dimensions;

(4) measurement of sample purity.

Figure 3.14: Bruker's X-ray Diffraction Equipment (source: Bruker Company)

3.5 Initial Water-Binder Ratio Effect on CO_2 Mineral Carbonation

3.5.1 Experimental Results

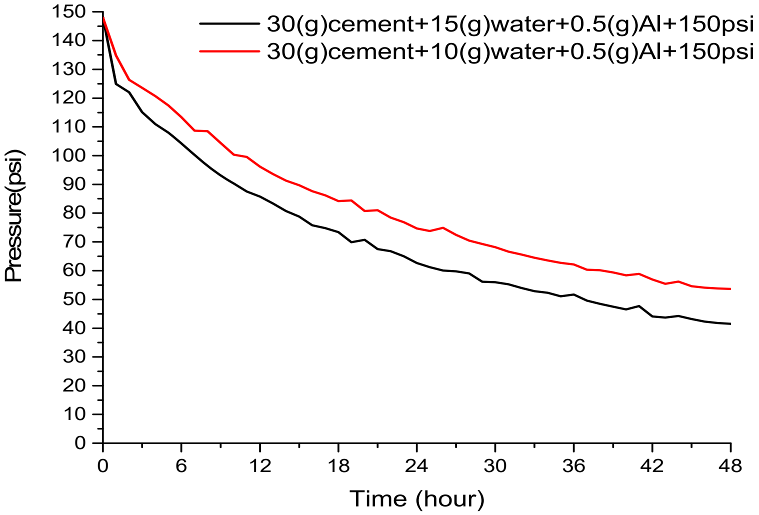

Figure 3.15: CO_2 void space pressure variation with different water-binder ratio

The water-binder ratios in Sample 1 (black curve) and Sample 2 (red curve) are 0.5 and 0.33. Figure 3.15 shows that CO_2 cavum pressure in Sample 1 drops faster than Sample 2. After 48 hours, Sample 1 pressure dropped to 41psi and Sample 2 pressure dropped to 54psi. This result indicates that Sample 1 consumed more CO_2 than Sample 2. This experiment shows that the higher water-binder ratio is, the more CO_2 would be consumed. Table 3.3 shows the weights between the two samples. A CO_2 consumption ratio is needed to quantify the amount of CO_2 sequestered, and is shown in Table 3.3.

Table 3.3: Experiment Result (Sample 1 and Sample 2)

	Mixture Weight	Initial Weight (before experiment)	Final Weight	Increased Weight	Initial CO_2 Weight	CO_2 Consumption Ratio
Sample 1	45.5 (g)	45.48 (g)	45.81 (g)	0.33 (g)	0.80 (g)	41.25%
Sample 2	40.5(g)	40.43 (g)	40.63 (g)	0.20 (g)	0.80 (g)	25.00%

3.5.2 ESEM and XRD Analysis

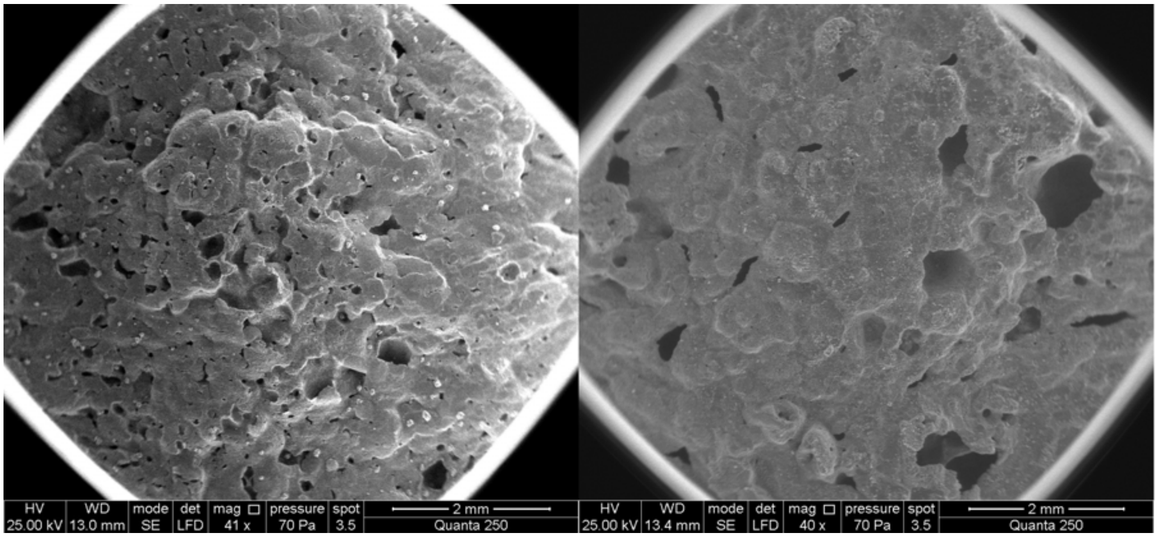

Figure 3.16: ESEM result (sample 1, left image & Sample 2, right image)

Figure 3.16 and Figure 3.17 show the ESEM results for sample 1 and sample 2. As shown in Figure 3.16, there are a lot of voids distributed on the sample surface. Some of the voids appeared to be very shallow shaped and were deep into the material. The deep voids may have the ability to diffuse the CO_2 into the sample. These porous structures increased the gas-solid contact area allowing more chemical reactions (carbonations) to take place.

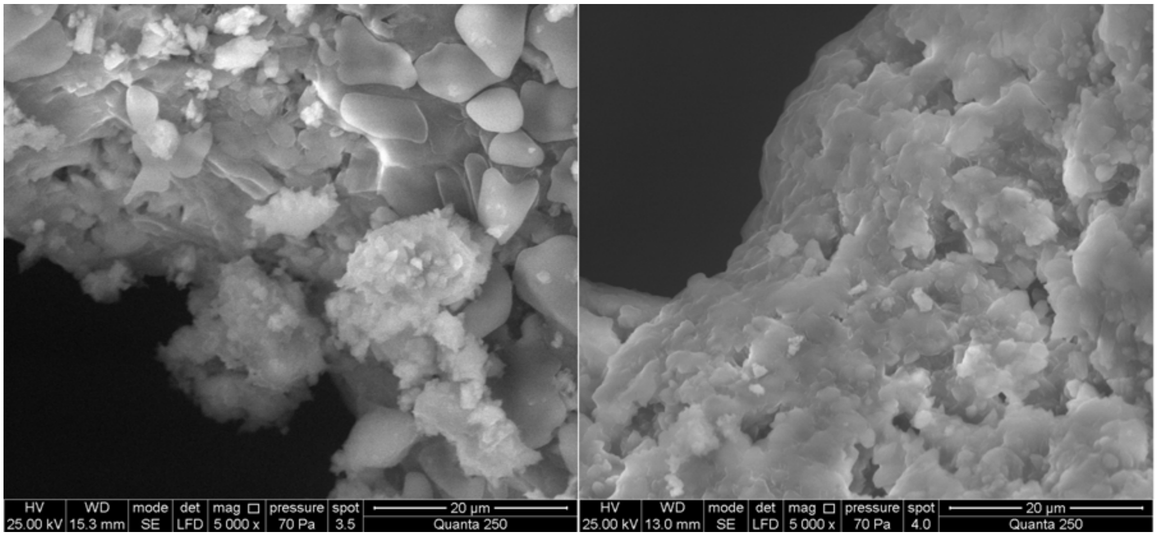

Figure 3.17: Micro-structure comparisons (sample 1 & sample 2)

We randomly pick a micro-void in both of samples and zoomed in (Figure 3.17). It is very clear to see in the left picture that some crystal clumps attached on the surface of the material. The right picture shows that it is very smooth on its inner wall and only limited crystal clumps can be observed. If we compared Figure 3.17 with Figure 3.12 and Figure 3.13, it is obvious that these clumps are actually $CaCO_3$ compounds. Thus, it is concluded that C_3S developed more complete in sample 1 than in sample 2.

From chemical reaction equations:

$$2C_3S+6H_2O \rightarrow 3CaO \cdot 2SiO_2 \cdot 3H_2O+3Ca(OH)_2 \tag{3.18}$$

$$2C_2S+4H_2O \rightarrow 3CaO \cdot 2SiO_2 \cdot 3H_2O+Ca(OH)_2 \tag{3.19}$$

The more C_3S, C_2S go to hydrate, the more $Ca(OH)_2$ can be generated to react with CO_2. This is evident that the higher the water-binder ratio, the more carbonate material can be formed.

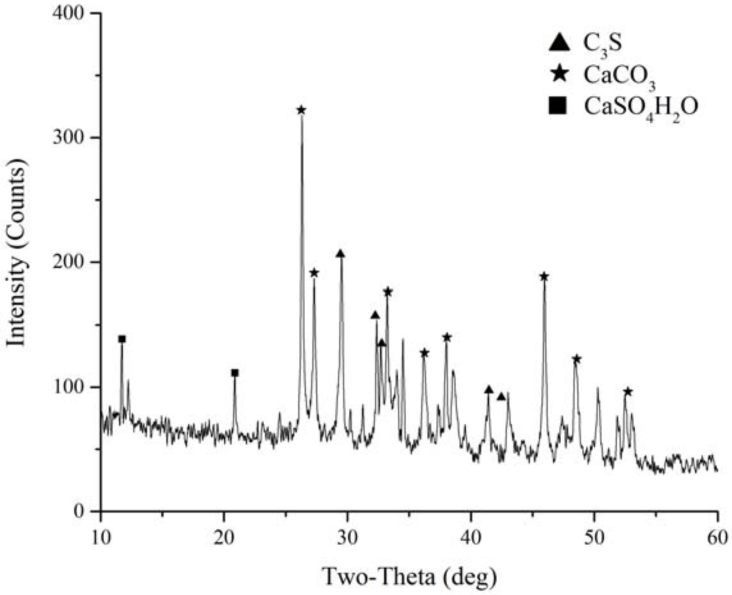

Figure 3.18: Sample 1 XRD result

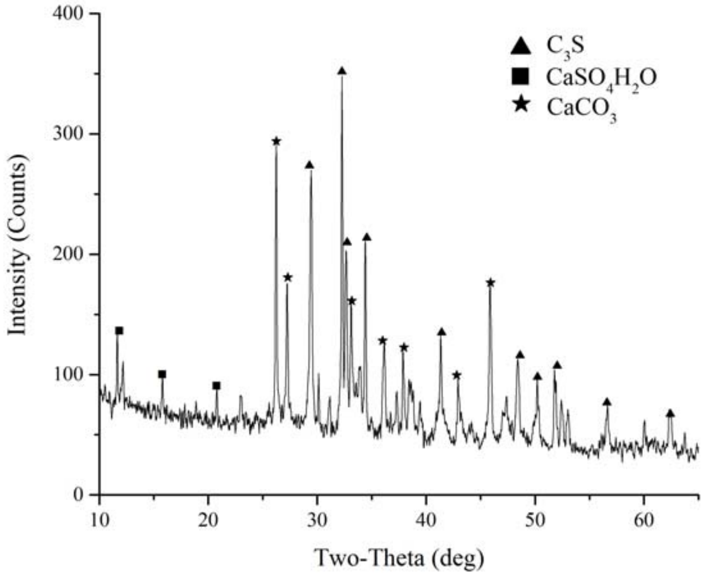

Figure 3.19: Sample 2 XRD result

XRD qualitative analysis results (Figures 3.18, 3.19) show that both of the samples have unhydrated C_3S, $CaSO_4 \cdot H_2O$ and $CaCO_3$ minerals. By comparing the two spectral lines (Figure 3.18, 3.19), the order for C_3S characteristic peaks can be shown to follow the order of water-binder ratio $0.5\Big|_{\text{water-binder ratio}}^{\text{sample 1}} < 0.33\Big|_{\text{water-binder ratio}}^{\text{sample 2}}$. This means that there are more unhydrated cement particle with reducing water-binder ratio. This further supports that the higher water-binder ratio will generate more $Ca(OH)_2$. In addition, the relative intensity of $CaCO_3$ is higher in Sample 1 than in Sample 2, which means there are more calcium carbonated material in Sample 1 than in Sample 2.

3.6 Initial Porosity Effect on CO_2 Mineral Carbonation

3.6.1 Experimental Results

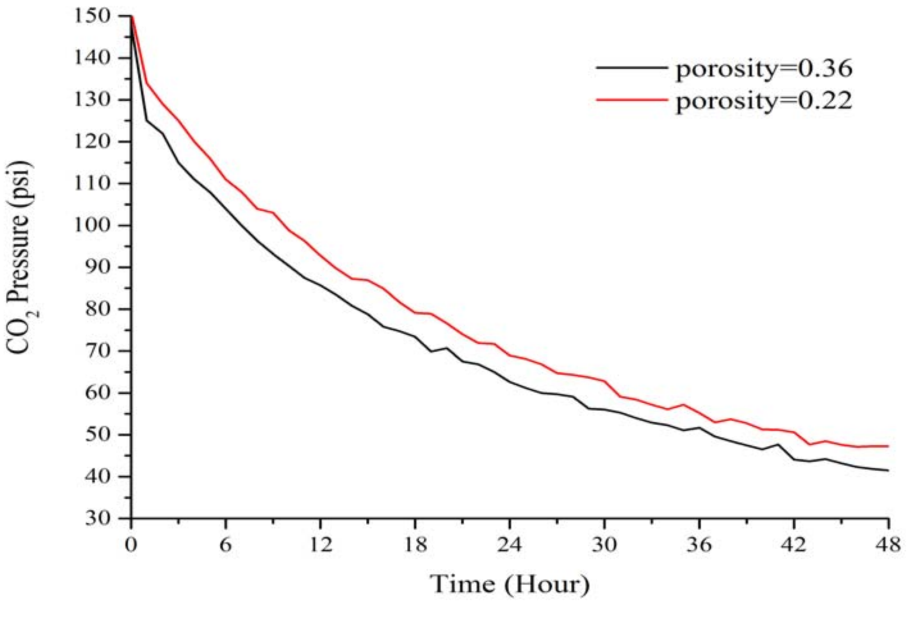

Figure 3.20: CO_2 void space pressure variation with different initial porosity

The initial porosity for Sample 3 (black curve) and Sample 4 (red curve) are 0.36 and 0.22. From Figure 3.20, CO_2 cavum pressure is shown to drop faster in Sample 3 than in Sample 4. After 48 hours, Sample 3 pressure dropped to 41psi and Sample 4 pressure dropped to 47psi, indicating that Sample 3 consumed more CO_2 than Sample 4.

Table 3.4: Experimental Results (Sample 3 and Sample 4)

	Mixture Weight	Initial Weight (before experiment)	Final Weight	Increased Weight	Initial CO2 Weight	CO2 Consumption Ratio
Sample 3	45.50 (g)	45.48 (g)	45.83 (g)	0.35 (g)	0.80 (g)	43.75%
Sample 4	45.30 (g)	45.28 (g)	45.54 (g)	0.26 (g)	0.80 (g)	32.50%

Table 3.4 shows the weights of both samples. This experiment shows that the higher porosity is, the more CO_2 would be consumed. This also reflected in the computed CO_2 consumption ratio.

3.6.2 ESEM and XRD Analysis

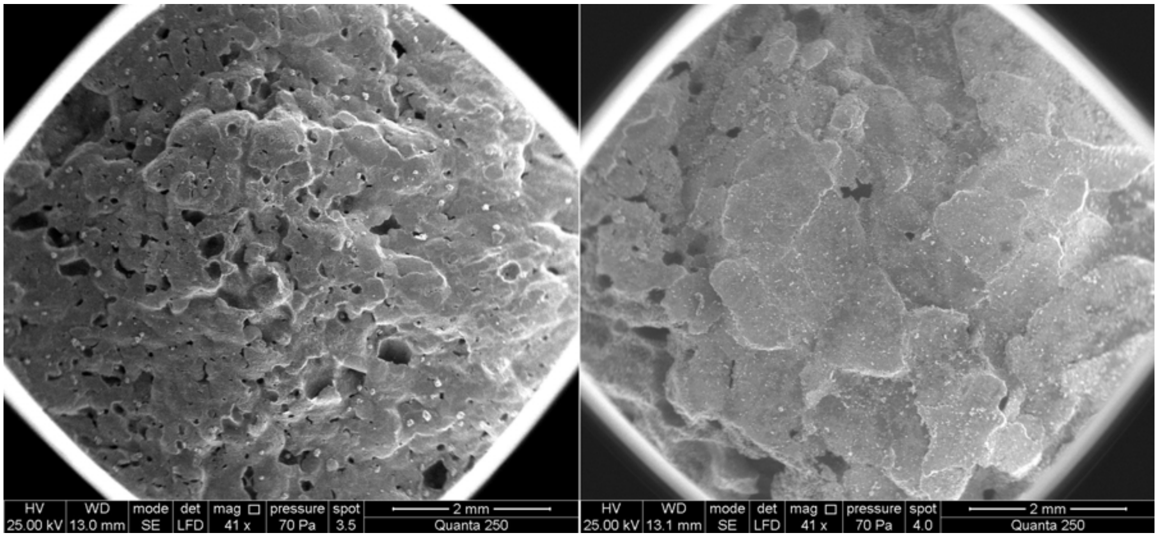

Figure 3.21: ESEM result (Sample 3, left image & Sample 4, right image)

Figure 3.21 and 3.22 show the ESEM pictures of Sample 3 and Sample 4. As shown in Figure 3.21, the left part of the picture shows a lot of voids distributed on the surface. By contrast, there are not too much pore structures in Sample 4. The porosity is

0.36 for Sample 3 and is 0.22 for Sample 4. This is the physical evidence about there are different porosity distributions in the samples.

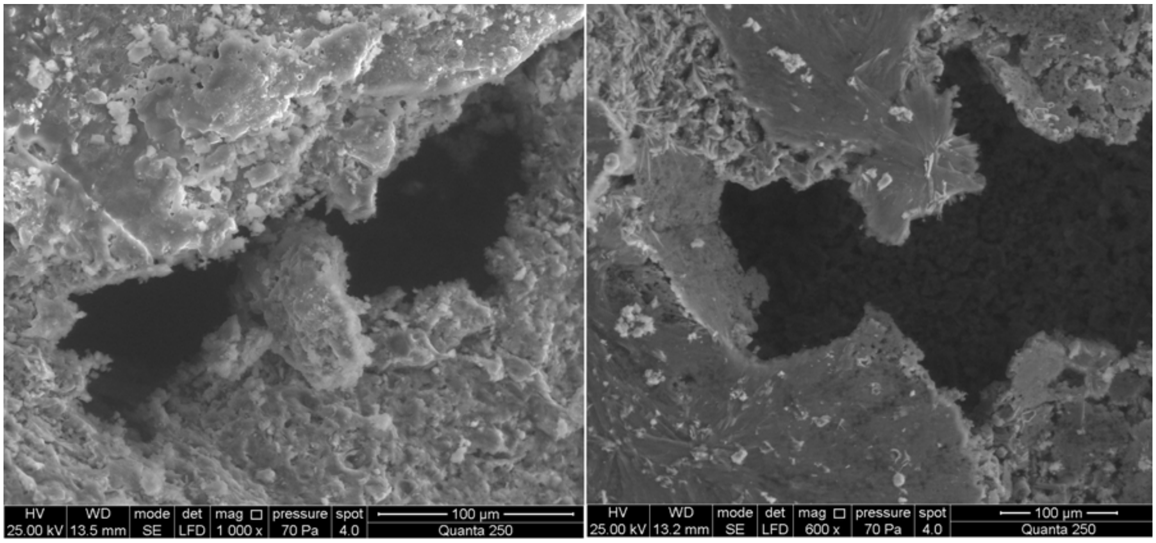

Figure 3.22: Micro-structure comparisons (Sample 3 & Sample 4)

As shown in Figure 3.22, blanket-like crystal covered more on the inner wall in Sample 3 and less in Sample 4. This means CO_2 gas did not diffuse through Sample 4. This observation indicates that the large porosity has more opportunity for gas-solid contact, and resulted in more carbonated materials generated.

Figure 3.23 and 3.24 shows the XRD results for Sample 3 and Sample 4. XRD qualitative analysis showed us that, both samples contained C_3S， $CaSO_4 \cdot H_2O$ and $CaCO_3$ minerals. By comparing those two spectral lines, the order for C_3S characteristic peaks followed the order of porosity: $0.36\Big|_{\text{porosity}}^{\text{sample 3}} < 0.22\Big|_{\text{porosity}}^{\text{sample 4}}$. There was more unhydrated cement particles remain in sample when the porosity decreased. This concludes that high porosity will increase the opportunity for gas-solid contact, which resulted in more CO_2 consumed in the alkaline environment. The relative intensity of

$CaCO_3$ is higher in Sample 3 than in Sample 4, which means more calcium carbonated material can be found in Sample 3.

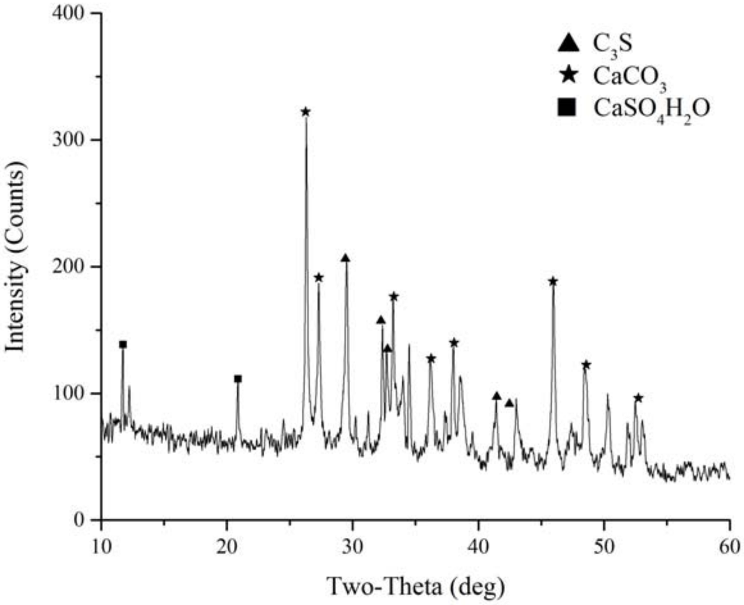

Figure 3.23: Sample 3 XRD result

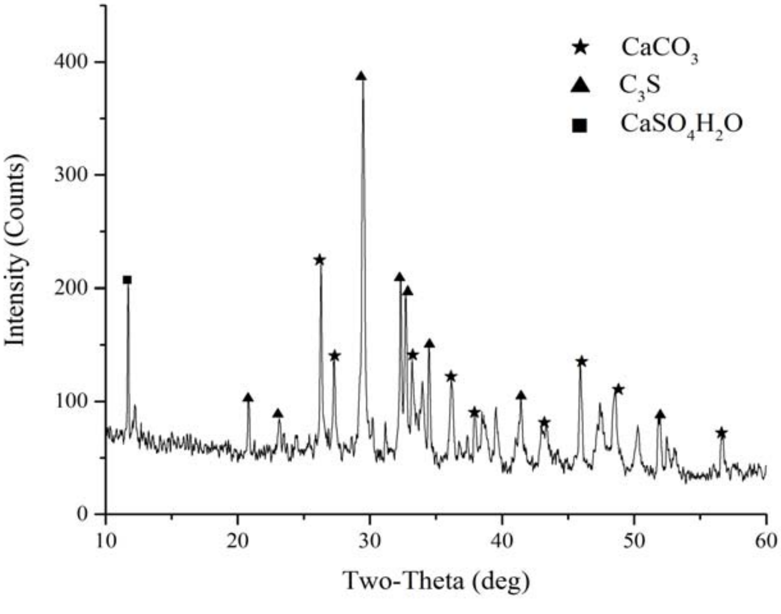

Figure 3.24: Sample 4 XRD result

3.7 Initial Pressure Effect on CO_2 Mineral Carbonation

3.7.1 Experimental Results

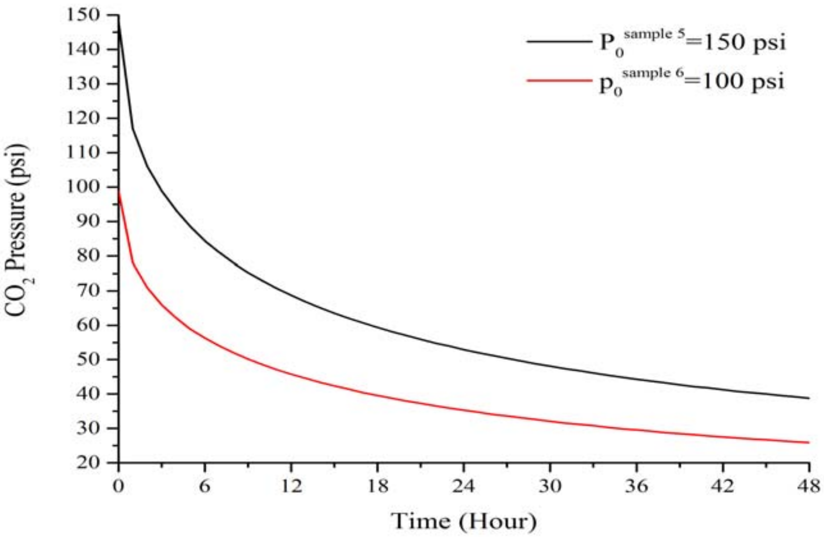

Figure 3.25: CO_2 void space pressure variation with different initial CO_2 pressures

The initial CO_2 pressures for Sample 5 (black curve) and Sample 6 (red curve) are 150psi and 100psi. Figure 3.25 shows both of the curves looked identical and the gradients for both curves are very close. However, after 48 hours, Sample 5 pressure dropped to 42psi and Sample 6 pressure dropped to 30psi. Therefore, Sample 5 consumed 72% CO_2 and Sample 6 consumed 70% CO_2. The pressure has very limited effect on the CO_2 consumption in this experiment. This experiment shows that the higher the initial pressure, the more CO_2 would be consumed. However, the effect is limited.

Table 3.5: Experiment Result (Sample 5 and Sample 6)

	Mixture Weight	Initial Weight (before experiment)	Final Weight	Increased Weight	Initial CO_2 Weight	CO_2 Consumption Ratio
Sample 5	45.50 (g)	45.48 (g)	45.80 (g)	0.32 (g)	0.80 (g)	40.00%
Sample 6	45.50 (g)	45.48 (g)	45.70 (g)	0.22 (g)	0.66 (g)	33.33%

3.7.2 ESEM and XRD Analysis

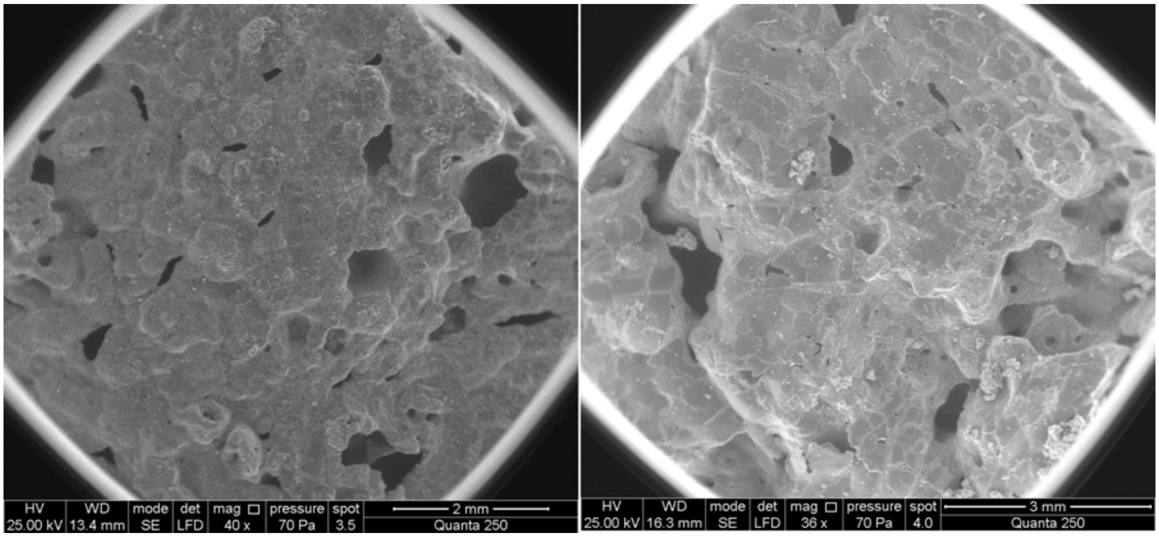

Figure 3.26: ESEM results (sample 5 & Sample 6)

Figure 3.26 and 3.27 showed the ESEM results for Sample 5 and Sample 6. From Figure 3.26 we can see that there is not very significant physical difference between those two figures. This is because those two samples were essentially identical. The only difference between those two samples is the CO_2 initial injection pressure, which did not cause any changes to the microstructure of the samples. Figure 3.27 shows us more carbonate material can be formed with high CO_2 pressure. In addition, it is noted that the C_3S material has grown more complete in Sample 5 than in Sample 6.

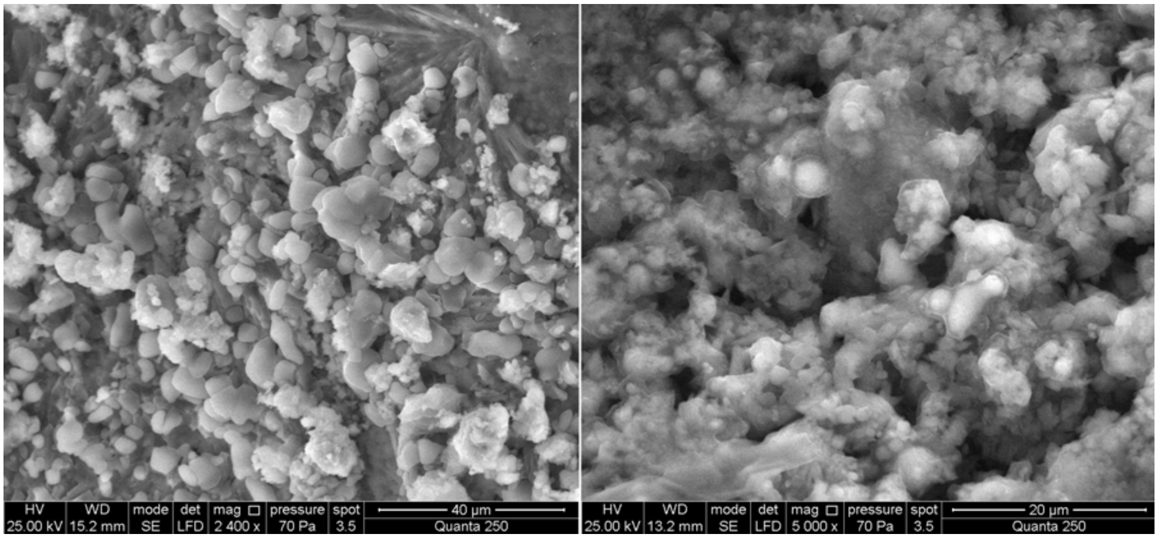

Figure 3.27: Micro-structural comparison (Sample 5 & Sample 6)

Figures 3.28 and 3.29 showed the XRD results for Sample 5 and Sample 6, respectively. XRD qualitative analysis showed us that both samples contained C_3S， $CaSO_4 \cdot H_2O$ and $CaCO_3$ minerals. By comparing the two spectral lines in Figure 3.28 and Figure 3.29, it is noted that the order for C_3S characteristic peaks followed the order of porosity: $150\text{psi}\Big|_{\text{pressure}}^{\text{sample 5}} < 100\text{psi}\Big|_{\text{pressure}}^{\text{sample 6}}$, which means that there were be more unhydrated cement particles remain in the samples when the pressure is reduced. It is apparent that the higher pressure will push more gas into the porous material, resulting in more CO_2 being consumed by gas diffusion. Furthermore, the relative intensity of $CaCO_3$ is higher in Sample 5 than in Sample 6, which means more calcium carbonated materials can be found in sample 5.

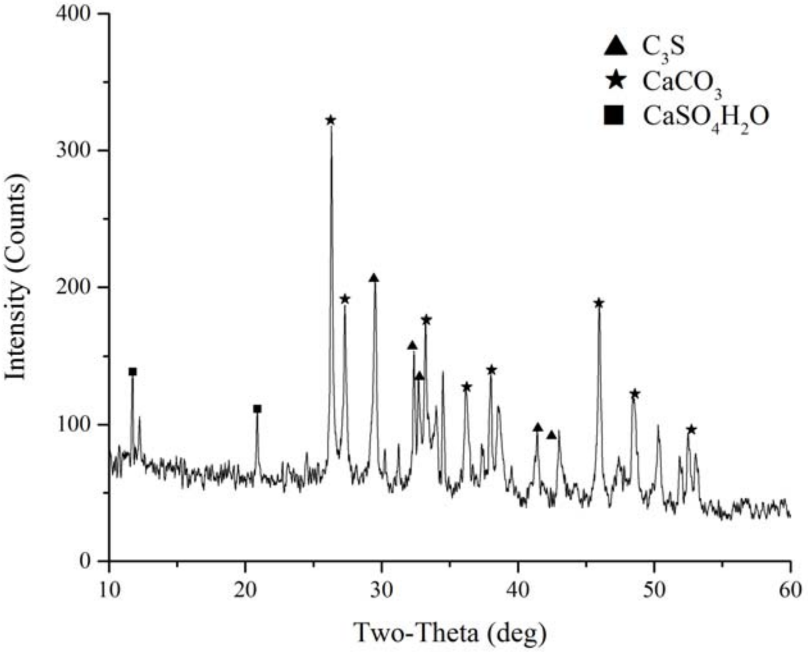

Figure 3.28: Sample 5 XRD result

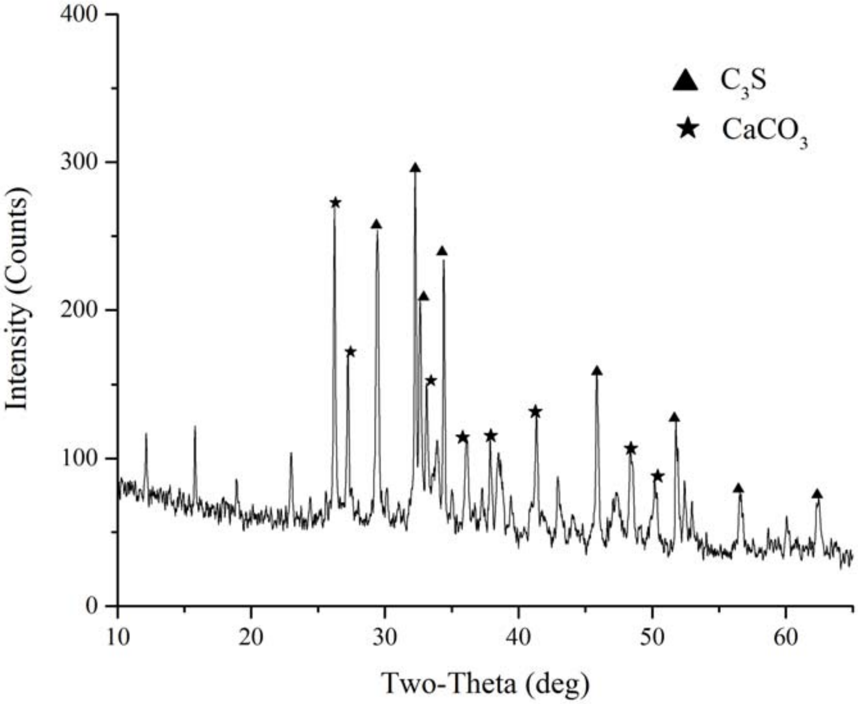

Figure 3.29: Sample 6 XRD result

3.8 Summary

In this chapter, we analyzed three key parameters which may have great impacts on CO_2 diffusion and carbonation. The CTPRC experiment and the other two analysis techniques proved that all of three parameters (initial water-binder ratio, initial porosity and initial CO_2 pressure) would affect CO_2 carbonation. The water-binder ratio would impact on the chemical processes during the experiment. The initial pressure condition is more effective on changing the external physical conditions during mineral carbonation. The initial porosity condition allows changing of the internal physical conditions for the sample during carbonation. Therefore, if we want to increase the material carbonation, we could optimize those parameters to reach the maximum CO_2 storage capacity.

The effects for the three parameters are all inversely correlated to the carbonation process, meaning that an increase in initial porosity, initial water-binder ratio and initial pressure will result in more carbonation. However, in all three cases, there will be an optimal limit to the effect.

CHAPTER 4: NUMERICAL ANALYSIS OF GAS DIFFUSION AND CHEMICAL REACTION KINETICS RESPONSES

4.1 Introduction

After forming agent (aluminum powder) is added to the specimen, the cement based material can be characterized as a porous medium, and CO_2 diffuses into the material through the pore structure. During the diffusion process, CO_2 will have the chemical reaction with the cement component, whilst the porous solid frame will deform under CO_2 pressure distribution. Finally, the material deformation will cause changes to the porosity value and diffusion coefficient, in return, further influences on the CO_2 diffusion rate and concentration ratio of the cementitious material. This chapter will formulate the dynamic model of this coupled process which includes concrete solid frame deformation, CO_2 diffusion and chemical reaction. The fundamental theory behind the formulation is explained in Chapter 2. This chapter will show the variables diagram and the development of a system response algorithm. The simulation program will analysis the effects of parameters such as different water-binder ratios, initial porosities and initial calcium contents on the CO_2 diffusion coefficients, diffusion rates and component concentrations.

4.2 Multi-Physics Model

The numerical model is usually simplified for engineering applications. But before the simple dynamic model can be established, we have to find out what kind of physical and chemical activities are involved in our samples, and then analyze how these activities act on each other. Then the geometrical characteristics, mechanical characteristics, and deformation behaviors on our samples can be analyzed. Reasonable assumptions have to be made, which include the deformation of the skeleton, CO_2 diffusion and chemical reaction rates, and the boundary and initial conditions. At last, a set of the governing equations and definite condition were built for the numerical simulation.

There are three key processes involved in our experiment: The first phenomenon is solid skeleton deformation; the second process is CO_2 diffusion, and the third process is the chemical reaction within the cementitious material.

The mechanisms involved in the CTPRC experiment is initiated when the sample is placed in the cylindrical chamber, and CO_2 is injected into the reaction chamber at a pressure, P_{chamber}, which then triggered subsequent physical and chemical activities. The inner diameter of the sample is $2a_s$, and the height of the specimen is h_s, the height of the cavity in the reaction chamber is h_c. Figure 4.1 shows the geometry of the CO_2 gas chamber. The specific mechanisms involved included CO_2 penetrates into the specimen through the pore structure and CO_2 migrates into the sample through the one-dimensional diffusion. Figure 4.2 shows the CO_2 diffusion flux is $J_{CO_2}^{\text{int}}$ and flows through one side of the specimen. The solid skeleton deformation has the following characteristics:

(1) The shape of the specimen is axis-symmetric. The pressure on the top surface of the specimen is even, and the bottom and the sides of the specimen are fixed by the container. Hence, the deformation of the cylindrical-shaped sample can be considered as axis-symmetry.

(2) The stiffness of the rigid sample container is assumed to be very large, and the

deformations in the radial direction and annulus direction are very small. So the deformation only happened along the axial direction.

(3) The deformation of the specimen is one dimensional. The displacement is only related to coordinate x_i . The radial deformation is not that obvious which is compared to the axial deformation.

CO_2 diffusion in the specimen has the following characteristics:

(1) CO_2 gas can only penetrate into the sample through the top espoused surface. The bottom and the sides are closed boundaries.

(2) The pore is assumed to be uniformly distributed in the sample, and the gas diffusion rate in the radial direction is much smaller than the gas diffusion rate in the axial direction. So the diffusion phenomenon in the sample can be described as one dimensional, and the diffusion rate, the diffusion coefficient and the CO_2 concentration ratio are only correlated to the coordinate x_i .

(3) The CO_2 flux on the gas-solid interface is determined by the volume of the reaction and the chamber pressure (P_{chamber}).

The chemical reactions in the specimen have the following characteristics:

(1) The chemical reaction area is the whole volume of the sample.

(2) The chemical reaction mode is considered as chain reaction. The total number of reactant and reaction product is 10. The number of the chemical reaction is 7.

(3) The chemical components in the radial and toroidal direction are uniformly distributed. The chemical reaction direction is considered as one-dimensional. So the chemical reaction rate and the concentration ratio of chemical component are only correlated to x_i .

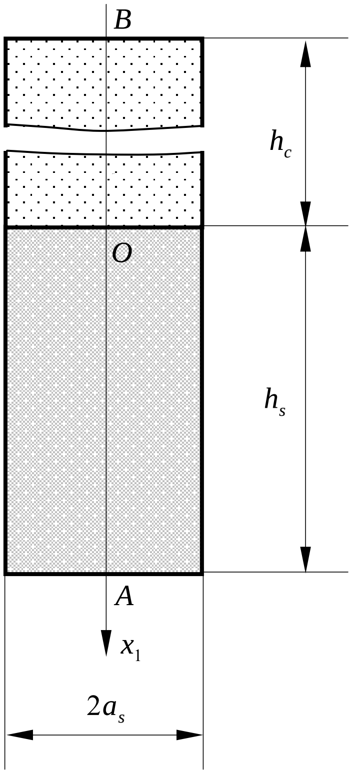

Figure 4.1: Specimen and gas CO_2 contained within a rigid chamber

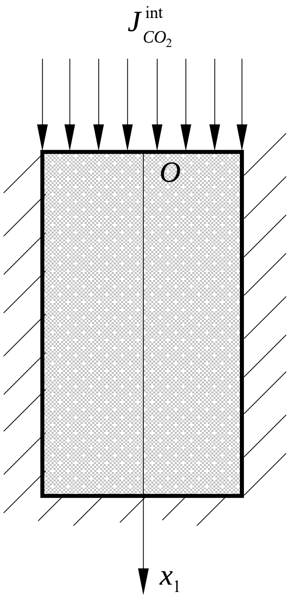

Figure 4.2: Peculiarity of specimen

In order to establish the multi-physical model, we have to make several assumptions on the aspects of deformation of the solid skeleton, diffusion of CO_2 and chemical reactions:

(1) The deformation of solid skeleton is always in elastic deformation range. The mechanical damage which is caused by the chemical reaction is neglected. So the elastic modulus and Poisson's ratio can be assumed as constant value in our study.

(2) The strain effect caused by the whisker growth id neglected.

(3) All the chemical reaction procedures are considered as irreversible.

(4) The chemical reaction ratios are varied due to the variation of the concentration ratios of the chemical components. However, the coefficients of the reaction ratio are constant.

(5) The diffusion coefficient is depending on the porosity of the specimen.

(6) Water only involves in the chemical reactions, does not involve in the chemical diffusion and also is not influenced by the gravitational force.

(7) The chemical reaction ratios are controlled by the low concentration components, and all chemical reactions are first order processes.

(8) The experiment is considered as isothermal.

4.3 Governing Equations

The coupling effect among the deformation of the solid skeleton, the diffusion of CO_2 and the chemical reactions in the cement based material are shown in Figure 4.3. Due to the one dimensional deformation (Biot 1972, Cowin and Nunziato 1983), the momentum equation can be stated as:

$$m_s \frac{\partial v_1}{\partial t} = \frac{\partial \sigma_{11}^{\mathrm{eff}}}{\partial x_1} - \frac{\partial(\alpha p)}{\partial x_1} + b_1 \tag{4.1}$$

In the above equation, v_1 represents the velocity, σ_{11}^{eff} represents the effective stress on the solid skeleton, b_1 is the body force, α is the coefficient of equivalent pore pressure, and p represents CO_2 pressure.

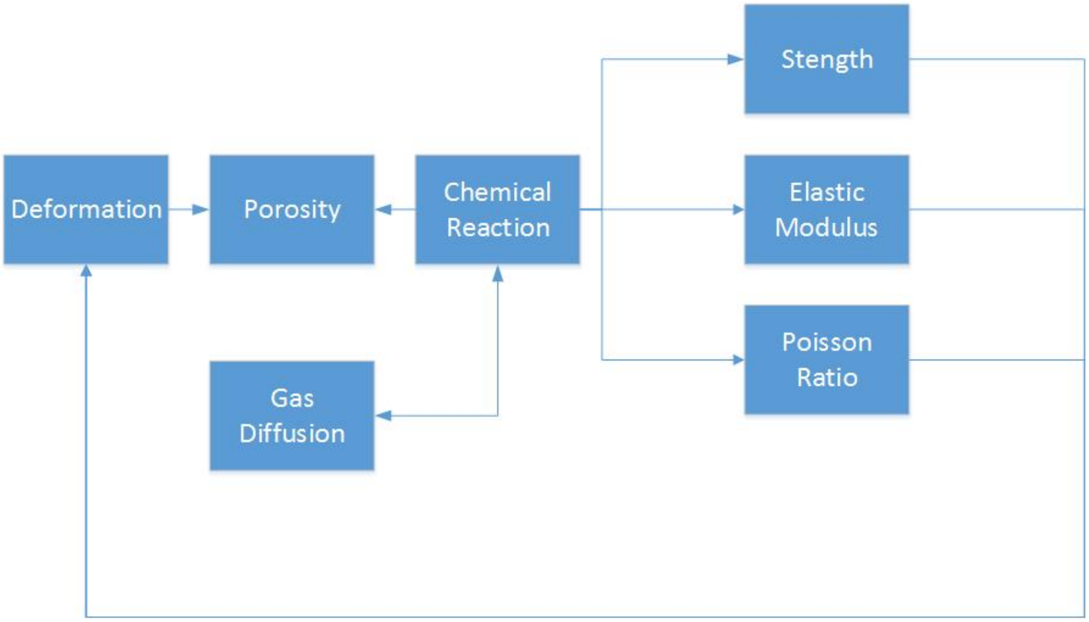

Figure 4.3: Impacts amongst the deformation, diffusion and chemical reactions

The geometric equations of the solid skeleton are then:

$$\begin{cases} B_{11} = \dfrac{\partial v_1}{\partial x_1} \\ B_{22} = 0 \\ B_{33} = 0 \\ B_{12} = 0 \\ B_{23} = 0 \\ B_{31} = 0 \end{cases} \tag{4.2}$$

$$v_1 = \frac{\partial u_1}{\partial t} \tag{4.3}$$

$$\varepsilon_{11} = \frac{\partial B_{11}}{\partial t} \tag{4.4}$$

where B_{11} represents the strain rate; u_1 represents the displacement of the solid skeleton.

The constitutive relationships can be described as:

$$\begin{cases} \sigma_{11}^{\text{eff}} = (\lambda + 2G)\varepsilon_{11} \\ \sigma_{22}^{\text{eff}} = \lambda\varepsilon_{11} \\ \sigma_{33}^{\text{eff}} = \lambda\varepsilon_{11} \\ \sigma_{12}^{\text{eff}} = 0 \\ \sigma_{23}^{\text{eff}} = 0 \\ \sigma_{31}^{\text{eff}} = 0 \end{cases} \tag{4.5}$$

In the above equation, λ and G represent the Lame's coefficients:

$$\lambda = \frac{E\nu}{(1+\nu)(1-2\nu)}, \quad G = \frac{E}{2(1+\nu)} \tag{4.6}$$

CO_2 will first diffuse into the sample and then it will react with the cementitious components, the Stoichiometric equations are listed below:

$$2C_3S + 6H_2O \rightarrow 3CaO \cdot 2SiO_2 \cdot 3H_2O + 3Ca(OH)_2 \tag{4.7}$$

$$2C_2S + 4H_2O \rightarrow 3CaO \cdot 2SiO_2 \cdot 3H_2O + Ca(OH)_2 \tag{4.8}$$

$$CaO + H_2O \rightarrow Ca(OH)_2 \tag{4.9}$$

$$Ca(OH)_2 + CO_2 \rightarrow CaCO_3 + H_2O \tag{4.10}$$

$$3CaO \cdot 2SiO_2 \cdot H_2O + 3CO_2 \rightarrow 3CaCO_3 \cdot 2SiO_2 \cdot 3H_2O \tag{4.11}$$

$$C_3S + 3CO_2 + \gamma H_2O \rightarrow SiO_2 \cdot \gamma H_2O + 3CaCO_3 \tag{4.12}$$

$$C_2S + 2CO_2 + \gamma H_2O \rightarrow SiO_2 \cdot \gamma H_2O + 2CaCO_3 \tag{4.13}$$

If A_i $(i = 1, 2, \cdots, 10)$ is used to represent C_3S 、 H_2O 、 $3CaO \cdot 2SiO_2 \cdot 3H_2O$ 、 $Ca(OH)_2$ 、 C_2S 、 CaO 、 CO_2 、 $CaCO_3$ 、 $3CaCO_3 \cdot 2SiO_2 \cdot 3H_2O$ and $SiO_2 \cdot \gamma H_2O$; and m_{ij} $(i = 1, 2, \cdots, 7; j = 1, 2, \cdots, 10)$ represents the stoichiometric coefficients involved in those chemical reactions, where the first subscript represents the order of the chemical process. The second subscript represents the reactant or reaction product. The value of the stoichiometric coefficient of the reactant is negative, and the stoichiometric coefficient of the reaction product is positive. Then,

$$\sum_{j=1}^{10} m_{ij} A_j = 0,\ (i = 1,2,\cdots,7) \tag{4.14}$$

where $\mu_i\ (i = 1,2,\cdots,10)$ represents the molecular weights of $A_i\ (i = 1,2,\cdots,10)$ materials; and $\rho_i\ (i = 1,2,\cdots,10)$ represents the concentration ratios of the materials. So the chemical reaction rate equations for those chemical reactions (4.7) ~ (4.13) can be described as:

$$\xi_1 = k_1 \rho_1^{\lambda_1^1} \rho_2^{\lambda_2^1} \tag{4.15}$$

$$\xi_2 = k_2 \rho_5^{\lambda_5^2} \rho_2^{\lambda_2^2} \tag{4.16}$$

$$\xi_3 = k_3 \rho_6^{\lambda_6^3} \rho_2^{\lambda_2^3} \tag{4.17}$$

$$\xi_4 = k_4 \rho_4^{\lambda_4^4} \rho_7^{\lambda_7^4} \tag{4.18}$$

$$\xi_5 = k_5 \rho_3^{\lambda_3^5} \rho_7^{\lambda_7^5} \tag{4.19}$$

$$\xi_6 = k_6 \rho_1^{\lambda_1^6} \rho_7^{\lambda_7^6} \rho_2^{\lambda_2^6} \tag{4.20}$$

$$\xi_7 = k_7 \rho_5^{\lambda_5^7} \rho_7^{\lambda_7^7} \rho_2^{\lambda_2^7} \tag{4.21}$$

Based on the chemical reaction kinetics theory, here are the mass conservation equations for each component are:

$$\frac{\partial \rho_1}{\partial t} = -2\mu_1 \xi_1 - \mu_1 \xi_5 \tag{4.22}$$

$$\frac{\partial \rho_2}{\partial t} = -6\mu_2 \xi_1 - 4\mu_2 \xi_2 - \mu_2 \xi_3 - \gamma\mu_2 \xi_6 - \gamma\mu_2 \xi_7 + \mu_2 \xi_4 \tag{4.23}$$

$$\frac{\partial \rho_3}{\partial t} = \mu_3 \xi_1 + \mu_3 \xi_2 - \mu_3 \xi_5 \tag{4.24}$$

$$\frac{\partial \rho_4}{\partial t} = 3\mu_4 \xi_1 + \mu_4 \xi_2 + \mu_4 \xi_3 - \mu_4 \xi_4 \tag{4.25}$$

$$\frac{\partial \rho_5}{\partial t} = -2\mu_5 \xi_2 - \mu_5 \xi_7 \tag{4.26}$$

$$\frac{\partial \rho_6}{\partial t} = -\mu_6 \xi_3 \tag{4.27}$$

$$\frac{\partial \rho_7}{\partial t} = -\mu_7 \xi_4 - 3\mu_7 \xi_5 - 3\mu_7 \xi_6 - 2\mu_7 \xi_7 - \frac{\partial J_1}{\partial x_1} \tag{4.28}$$

$$\frac{\partial \rho_8}{\partial t} = \mu_8 \xi_4 + 3\mu_8 \xi_6 + 2\mu_8 \xi_7 \tag{4.29}$$

$$\frac{\partial \rho_9}{\partial t} = \mu_9 \xi_5 \tag{4.30}$$

$$\frac{\partial \rho_{10}}{\partial t} = \mu_{10} \xi_6 + \mu_{10} \xi_7 \tag{4.31}$$

Introducing

$$\delta_{i7} = \begin{cases} 1, & i = 7 \\ 0, & i \neq 7 \end{cases} \tag{4.32}$$

so we can combine equations from (4.22) to equation (4.31) as:

$$\frac{\partial \rho_i}{\partial t} = \sum_{k=1}^{7} \left[m_{ki} \mu_i \xi_k \right] - \delta_{7i} \frac{\partial J}{\partial X_1}, \quad (i = 1, 2, \cdots, 7) \tag{4.33}$$

It can be shown that:

$$\sum_{i=1}^{10} \frac{\partial \rho_i}{\partial t} = -\frac{\partial J_1}{\partial x_1} \tag{4.34}$$

Equations (4.15) ~ (4.21) substitute into (4.22) ~(4.31), we get:

$$\frac{\partial \rho_1}{\partial t} = -2\mu_1 k_1 \rho_1^{\lambda_1^1} \rho_2^{\lambda_2^1} - \mu_1 k_6 \rho_1^{\lambda_1^6} \rho_7^{\lambda_7^6} \rho_2^{\lambda_2^6} \tag{4.35}$$

$$\frac{\partial \rho_2}{\partial t} = -6\mu_2\xi_1 - 4\mu_2\xi_2 - \mu_2\xi_3 - \gamma\mu_2\xi_6 - \gamma\mu_2\xi_7 + \mu_2\xi_4 \tag{4.36}$$

$$\frac{\partial \rho_3}{\partial t} = \mu_3\xi_1 + \mu_3\xi_2 - \mu_3\xi_5 \tag{4.37}$$

$$\frac{\partial \rho_4}{\partial t} = 3\mu_4\xi_1 + \mu_4\xi_2 + \mu_4\xi_3 - \mu_4\xi_4 \tag{4.38}$$

$$\frac{\partial \rho_5}{\partial t} = -2\mu_5\xi_2 - \mu_5\xi_7 \tag{4.39}$$

$$\frac{\partial \rho_6}{\partial t} = -\mu_6\xi_3 \tag{4.40}$$

$$\frac{\partial \rho_7}{\partial t} = -\mu_7\xi_4 - 3\mu_7\xi_5 - 3\mu_7\xi_6 - 2\mu_7\xi_7 - \frac{\partial J_1}{\partial x_1} \tag{4.41}$$

$$\frac{\partial \rho_8}{\partial t} = \mu_8\xi_4 + 3\mu_8\xi_6 + 2\mu_8\xi_7 \tag{4.42}$$

$$\frac{\partial \rho_9}{\partial t} = \mu_9\xi_5 \tag{4.43}$$

$$\frac{\partial \rho_{10}}{\partial t} = \mu_{10}\xi_6 + \mu_{10}\xi_7 \tag{4.44}$$

In the above equations, $J_1 = -D\frac{\partial \rho_7}{\partial x_1}$ represents the diffusion rate, and the diffusion coefficient D is dependant on the porosity of the sample (Jaynes and Rogowski 1983, Webb and Pruess 2003). So

$$D = D_r\left(\frac{\phi}{\phi_r}\right)^{p_d} \tag{4.45}$$

Based on ideal gas law, the free space CO_2 gas density can be described as:

$$m_{\mathrm{CO}_2} = \frac{\mu_{\mathrm{CO}_2}}{RT} p_{\mathrm{chamb}} \tag{4.46}$$

where T is thermodynamic temperature, and R is the ideal gas constant. It is obvious that CO_2 mass density under standard atmospheric pressure (P_{atm}) can be written as:

$$m_{\mathrm{CO_2}}^{\mathrm{atm}} = \frac{\mu_{\mathrm{CO_2}}}{RT} p_{\mathrm{atm}} \tag{4.47}$$

If we divide equation (4.47) by equation (4.46) we can get:

$$m_{\mathrm{CO_2}} = m_{\mathrm{CO_2}}^{\mathrm{atm}} \frac{p_{\mathrm{chamb}}}{p_{\mathrm{atm}}} \tag{4.48}$$

Due to gas diffusion, the CO_2 pressure on the void space will decrease. The mass density will decrease along with its pressure variation. The gradient of mass density can be calculated as:

$$\frac{\partial m_{\mathrm{CO_2}}}{\partial t} = \frac{m_{\mathrm{CO_2}}^{\mathrm{atm}}}{p_{\mathrm{atm}}} \frac{\partial p_{\mathrm{chamb}}}{\partial t} \tag{4.49}$$

The mass flow rate in the sample can be written as:

$$Q_{\mathrm{CO_2}} = AH \frac{\partial m_{\mathrm{CO_2}}}{\partial t} = AH \frac{m_{\mathrm{CO_2}}^{\mathrm{atm}}}{p_{\mathrm{atm}}} \frac{\partial p_{\mathrm{chamb}}}{\partial t} \tag{4.50}$$

So the CO_2 diffusion rate on the gas-solid interface can be described as:

$$J_{\mathrm{CO_2}}^{\mathrm{int}} = \frac{Q_{\mathrm{CO_2}}}{A} = H \frac{m_{\mathrm{CO_2}}^{\mathrm{atm}}}{p_{\mathrm{atm}}} \frac{\partial p_{\mathrm{chamb}}}{\partial t} \tag{4.51}$$

where the superscript “int” means the gas-solid interface. All three behaviors are transmitted through the porous structure, so the porosity evolution is:

$$\frac{D\phi}{Dt} = \frac{\partial v_1}{\partial x_1} - \frac{1}{m_s} \sum_{i=1}^{10} \frac{\partial \rho_i}{\partial t} \tag{4.52}$$

4.4 Coupling Effect

Based on the above discussions, we can describe the coupling effect among the deformation of matrix, the diffusion of CO_2 and the chemical reaction in the components of concrete in a flow diagram (Figure. 4.4).

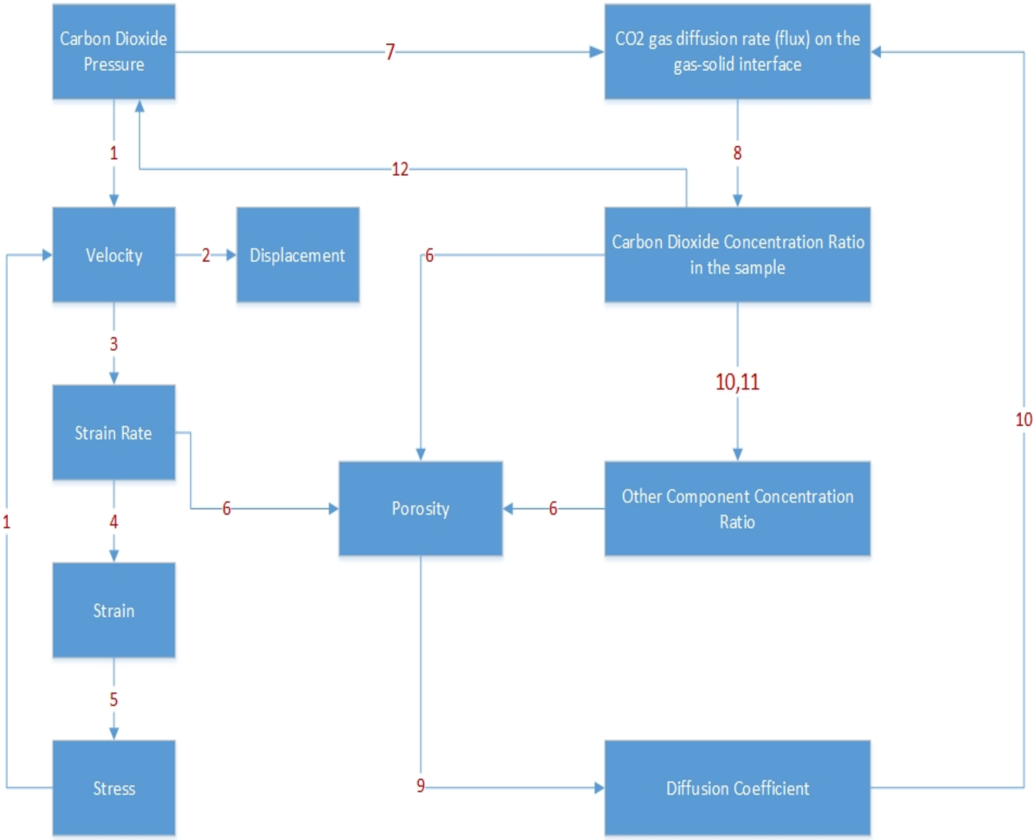

Figure 4.4: Variable relationship involved in the CTPRC experiment

4.4.1 State Conditions

CO_2 will diffuse through the sample and simultaneously reacting with the chemical components in the specimen. Before we start our simulation, we have to give the initial and boundary conditions of the simulation. Due to the immobilization of the chemical components, all the boundary conditions are assumed fixed. So, we only need to define the initial condition.

4.4.2 Boundary Conditions

(1) Displacement boundary condition

The displacement at the bottom of the sample is assumed to be zero, so that:

$$u_1\big|_{x_1=h_c} = 0 \tag{4.53}$$

(2) Stress boundary condition

The effective stress on the top surface of the sample is given as:

$$\sigma^{\text{eff}}\big|_{x_1=0} = -p_{\text{chamb}} \tag{4.54}$$

The CO$_2$ pressure at the top surface can be written as:

$$p\big|_{x_1=0} = p_{\text{chamb}} \tag{4.55}$$

It should be noted here, that the CO$_2$ pressure on the top of the specimen is variable with time.

(3) The boundary conditions of CO$_2$ concentration ratio and diffusion flux

Due to the no flow condition at the bottom of the sample, the CO$_2$ diffusion flux will be zero.

$$\left.\frac{\partial \rho_7}{\partial t}\right|_{x_1=h_s} = 0 \text{ (or } J\big|_{x_1=h_s} = 0) \tag{4.56}$$

CO$_2$ diffusion at the gas-solid interface can be given as:

$$J\big|_{x_1=0} = \frac{\mu_6 H}{Rt}\frac{\partial p_{\text{chamb}}}{\partial t} \tag{4.57}$$

4.4.3 Initial Conditions

(1) Initial Porosity

The initial porosity is assumed to be distributed evenly in the sample,

$$\phi\big|_{t=0} = \phi_0 \tag{4.58}$$

where, ϕ_0 is determined by the porosity tests.

(2) Initial displacement, stress and strain

Based on boundary conditions, we can get the state equilibrium solutions for the initial displacement, stress and strain. And then we can preset those values as the initial conditions.

(3) Initial CO_2 concentration

Initial CO_2 concentration at the top surface of the sample equals to the concentration at free space times the sample porosity:

$$\rho_7\Big|_{t=0,X=0} = m_{CO_2}\phi_0 = \frac{\mu_{CO_2} p^0_{\text{chamb}}}{Rt}\phi_0 \tag{4.59}$$

Then, we assume the distribution of CO_2 mass concentration in the sample as:

$$\rho_7\Big|_{t=0} = \frac{\mu_{CO_2} p^0_{\text{chamb}}}{Rt}\phi_0\, f_7\,(x_1) \tag{4.60}$$

where $f_7\,(\,x_1\,)$ is determined by the experiment.

(4) Other component initial concentrations

$$\rho_i\Big|_{t=0} = f_i\,(x_1)(i=1,2,3,4,5,7,8,9,10) \tag{4.61}$$

where $f_i\,(x_1)\,(i=1,2,3,4,5,7,8,9,10)$ is determined by experiment.

4.5 Summary

In this chapter we made a kinetic coupling model of gas diffusion, chemical reaction and solid deformation for the CO_2 sorption study in the cement based porous material. This numerical simulation model is using fast Lagrangian analysis method for its dynamic response computation. With the help of FORTRAN language, we made a simulation program to do the dynamic response computation. The details of the programming algorithm development and coding are documented in Appendix A. The FORTRAN program is attached in Appendix B.

CHAPTER 5: EXAMPLE OF NUMERICAL SIMULATION

This chapter describes the numerical simulation of the baseline CTPRC experiment. The results of simulation are used to verify the normal operation of the computer program.

5.1 Initial Conditions

The following are specific input constants that are associated with the CTPRC experiment.

The total weights of the cement, water and aluminum powder in the sample are $\mathrm{M_{cement}}=30\ \mathrm{g}$, $\mathrm{M_{water}}=15\ \mathrm{g}$ and $\mathrm{M_{Al}}=0.5\ \mathrm{g}$, respectively. The reaction chamber inner diameter is $a_{\mathrm{chamb}}=0.02\ \mathrm{m}$; the height of cavum is $h_{\mathrm{chamb}}=0.2\ \mathrm{m}$, and the initial pressure in the reaction chamber is set as $p^{0}_{\mathrm{chamb}}=150\ \mathrm{psi}$. The original height of the sample is $h_s=0.03\ \mathrm{m}$; the initial porosity of the sample is $\phi_{\mathrm{undeformed}}=0.36$; the elasticity modulus of the sample is roughly close to $E=2.00\ \mathrm{GPa}$; Poisson's ratio is $v=0.26$; Lame's coefficients are $\lambda=\dfrac{Ev}{(1+v)(1-2v)}=806\ \mathrm{MPa}$ and $G=\dfrac{E}{2(1+v)}=794\ \mathrm{MPa}$; the deformation modulus is $\lambda+2G=2.45\ \mathrm{GPa}$. Initially, the CO_2 mass concentration can be described as:

$$\rho_7^0\left(0,x_1\right)=m^{\mathrm{atm}}_{\mathrm{CO_2}}\frac{p_{\mathrm{chamb}}}{p_{\mathrm{atm}}}\phi_{\mathrm{undeformed}}\left(1-\frac{x_1}{h_s}\right)^4 \tag{5.1}$$

In the numerical model, the sample is divided into $N_e = 100$ units and each of the unit height is $h_e = \frac{h_s}{N_e} = 3\times 10^{-4}$ m. The step in the numerical simulation is $h_t = 1$ s, and the total time integration is $T = 48$ hour.

The first part in the numerical simulation is using genetic algorithm to estimate the CO2 diffusion coefficient reference number D_r, power component p_d and chemical reaction rate $k_i \left(i = 1, 2, \cdots, 7\right)$. In particular, D_r and p_d are the decision variables in the program and $q_{dv}^i \left(i = 1, 2, \cdots, 9\right)$ is used to represent those numbers in the program. The length of the gene is $I_i = 6\left(i = 1, 2, \cdots, 9\right)$; the length of chromosome is $m = 54$. The coding and decoding setup of decision variables is found in Table 5.1.

Table 5.1: Coding and decoding setup of decision variables

		Represent	Coding	Search Boundary		Decoding Equation
				Left	Right	
1	q_{dv}^1	k_1	$I_{11}I_{12}\cdots I_{16}$	0.1×10^{-9}	0.1×10^{-7}	$k_1^j = 0.1\times 10^{-9}\left(1+\frac{99}{63}j\right), j = \sum_{i=1}^{6} 2^{6-i} I_{1i}$
2	q_{dv}^2	k_2	$I_{21}I_{22}\cdots I_{26}$	0.1×10^{-9}	0.1×10^{-7}	$k_2^j = 0.1\times 10^{-9}\left(1+\frac{99}{63}j\right), j = \sum_{i=1}^{6} 2^{6-i} I_{2i}$
3	q_{dv}^3	k_3	$I_{31}I_{32}\cdots I_{36}$	0.1×10^{-9}	0.1×10^{-6}	$k_3^j = 0.1\times 10^{-9}\left(1+\frac{999}{63}j\right), j = \sum_{i=1}^{6} 2^{6-i} I_{3i}$
4	q_{dv}^4	k_4	$I_{41}I_{42}\cdots I_{46}$	0.1×10^{-9}	0.1×10^{-7}	$k_4^j = 0.1\times 10^{-9}\left(1+\frac{99}{63}j\right), j = \sum_{i=1}^{6} 2^{6-i} I_{4i}$
5	q_{dv}^5	k_5	$I_{51}I_{52}\cdots I_{56}$	0.1×10^{-9}	0.1×10^{-7}	$k_5^j = 0.1\times 10^{-9}\left(1+\frac{99}{63}j\right), j = \sum_{i=1}^{6} 2^{6-i} I_{5i}$

6	q_{dv}^{6}	k_6	$I_{61}I_{62}\cdots I_{66}$	0.1×10^{-9}	0.1×10^{-7}	$k_6^j=0.1\times10^{-9}\left(1+\frac{99}{63}j\right),\ j=\sum_{i=1}^{6}2^{6-i}I_{6i}$
7	q_{dv}^{7}	k_7	$I_{71}I_{72}\cdots I_{76}$	0.1×10^{-9}	0.1×10^{-7}	$k_7^j=0.1\times10^{-9}\left(1+\frac{99}{63}j\right),\ j=\sum_{i=1}^{6}2^{6-i}I_{7i}$
8	q_{dv}^{8}	D_r	$I_{81}I_{82}\cdots I_{86}$	0.1×10^{-10}	0.1×10^{-9}	$D_r^j=0.1\times10^{-10}\left(1+\frac{9}{63}j\right),\ j=\sum_{i=1}^{6}2^{6-i}I_{8i}$
9	q_{dv}^{9}	p_d	$I_{91}I_{92}\cdots I_{96}$	1.06	2.65	$p_d^j=1.06\left(1+\frac{5}{210}j\right),\ j=\sum_{i=1}^{6}2^{6-i}I_{9i}$

The crossover and mutation operation has been introduced in Chapter 4, in this example, the crossover rate is $p_c=0.8$ and the mutation rate is $p_m=0.2$. The initial population size is preset as $k_{\text{group}}=100$. After 11 generations of evolution, the best chromosome is represented as 000000 000000 010000 000001 000010 010100 001000 000000 000000.

The corresponding phenotypes are $k_1^{\text{best}}=0.1\times10^{-9}$, $k_2^{\text{best}}=0.1\times10^{-9}$, $k_3^{\text{best}}=1.57\times10^{-7}$, $k_4^{\text{best}}=4.14\times10^{-10}$, $k_5^{\text{best}}=7.29\times10^{-10}$, $k_6^{\text{best}}=6.39\times10^{-9}$, $k_7^{\text{best}}=2.61\times10^{-9}$, $D_r^{\text{best}}=1.0\times10^{-11}$ and $p_d^{\text{best}}=1.06$. The best fitness unit is $\text{fitn\_max=0.146}\cdot$

The FORTRAN program sets the above numbers as the initial values for the numerical simulation. The simulation gives us the CO2 pressure (p), porosity (ϕ), effective axial stress (σ^{eff}), effective axial strain (ε), axial displacement (u_1), diffusion coefficient (D), diffusion rate (J_1), chemical reaction rate $(\xi_i\ (i=1,2,\cdots,7))$, mass density $\left(\rho_i \left(i=1,2,\cdots,10\right)\right)$, mass density gradient $\left(\frac{\partial \rho_i}{\partial t}\left(i=1,2,\cdots.10\right)\right)$ and $\left(\lambda_i^j \left(i=1,2,\cdots,7,\, j=1,2,\cdots,10\right)\right)$ at each node.

5.2 Cavum Pressure Analysis

The experiment and the numerical simulation results of CO_2 pressure at cavum in the reaction chamber is shown in Figure 5.1. The difference between experiment and simulation is shown in Figure 5.2.

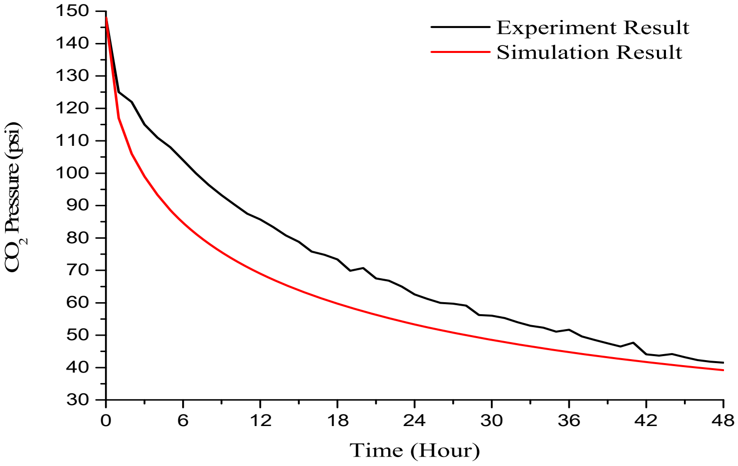

Figure 5.1: CO_2 pressure in cavum

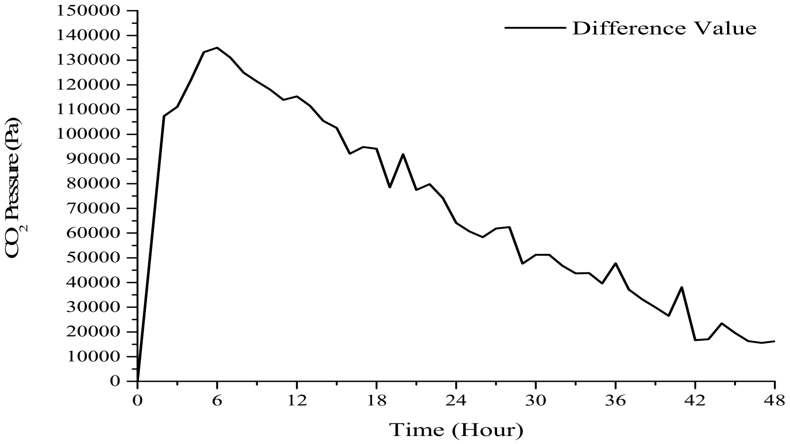

Figure 5.2: CO_2 pressure difference between experiment and simulation results

Due to CO_2 in the cavum is kept diffusing into the sample without any supplemental forcing, $p_{\text{chamb}}^{\text{test}}$ and $p_{\text{chamb}}^{\text{cal}}$ will be assumed to monotonic decrease over time. After 48 hours, $p_{\text{chamb}}^{\text{test}}$ and $p_{\text{chamb}}^{\text{cal}}$ drop to 0.734MPa and $0.751\ \text{MPa}$, respectively. From Figure 5.2 we noted that the biggest difference between $p_{\text{chamb}}^{\text{test}}$ and $p_{\text{chamb}}^{\text{cal}}$ happened at $t = 6$ hour and $\left(p_{\text{chamb}}^{\text{test}} - p_{\text{chamb}}^{\text{cal}}\right)_{\max} = 0.135\text{MPa}$.

The results of simulating cavum pressure change indicate reasonable closeness between experimental and numerical results.

5.3 Effective Axial Stress

Figure 5.3 shows the effective axial stress distribution at each node throughout the 48-hour experiment. Based on strain component sign convention in continuum mechanics, we can assume tension strain point to be positive. We can see from Figure 5.3 that the effective axial strain at the nodes remained negative throughout the 48 hours- indicating that every node in the sample remained in compression. Due to the pressure at $x_1 = 0$ will always be higher than at $x_1 = h_s$, the pressure should decrease along x_1 direction. Based on $\varepsilon_{11} = \dfrac{\sigma_{11}^{\text{eff}}}{\lambda + 2G} = \dfrac{-p_{\text{chamb}} + \alpha p}{\lambda + 2G}$, the algebraic value of effective stress is found to monotonically decrease along x_1 direction. So the effective stress at each section of the sample should follow the above orderliness.

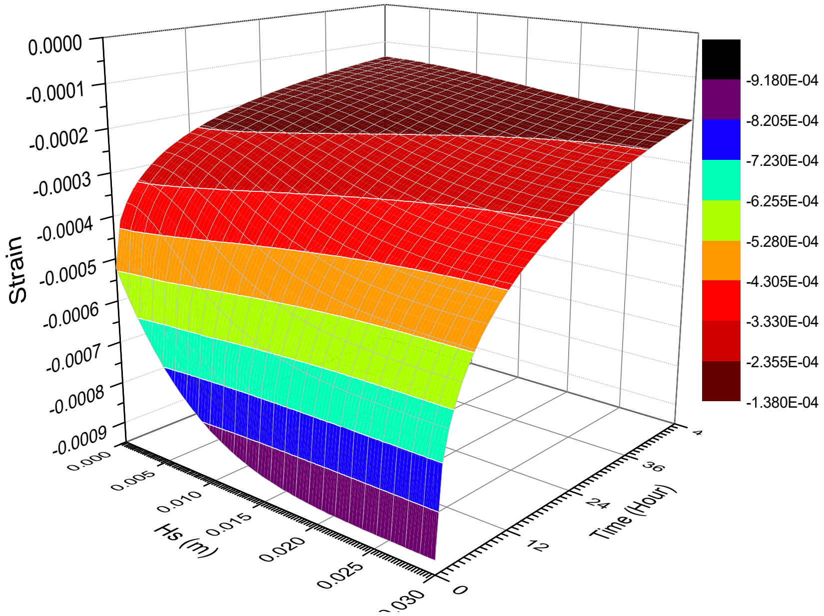

Figure 5.3: Effective axial displacement

5.4 Porosity

The variation of porosity can be explained in two parts: the first part is caused by solid skeleton deformation ($\dot{\phi}_1 \triangleq \frac{\partial v_1}{\partial x_1}$) and the second part is due to the chemical reaction ($\dot{\phi}_2 \triangleq -\frac{1}{m_s}\sum_{i=1}^{10}\frac{\partial \rho_i}{\partial t}$). So the porosity equation can be described as:

$$\phi = \phi_0 + \int_0^t \dot{\phi}_1 (z, x_1) dz + \int_0^t \dot{\phi}_2 (z, x_1) dz \tag{5.2}$$

Due to gas diffusion into the sample; the concentration of CO_2 cannot be uniformly distributed throughout the sample. The concentration of the rest 9 materials only changed locally. We assume w_i as the migration velocity of $i\left(i = 1, 2, \cdots 10\right)$ material.

$$\sum_{i=1}^{10}\frac{D\rho_i}{Dt} = \sum_{i=1}^{10}\left(\frac{\partial \rho_i}{\partial t} + w_i \frac{\partial \rho_i}{\partial x_1}\right) \tag{5.3}$$

Only CO_2's migration velocity is nonzero, hence, the equation is simplified as:

$$\sum_{i=1}^{10} \frac{D\rho_i}{Dt} = \sum_{i=1}^{10} \frac{\partial \rho_i}{\partial t} + w_7 \frac{\partial \rho_7}{\partial x_1} \tag{5.4}$$

Based on the law of conservation of mass, $\sum_{i=1}^{10} \frac{D\rho_i}{Dt} = 0$, therefore,

$$-\sum_{i=1}^{10} \frac{\partial \rho_i}{\partial t} = w_7 \frac{\partial \rho_7}{\partial x_1} \tag{5.5}$$

Consider the fact that CO_2 migration velocity is very small, so $\left|\dot{\phi}_2\right| \ll \left|\dot{\phi}_1\right|$. The porosity equation can be revised as:

$$\phi = \phi_0 + \int_0^t \frac{\partial v_1(z, x_1)}{\partial x_1} dz = \phi_0 + \int_0^t \frac{\partial \varepsilon_{11}}{\partial z} dz = \phi_0 + \varepsilon_{11} - \varepsilon_{11}^0 \tag{5.6}$$

What needs to be stressed here is that the porosity at initial moment is different from the non-deformed porosity. Because at the beginning of the experiment, CO_2 will work on the sample, that is $\phi_0 = \phi_{\text{undeformed}} + \varepsilon_{11}^0$, So the porosity equation should be:

$$\phi = \phi_{\text{undeformed}} + \varepsilon_{11} \tag{5.7}$$

As shown in Figure 5.4, we found out the porosity value monotonically decreases along with x_1 direction and monotonically increases with time. This is consistent with our assumptions made.

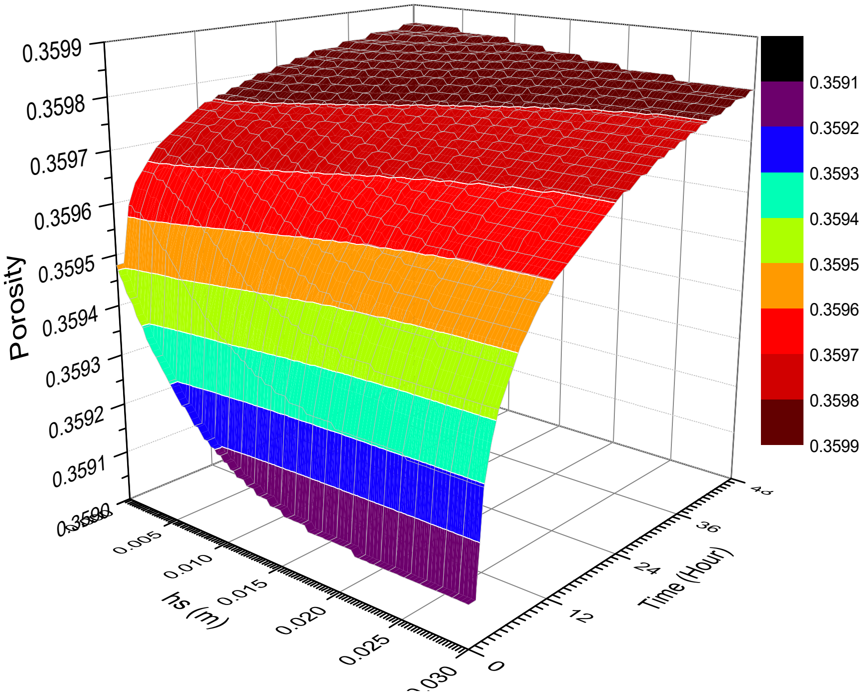

Figure 5.4: Porosity distribution with time and space

5.5 Diffusion Coefficient

Figure 5.5 shows the diffusion coefficient distribution at every node as a function of time. The diffusion equation ($D = D_r \left(\frac{\phi}{\phi_r} \right)^{p_d}$) indicates that diffusion coefficient is dependent on the porosity. In this simulation example, $D_r = 1.0 \times 10^{-11}$ and $p_d = 1.06$. Since D_r and p_d are constants, the appearance of diffusion coefficient figure should be the same as the porosity figure. As shown in Figure 5.5, the diffusion coefficient decreases monotonically along with x_1 direction and increases monotonically with time.

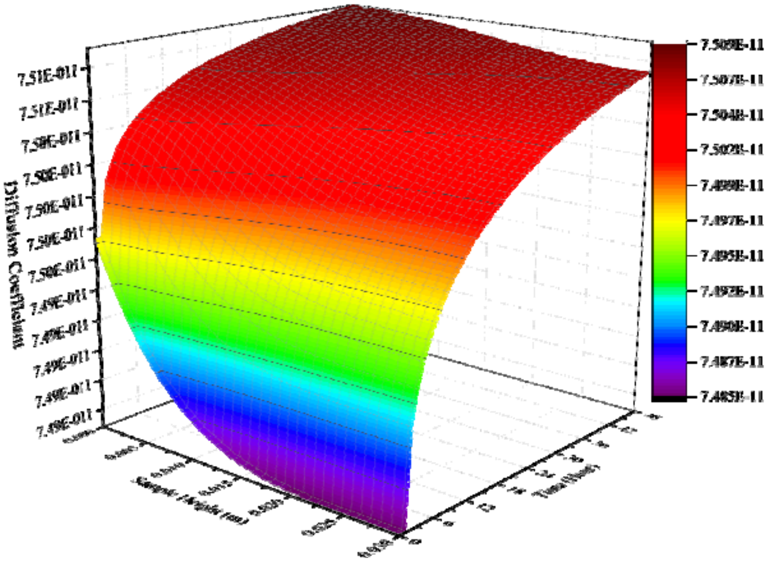

Figure 5.5: Diffusion coefficient distribution with time and space

5.6 Diffusion Rate and Chemical Reaction Rate

The concentrations of 10 materials $(i = 1, 2, \cdots, 10)$ are determined by 7 chemical reactions $\xi_k \, (k = 1, \cdots, 7)$. Figure 5.6 shows the diffusion rate distribution at each node.

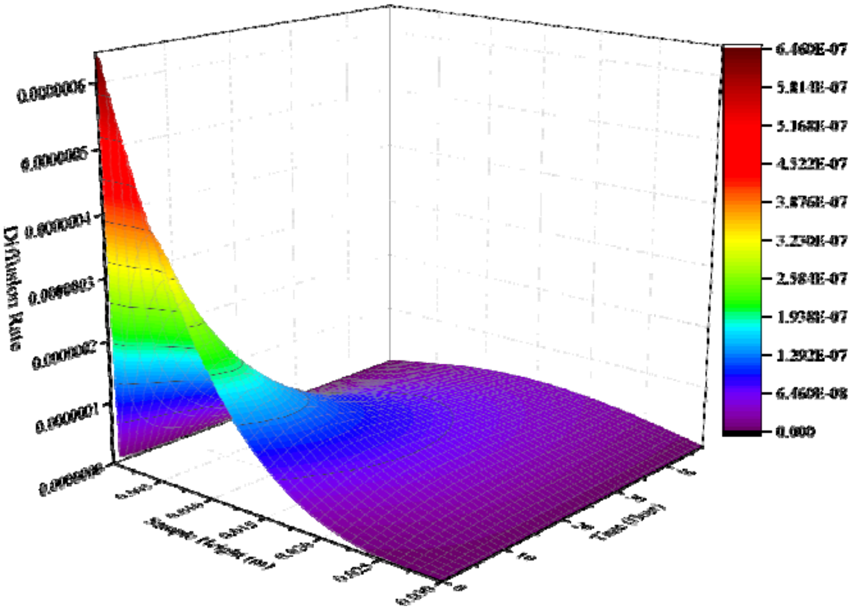

Figure 5.6: Diffusion rate distribution with time and space

Shown in Figure 5.7, the peak value of the diffusion rate appears initially at section $x_1 = 0$ (at t=0), but as time increases, the overall trend of diffusion rate for all sections decreases.

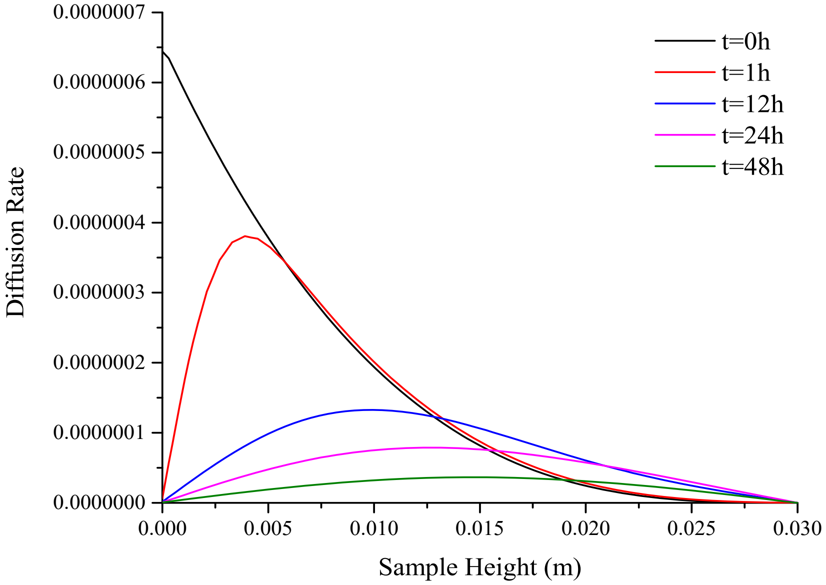

Figure 5.7: Diffusion rate at different moments

The distribution of CO_2 mass concentration at the initial moment can be given by a definite condition. So,

$$\rho_7(0,x_1)=m_{CO_2}^{atm}\frac{p_{chamb}}{p_{atm}}\phi_0\left(1-\frac{x_1}{h_s}\right)^4 \tag{5.8}$$

And the initial CO_2 diffusion velocity can be written as:

$$J(0,x_1)=4m_{CO_2}^{atm}\frac{p_{chamb}}{p_{atm}h_s}\phi_0\left(1-\frac{x_1}{h_s}\right)^3 \tag{5.9}$$

From Figure 5.7 we can clearly see that $J_1\left(0,x_1\right)$ monotonically decrease with material thickness. Thus, CO_2 diffusion velocity will rise first and fall later. Figure 5.8 shows us the peak values at different node throughout the time history, where main y axis represents node number in the numerical simulation and auxiliary y axis means the height of the sample.

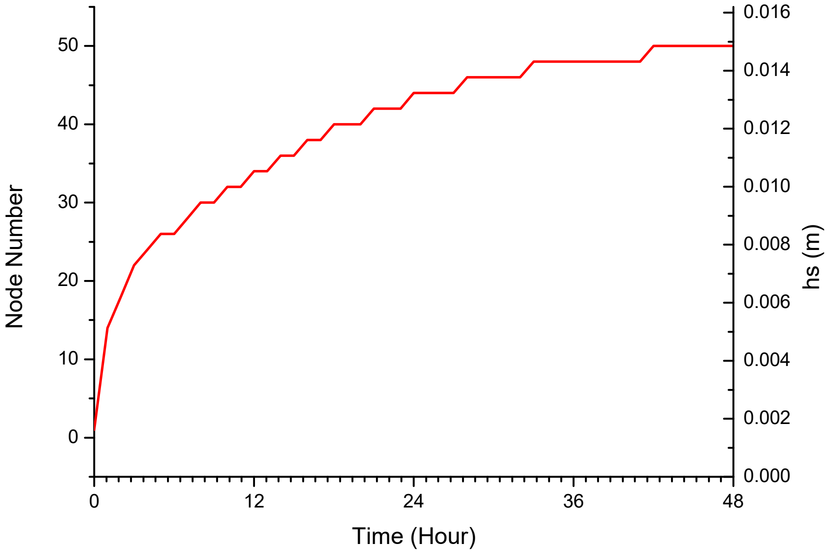

Figure 5.8: Diffusion rate peak value distribution

The diffusion velocity vary with time at section $x_1 = 0$, $x_1 = 0.5h_s$, $x_1 = 0.99h_s$ and $x_1 = h_s$ and is illustrated in Figure 5.9.

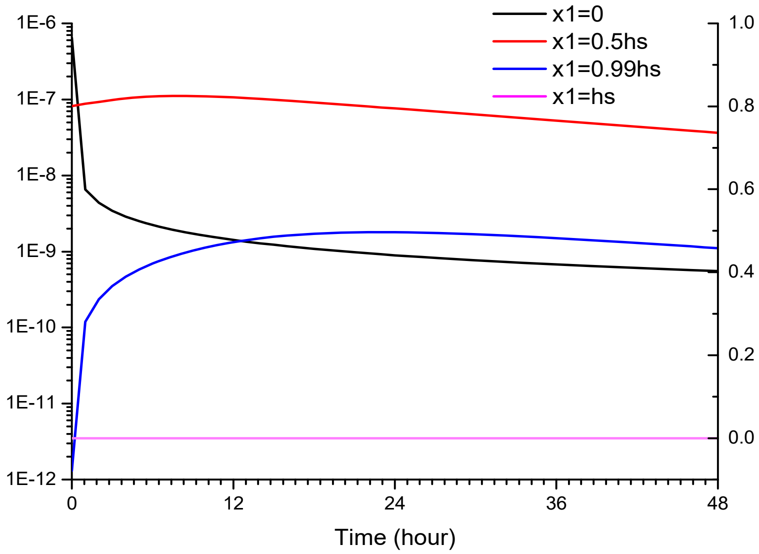

Figure 5.9: Diffusion velocity vary with time at different sections

Several observations can be made from Figure 5.9, which shows the diffusion velocity as a function of time.

(1) At section $x_1 = 0$, the diffusion velocity monotonically decreased over time indicating that the gradient of CO_2 pressure ($\frac{\partial p_{\text{chamb}}}{\partial t}$) also decreased in the cavum.

(2) At section $x_1 = h_s$, the diffusion velocity was equal to zero due to the boundary effect.

(3) At section $x_1 = 0.5h_s$, the diffusion velocity increased at the time interval ($0 \le t \le 8(\text{h})$). After that, it decreased at the time interval ($8(\text{h}) \le t \le 48(\text{h})$).

(4) At section $x_1 = 0.99h_s$, this section is very close to the closed boundary, so the diffusion velocity should be very slow. The shape of the curve shows that the tendency raised first and then fell. And the maximum point is located at $t = 23\text{hr}$.

5.7 Mass Concentrations

Mass concentrations of 10 elements from the cement material will be changed due to chemical reaction with CO_2 taking place within the sample. At the same time, CO_2 mass concentration is affected by gas diffusion. Initially, CO_2 mass concentration is given by $\rho_7(0,x_1)=m_{CO_2}^{\text{atm}} \frac{p_{\text{chmb}}}{p_{\text{atm}}} \phi_0 \left(1-\frac{x_1}{h_s}\right)^4$. The mass concentrations of the other nine materials are determined by initial conditions, $\rho_1(0,x_1)=0.6\frac{M_{\text{cement}}}{\pi a_{\text{chamb}}^2 h_{\text{chamb}}}$, $\rho_2(0,x_1)=\frac{M_{\text{total}} - M_{\text{cement}} - M_{\text{Al}}}{\pi a_{\text{chamb}}^2 h_{\text{chamb}}}$, $\rho_3(0,x_1)=0$, $\rho_4(0,x_1)=0$, $\rho_5(0,x_1)=0.3\frac{M_{\text{cement}}}{\pi a_{\text{chamb}}^2 h_{\text{chamb}}}$, $\rho_6(0,x_1)=0.1\frac{M_{\text{cement}}}{\pi a_{\text{chamb}}^2 h_{\text{chamb}}}$, $\rho_8(0,x_1)=0$, $\rho_9(0,x_1)=0$, $\rho_{10}(0,x_1)=0$.

In the following sections, we will take a closer look at the sorption effect on each of the material concentrations.

5.7.1 C_3S Mass Concentration

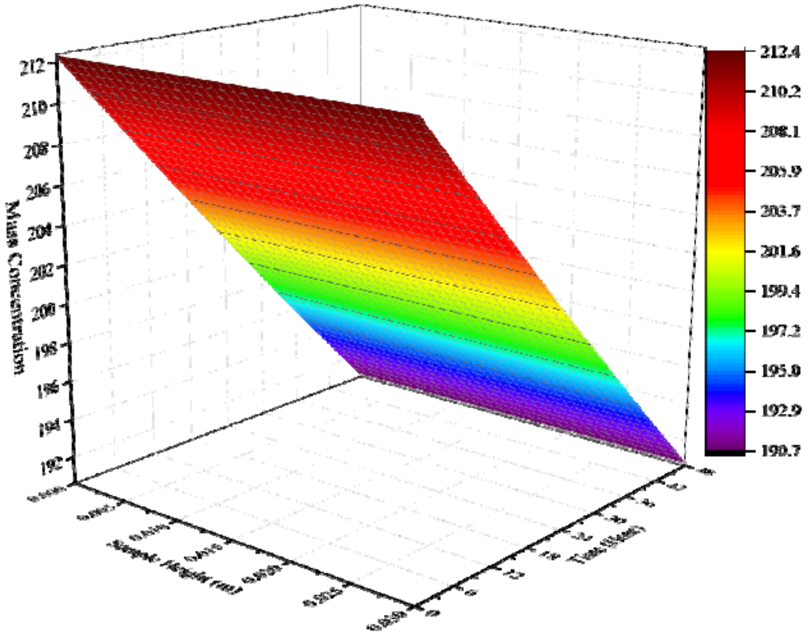

Figure 5.10: C_3S mass concentration distribution with time and space

Figure 5.10 shows the mass concentration of C_3S throughout the sorption process. The initial mass concentration of C_3S is $\rho_1^0 = 212(\text{kg/m}^3)$. C_3S is consumed throughout the chemical reaction chain due to its reactant property. So its mass concentration ρ_1 will keep decreasing at all sections during the reaction process. Since the mass concentration is uniformly distributed within the sample, the CO_2 diffusion will not affect the C_3S reaction very much.

5.7.2 H_2O Mass concentration

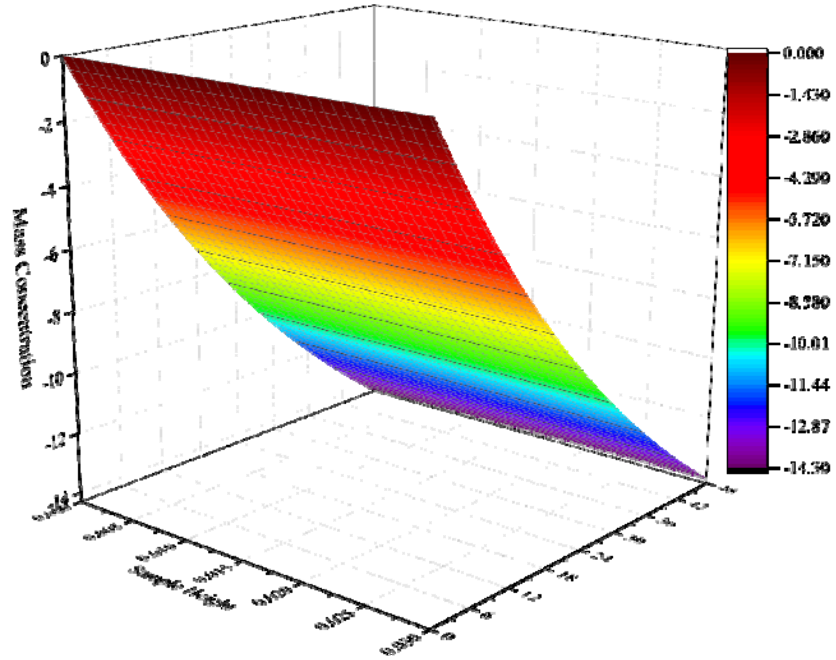

Figure 5.11: H_2O Mass concentration distribution with time and space

Figure 5.11 shows the H_2O mass concentration throughout the sorption experiment. The mass concentration of H_2O at the initial moment is $\rho_2^0 = 183(\text{kg/m}^3)$. Water is not only taken up to produce the products from the chemical reactions according to chemical equation (4.10), but also is consumed as the reactants in chemical equations (4.7), (4.8), (4.9), (4.12) and (4.13). So the mass concentration of H_2O would keep decreasing. Figure 5.11 shows the mass concentration variation of H_2O ($\hat{\rho}_2 = \rho_2 - \rho_2^0$) in one of the simulation results. From Figure 5.11 the mass concentration of water is uniformly distributed throughout the sample. There is very little water produced during the CO_2 reactions.

5.7.3 $2CaO{\cdot}2SiO_2{\cdot}3H_2O$ Mass Concentration

As a byproduct of cement hydration, initial mass concentration of

$2\mathrm{CaO}\cdot 2\mathrm{SiO}_2\cdot 3\mathrm{H}_2\mathrm{O}$ is $\rho_3^0 = 0\mathrm{kg/m}^3$. $2\mathrm{CaO}\cdot 2\mathrm{SiO}_2\cdot 3\mathrm{H}_2\mathrm{O}$ is not only taken up by the chemical reactions (4.7) and (4.8), but is also one of the reactants in chemical equation (4.11). The mass concentration of $2\mathrm{CaO}\cdot 2\mathrm{SiO}_2\cdot 3\mathrm{H}_2\mathrm{O}$ increases with time due to its production is much larger than its consumption. From Figure 5.12 the mass concentration of $2\mathrm{CaO}\cdot 2\mathrm{SiO}_2\cdot 3\mathrm{H}_2\mathrm{O}$ is shown to be uniformly distributed throughout the sample- this means that the creation of this material does not rely on CO_2. Figure 5.12 shows the mass concentration variation of $\hat{\rho}_3\left(\hat{\rho}_3 = \rho_3 - \rho_3^0\right)$.

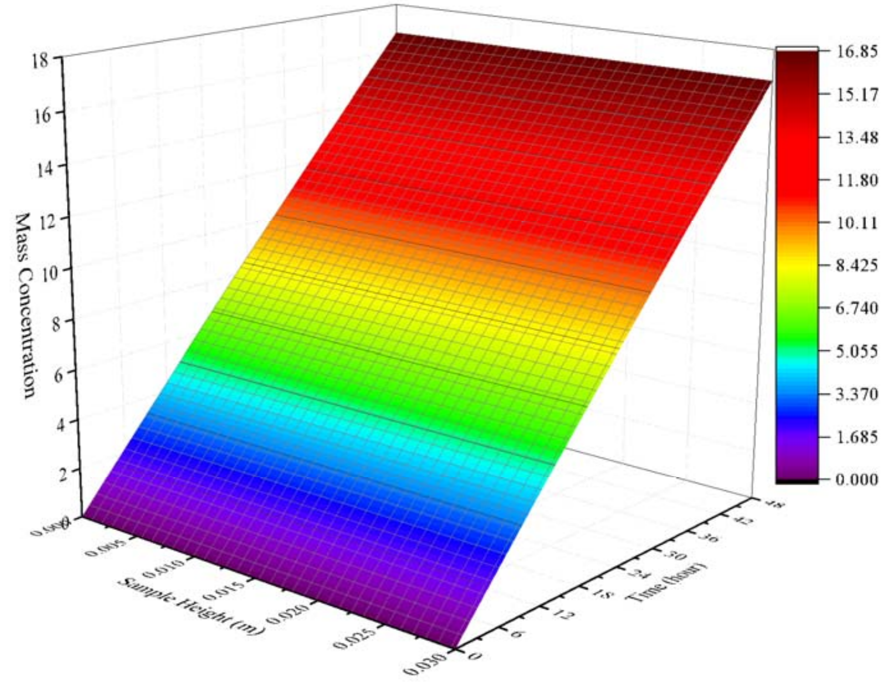

Figure 5.12: $2\mathrm{CaO}\cdot 2\mathrm{SiO}_2\cdot 3\mathrm{H}_2\mathrm{O}$ Mass Concentration

5.7.4 $Ca(OH)_2$ Mass Concentration

Figure 5.13 shows the initial mass concentration of $\mathrm{Ca}\left(\mathrm{OH}\right)_2$ should be $\rho_4^0 = 0(\mathrm{kg/m}^3)$. $\mathrm{Ca}\left(\mathrm{OH}\right)_2$ is not only being taken up during chemical reactions (4.7) and (4.8), but also represents the reactant in chemical reaction (4.10). The mass concentration of $\mathrm{Ca}\left(\mathrm{OH}\right)_2$ increases with time due to its own production is much larger than its consumption. As shown in Figure 5.13, the mass concentration of $\mathrm{Ca}\left(\mathrm{OH}\right)_2$ is uniformly distributed in the sample, meaning that the creation of this material does not relying on CO_2. Figure 5.13 shows us the mass concentration variation of $\hat{\rho}_4\left(\hat{\rho}_4=\rho_4-\rho_4^0\right)$.

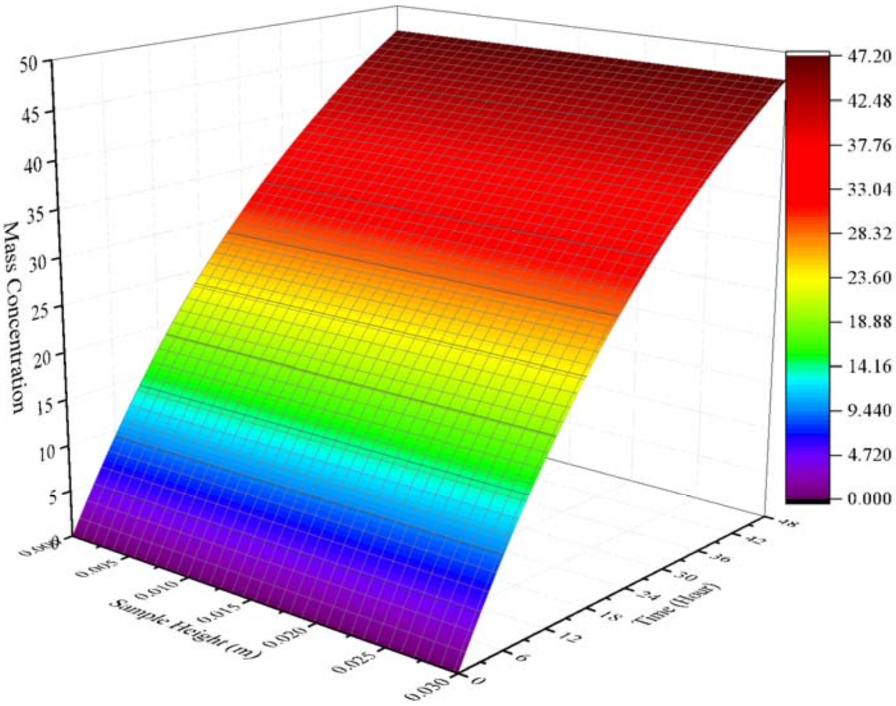

Figure 5.13: $Ca(OH)_2$ Mass concentration distribution with time and space

5.7.5 C_2S Mass Concentration

The mass concentration of C_2S monotonically decreases with time due to its reactant property. In chemical reaction equation (4.8), the reaction order are $\lambda_5^2=1$ and $\lambda_2^2=0$; the reaction rate would be $\xi_2=-k_2\mu_5\rho_5$. Because the mass concentration of ρ_5 is uniformly distributed initially, its variation at all sections should be the same. Therefore, the chemical reaction (4.8) should not cause the heterogeneity of mass concentration of

ρ_5. In chemical reaction equation (4.14), the reaction orders are $\lambda_7^5 = 0$, $\lambda_7^7 = 1$ and $\lambda_7^2 = 0$. In this case, the reaction rate should be $\xi_7 = -k_7 \mu_5 \rho_7$. Because CO_2 diffusion follows a positive direction along the axis x_1, so the mass concentration of CO_2 should reduce along axis x_1 and the reaction rate ξ_7 should increase along x_1. Therefore, the mass concentration of material 5 should increase throughout the sorption process. (Figure 5.14)

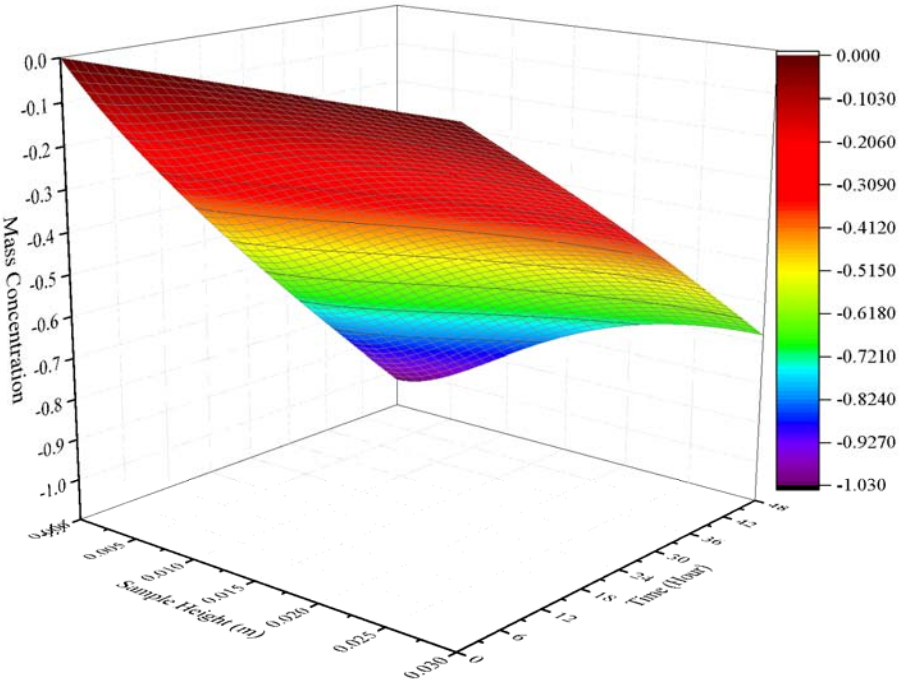

Figure 5.14: C_2S Mass concentration distribution with time and space

5.7.6 CaO Mass Concentration

Figure 5.15 shows us the mass concentration variation of CaO. As shown in Figure 5.15, the initial CaO mass concentration is $\rho_4^0 = 35.4(\text{kg/m}^3)$. CaO represents the reactant in chemical equation (4.9). At any given moment, mass concentration of CaO is uniformly throughout the sample. Hence, the consumption of CaO is not at the cost of consuming CO_2.

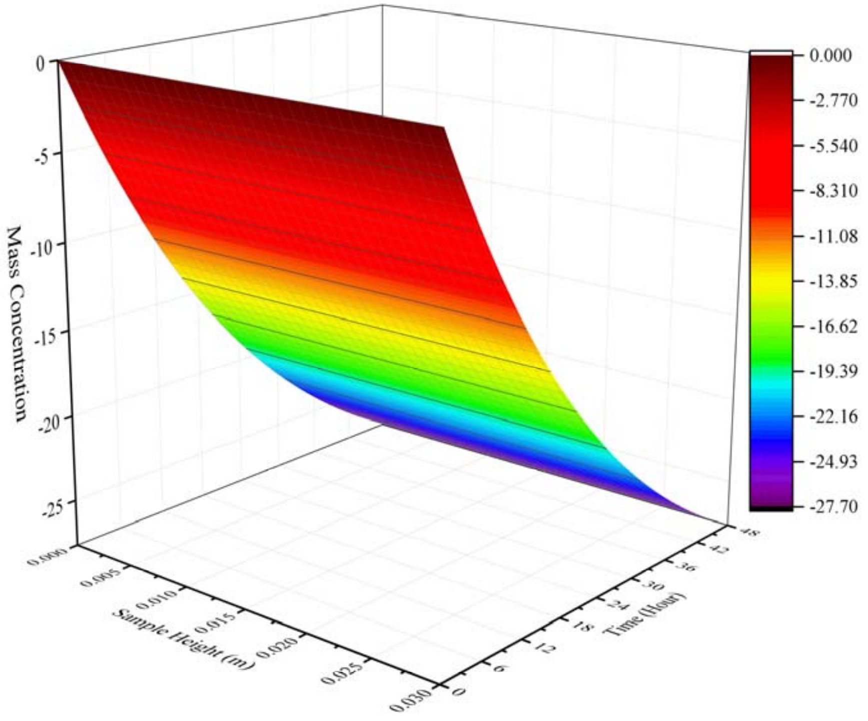

Figure 5.15: CaO Mass concentration distribution with time and space

5.7.7 CO_2 Mass concentration

The most critical player throughout the sorption experiment is CO_2 and its initial mass concentration is $\rho_7^0=6.53\left(1-\frac{x_1}{h_s}\right)^4$. Figure 5.16 shows the CO_2 distribution as a function of time and position within the specimen height (space).

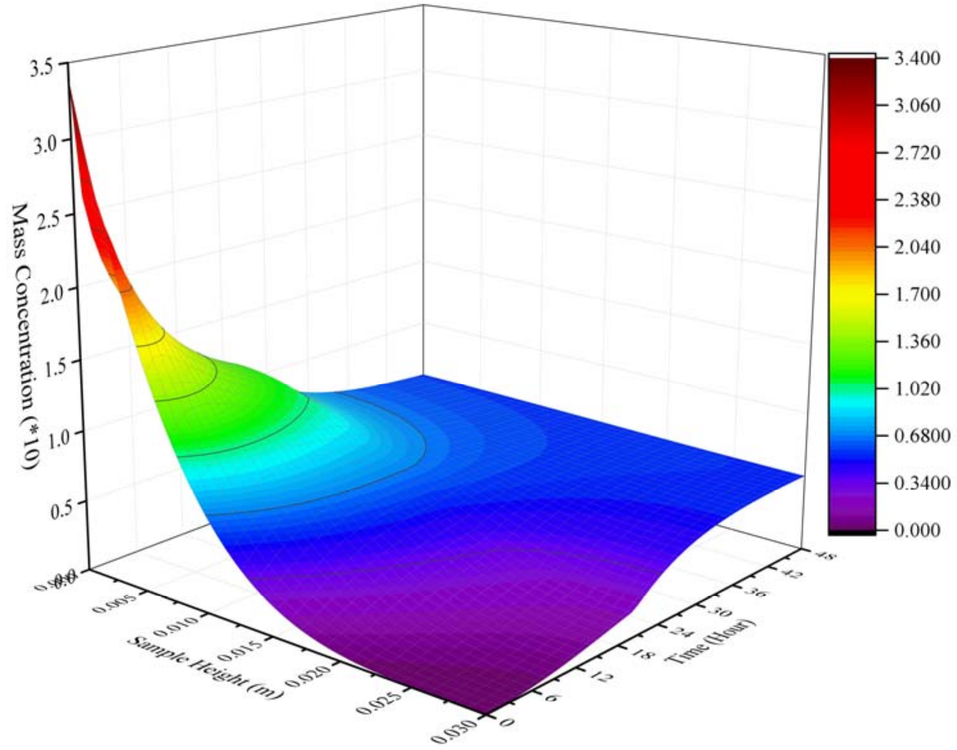

Figure 5.16: CO_2 Mass concentration distribution with time and space

The following can be observed from Figure 5.16:

(1) CO_2 gas will diffuse from top surface of the sample to its interior, and there is no supply of CO_2 after it is being consumed. Therefore, CO_2 mass concentration continued decreasing at the top surface.

(2) Due to the closed boundary at the bottom of the sample, CO_2 mass concentration remained increasing.

(3) CO_2 mass concentration continued to reduce along with time and to be gently and gradually progress along with the x_1 direction.

5.7.7.1 The Distribution Characteristic of CO_2 Mass Concentration at Different Moments

Initially ($t = 0$), the pressure at cavum is $p_0 = 0.683 \times 10^{+06}\,\mathrm{Pa}$, the initial mass density is $m_{\mathrm{CO}_2}\Big|_{t=0} = \dfrac{p_0}{p_{\mathrm{atm}}} m_{\mathrm{CO}_2}^{\mathrm{atm}} = \dfrac{0.683\times10^{+06}}{0.1\times10^{+06}}\times16.5 = 113\mathrm{kg/m}^3$, and the initial porosity is $\phi_0 = 0.280$. Therefore, the mass density is ($\rho_7\Big|_{\substack{x_1=0\\t=0}} = \phi_0\ m_{\mathrm{CO}_2}\Big|_{\substack{t=0\\x=0}}$) at the top surface $(x_1 = 0, \text{Node } 1)$. The mass density at the bottom surface $(x_1 = h_s, \text{Node } 101)$ should be approximately zero. Figure 5.17 shows us the CO$_2$ mass concentration profile is a concave-shape curve at the initial moment ($t = 0$), and there is a sudden drop along x_1 direction.

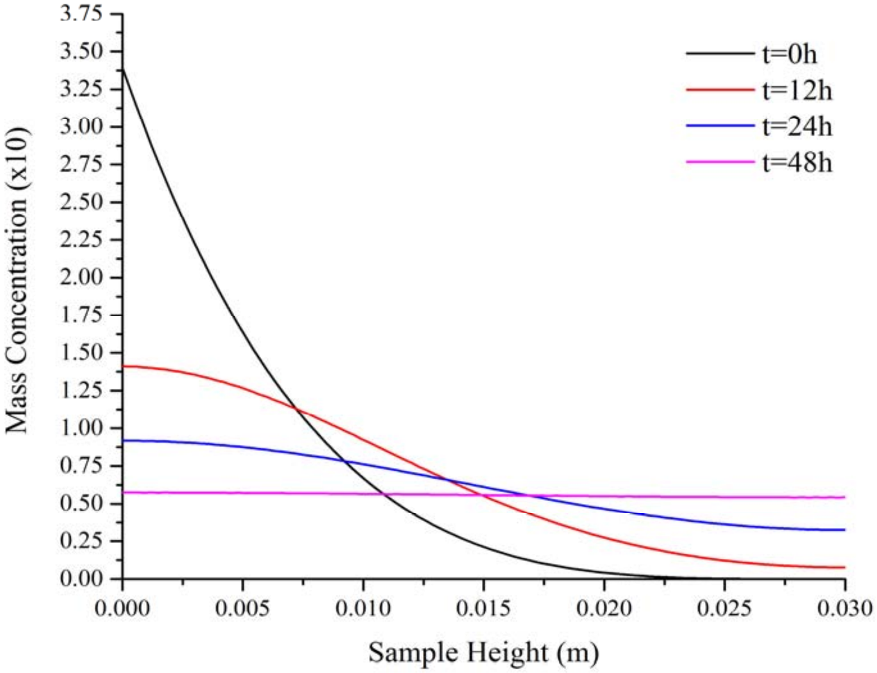

Figure 5.17: CO$_2$ mass concentrations at representative moments

As showing in Figure 5.17, at $t = 12\mathrm{hr}$ moment, the curvature of CO$_2$ mass concentration at $x_1 = 12(\mathrm{mm})$ location is an inflection point. The curve is convex between the interval $\left[0,0.0122\right]$ and concave between the interval $\left[0.0122,0.003\right]$. At the inflection point, the mass concentration at the sample surface dropped to $\rho_7\Big|_{\substack{x_1=0\\t=24(\mathrm{h})}} = 13.2(\mathrm{kg/m^3})$. Simultaneously, the bottom CO_2 mass concentration increased to $\rho_7\Big|_{\substack{x_1=h_s\\t=24(\mathrm{h})}} = 0.825(\mathrm{kg/m^3})$.

At $t = 24\mathrm{hr}$, the shape of the curve remained as with convex left side and with concave on the right side. The inflection point is not that obvious in the figure. The CO_2 mass concentration at the surface dropped to $8.47(\mathrm{kg/m^3})$, and the bottom CO_2 mass concentration rose to $3.07(\mathrm{kg/m^3})$.

At $t = 48\mathrm{hr}$, the shape of the curve resembled a horizontal linear distribution and the CO_2 mass concentration was even at both surface and bottom.

5.7.7.2 The Distribution Characteristic of CO_2 Mass Concentration at Different Cross Section

The variations of CO_2 mass concentration are caused by two major parameters. The first one is gas diffusion, and the second parameter is the participating chemical reactions. Those two influences can be represented as:

$$^{1}\frac{\partial \rho_7}{\partial t} = -\frac{\partial J_1}{\partial x_1} = \frac{\partial}{\partial x_1}\left(D\frac{\partial \rho_7}{\partial x_1} \right) \tag{5.10}$$

And

$$^{2}\frac{\partial \rho_7}{\partial t} = -\mu_7\xi_4 - 3\mu_7\xi_5 - 3\mu_7\xi_6 - 2\mu_7\xi_7 \tag{5.11}$$

As shown in Figure 5.18, CO2 mass concentration kept decreasing along with time. This is because the leading factor that consumes CO_2 is the gas diffusion process.

The diffusion velocity $\left(J = -D\frac{\partial \rho_7}{\partial x_1} \right)$ will go down as the concentration differences decrease at both ends.

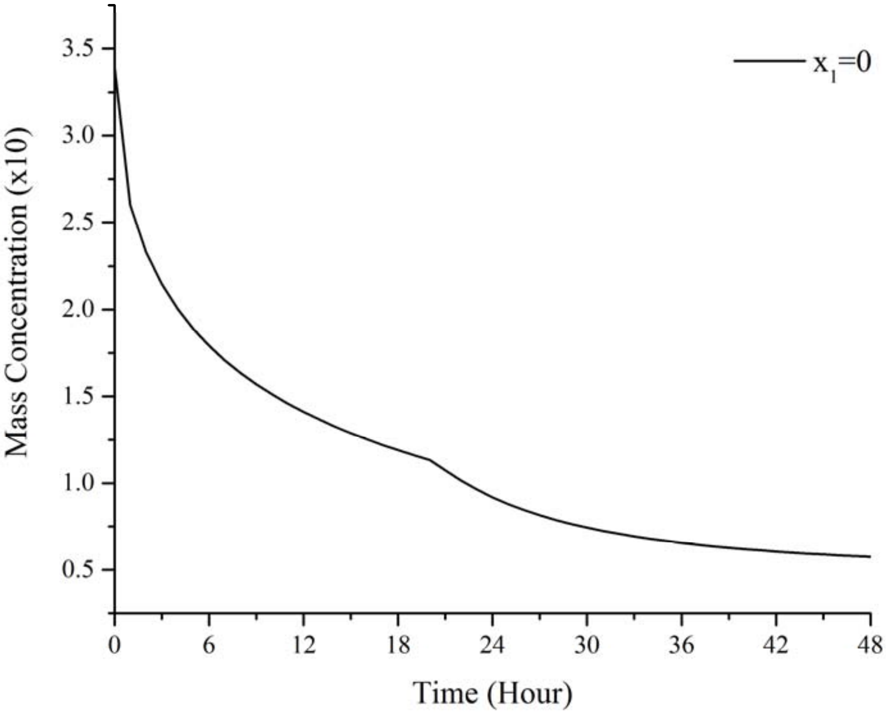

Figure 5.18: CO_2 mass concentration on $x_1 = 0$ section

Figure 5.19 shows that CO_2 mass concentration would keep increasing at the bottom section $\left(x_1 = h_s \right)$. The main reason for the mass concentration change is gas diffusion before $t = 20\text{hr}$. So the mass concentration shows like a convex curve. After $t = 20\text{hr}$, gas diffusion and chemical reaction influences on the results are of the same order. And as time goes, the ratio of gas diffusion mass changing rate $\frac{{}^{1}\partial \rho_7}{\partial t}$ and chemical reaction mass changing rate $\frac{{}^{2}\partial \rho_7}{\partial t}$ are reduced gradually.

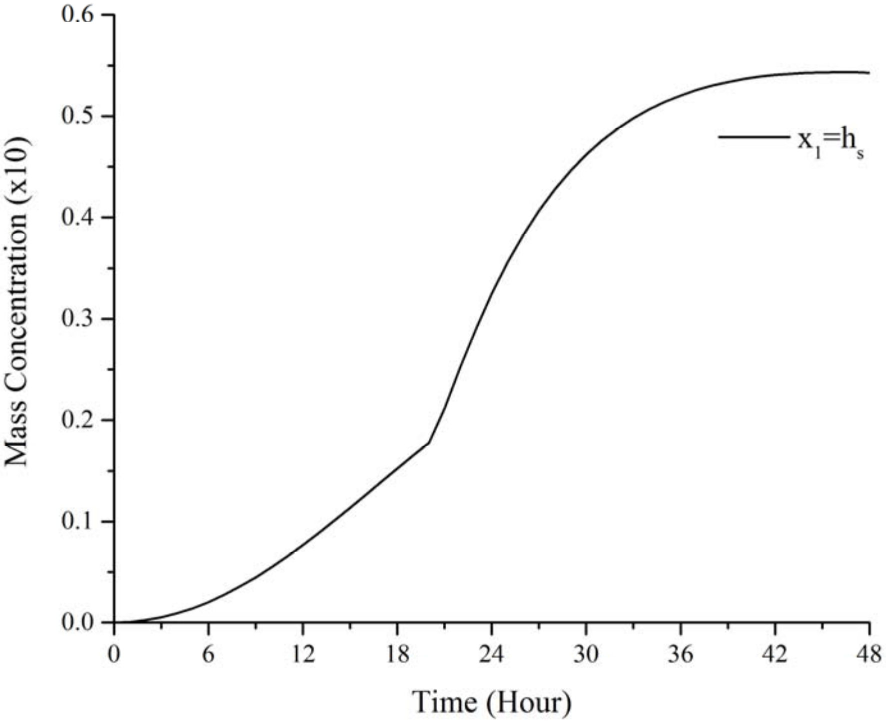

Figure 5.19: CO2 mass concentration at $x_1 = h_s$ section

Figure 5.20 shows CO2 mass concentration at the $x_1 = 0.5h_s$ cross section, where it is shown that the mass concentration kept increasing before $t \le 22\text{hr}$. And the value started to drop during $22\text{hr} \le t \le 50\text{hr}$. As shown in Figure 5.21, the rate of gas diffusion mass density change rage is greater than the chemical reaction mass density change rate, ${}^{1}\left|\frac{\partial \rho_7}{\partial t}\right|_{x_1 = \frac{1}{2}h_s} > {}^{2}\left|\frac{\partial \rho_7}{\partial t}\right|_{x_1 = \frac{1}{2}h_s}$; hence, the total mass concentration at this section increased.

At $22\text{hr} \le t \le 50\text{hr}$ time zone, ${}^{1}\left|\frac{\partial \rho_7}{\partial t}\right|_{x_1 = \frac{1}{2}h_s} < {}^{2}\left|\frac{\partial \rho_7}{\partial t}\right|_{x_1 = \frac{1}{2}h_s}$, as a result, the mass concentration decreased.

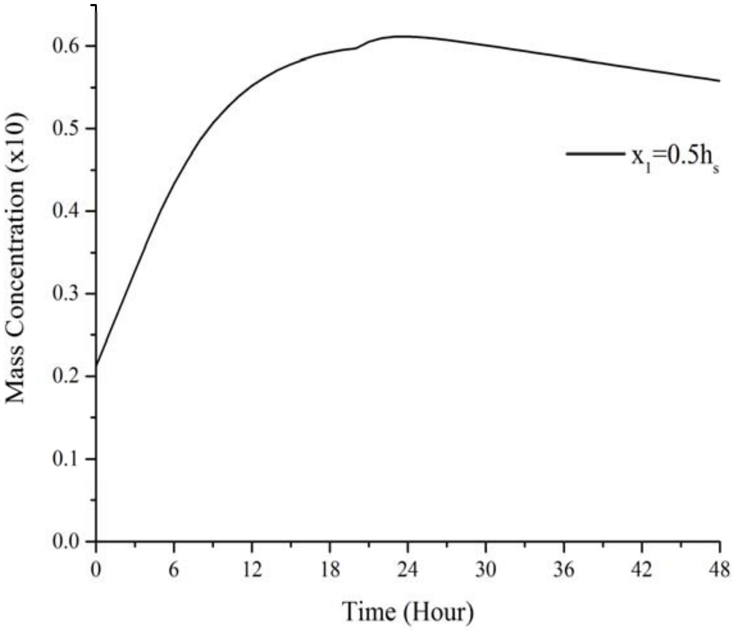

Figure 5.20: CO_2 mass concentration at $x_1 = 0.5h_s$ section

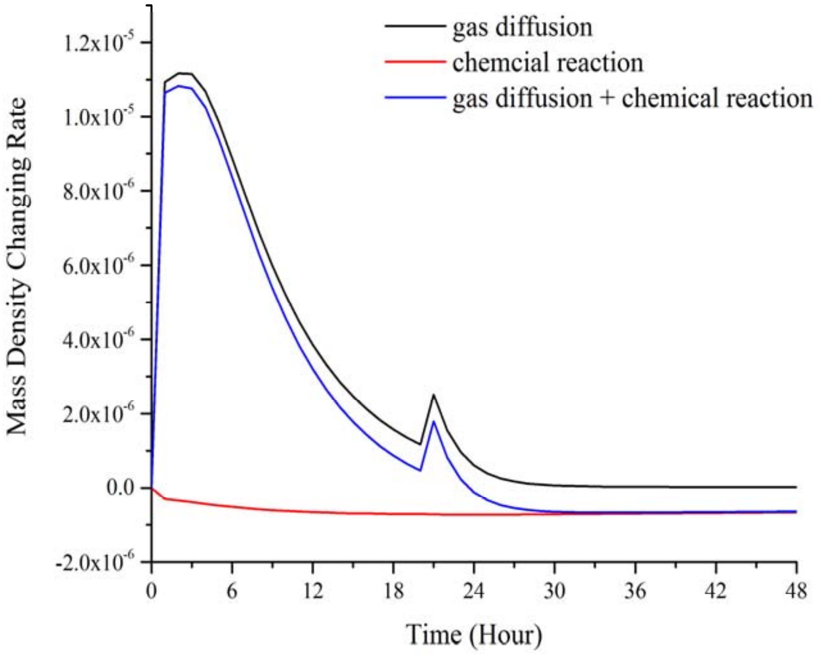

Figure 5.21 Mass changing rate along with time on $x_1 = 0.5h_s$ section

At other sections, the sign of CO_2 mass density changing rate would change as well. The only difference is that at the moment (t_1), the mass concentration changes from decreasing to increasing. Figure 5.22 shows t_1 varying with cross-section coordinate.

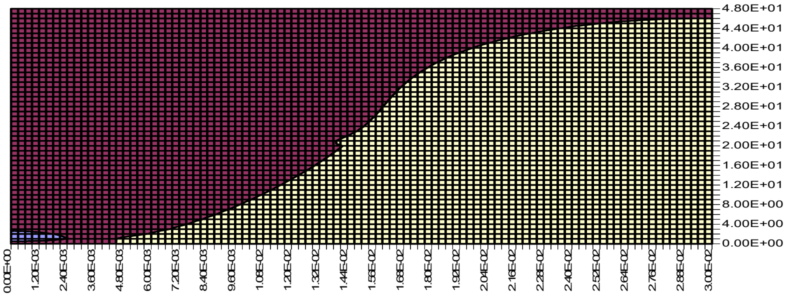

Figure 5.22 t_1 changes at cross-section (a)

5.7.8 $CaCO_3$ Mass Concentration

The mass density rate of $CaCO_3$ can be given as:

$$\frac{\partial \rho_8}{\partial t} = \begin{cases} \mu_8 k_4 \rho_4 + 3\mu_8 k_6 \rho_7 + 2\mu_8 k_7 \rho_7, t \le 2(\mathrm{h}) \\ \mu_8 k_4 \rho_7 + 3\mu_8 k_6 \rho_7 + 2\mu_8 k_7 \rho_7, t > 2(\mathrm{h}) \end{cases} \tag{5.12}$$

which can be modified as:

$$\frac{\partial \rho_8}{\partial t} = \begin{cases} \mu_8 k_4 \rho_4 + \mu_8 \left(3k_6 + 2k_7\right) \rho_7, t \le 2(\mathrm{h}) \\ \mu_8 \left(k_4 + 3k_6 + 2k_7\right) \rho_7, t > 2(\mathrm{h}) \end{cases} \tag{5.13}$$

$CaCO_3$ is the resultant from the chemical reactions; hence, its mass concentration should increase with time, $\frac{\partial \rho_8}{\partial t} > 0$. At time $t \le 2\text{hr}$, ρ_4 was well distributed throughout the specimen, and ρ_7 reduced along x_1 direction. Therefore, $\frac{\partial \rho_8}{\partial t} = \mu_8 k_4 \rho_4 + \mu_8 \left(3k_6 + 2k_7\right) \rho_7$ would monotonically decrease along the x_1 direction.

At $t > 2\text{hr}$, ρ_7 declined along with x_1 direction, and $\frac{\partial \rho_8}{\partial t} = \mu_8 \left(k_4 + 3k_6 + 2k_7\right) \rho_7$ also decreased along the x_1 direction. During the gas diffusion and chemical reaction processes, $\frac{\partial \rho_8}{\partial t}$ is shown to keep decreasing along the x_1 axis. With the conditions $\rho_8^0(0, x_1) = 0$ and $\frac{\partial \rho_8}{\partial t} > 0$, it is easy to determine the mass density ρ_8 which should decrease along the x_1 direction.

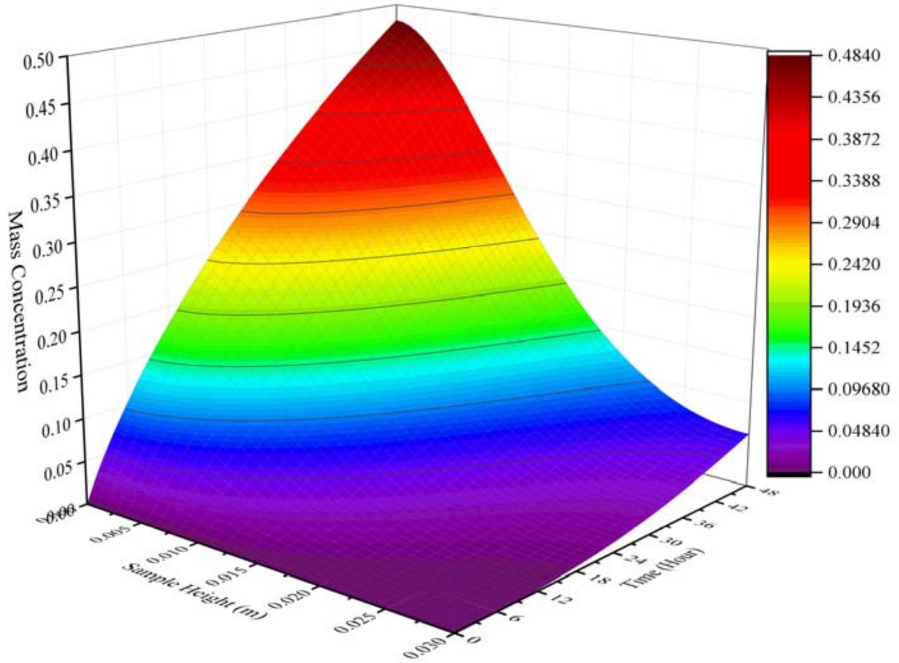

Figure 5.23: $CaCO_3$ mass concentration

5.7.9 $3CaCO_3 \cdot 2SiO_2 \cdot 3H_2O$ and $SiO_2 \cdot \gamma H_2O$ Mass Concentrations

Figure 5.24 and Figure 5.25 have the same pattern as in Figure 5.23. This is because the trends have similar logics. From Figures 5.23, 5.24 and 5.25, it is noticed that only the mass concentration of CO_2 and of those resultants containing CO_2 ($CaCO_3$, $3CaCO_3 \cdot 2SiO_2 \cdot 3H_2O$) will change along x_1 axis. The other 7 materials are uniformly distributed. Throughout the sample, the gas diffusion process has little effect on their mass concentration.

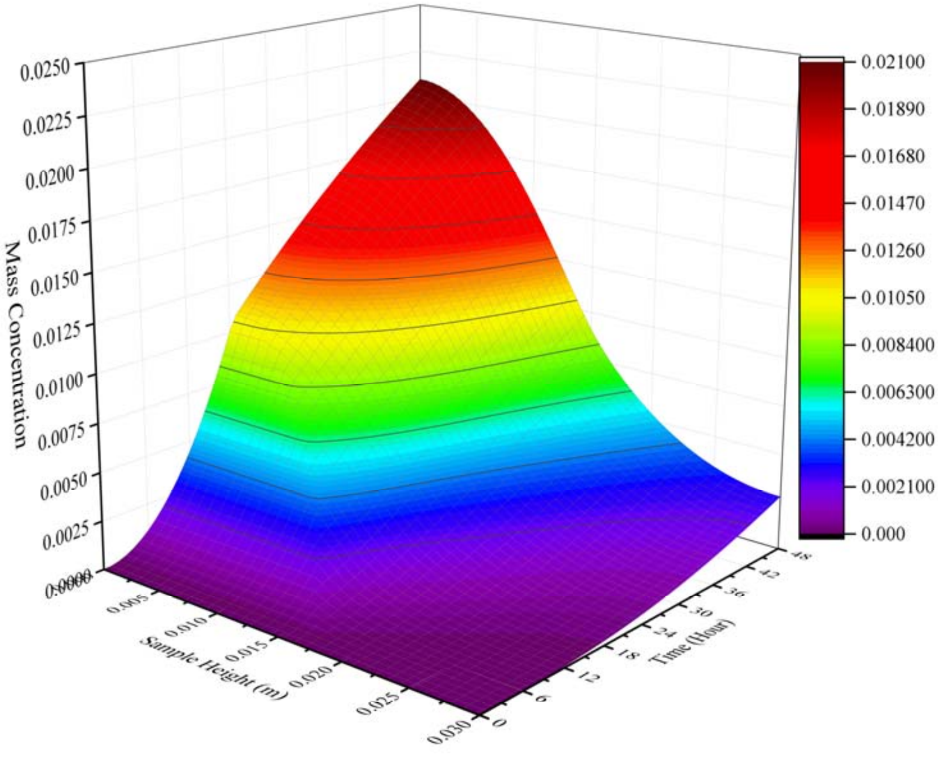

Figure 5.24: $3CaCO_3 \cdot 2SiO_2 \cdot 3H_2O$ mass concentration

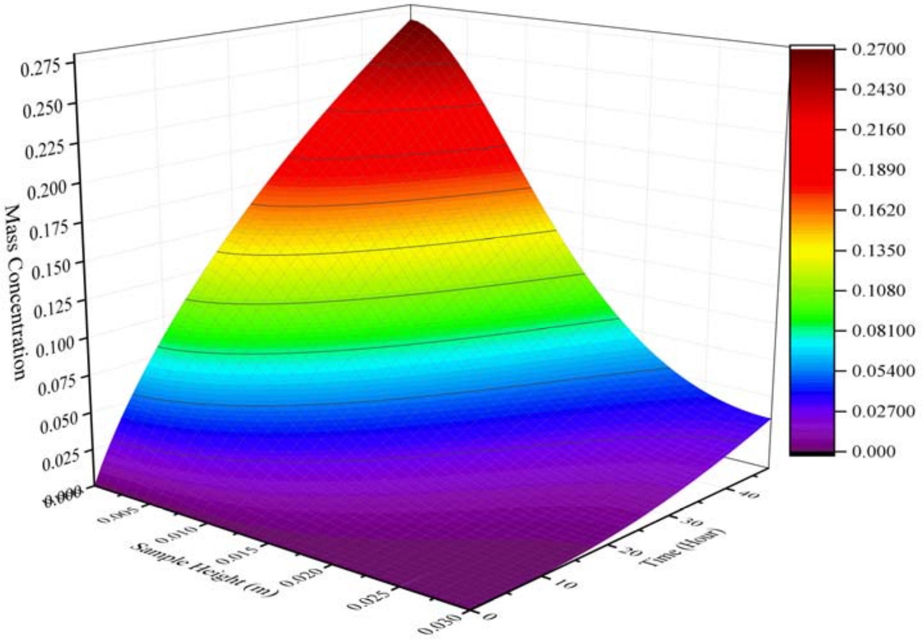

Figure 5.25: $SiO_2{\cdot}\gamma H_2O$ mass concentration

5.8 Summary

In this chapter, the feasibility of the response computation method is validated by running one computation example. The performances are quantified by mass concentration distribution, the diffusion and chemical reaction rates. The performances consistent with our expectations.

This concludes that the numerical modeling is accurate and the assumptions made are reasonable. In the following chapter, we ran different cases and compare the results to the experimental results.

CHAPTER 6: PARAMETRIC STUDY

6.1 Introduction

This chapter will present a technical discussion on the comparison (Chapter 3) between the experimental results and the simulation results. Several experiments have been performed throughout this study. However, focus of this chapter will be placed on limited parameters. Hence, comparisons will be made on six different samples and will include factors specifically including initial water contents (section 6.2), initial porosity (section 6.3) and initial gas pressure (section 6.4). Additional experimental results are presented in Appendix B. The purposes of the comparisons are to validate the numerical models with the experiment results and at the same time, investigate effects of these three parameters of the CO_2 sorption responses. To a very limited scale, we will also investigate the sensitivity of CO_2 trapping within the specimen.

6.2 Water Content Impacts on CO_2 Diffusion and Chemical Reaction

Cement hydraulic reactions include three major chemical reactions, which are:

$$\mathrm{2C_3S+6H_2O \rightarrow 3CaO\cdot 2SiO_2\cdot 3H_2O+3Ca(OH)_2} \tag{6.1}$$

$$\mathrm{2C_2S+4H_2O \rightarrow 3CaO\cdot 2SiO_2\cdot 3H_2O+Ca(OH)_2} \tag{6.2}$$

$$\mathrm{CaO+H_2O \rightarrow Ca(OH)_2} \tag{6.3}$$

The resulting three reaction rates, ξ_1, ξ_2, ξ_3, are closely associated with water content in the above chemical reactions. This is because water is the key element which dictates the reaction order ($\lambda_1^1, \lambda_2^1, \lambda_2^2, \lambda_5^2, \lambda_2^3$). In return, the reaction rates (ξ_1, ξ_2, ξ_3) would affect the product ($3CaO \cdot 2SiO_2 \cdot 3H_2O$ and $Ca(OH)_2$) concentrations. Moreover, $3CaO \cdot 2SiO_2 \cdot 3H_2O$ and $Ca(OH)_2$ would react with free CO_2 and cause the CO_2 concentration to change. Since the other reason for CO_2 mass concentration change is gas diffusion. Thus, it is reasonable to conclude that the water content in the sample has significant impacts on CO_2 mass concentration distribution and possible variation.

In this comparative study, two Samples (No. 1 and 2) are used, the cement mass is 30g in both samples and the water contents are 15g and 10g, respectively. The initial porosity of both samples is given as 0.36. The initial height of the samples is 30mm. The initial CO_2 pressure is given as 148psi. The total time of test is 48 hours. Power component for the diffusion coefficient equation is assumed to be $p_d = 1.5$. The decision variables for the diffusion-chemical reaction kinetics are listed in Table 6.1.

Table 6.1 Decision variables for the diffusion-chemical reaction kinetics

k_1	k_2	k_3	k_4	k_5	k_6	k_7	D_r
1×10^{-10}	2.61×10^{-9}	1×10^{-8}	1×10^{-10}	7.29×10^{-10}	1.36×10^{-9}	2.61×10^{-9}	5.57×10^{-11}

With an integration step assumed as $h_t = 1\ \text{second}$, the simulation program is set to output the physical quantities at every hour. To determine the effect of water content on CO_2 uptake, we will analysis the cavum pressure, the CO_2 decrement in the cavum, the CO_2 trapped in the cement based porous material, the CO_2 chemical consumption amount, the reaction rates ($\xi_1, \cdots, \xi_7$) and the material mass concentrations.

6.2.1 CO_2 Pressure in Cavum

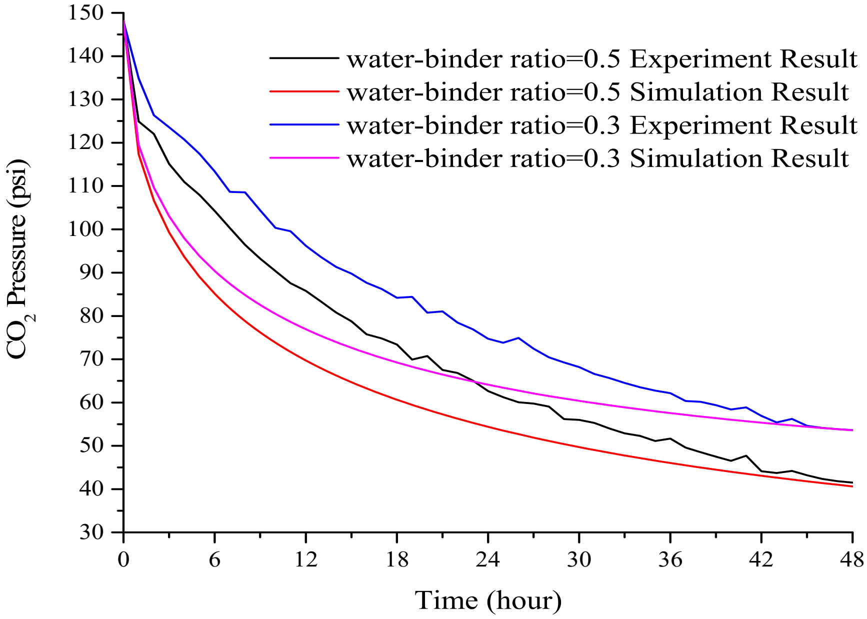

Figure 6.1: Experimental results of CO_2 cavum pressure variation in Sample 1 and Sample 2

Pressure change curves from CTPRC experiment are shown in Figure 6.1. As shown in the figure, the decline of CO_2 pressure in Sample 1 is larger than Sample 2. The water content is much higher in Sample 1 than Sample 2, so the reaction rates in Sample 1 ($\xi_6 = k_6 \rho_1^{\lambda_1^6} \rho_7^{\lambda_7^6} \rho_2^{\lambda_2^6}$ and $\xi_7 = k_7 \rho_5^{\lambda_5^7} \rho_7^{\lambda_7^7} \rho_2^{\lambda_2^7}$) is expected to also be higher than Sample 2. Therefore, the CO_2 chemical consumption in Sample 1 ($\left.\frac{\partial \rho_7}{\partial t}\right|_{\text{reaction}} = -\mu_7 \xi_4 - 3\mu_7 \xi_5 - 3\mu_7 \xi_6 - 2\mu_7 \xi_7$) is greater than Sample 2.

6.2.2 CO_2 Decrement in Cavum

The cavum CO_2 amount can be determined by the chamber pressure, p_{chamb},

$$M_{CO_2}^{0} = \pi a_s^2 h_{\text{chamb}} m_{CO_2}^{0} = \pi a_s^2 h_{\text{chamb}} m_{CO_2}^{\text{atm}} \frac{p_{\text{chamb}}^{0}}{p_{\text{atm}}} \tag{6.4}$$

The superscript “0” in the above equation means its physical quantity at the initial stage ($t=0$). Within the $\left[0,t\right]$ time interval, the CO2 mass which is diffused from the void space to the sample can be described as:

$$M_{\mathrm{CO_2}}^{\mathrm{diff}} = \pi a_{\mathrm{s}}^{2} h_{\mathrm{chamb}} m_{\mathrm{CO_2}}^{\mathrm{atm}} \frac{p_{\mathrm{chamb}}^{0} \text{-} p_{\mathrm{chamb}}}{p_{\mathrm{atm}}} \tag{6.5}$$

Figure 6.2 shows the numerical simulation results of cavum CO2 mass consumption in Sample 1 (15g water) and Sample 2 (10g water).

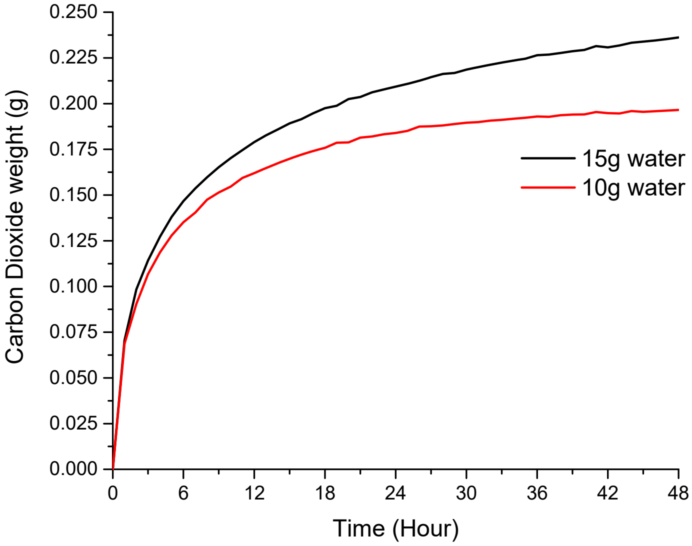

Figure 6.2: Void space CO_2 mass consumption in Sample 1 and Sample 2

From Figure 6.2, the different water contents are shown to have very limited impact on CO_2 mass consumption in cavum. At $t=1\mathrm{hr}$, CO_2 mass consumptions in the void space are $M_{\mathrm{CO_2}}^{\mathrm{diff}}\Big|_{\mathrm{t=1h}}^{15g}$ =70.5(mg) and $M_{\mathrm{CO_2}}^{\mathrm{diff}}\Big|_{\mathrm{t=1h}}^{10g}$ =68.7(mg) , and the ratios are $M_{\mathrm{CO_2}}^{\mathrm{diff}}\Big|_{\mathrm{t=1h}}^{\mathrm{15g}} : M_{\mathrm{CO_2}}^{\mathrm{diff}}\Big|_{\mathrm{t=1h}}^{\mathrm{10g}}$ =1.03:1 respectively. At $t=48\mathrm{hr}$, the CO_2 mass consumptions in the void space are $M_{\mathrm{CO_2}}^{\mathrm{diff}}\Big|_{\mathrm{t=48h}}^{\mathrm{15g}}$ =236(mg) and $M_{\mathrm{CO_2}}^{\mathrm{diff}}\Big|_{\mathrm{t=48h}}^{\mathrm{10g}}$ =197(mg) , and the ratios are

$M_{\mathrm{CO_2}}^{\mathrm{diff}}\Big|_{\mathrm{t=48h}}^{\mathrm{15g}} : M_{\mathrm{CO_2}}^{\mathrm{diff}}\Big|_{\mathrm{t=48h}}^{\mathrm{10g}}$ =1.20:1 respectively. Hence, $M_{\mathrm{CO_2}}^{\mathrm{diff}}\Big|^{\mathrm{15g}} : M_{\mathrm{CO_2}}^{\mathrm{diff}}\Big|^{\mathrm{10g}}$ would increase with time and remains always less than the water content ratio.

6.2.3 CO_2 Trapping

Figure 6.3 shows the trapped mass ($Q'_{\mathrm{CO_2}}$) variation in Sample 1 and Sample 2 throughout the study period. The trapped CO_2 represents CO_2 in the void space.

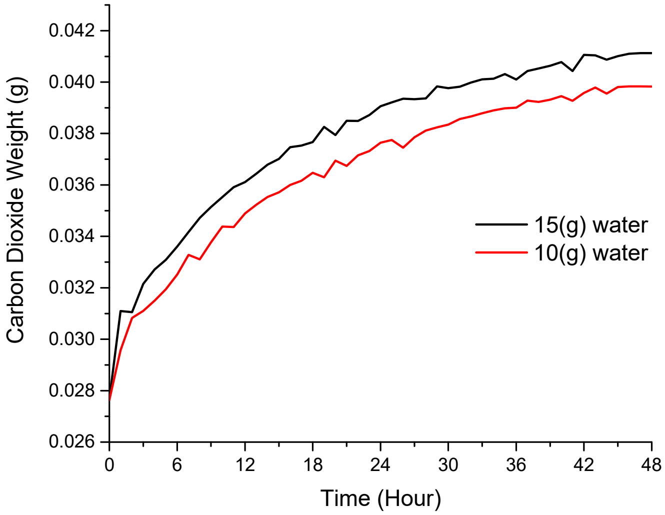

Figure 6.3: Trapped CO_2 mass in Sample 1 and Sample 2

Comparing Figure 6.2 and 6.3, $Q'_{\mathrm{CO_2}}\Big|_{\mathrm{15g}}$ is always larger than $Q'_{\mathrm{CO_2}}\Big|_{\mathrm{10g}}$. Most of the CO_2 was consumed by chemical reaction during its diffusion procedure and only a small quantity of the CO_2 would be trapped in the pore space.

6.2.4 CO_2 Consumption during Chemical Reaction

Figure 6.4 shows the chemical reaction consumption of CO_2 mass in Sample 1 and Sample 2.

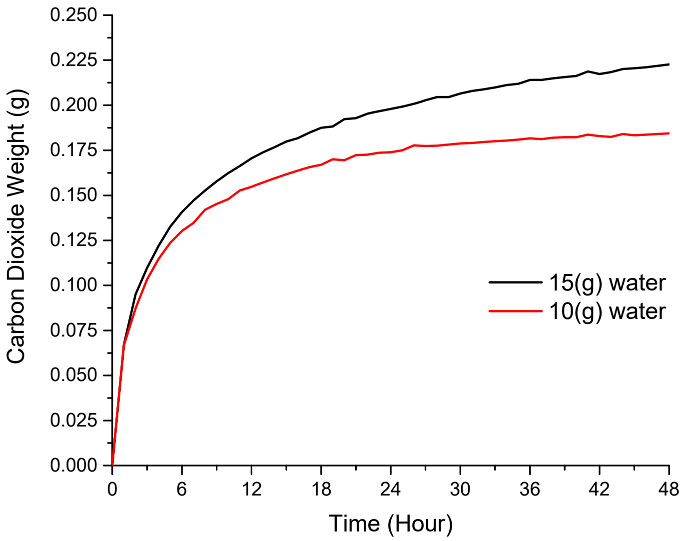

Figure 6.4: Chemical reaction consumption of CO_2 mass variation

As shown in Figure 6.4, the consumption during chemical reaction in Sample 1 ($Q_{\text{consume}}\big|_{15\text{g}}$) is larger than Sample 2 ($Q_{\text{consume}}\big|_{10\text{g}}$). The CO_2 consumption caused by the chemical reaction can be described as:

$$-\frac{\partial \rho_7}{\partial t}\bigg|_{\text{reaction}} = \mu_7 \xi_4 + 3\mu_7 \xi_5 + 3\mu_7 \xi_6 + 2\mu_7 \xi_7 \tag{6.6}$$

It is obvious that great water content means higher reaction rates (ξ_6 and ξ_7). Therefore, in the sorption process, chemical reactions would result in large gas concentration decay rates.

6.2.5 Chemical Reaction Rate Comparison

The first chemical equation is shown to be:

$$\text{2C}_3\text{S+6H}_2\text{O} \rightarrow \text{3CaO} \cdot \text{2SiO}_2 \cdot \text{3H}_2\text{O+3Ca}\left(\text{OH}\right)_2 \tag{6.7}$$

where, the chemical reaction rate ξ_1 is determined by the mass density of reactants C_3S (ρ_1) and H_2O (ρ_2), and $\xi_1 = k_1 \rho_1^{\lambda_1^1} \rho_2^{\lambda_2^1}$. Due to $\rho_1 > \rho_2$, there are significant reaction rate difference between Sample 1 and Sample 2. At $t = 0hr$, reaction rate $\xi_1 = k_1 \rho_1^{\lambda_1^1} \rho_2^{\lambda_2^1}$ is evenly distributed throughout due to C_3S and H_2O are uniformly distributed in both samples.

At $t > 0hr$, because the influence of CO_2 mass concentration at one end of the sample, the mass concentration of C_3S and H_2O would gradually step away from their uniformly distributions. Therefore, the reaction rate curves cannot keep horizontal in x_1 direction. Figure 6.5 and Figure 6.6 show the chemical reaction rate ξ_1 distributions change throughout time and space. Figure 6.7 shows the chemical reaction rates at $t = 48hr$. Figure 6.8 shows the chemical reaction rates at section $x_1 = 0$. Figure 6.7 and 6.8 also show linear curve fits for the reaction rate curves. The reaction rate curves are conclusively linear in nature.

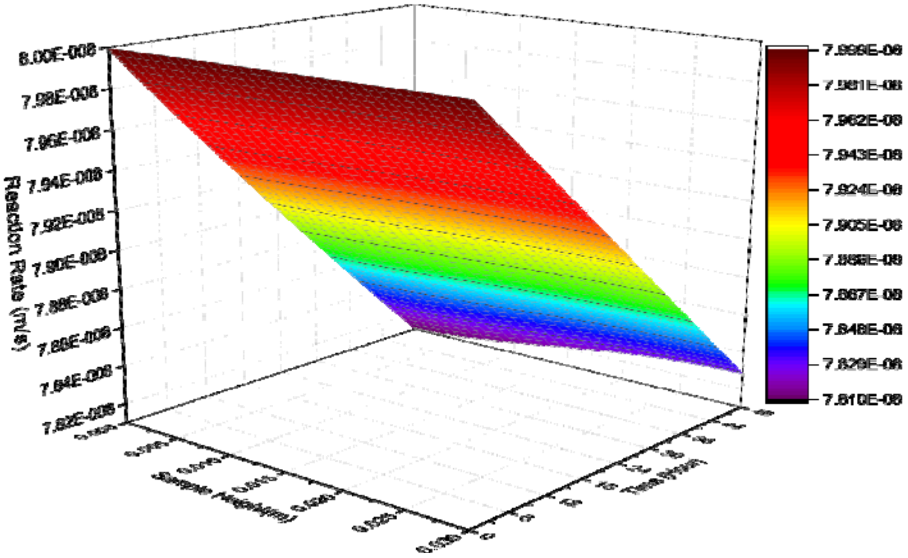

Figure 6.5: Sample 1 reaction rate (ξ_1) time-space distribution

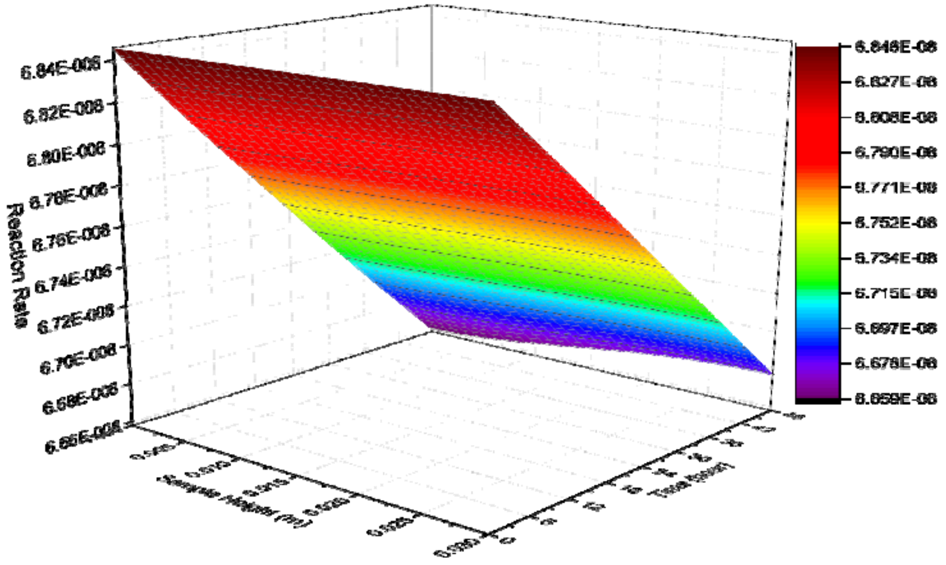

Figure 6.6: Sample 2 reaction rate (ξ_1) time-space distribution

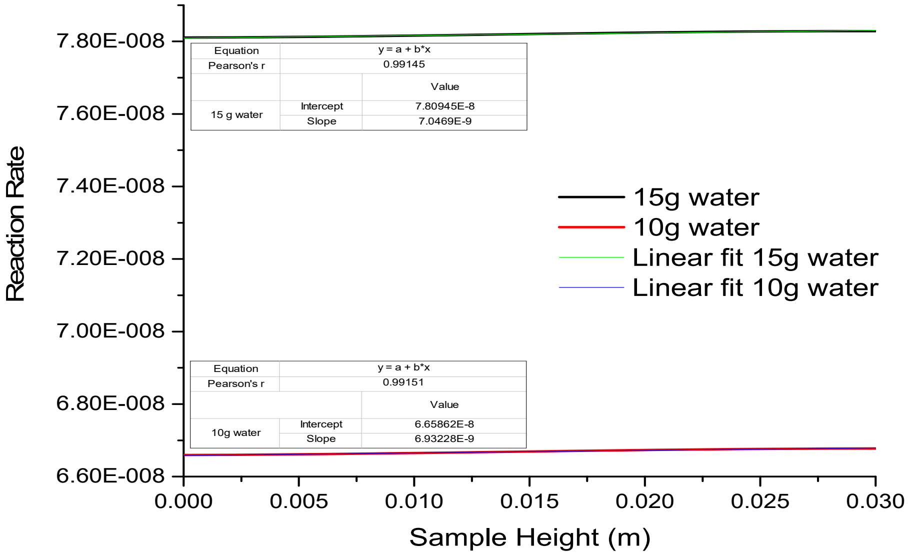

Figure 6.7: Reaction rates ($\xi_1 \Big|_{15\mathrm{g}}^{10\mathrm{g}}$) comparison between the samples at $t = 48\,\mathrm{hr}$

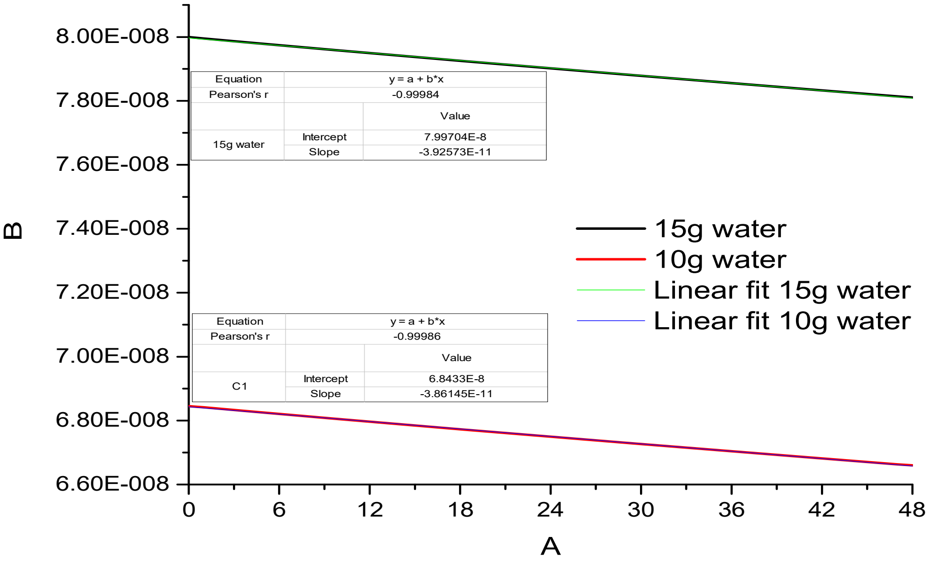

Equation		y = a + b*x
Pearson's r		-0.99984
		Value
15g water	Intercept	7.99704E-8
	Slope	-3.92573E-11

Equation		y = a + b*x
Pearson's r		-0.99986
		Value
C1	Intercept	6.8433E-8
	Slope	-3.86145E-11

Figure 6.8: Reaction rates ($\xi_1 \Big|_{15\text{g}}^{10\text{g}}$) comparison at section $x_1 = 0$

From Figure 6.5 and Figure 6.6, it is shown that the reaction rate $\xi_1 \Big|_{15\text{g}}$ will always be larger than $\xi_1 \Big|_{10\text{g}}$. So,

$$\left| \frac{\partial \xi_1 \Big|_{15\text{g}}}{\partial x_1} \right| > \left| \frac{\partial \xi_1 \Big|_{10\text{g}}}{\partial x_1} \right| \tag{6.8}$$

As the samples have different initial water contents, the reaction rates at each section $x_1 = 0$ will always obey the following relationship.

$$\left| \frac{\partial \xi_1 \Big|_{15\text{g}}}{\partial t} \right|_{x_1 = 0} > \left| \frac{\partial \xi_1 \Big|_{10\text{g}}}{\partial t} \right|_{x_1 = 0} \tag{6.9}$$

In the second chemical reaction:

$$2\text{C}_2\text{S} + 4\text{H}_2\text{O} \rightarrow 3\text{CaO} \cdot 2\text{SiO}_2 \cdot 3\text{H}_2\text{O} + \text{Ca(OH)}_2 \tag{6.10}$$

The reaction rate (ξ_2) is determined by the mass concentration of C_2S (ρ_1) and H_2O (ρ_2) and $\xi_2 = k_2 \rho_5^{\lambda_5^2} \rho_2^{\lambda_2^2}$. At $t = 0hr$, ξ_2 is evenly distributed. At $t > 0hr$, because the influence of CO_2, the mass concentration of C_3S and H_2O gradually reduced from the uniformly distribution form. Figure 6.9 – Figure 6.10 show Sample 1 and Sample 2 reaction rates distributed along space and time. Figure 6.11 shows the reaction rates compared at $t = 48hr$. Figure 6.12 shows the reaction rates at section $x_1 = 0$ when compared over 48 hours. Also shown in Figure 6.12 are the linear fit curves.

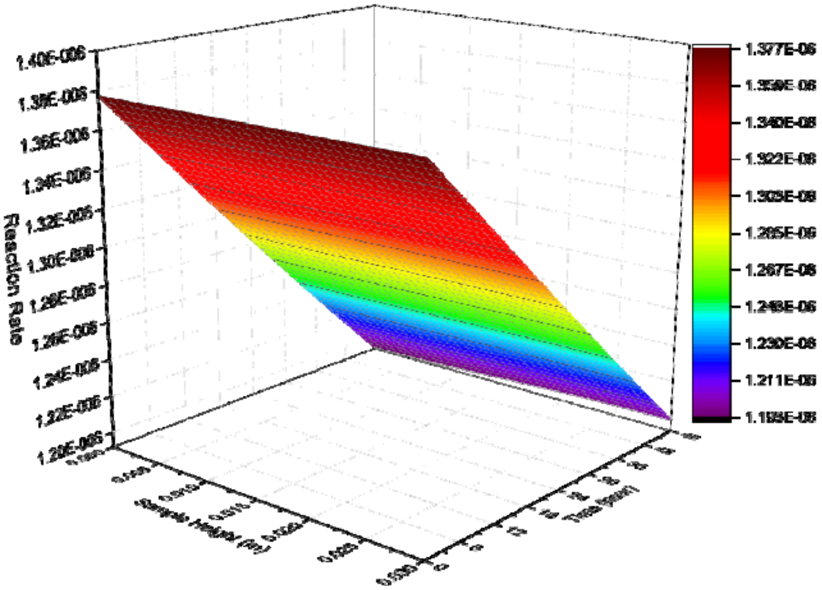

Figure 6.9: Sample 1 reaction rate (ξ_2) time-space distribution

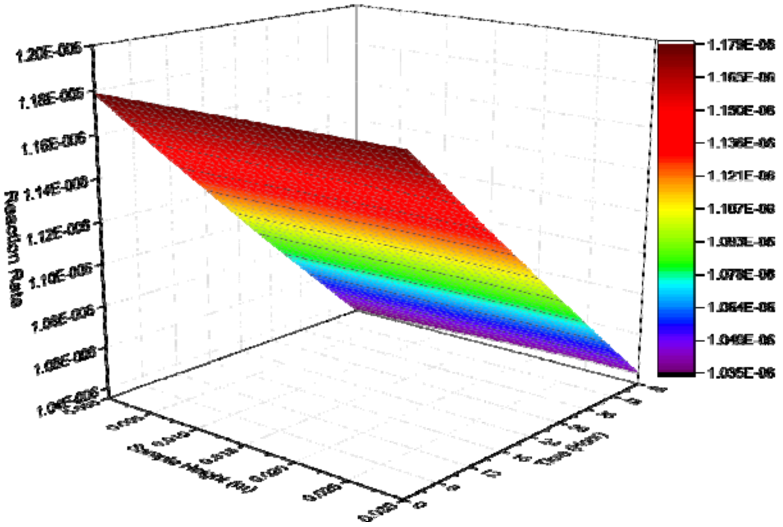

Figure 6.10: Sample 2 reaction rates (ξ_2) time-space distribution

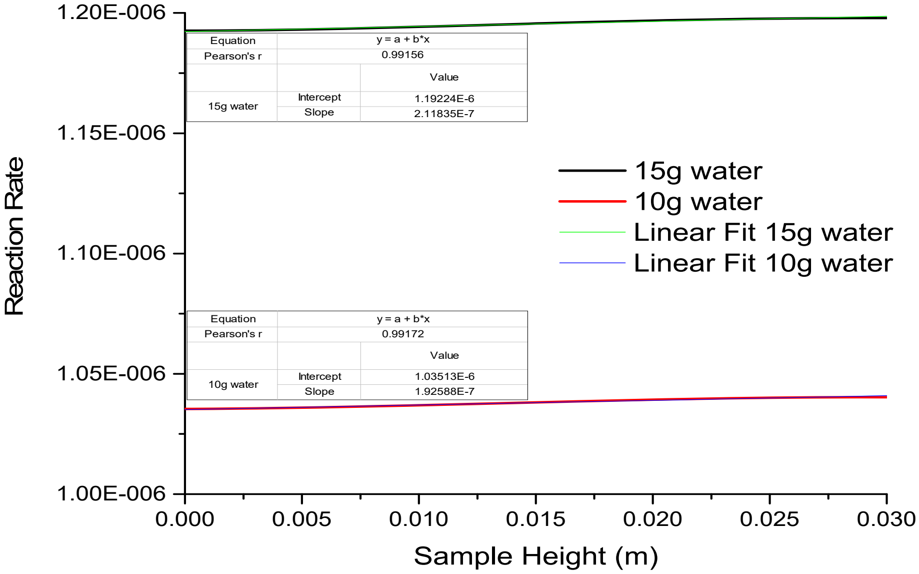

Equation	y = a + b*x	
Pearson's r	0.99156	
		Value
15g water	Intercept	1.19224E-6
	Slope	2.11835E-7

Equation	y = a + b*x	
Pearson's r	0.99172	
		Value
10g water	Intercept	1.03513E-6
	Slope	1.92588E-7

Figure 6.11: Reaction rates ($\xi_2 \Big|_{15\text{g}}^{10\text{g}}$) comparison over $t = 48hr$

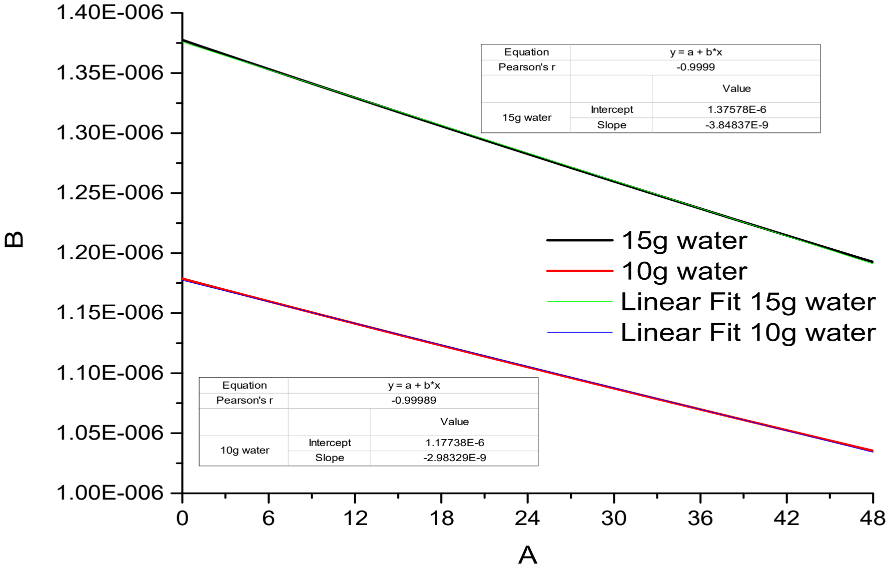

Figure 6.12: Reaction rates ($\xi_2 \Big|_{15\text{g}}^{10\text{g}}$) comparison on section $x_1 = 0$

From Figure 6.9 – Figure 6.12, we can clearly see that the reaction rate $\xi_2 \Big|_{15\text{g}}$ always larger than $\xi_2 \Big|_{10\text{g}}$ and the gradient of $\xi_2 \sim x_1$ curve is increasing with time, so (same question as before):

$$\left| \frac{\partial \xi_2 \big|_{15\text{g}}}{\partial x_1} \right| > \left| \frac{\partial \xi_2 \big|_{10\text{g}}}{\partial x_1} \right| \tag{6.11}$$

As the samples keep different water contents, the reaction rates at each section $x_1 = 0$ will obey the following relationship,

$$\left| \frac{\partial \xi_2 \big|_{15g}}{\partial t} \right|_{x_1 = 0} > \left| \frac{\partial \xi_2 \big|_{10g}}{\partial t} \right|_{x_1 = 0} \tag{6.12}$$

In the third chemical reaction equation:

$$\text{CaO+H}_2\text{O} \rightarrow \text{Ca(OH)}_2 \tag{6.13}$$

CaO and H_2O are the reactants. The reaction rate ξ_3 is determined by the mass concentrations of CaO (ρ_6) and of H_2O (ρ_2). Figure 6.13 – Figure 6.14 show the reaction rate distributions along as a function of time and space. Figure 6.15 shows the reaction rates over 48 hours. Figure 6.16 shows the reaction rate at section $x_1 = 0$.

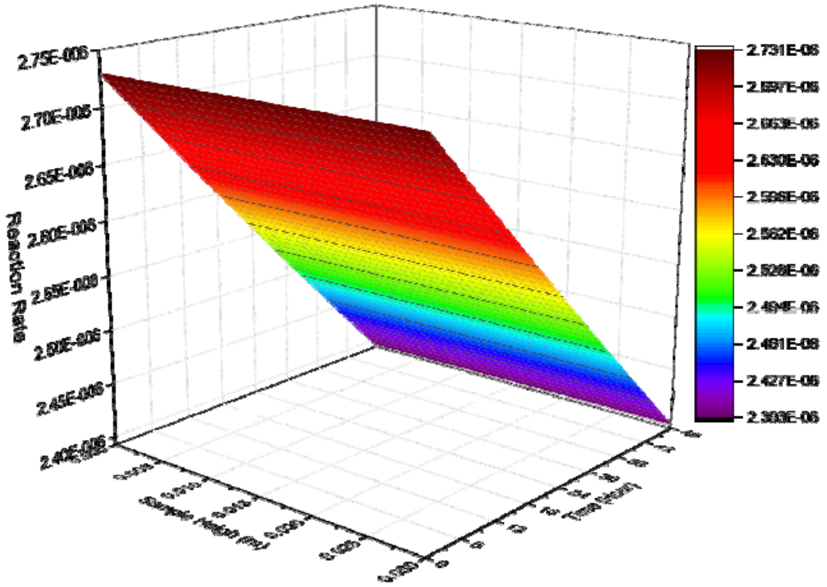

Figure 6.13: Sample 1 reaction rates (ξ_3) time-space distribution

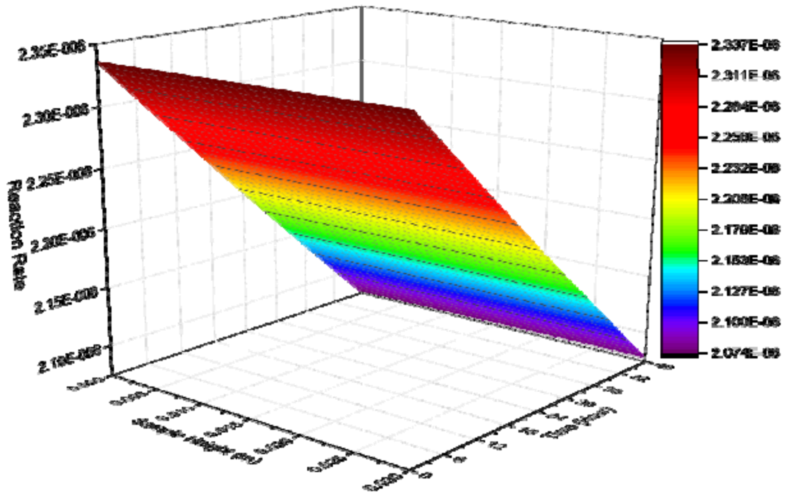

Figure 6.14: Sample 2 reaction rates (ξ_3) time-space distribution

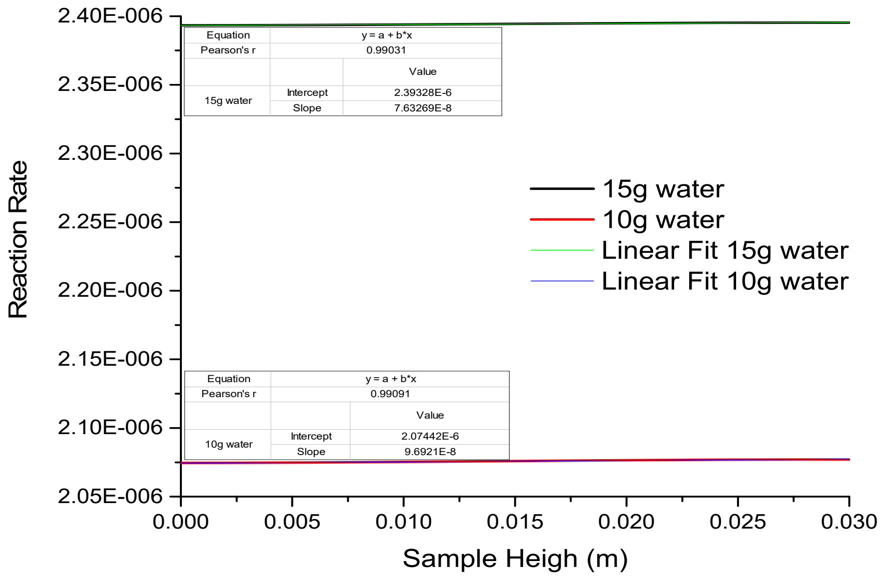

Figure 6.15: Reaction rates ($\xi_3 \Big|_{15g}^{10g}$) comparison over $t = 48(\text{hour})$

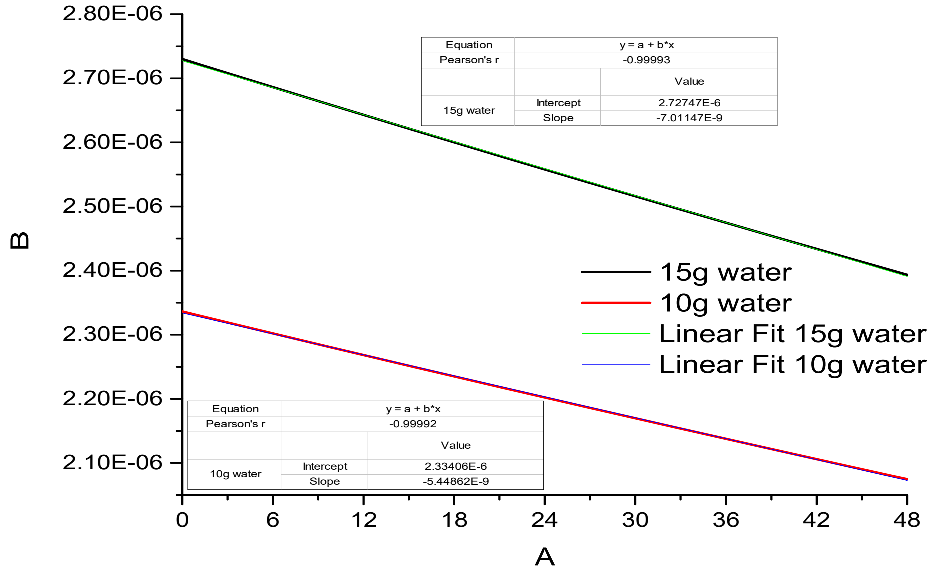

Figure 6.16: Reaction rates ($\xi_3 \Big|_{15g}^{10g}$) comparison on section $x_1 = 0$

From Figure 6.13 – Figure 6.14, we can clearly see that the reaction rate $\xi_3\big|_{15\mathrm{g}}$ is always larger than $\xi_3\big|_{10\mathrm{g}}$:

$$\left|\frac{\partial \xi_3\big|_{15\mathrm{g}}}{\partial x_1}\right| > \left|\frac{\partial \xi_3\big|_{10\mathrm{g}}}{\partial x_1}\right| \tag{6.14}$$

As the samples have different water contents, the reaction rates at each section $x_1 = 0$ will obey:

$$\left|\frac{\partial \xi_3\big|_{15g}}{\partial t}\right|_{x_1=0} > \left|\frac{\partial \xi_3\big|_{10g}}{\partial t}\right|_{x_1=0} \tag{6.15}$$

Figure 6.15-6.17 describe the reaction rates for 48 hours and at section $x_1 = 0$, respectively. In the chemical reaction,

$$\mathrm{Ca(OH)_2{+}CO_2 \rightarrow CaCO_3{+}H_2O} \tag{6.16}$$

H_2O represents a resultant. The chemical reaction rate (ξ_4) does not have direct connection with initial H_2O mass concentration (ρ_2) and is determined by $\mathrm{Ca(OH)_2}$ mass concentration (ρ_4) and CO_2 mass concentration (ρ_7), and $\xi_4 = k_4 \rho_4^{\lambda_4^4} \rho_7^{\lambda_7^4}$. ρ_2 is affected by the combined action of $\mathrm{3CaO \cdot 2SiO_2 \cdot 3H_2O}$ mass concentration (ρ_3) and $\mathrm{Ca(OH)_2}$ mass concentration (ρ_4), which has the indirect impact on the chemical reaction rate (ξ_4).

$\mathrm{Ca(OH)_2}$ is not only present as the reactant in the chemical reaction equation (4.10), but also present as the resultant in the first three chemical reactions. So its mass concentration equation can be derived as:

$$\frac{\partial \rho_4}{\partial t} = 3\mu_4\xi_1 + \mu_4\xi_2 + \mu_4\xi_3 - \mu_4\xi_4 \tag{6.17}$$

As $\mathrm{Ca(OH)_2}$ is the resultant in the first three chemical reaction, its mass concentration (ρ_4) is equal to zero initially. However, CO_2 mass concentration is not zero at the beginning, so $\lambda_4^4 = 1$, $\lambda_4^7 = 0$. The initial reaction rate (ξ_4) can be describe as $\xi_4\big|_{t=0} = 0$. When $t > 0$, the reaction rate (ξ_4) is decreasing along the x_1 direction. Figure 6.17 and Figure 6.18 show the Sample 1 and Sample 2 reaction rate (ξ_4) distributions along time and space. Figure 6.19 shows the reaction rate.

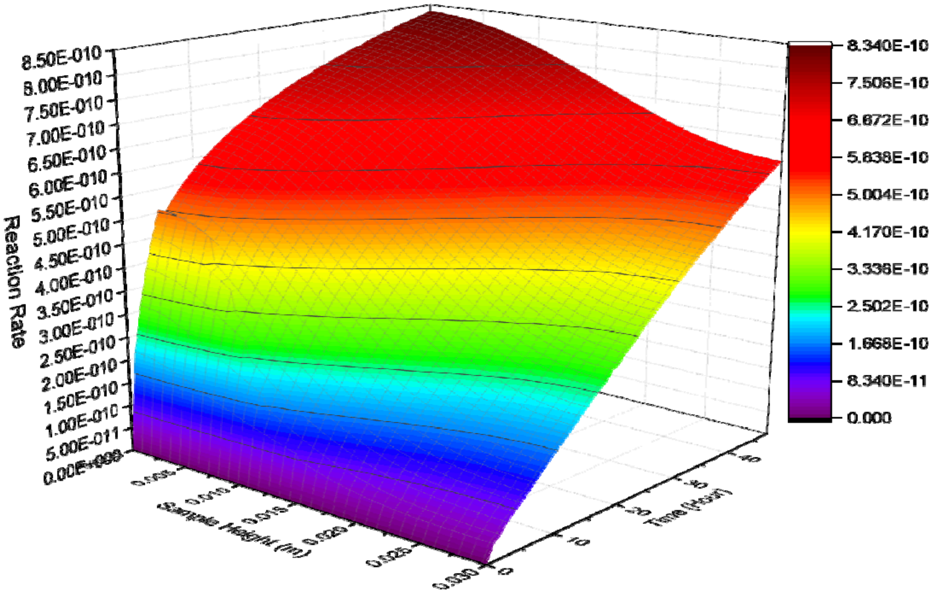

Figure 6.17: Sample 1 reaction rate (ξ_4) with time and space

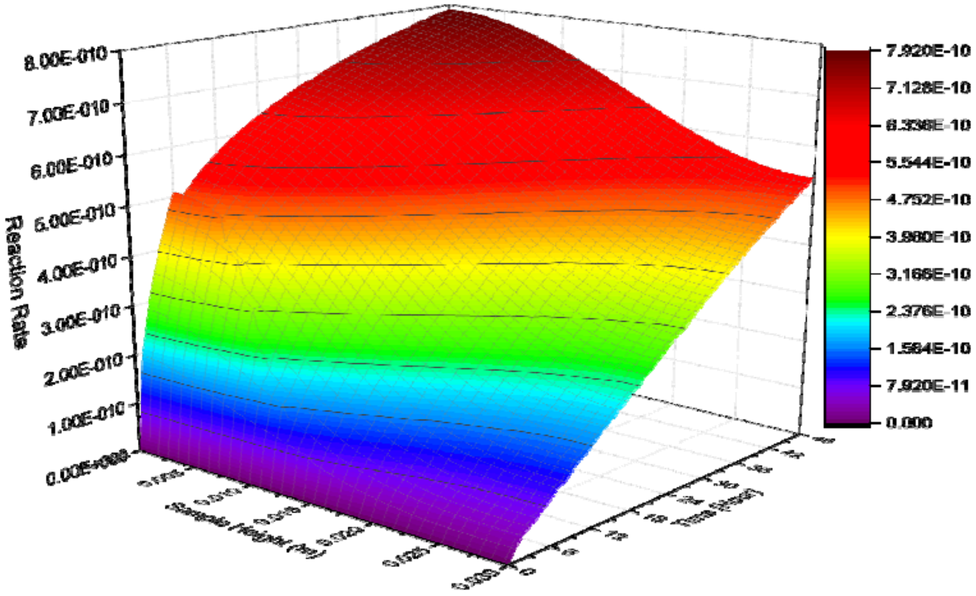

Figure 6.18: Sample 2 reaction rate (ξ_4) with time and space

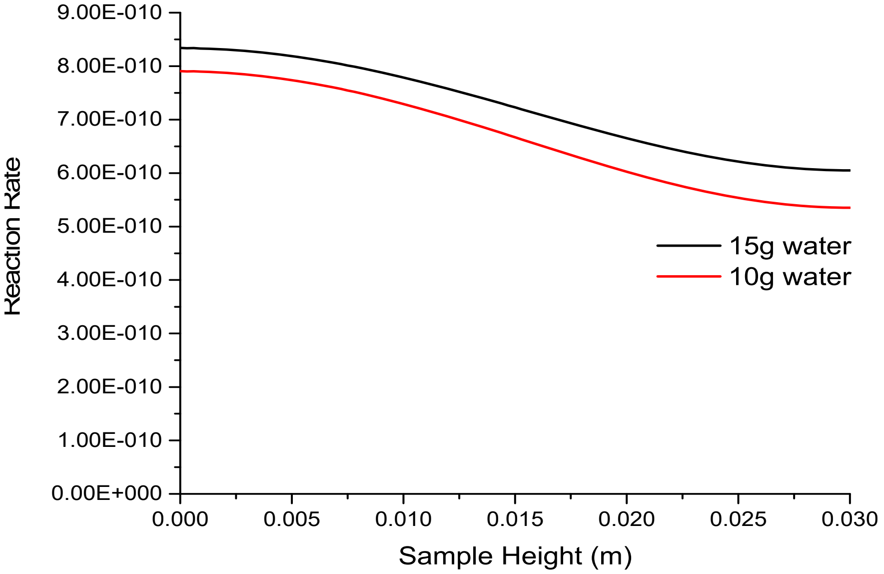

Figure 6.19: Reaction rate ($\xi_4 \Big|_{15\text{g}}^{10\text{g}}$) comparison at $t = 48hr$

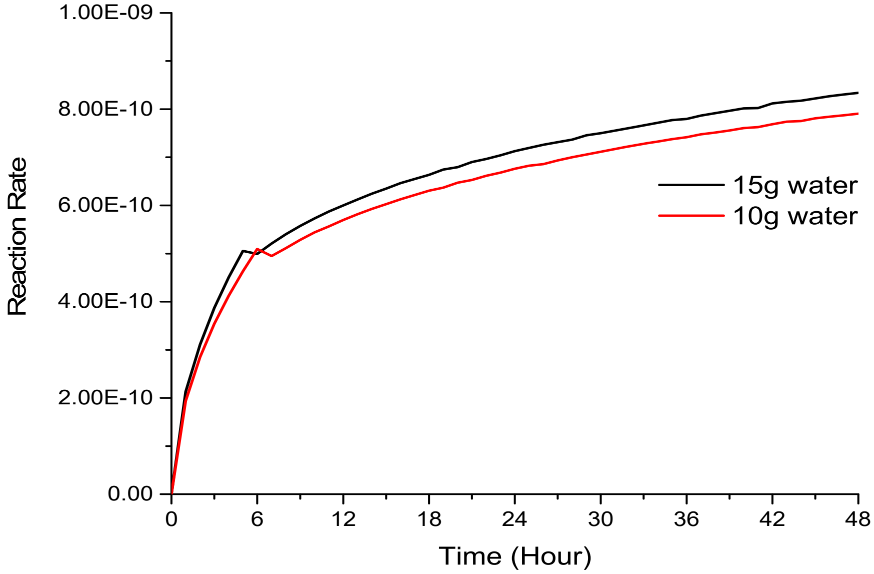

Figure 6.20: Reaction rate ($\xi_4 \big|_{15\text{g}}^{10\text{g}}$) comparison on section $x_1 = 0$

From Figure 6.17 – Figure 6.20, we can clearly see that the reaction rate $\xi_4 \big|_{15\text{g}}$ is larger than $\xi_4 \big|_{10\text{g}}$ and

$$\left| \frac{\partial \xi_4 \big|_{15\text{g}}}{\partial x_1} \right| > \left| \frac{\partial \xi_4 \big|_{10\text{g}}}{\partial x_1} \right| \tag{6.18}$$

Note also that the curves of reaction rates have a jump in Figure 6.20 - this implies that the reaction orders λ_4^4 and λ_4^7 are transforming during the process. However, what kind of transformation is taking place is not known.

The fifth chemical reaction equation is

$$3\text{CaO} \cdot 2\text{SiO}_2 \cdot \text{H}_2\text{O} + 3\text{CO}_2 \rightarrow 3\text{CaCO}_3 \cdot 2\text{SiO}_2 \cdot 3\text{H}_2\text{O} \tag{6.19}$$

From equation (6.19), it is noted that free H_2O does not exist in both sides of the equation. Hence, the reaction rate (ξ_5) has no direct connection with H_2O mass concentration (ρ_2), and is determined by $3CaO \cdot 2SiO_2 \cdot 3H_2O$ mass concentration (ρ_3) and CO_2 mass concentration (ρ_7), $\xi_5 = k_5 \rho_3^{\lambda_3^5} \rho_7^{\lambda_7^5}$. H_2O mass concentration (ρ_2) is affected by the combined action of $3CaO \cdot 2SiO_2 \cdot 3H_2O$ mass concentration (ρ_3) and CO_2 mass concentration (ρ_7), which has indirect impact on the chemical reaction rate (ξ_5). Therefore, the water content has very limited effect on the reaction rate (ξ_5).

Figure 6.21 and Figure 6.22 show Sample 1 and Sample 2 reaction rates distributed along time and space. It is very clear that the Sample 1 reaction rate ($\xi_5 \big|_{15g}$) is little more than the Sample 2 reaction rate ($\xi_5 \big|_{10g}$). Also from Figure 6.23 and Figure 6.24 we could see that the curves of reaction rates have a jump, which means the reaction orders λ_3^5 and λ_7^5 are transforming.

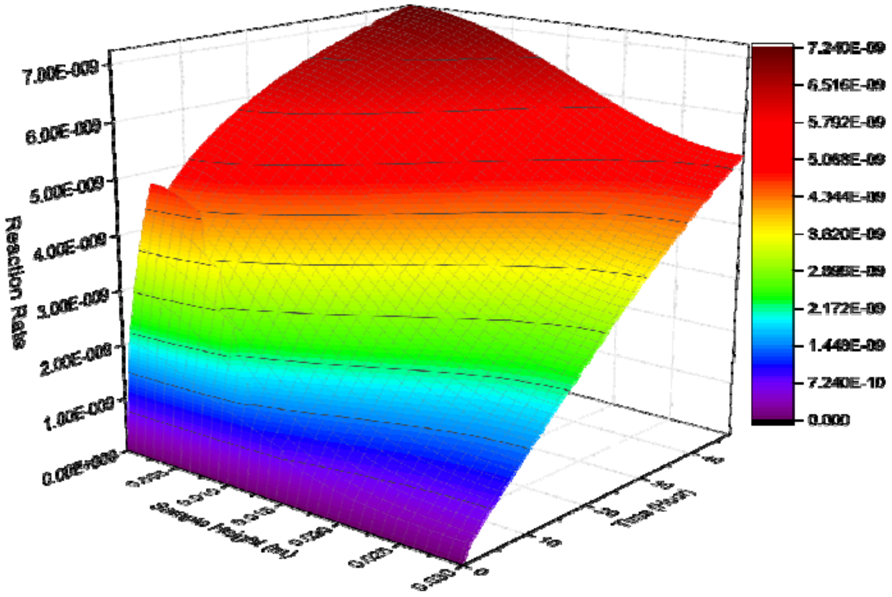

Figure 6.21: Sample 1 reaction rate (ξ_5) time-space distribution

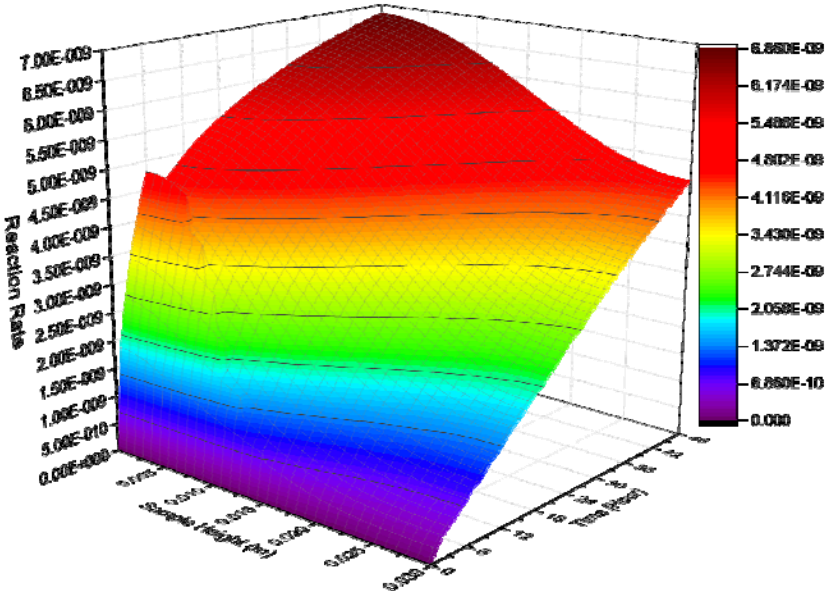

Figure 6.22 Sample 2 reaction rate (ξ_5) time-space distribution

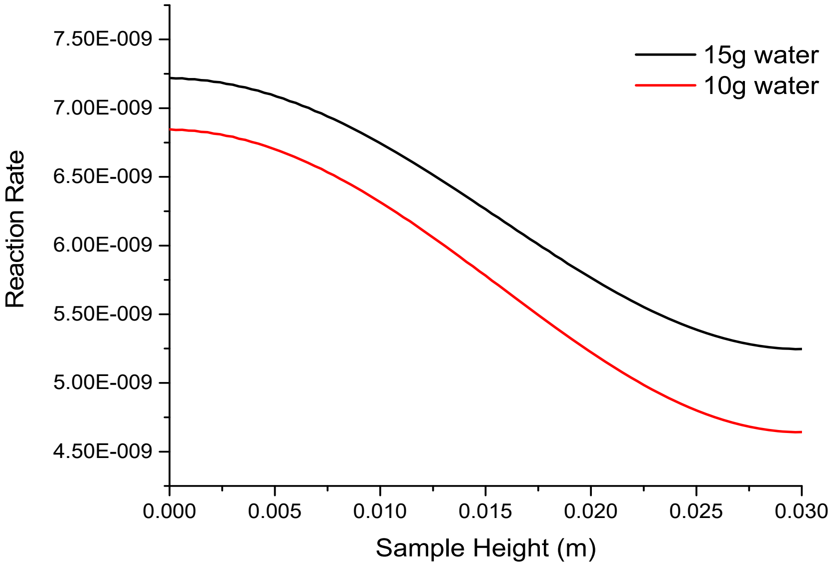

Figure 6.23: Reaction rates ($\xi_5 \Big|_{15g}^{10g}$) comparison at $t = 48hr$

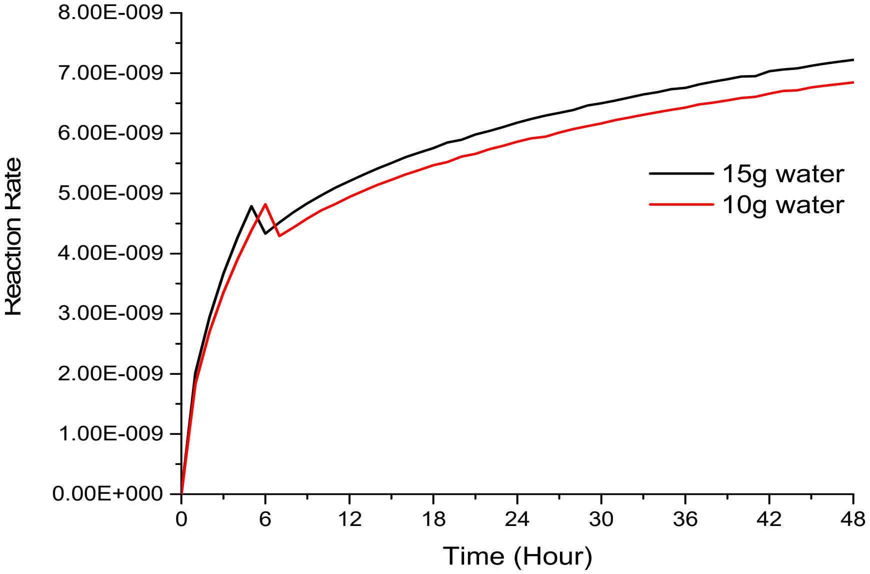

Figure 6.24: Reaction rates ($\xi_5 \Big|_{15g}^{10g}$) comparison on section $x_1 = 0$

The sixth chemical equation can be expressed as

$$C_3S+3CO_2+\gamma H_2O \rightarrow SiO_2 \cdot \gamma H_2O+3CaCO_3 \tag{6.20}$$

In above equation, the chemical reaction rate (ξ_6) is determined by the concentrations of C_3S (ρ_1), H_2O (ρ_2), CO_2 (ρ_7), and $\xi_6 = k_6 \rho_1^{\lambda_1^6} \rho_7^{\lambda_7^6} \rho_2^{\lambda_2^6}$. Because the CO_2 mass concentration is not evenly distributed initially, the reaction rate (ξ_6) is strictly decreasing along x_1 direction and then goes to flat as time increases.

Figure 6.25 and Figure 6.26 show the Sample 1 and Sample 2 reaction rates distributed along time and space. Figure 6.27 - 6.30 show Sample 1 reaction rate ($\xi_6 \big|_{15g}$) is larger than Sample 2 reaction rate ($\xi_6 \big|_{10g}$).

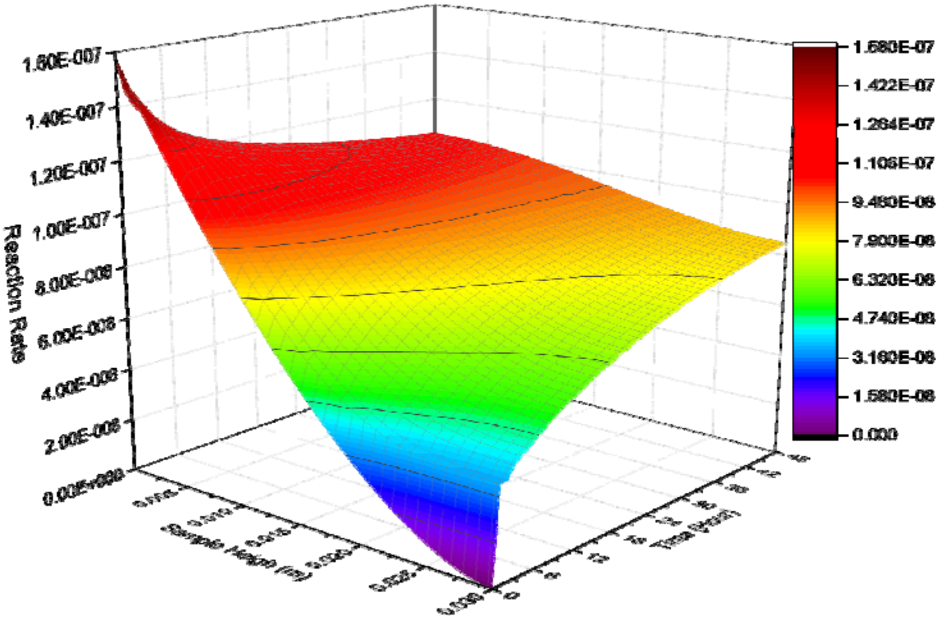

Figure 6.25: Sample 1 reaction rate (ξ_6) time-space distribution

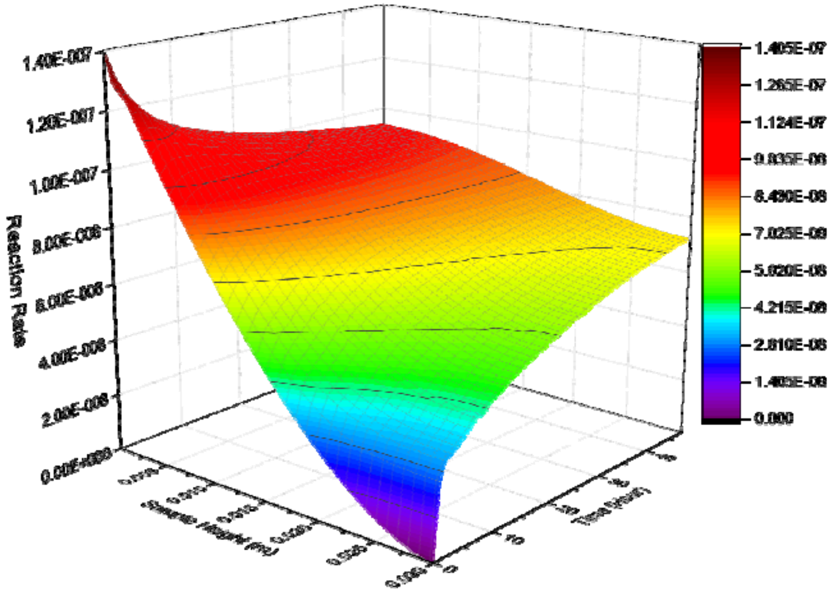

Figure 6.26: Sample 2 reaction rate (ξ_6) time-space distribution

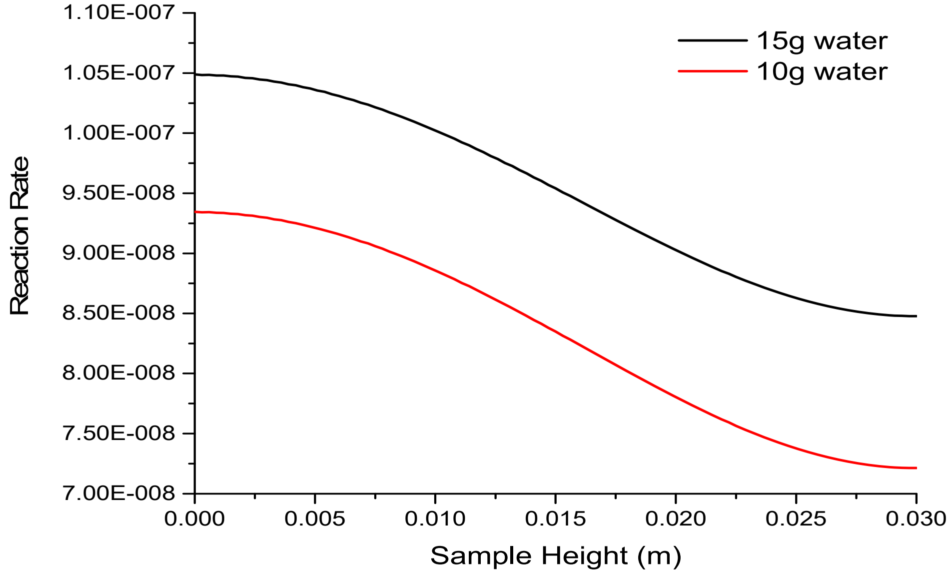

Figure 6.27: Reaction rates ($\xi_6 \Big|_{15\text{g}}^{10\text{g}}$) comparison at $t = 48hr$

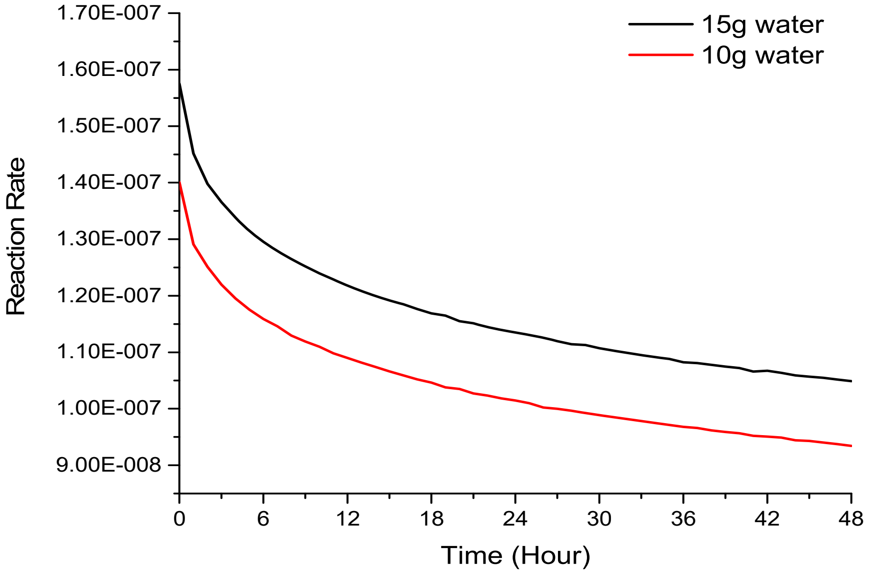

Figure 6.28: Reaction rates ($\xi_6 \Big|_{15\text{g}}^{10\text{g}}$) comparison on section $x_1 = 0$

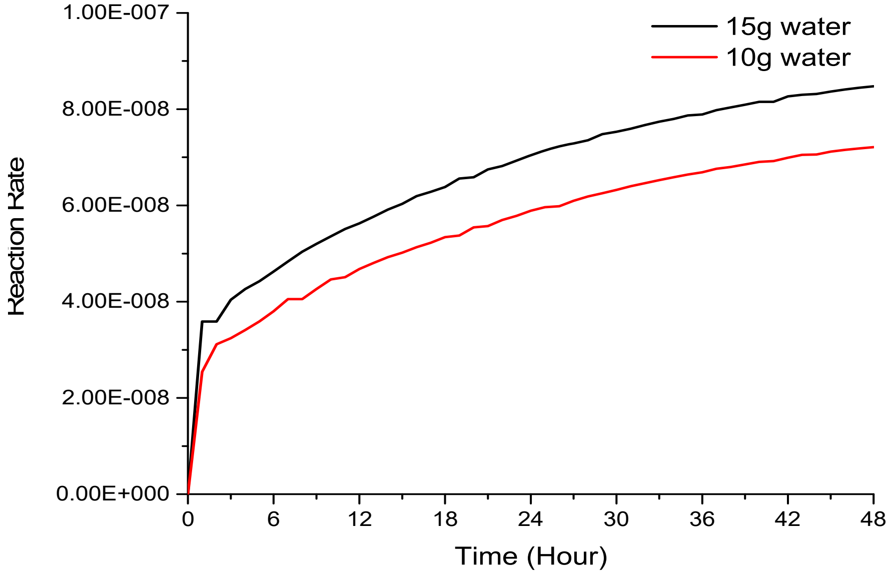

Figure 6.29: Reaction rates ($\xi_6 \big|_{15\text{g}}^{10\text{g}}$) comparison on section $x_1 = h_s$

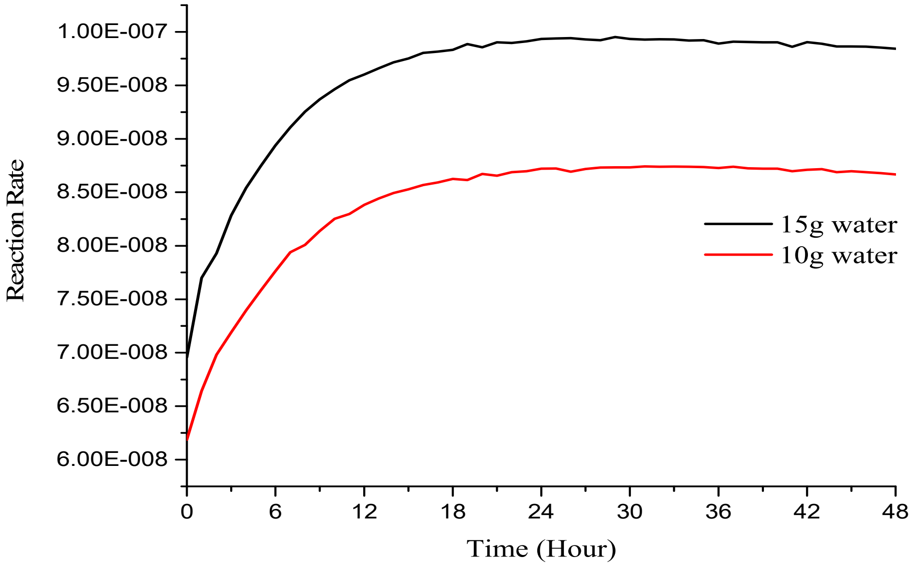

Figure 6.30: Reaction rates ($\xi_6 \big|_{15\text{g}}^{10\text{g}}$) comparison on section $x_1 = 0.4h_s$

From Figure 6.31, the reaction rate (ξ_6) is shown to monotonically decrease with time at section $x_1 \leq \frac{13}{100}h_s$. The same pattern is observed at section $x_1 \geq \frac{50}{100}h_s$. The reaction rate decreased at first and then rose at section $\frac{14}{100}h_s \le x_1 \le \frac{49}{100}h_s$. The "zigzag" pattern of both curves is very obvious for both samples. This "changing characteristics" may be due to competing sorption throughout the hydration process. This further illustrates the play of water in the sorption process.

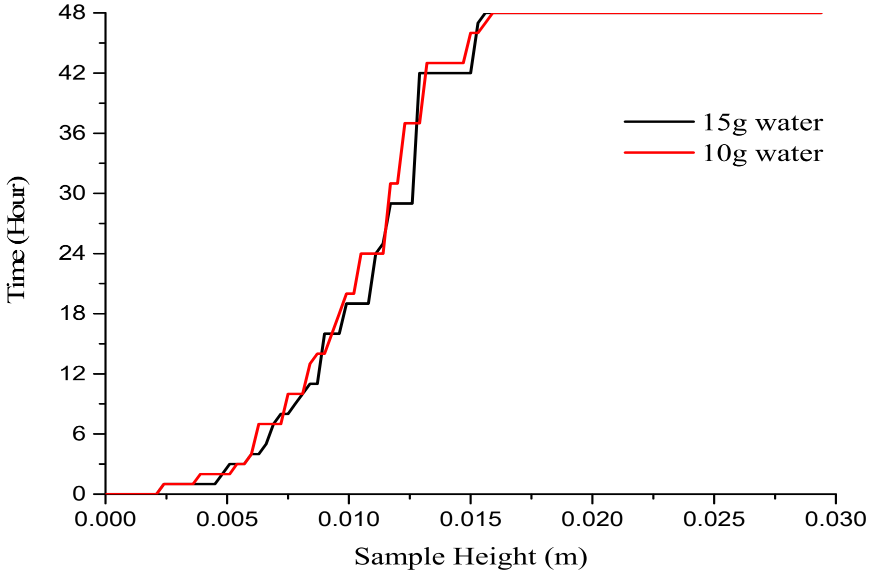

Figure 6.31: Reaction rate ($\xi_6 \Big|_{15g}^{10g}$) changing characteristics along with time and space

The seventh chemical reaction is described as:

$$C_2S+2CO_2+\gamma H_2O \rightarrow SiO_2 \cdot \gamma H_2O+2CaCO_3 \qquad (6.21)$$

The reaction rate (ξ_7) is determined by the mass concentration of C_2S (ρ_5), H_2O (ρ_2) and CO2 (ρ_7), $\xi_7 = k_7 \rho_5^{\lambda_5^7} \rho_7^{\lambda_7^7} \rho_2^{\lambda_2^7}$ .and $\xi_6 = k_6 \rho_1^{\lambda_1^6} \rho_7^{\lambda_7^6} \rho_2^{\lambda_2^6}$. Because of CO2 mass concentration is not evenly distributed initially, the reaction rate (ξ_7) is strictly decreasing along x_1 direction and then became flat.

Figures 6.32, 6.33, 6.34, 6.35, 6.36 and 6.37 show that Sample 1 and Sample 2 reaction rates distribution with time and space. And those figures indicate that Sample 1 reaction rate ($\xi_7 \big|_{15g}$) is large than Sample 2 reaction rate ($\xi_7 \big|_{10g}$).

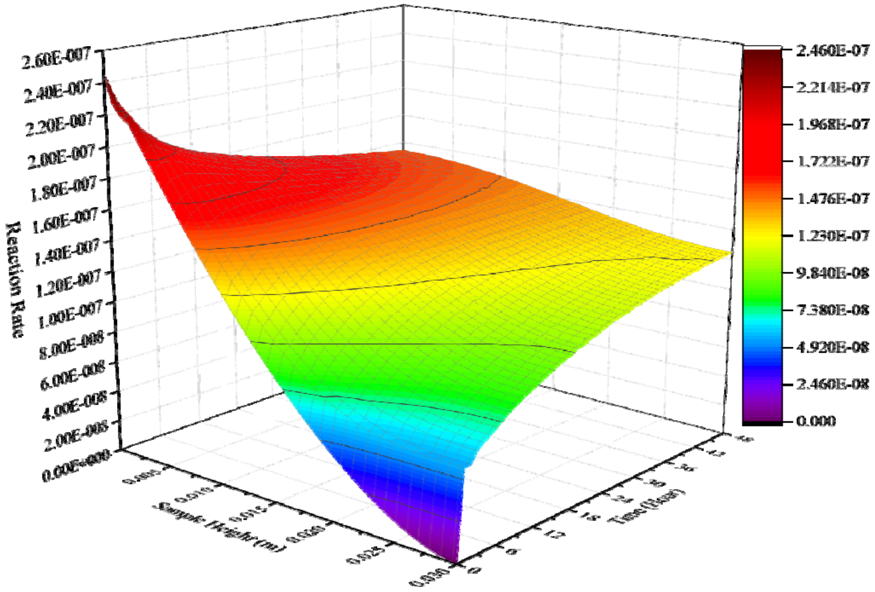

Figure 6.32: Sample 1 reaction rate (ξ_7) time-space distribution

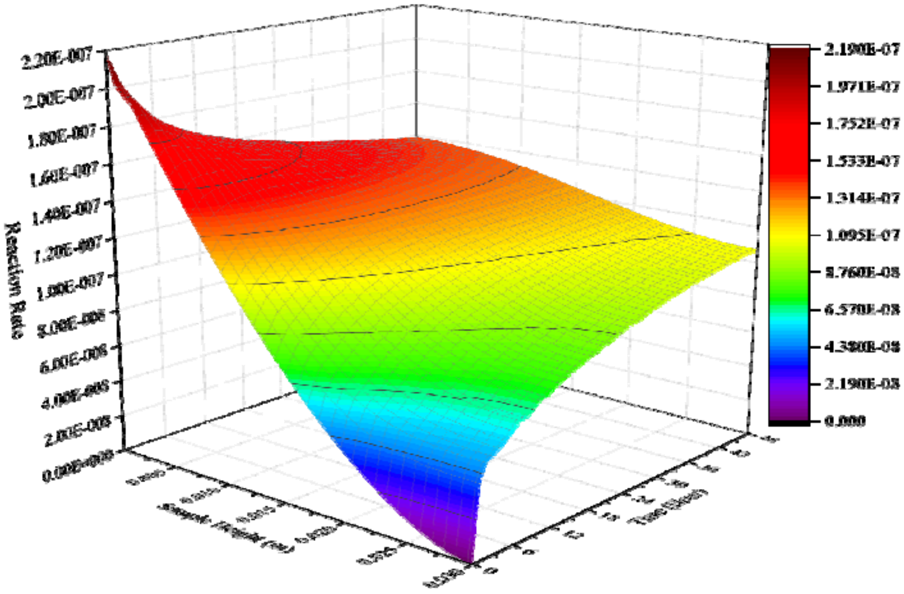

Figure 6.33: Sample 2 reaction rate (ξ_7) time-space distribution

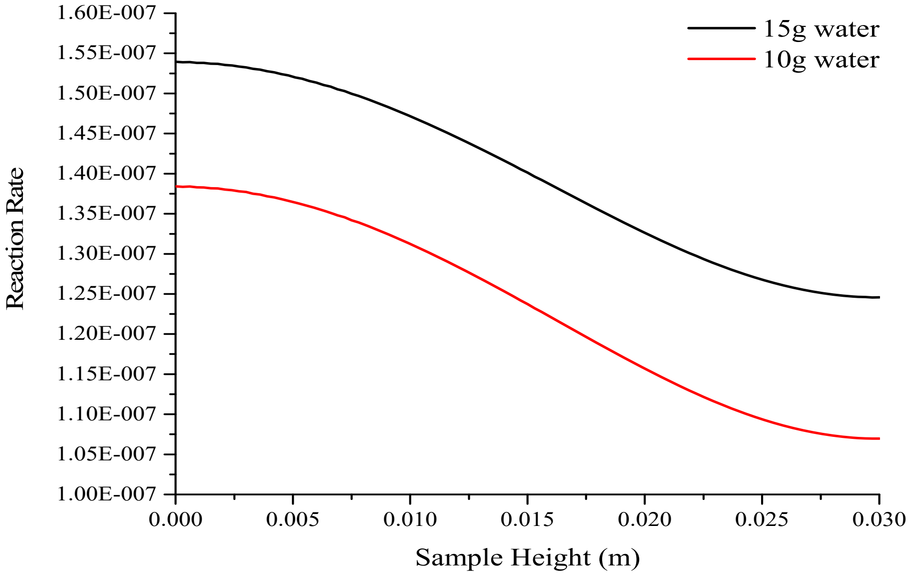

Figure 6.34: Reaction rates ($\xi_7 \Big|_{15\text{g}}^{10\text{g}}$) comparison at $t = 48hr$

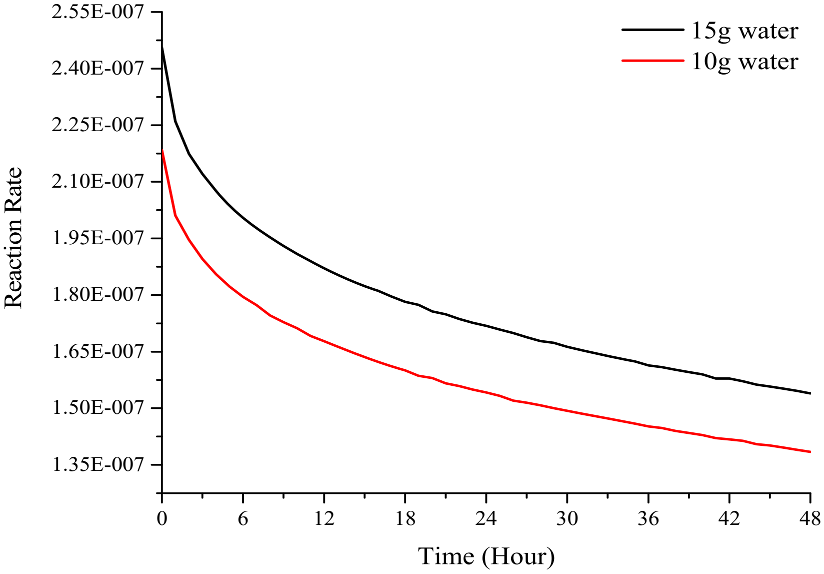

Figure 6.35: Reaction rates ($\xi_7 \Big|_{15\text{g}}^{10\text{g}}$) comparison on section $x_1 = 0$

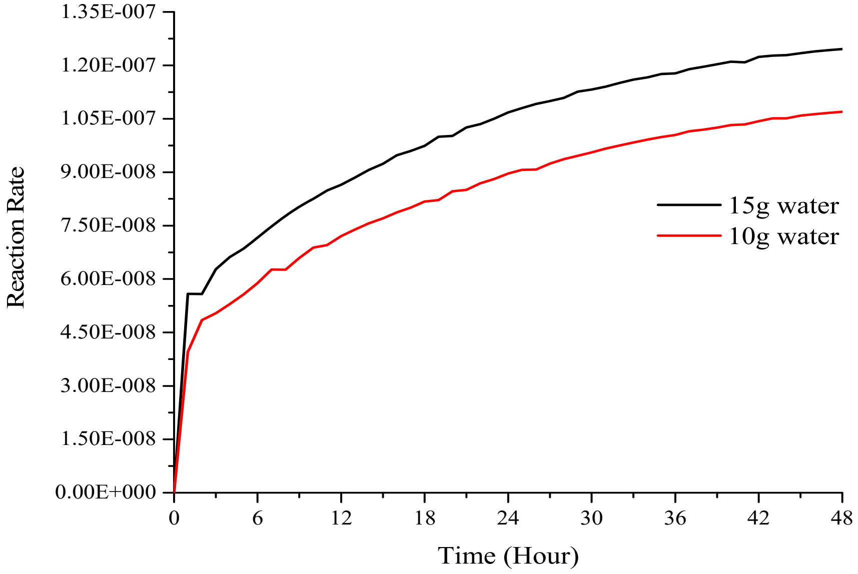

Figure 6.36: Reaction rates ($\xi_7 \Big|_{15g}^{10g}$) comparison at section $x_1 = h_s$

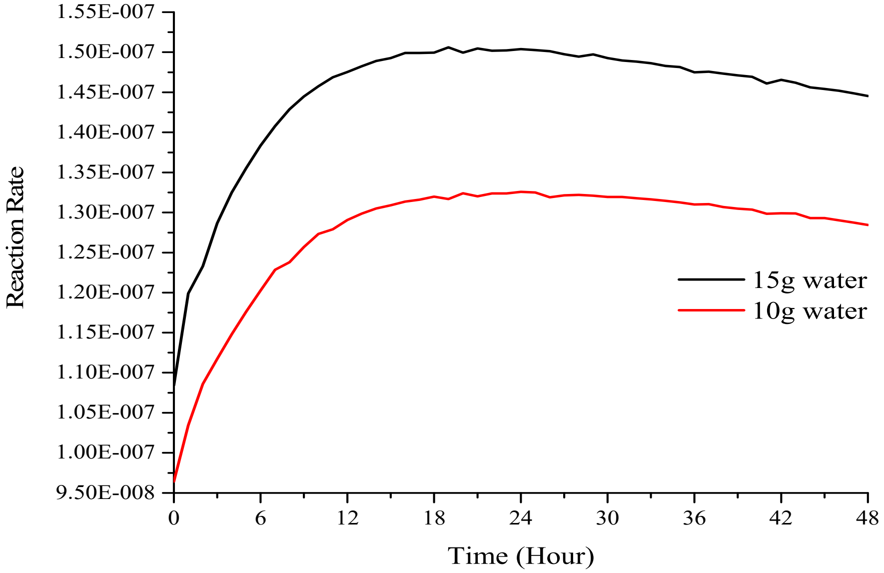

Figure 6.37: Reaction rates ($\xi_7 \Big|_{15g}^{10g}$) comparison at section $x_1 = 0.4h_s$

From Figure 6.38, we observed that the reaction rate (ξ_7) decreases monotonically with time at section $x_1 \leq \frac{13}{100} h_s$. The same pattern is shown at section

$x_1 \geq \frac{50}{100} h_s$. And the reaction rate decreases at first and then rise at section $\frac{14}{100} h_s \leq x_1 \leq \frac{49}{100} h_s$. The "zigzag" of reaction rate curve is identical for both samples.

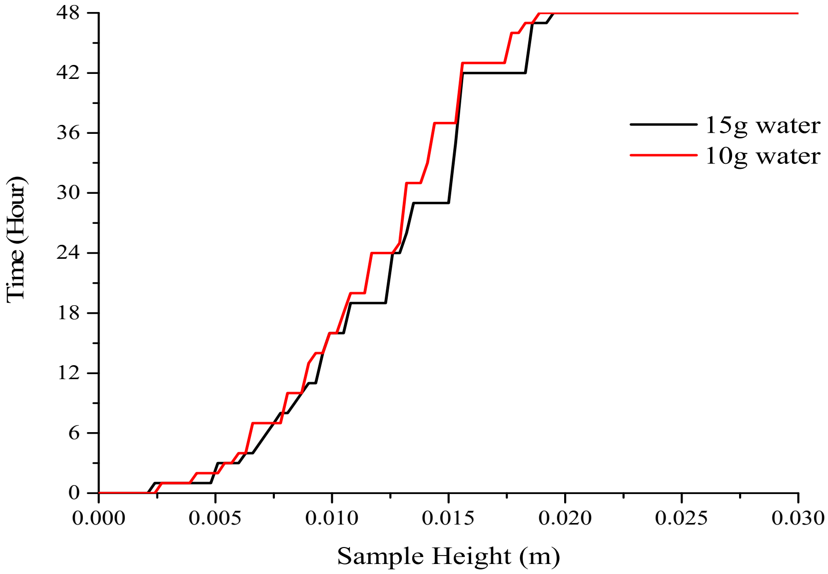

Figure 6.38: Reaction rate ($\xi_7 \Big|_{15g}^{10g}$) changing characteristics with time and space

6.2.6 Mass Concentration Comparisons

Mass concentration $\rho_i \ (i = 1, 2, \cdots, 7)$ is the key parameter to learn about the hydration effect. The first material C_3S, is a reactant from chemical equations (6.7) and (6.20). The mass concentration (ρ_1) decreases with time and $\frac{\partial \rho_1}{\partial t} = -2\mu_1 \xi_1 - \mu_1 \xi_6$. From the previous section we know that the reaction rates in Sample 1 ($\xi_1 \Big|_{15g}$ and $\xi_6 \Big|_{15g}$) are always large than the reaction rates in Sample 2 ($\xi_1 \Big|_{10g}$ and $\xi_6 \Big|_{10g}$) . Therefore, the mass concentration gradient $\left(\frac{\partial \rho_1}{\partial t}\right)$ reduced faster in Sample 1 than Sample 2, $\left|\frac{\partial \rho_1}{\partial t}\right|_{15\mathrm{g}} > \left|\frac{\partial \rho_1}{\partial t}\right|_{10\mathrm{g}}$. Figure 6.39 and Figure 6.40 show the mass concentration (ρ_1) distribution along time and space.

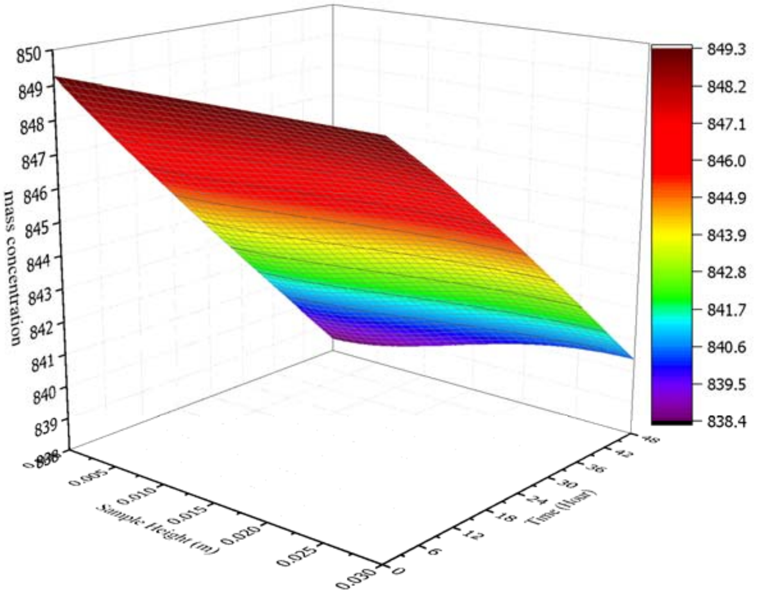

Figure 6.39 C_3S mass concentration (ρ_1) time-space distribution

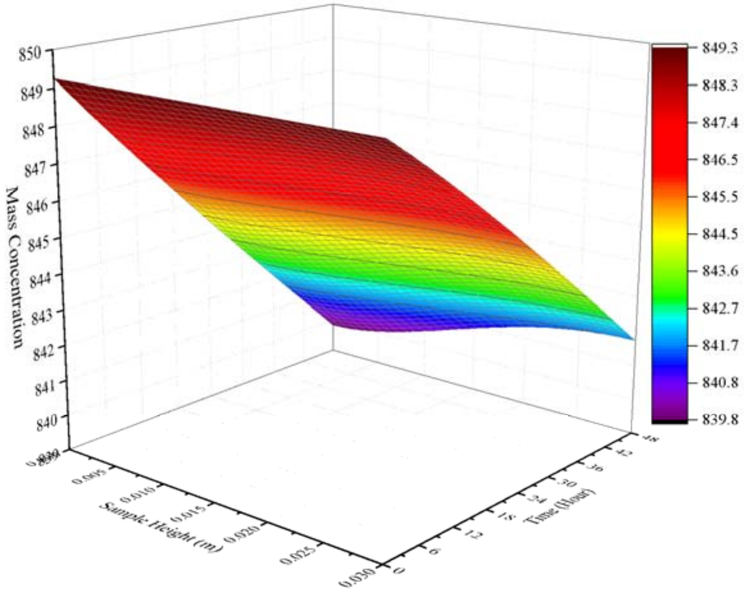

Figure 6.40: C_3S mass concentration (ρ_1) time-space distribution

The following can be concluded from Figure 6.41 and Figure 6.42:

Initially, C_3S mass concentration (ρ_1^0) is uniformly distributed. Sample 1 (15g water) and Sample 2 (10g water) have the same concentration.

(1) With the increase in time, the distribution of ρ_1^0 gradually becomes less uniform. At $t = 48hr$, $\rho_1 \big|_{15\text{g}}$ is less than $\rho_1 \big|_{10\text{g}}$, and $\rho_1 \big|_{15\text{g}} < \rho_1 \big|_{10\text{g}}$.

(2) Sample 1 mass concentration gradient ($\left|\frac{\partial \rho_1}{\partial t}\right|_{15\text{g}}^{x_1=0}$) is larger than Sample 2 mass concentration gradient ($\left|\frac{\partial \rho_1}{\partial t}\right|_{10\text{g}}^{x_1=0}$), hence, $\left|\frac{\partial \rho_1}{\partial t}\right|_{15\text{g}}^{x_1=0} > \left|\frac{\partial \rho_1}{\partial t}\right|_{10\text{g}}^{x_1=0}$. Figure 6.41 and Figure 6.42 show the C_3S mass concentration increased along sample height and decreased with time, respectively.

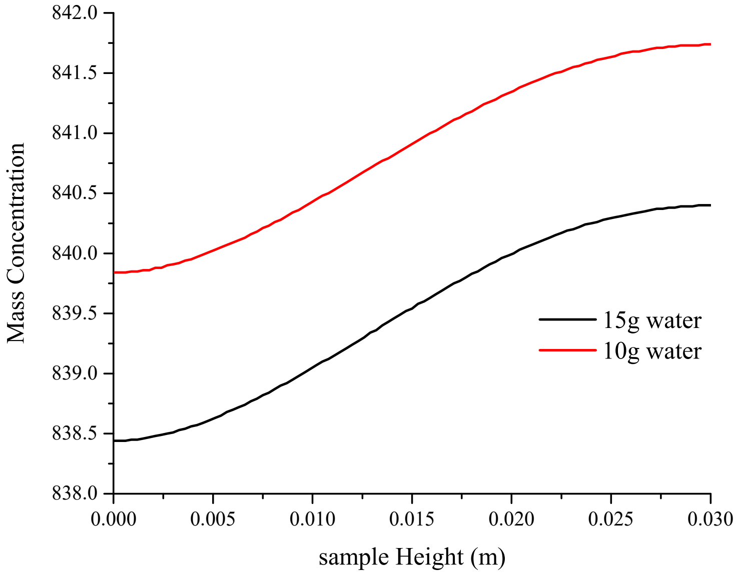

Figure 6.41: C_3S mass concentrations ($\rho_1 \Big|_{10g}^{15g}$) comparison at $t = 48hr$

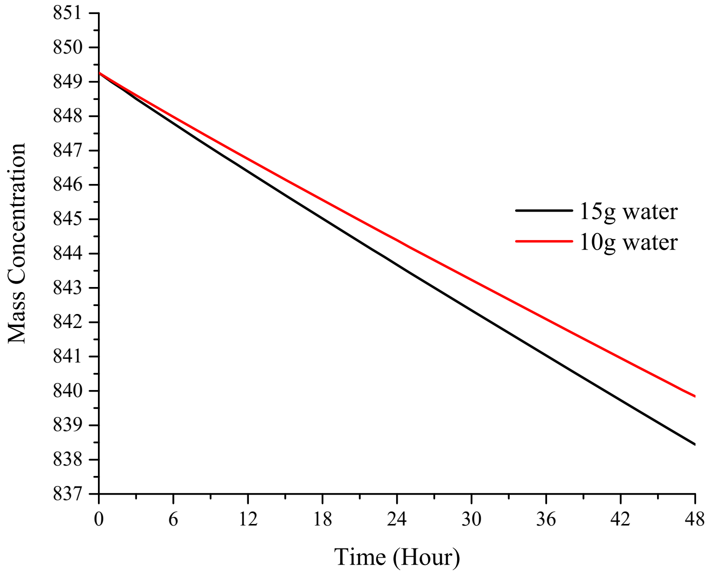

Figure 6.42: C_3S mass concentrations ($\rho_1 \Big|_{10g}^{15g}$) comparison at section $x_1 = 0$

H_2O represents the reactants in chemical equations (6.7), (6.10), (6.13), (6.20) and (6.21). And water also represents the resultant in chemical reaction equation (6.16). Its mass concentration gradient can be expressed as:

$$\frac{\partial \rho_2}{\partial t} = -6\mu_2\xi_1 - 4\mu_2\xi_2 - \mu_2\xi_3 - \gamma\mu_2\xi_6 - \gamma\mu_2\xi_7 + \mu_2\xi_4 \qquad (6.22)$$

Figure 6.43 and Figure 6.44 show the distribution of H_2O mass concentration gradients over time. Figure 6.45 shows the comparison of mass concentrations ($\rho_2 \Big|_{10g}^{15g}$) at $t = 48hr$. Figure 6.46 shows the comparison of mass concentrations ($\rho_2 \Big|_{10g}^{15g}$) at section $x_1 = 0$ over 48 hours. Curve fits are also presented in each figure.

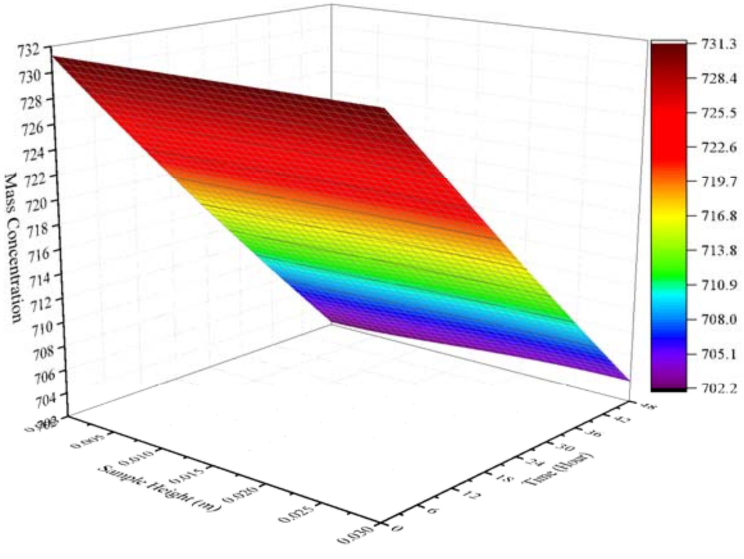

Figure 6.43 H_2O mass concentration ($\rho_2 \Big|_{15g}$) time-space distribution

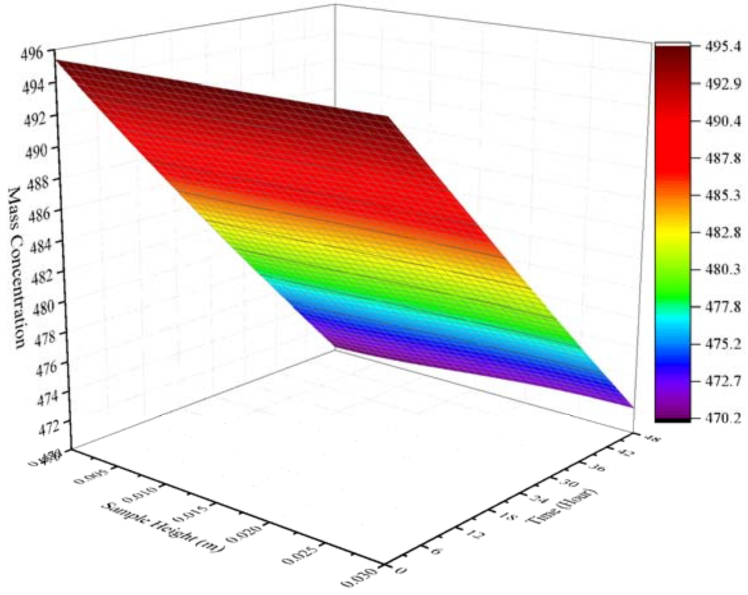

Figure 6.44: H_2O mass concentration ($\rho_2\big|_{10g}$) time-space distribution

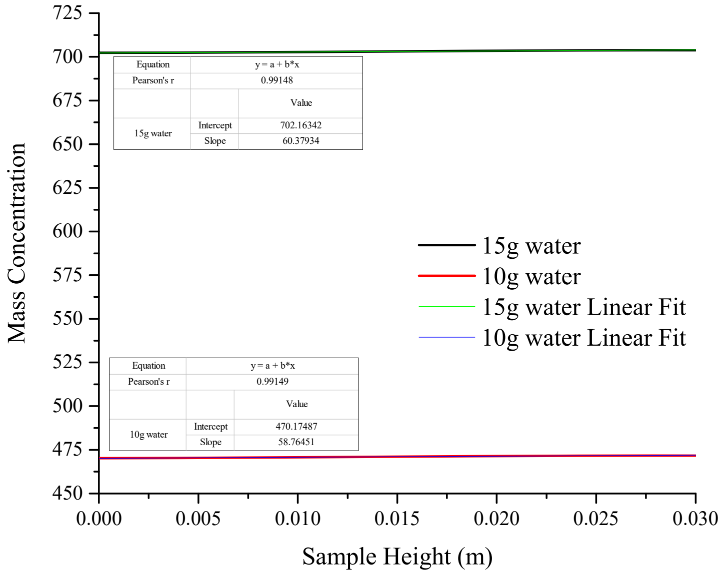

Figure 6.45: H_2O mass concentrations ($\rho_2\Big|_{10g}^{15g}$) comparison of at $t = 48hr$

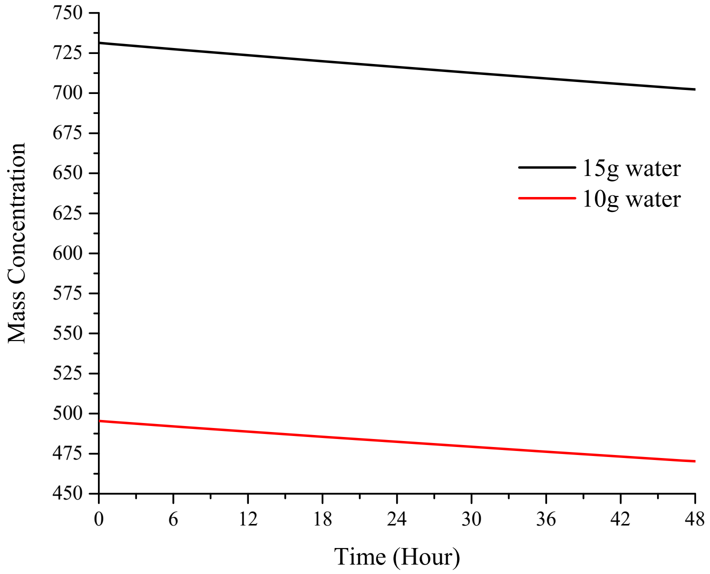

Figure 6.46: H_2O mass concentrations ($\rho_2\big|_{10g}^{15g}$) comparison on section $x_1 = 0$

From Figure 6.45 and Figure 6.46, we noticed that:

(1) Mass concentration $\left(\rho_2\right)$ is monotonically decreased with time of any section of the sample.

(2) Mass concentration $\left(\rho_2\right)$ is approximately linearly distributed along x_1 direction.

(3) Mass concentration $\left(\rho_2\right)$ at the bottom of sample is larger than its top surface value when $t > 0$.

(4) Sample 1 mass concentration $\left(\rho_2\big|_{15g}\right)$ is always larger than Sample 2 mass concentration $\left(\rho_2\big|_{10g}\right)$, $\rho_2\big|_{15g} > \rho_2\big|_{10g}$.

(5) At $t = 48hr$, the mass concentration gradient $\left(\frac{\partial \rho_2}{\partial t} \Big|_{15\text{g}} \right)$ is larger than mass concentration gradient $\left(\frac{\partial \rho_2}{\partial t} \Big|_{10\text{g}} \right)$.

$3CaO \cdot 2SiO_2 \cdot 3H_2O$ represents one of the reactants in chemical reaction (6.7) and (6.10). This material is also present as the resultant in chemical reaction (6.19). Its mass concentration gradient can be written as:

$$\frac{\partial \rho_3}{\partial t} = \mu_3 \xi_1 + \mu_3 \xi_2 - \mu_3 \xi_5 \tag{6.23}$$

Figure 6.47 and Figure 6.48 show the distribution of $3CaO \cdot 2SiO_2 \cdot 3H_2O$ mass concentration gradients over time and space. Figure 6.49 shows the comparison of mass concentrations ($\rho_3 \Big|_{10\text{g}}^{15\text{g}}$) at $t = 48hr$. Figure 6.50 shows us the comparison of mass concentrations ($\rho_3 \Big|_{10\text{g}}^{15\text{g}}$) at section $x_1 = 0$.

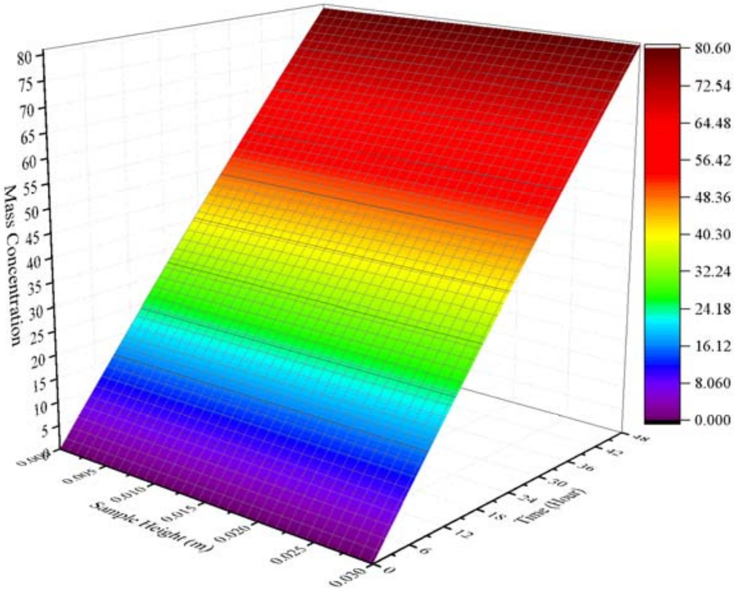

Figure 6.47: $3CaO \cdot 2SiO_2 \cdot 3H_2O$ mass concentration ($\rho_3 \Big|_{15\text{g}}$) time-space distribution

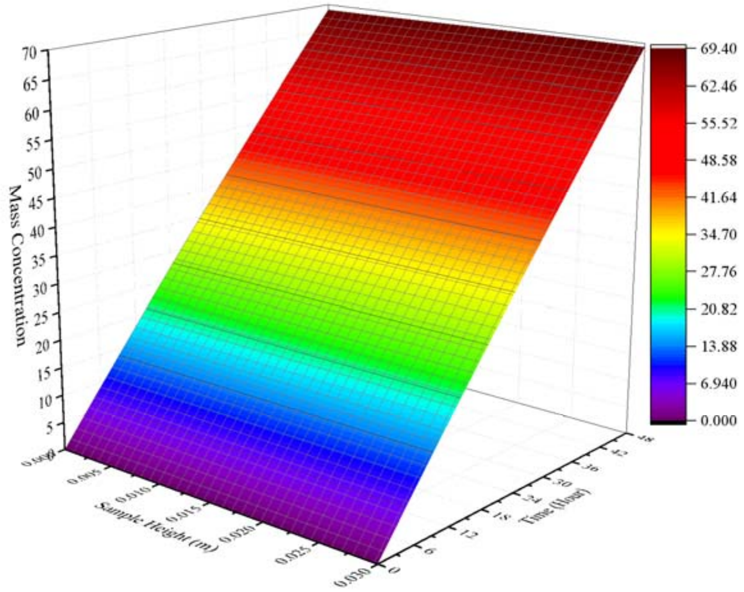

Figure 6.48: 3CaO·2SiO$_2$·3H$_2$O mass concentration ($\rho_3 \big|_{10\mathrm{g}}$) time-space

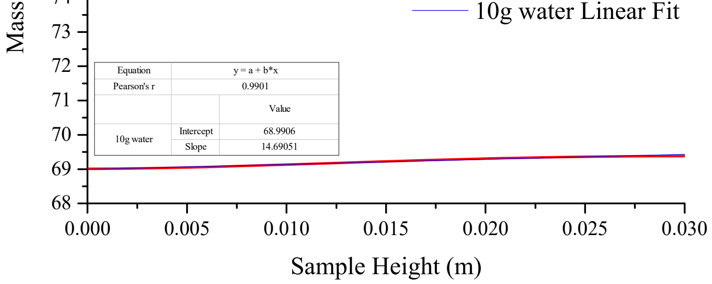

Figure 6.49: 3CaO·2SiO$_2$·3H$_2$O mass concentrations ($\rho_3 \big|_{10\mathrm{g}}^{15\mathrm{g}}$) comparison on $t = 48hr$

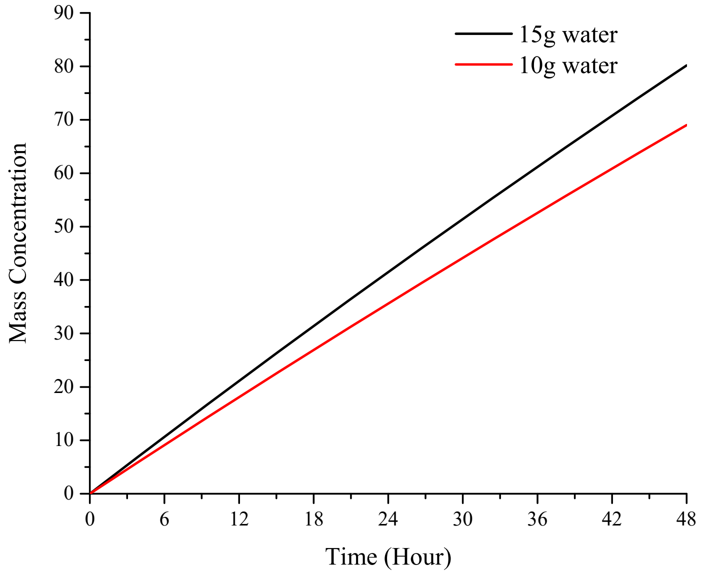

Figure 6.50: $3CaO{\cdot}2SiO_2{\cdot}3H_2O$ mass concentrations ($\rho_3 \Big|_{10g}^{15g}$) comparison on section $x_1 = 0$

From Figure 6.49 and Figure 6.50, we can find out:

(1) Mass concentration (ρ_3) is monotonically increased with time at any section of the sample.

(2) Mass concentration (ρ_3) is approximately linearly distributed along x_1 direction.

(3) Mass concentration (ρ_3) at bottom ($x_1 = h_s$) is larger than at the top ($x_1 = 0$) when $t > 0hr$.

(4) At $t = 48hr$, the mass concentration gradient $\left(\frac{\partial \rho_3}{\partial t} \Big|_{15g} \right)$ of Sample 1 is larger than Sample 2 mass concentration gradient $\left(\frac{\partial \rho_3}{\partial t} \Big|_{10g} \right)$.

(5) At section $x_1 = 0$, the mass concentration gradient $\left(\frac{\partial \rho_3}{\partial t} \Big|_{15\text{g}} \right)$ is larger Sample 2 than mass concentration gradient $\left(\frac{\partial \rho_3}{\partial t} \Big|_{10\text{g}} \right)$.

$\mathrm{Ca(OH)_2}$ is present as one of the reactants in chemical reactions (6.7), (6.10) and (6.13). And it is also present as the resultant in chemical reaction (6.16). Therefore, its mass concentration gradient can be expressed as:

$$\frac{\partial \rho_4}{\partial t} = 3\mu_4 \xi_1 + \mu_4 \xi_2 + \mu_4 \xi_3 - \mu_4 \xi_4 \tag{6.24}$$

Figure 6.51 and Figure 6.52 show the distribution of $\mathrm{Ca(OH)_2}$ mass concentration over time and space. Figure 6.53 shows the comparison of mass concentrations ($\rho_4 \Big|_{10\text{g}}^{15\text{g}}$) at $t = 48hr$. Figure 6.54 shows the comparison of mass concentrations ($\rho_4 \Big|_{10\text{g}}^{15\text{g}}$) at section $x_1 = 0$.

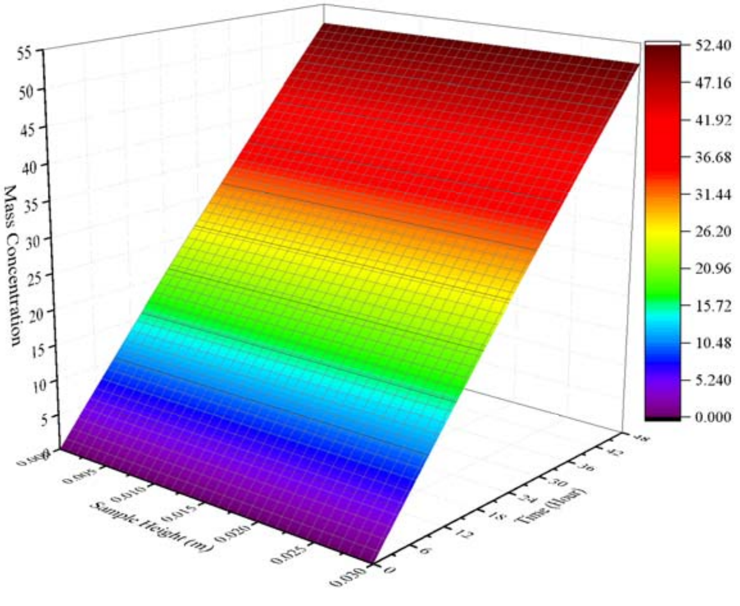

Figure 6.51: $\mathrm{Ca(OH)_2}$ mass concentration ($\rho_4 \Big|_{15\text{g}}$) time-space distribution

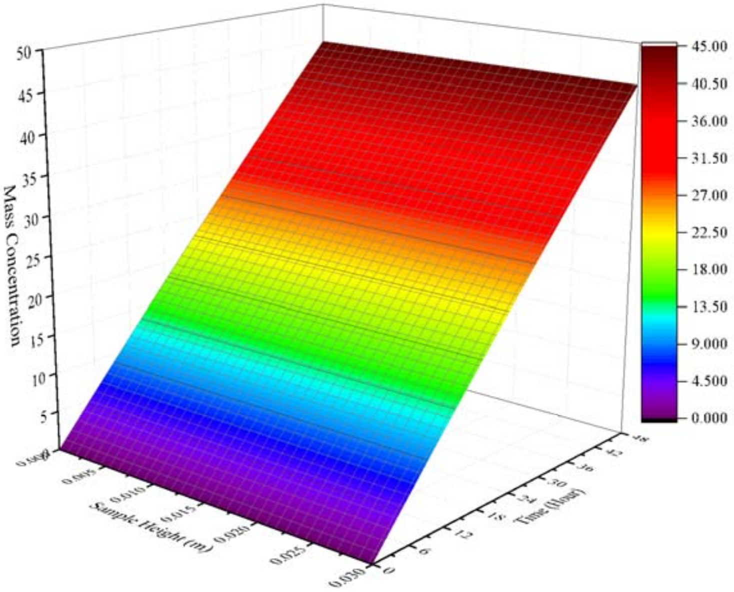

Figure 6.52: $\mathrm{Ca(OH)_2}$ mass concentration ($\rho_4\big|_{10\mathrm{g}}$) time-space distribution

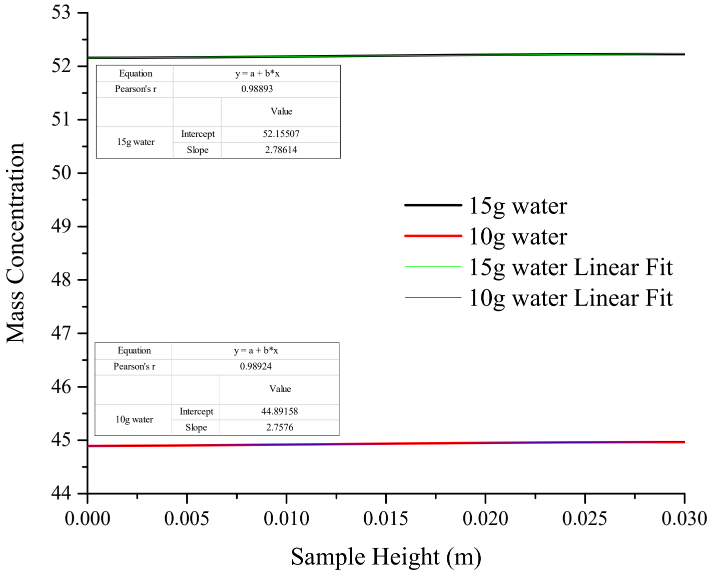

Figure 6.53: $\mathrm{Ca(OH)_2}$ mass concentrations ($\rho_4\Big|_{10\mathrm{g}}^{15\mathrm{g}}$) comparison of at $t = 48hr$

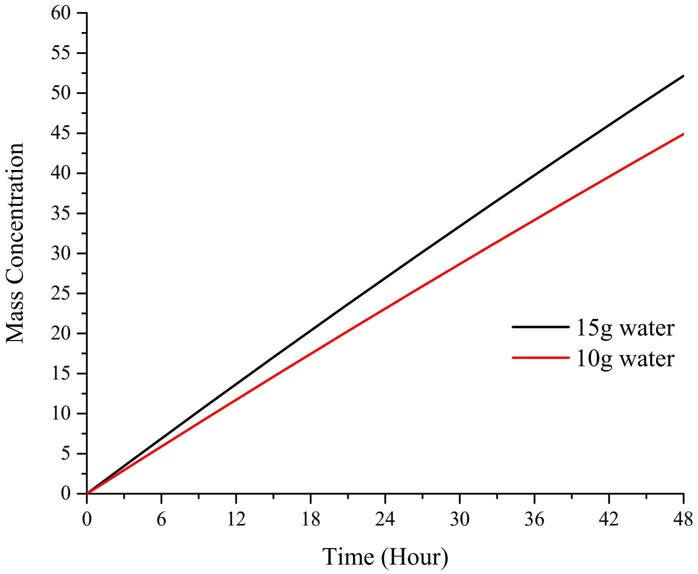

Figure 6.54 $Ca(OH)_2$ mass concentration ($\rho_4 \Big|_{10g}^{15g}$) comparison of on section $x_1 = 0$

From Figure 6.53 and Figure 6.54, the following observations can be made:

(1) Mass concentration (ρ_4) monotonically increases with time at any section of the sample.

(2) Mass concentration (ρ_4) is approximately linearly distributed along x_1 direction at anytime.

(3) At $t = 48hr$, Sample 1 mass concentration gradient $\left(\frac{\partial \rho_4}{\partial t} \Big|_{15g} \right)$ is larger than Sample 2 mass concentration gradient $\left(\frac{\partial \rho_4}{\partial t} \Big|_{10g} \right)$.

(4) At section $x_1 = 0$, Sample 1 mass concentration gradient $\left(\frac{\partial \rho_4}{\partial t} \Big|_{15\mathrm{g}} \right)$ is larger than Sample 2 mass concentration gradient $\left(\frac{\partial \rho_4}{\partial t} \Big|_{10\mathrm{g}} \right)$.

C_2S represents one of the reactants in chemical reactions (6.10) and (6.21). Its mass concentration gradient can be given as:

$$\frac{\partial \rho_5}{\partial t} = -2\mu_5 \xi_2 - \mu_5 \xi_7 \tag{6.25}$$

Figure 6.55 and Figure 6.56 show the distributions of C_2S mass concentration for Samples 1 and 2 over time and space. Figure 6.57 shows the comparison of mass concentrations ($\rho_5 \Big|_{10\mathrm{g}}^{15\mathrm{g}}$) at $t = 48hr$. Figure 6.58 shows the comparison of mass concentration ($\frac{\partial \rho_5}{\partial t} \Big|_{10\mathrm{g}}^{15\mathrm{g}}$) at section $x_1 = 0$.

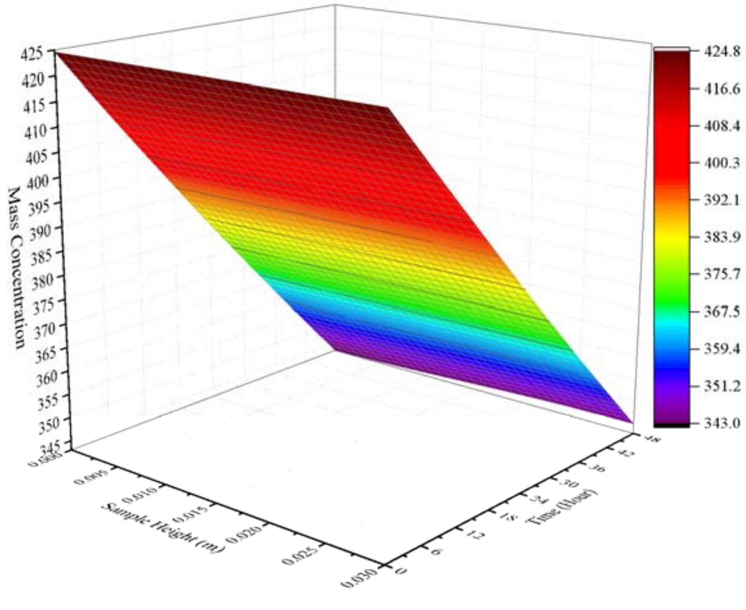

Figure 6.55: C_2S mass concentration ($\rho_5 \Big|_{15\mathrm{g}}$) time-space distribution

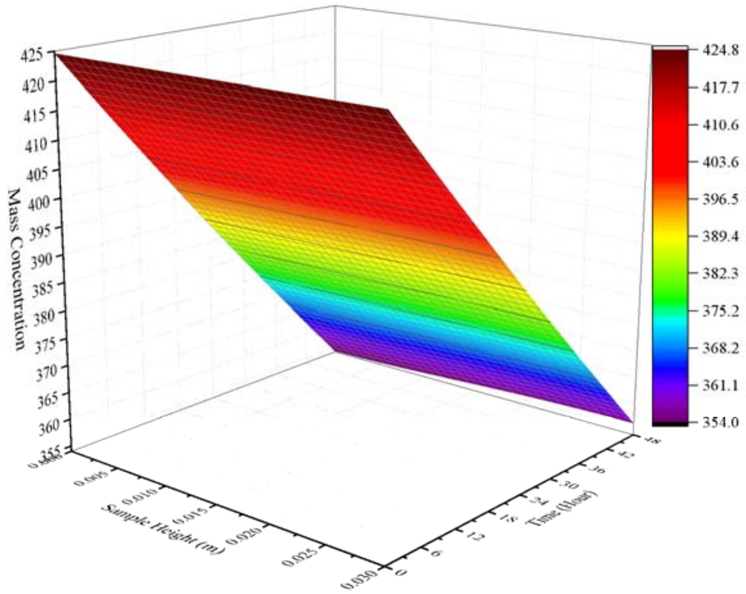

Figure 6.56: C_2S mass concentration ($\rho_5 \Big|_{10g}$) time-space distribution

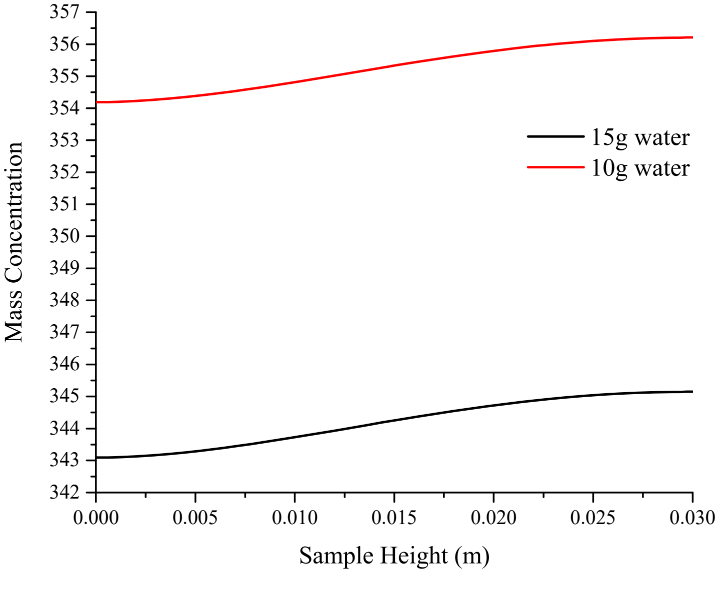

Figure 6.57: C_2S mass concentrations ($\rho_5 \Big|_{10g}^{15g}$) comparison of at $t = 48hr$

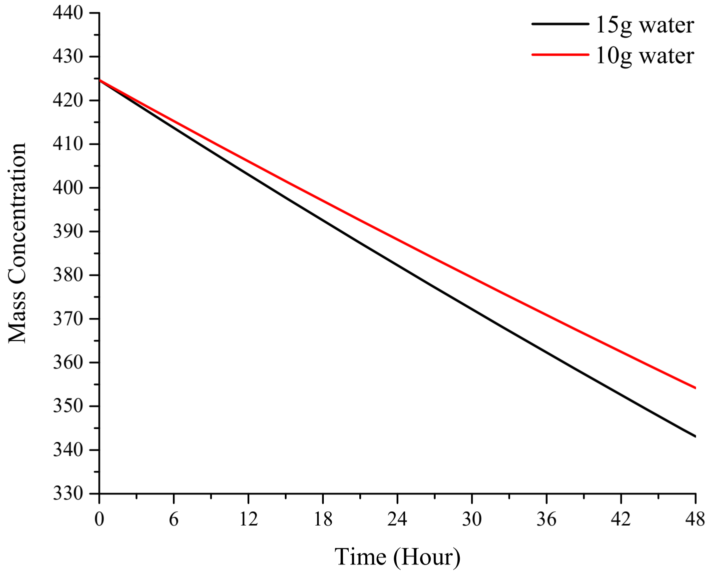

Figure 6.58: C_2S mass concentrations ($\rho_5 \Big|_{10g}^{15g}$) comparison of on section $x_1 = 0$

From Figure 6.57 and Figure 6.58, we learned that:

(1) Mass concentration $\left(\rho_5\right)$ is strictly monotonically decreased with time at any section of the sample.

(2) Mass concentration $\left(\rho_5\right)$ is approximately linearly distributed along x_1 direction at anytime.

(3) Mass concentrations (ρ_5) of Sample 1 and Sample 2 are equal initially. However, the Sample 1 reaction rates (ξ_5 and ξ_7) are larger than those of Sample 2. Therefore, Sample 1's mass concentration gradient ($\left|\frac{\partial \rho_5}{\partial t}\right|$) should be less than its value in Sample 2 ($\left|\frac{\partial \rho_5}{\partial t}\right|_{15g} < \left|\frac{\partial \rho_5}{\partial t}\right|_{10g}$).

(4) At $t = 48hr$, Sample 1 mass concentration gradient $\left(\rho_5 \big|_{15\text{g}}\right)$ is less than Sample 2 mass concentration gradient $\left(\rho_5 \big|_{10\text{g}}\right)$.

(5) At section $x_1 = 0$, Sample 1 mass concentration gradient $\left(\frac{\partial \rho_5}{\partial t}\Big|_{15\text{g}}\right)$ is larger than Sample 2 mass concentration gradient $\left(\frac{\partial \rho_5}{\partial t}\Big|_{10\text{g}}\right)$.

CaO is one of as the reactants in chemical reaction (6.13). Its mass concentration gradient can be given as:

$$\frac{\partial \rho_6}{\partial t} = -\mu_6 \xi_3 \tag{6.26}$$

Figure 6.59 and Figure 6.60 show the distribution of CaO mass concentration over time and space. Figure 6.61 shows the comparison of mass concentrations ($\rho_6 \Big|_{10\text{g}}^{15\text{g}}$) at $t = 48hr$. Figure 6.62 shows the comparison of mass concentration gradients ($\frac{\partial \rho_6}{\partial t}\Big|_{10\text{g}}^{15\text{g}}$).

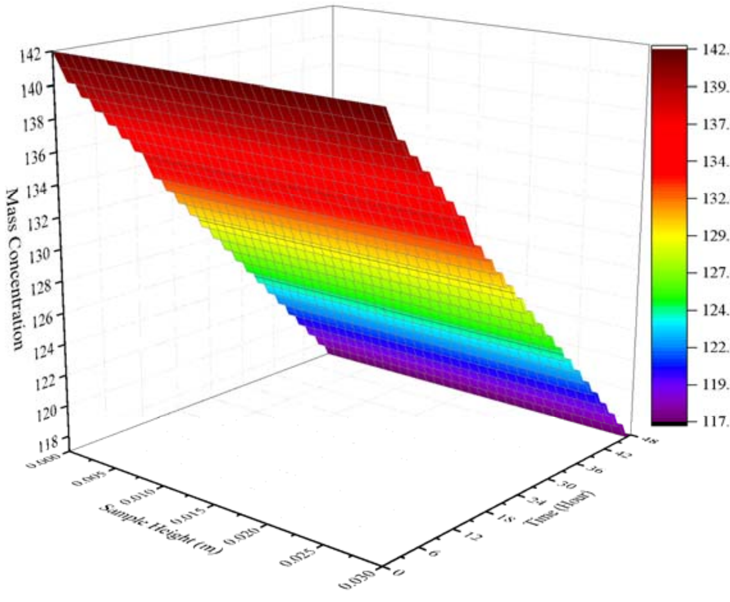

Figure 6.59: CaO mass concentration ($\rho_6 \big|_{15g}$) time-space distribution

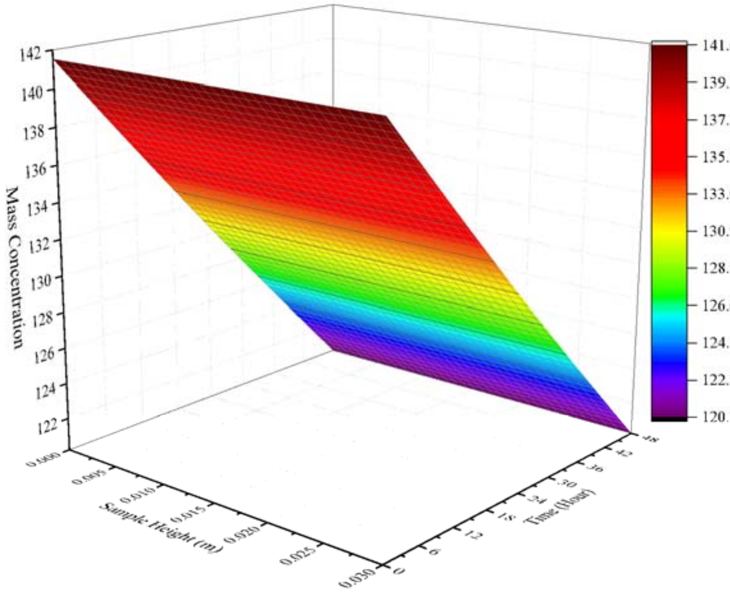

Figure 6.60: CaO mass concentration ($\rho_6 \big|_{10g}$) time-space distribution

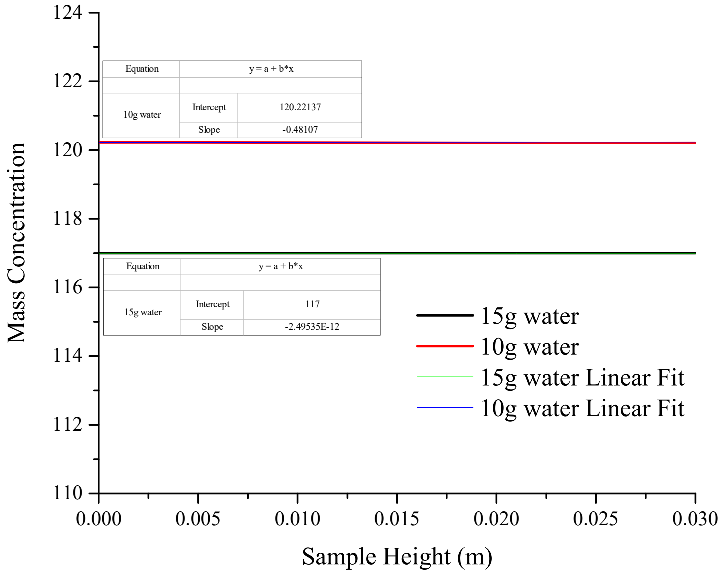

Figure 6.61: CaO mass concentrations ($\rho_6 \Big|_{10\text{g}}^{15\text{g}}$) comparison of at $t = 48hr$

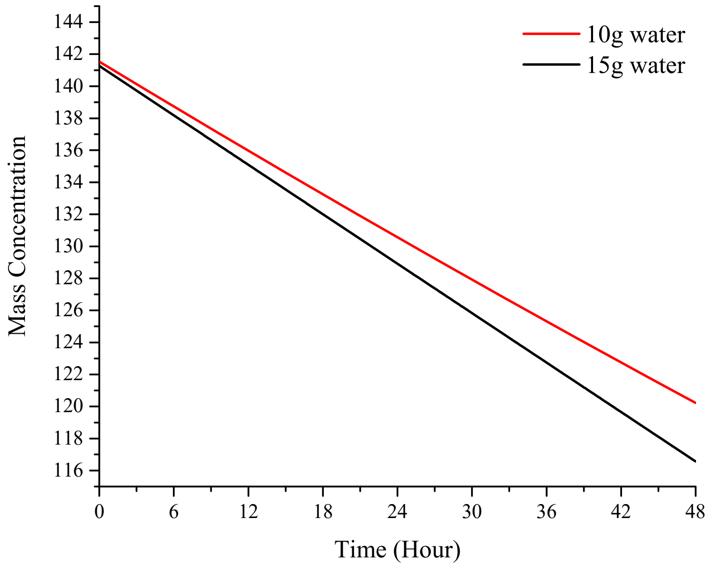

Figure 6.62: CaO mass concentrations ($\rho_6 \Big|_{10\text{g}}^{15\text{g}}$) comparison of on section $x_1 = 0$

From Figure 6.61 and Figure 6.62, we learned:

(1) Mass concentration $\left(\rho_6\right)$ is strictly monotonically decreased with time on any section of the sample.

(2) Mass concentration $\left(\rho_6\right)$ is linearly distributed along x_1 direction.

(3) Mass concentrations (ρ_6) of Sample 1 and Sample 2 are equal initially. However, Sample 1 reaction rates (ξ_3) is larger than those of Sample 2. Therefore, Sample 1 mass concentration ($\rho_6\left|_{15\mathrm{g}}\right.$) should be less than its value in Sample 2 ($\rho_6\left|_{10\mathrm{g}}\right.$), $\rho_6\big|_{15\mathrm{g}} < \rho_6\big|_{10\mathrm{g}}$.

(4) At $t = 48hr$, Sample 1 mass concentration gradient $\left(\rho_6\left|_{15\mathrm{g}}\right.\right)$ is less than Sample 2 mass concentration gradient $\left(\rho_6\left|_{10\mathrm{g}}\right.\right)$.

(5) At section $x_1 = 0$, the mass concentration gradient $\left(\frac{\partial\rho_6}{\partial t}\Big|_{15\mathrm{g}}\right)$ is larger than the mass concentration gradient $\left(\frac{\partial\rho_6}{\partial t}\Big|_{10\mathrm{g}}\right)$.

CO_2 is a reactant in chemical reactions (6.17), (6.19), (6.20) and (6.21). On the other hand, CO_2 has experienced diffusion during the chemical reactions. So the mass concentration gradient can be written as:

$$\frac{\partial\rho_7}{\partial t} = -\mu_7\xi_4 - 3\mu_7\xi_5 - 3\mu_7\xi_6 - 2\mu_7\xi_7 - \frac{\partial J_1}{\partial x_1} \tag{6.27}$$

Figure 6.63 and Figure 6.64 show the distributions of CO_2 mass concentration over time and space.

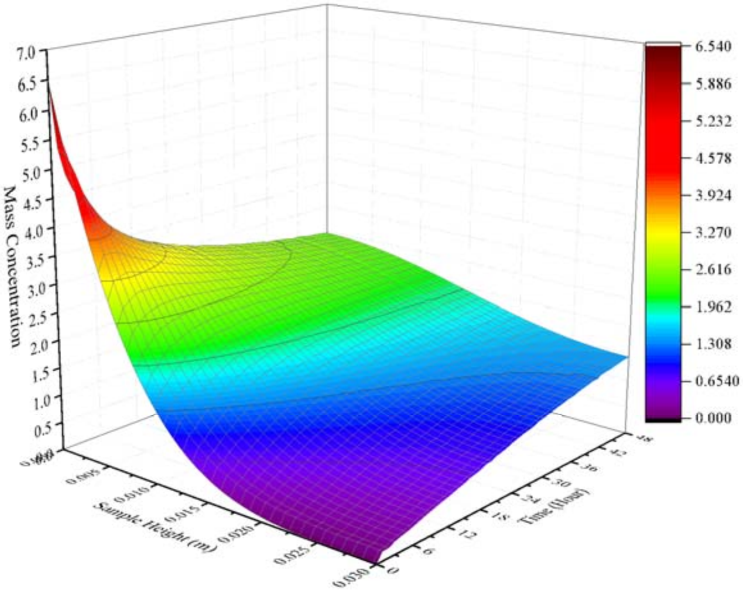

Figure 6.63: CO_2 mass concentration ($\rho_7\big|_{15g}$) time-space distribution

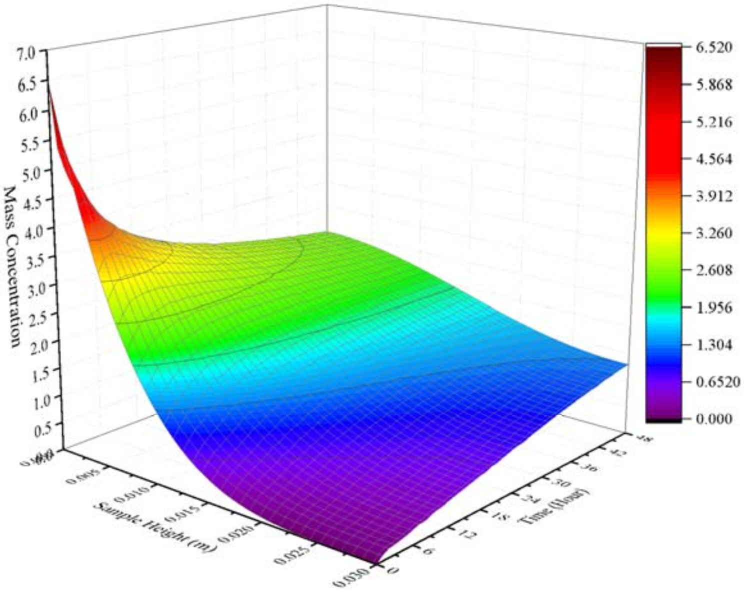

Figure 6.64: CO_2 mass concentration ($\rho_7\big|_{10g}$) time-space distribution

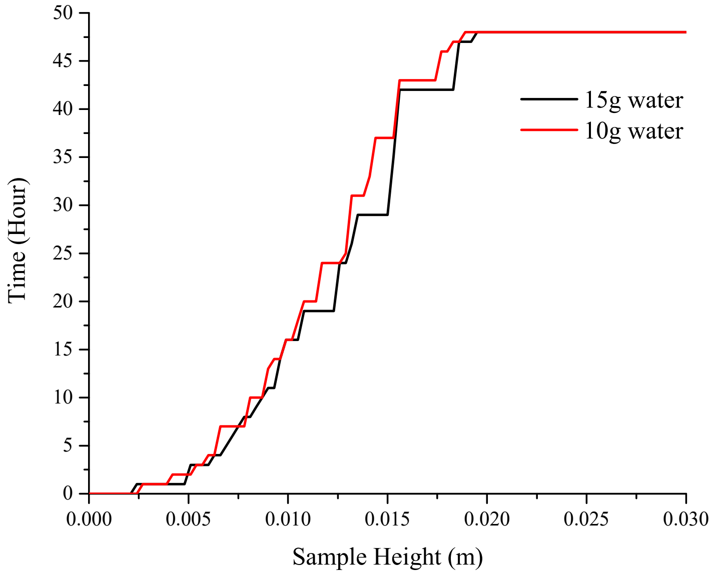

Figure 6.65: Reaction rates ($\xi_7\big|_{15\mathrm{g}}^{10\mathrm{g}}$) changing characteristics along with time and space

From Figure 6.64 and Figure 6.65, we learned that:

(1) The distributions of CO_2 mass concentration are very similar for both samples. CO_2 mass concentrations decreased with time at the upper surface. And CO_2 mass concentrations increased with time on the lower end surface.

(2) The general characteristics of mass concentrations in both samples are very close. At the beginning, the $\rho_7 \sim x_1$ curve has the maximum value of curvature. As time goes on, the mass concentration curve is gradually flattened in the x_1 direction.

(3) Sample 1 CO_2 mass concentration ($\rho_7\big|_{15\mathrm{g}}$) decreased with time at section $0 < x_1 \le \frac{7}{100} h_s = 2.10\times10^{-3}\left(\mathrm{m}\right)$ and increased at section

$1.44\times10^{-2}\left(\mathrm{m}\right)=\frac{48}{100}h_s\le x_1\le3\times10^{-2}\left(\mathrm{m}\right)$. Between section $2.40\times10^{-3}\left(\mathrm{m}\right)=\frac{8}{100}h_s\le x_1\le1.44\times10^{-2}\left(\mathrm{m}\right)$, the value decreased first and rose later.

(4) Sample 2 CO_2 mass concentration ($\rho_7\big|_{10\mathrm{g}}$) decreased with time at section $0\le x_1\le2.10\times10^{-3}\left(\mathrm{m}\right)$ and increased at section $1.50\times10^{-2}\left(\mathrm{m}\right)\le x_1\le3\times10^{-2}\left(\mathrm{m}\right)$. The value decreased first and rose later at the section $2.40\times10^{-3}\left(\mathrm{m}\right)\le x_1\le1.53\times10^{-2}\left(\mathrm{m}\right)$.

(5) The different water contents do not make a big difference for the CO_2 concentration level.

$CaCO_3$ is one of the resultants in chemical reactions (6.16), (6.20) and (6.21). Its mass concentration gradient is:

$$\frac{\partial\rho_8}{\partial t}=\mu_8\xi_4+3\mu_8\xi_6+2\mu_8\xi_7 \tag{6.28}$$

Figure 6.66 and Figure 6.67 show the distributions of $CaCO_3$ mass concentration over time and space. Figure 6.68 shows the comparison of mass concentrations ($\rho_8\big|_{10\mathrm{g}}^{15\mathrm{g}}$) at $t=48hr$. Figure 6.69 shows the comparison of mass concentration at section $x_1=0$.

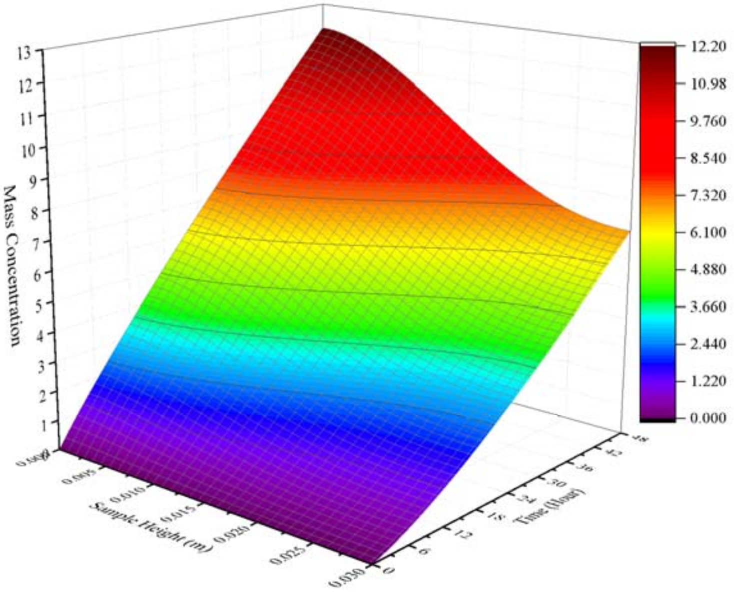

Figure 6.66: CaCO$_3$ mass concentration ($\rho_8 \big|_{15g}$) time-space distribution

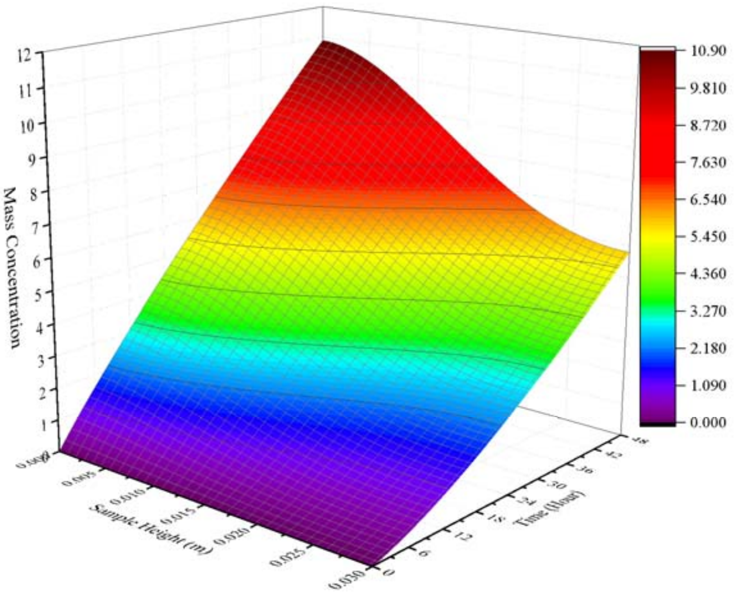

Figure 6.67: CaCO$_3$ mass concentration ($\rho_8 \big|_{10g}$) time-space distribution

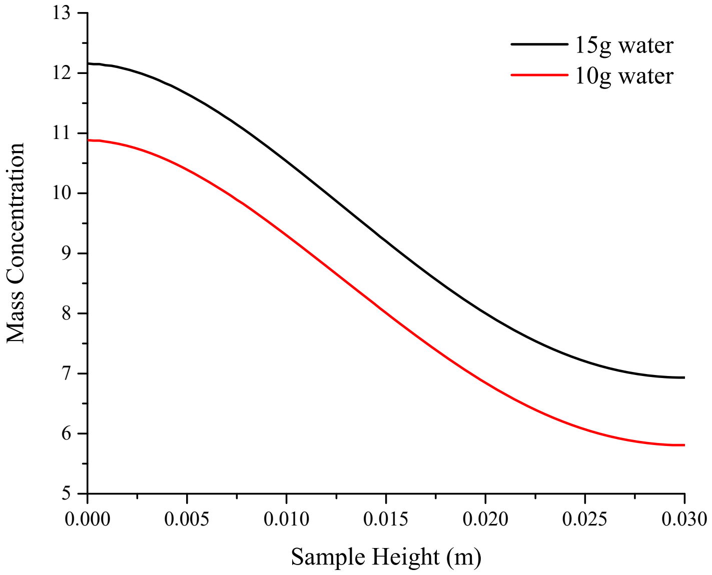

Figure 6.68: $CaCO_3$ mass concentrations ($\rho_8 \Big|_{10g}^{15g}$) comparison of at $t = 48hr$

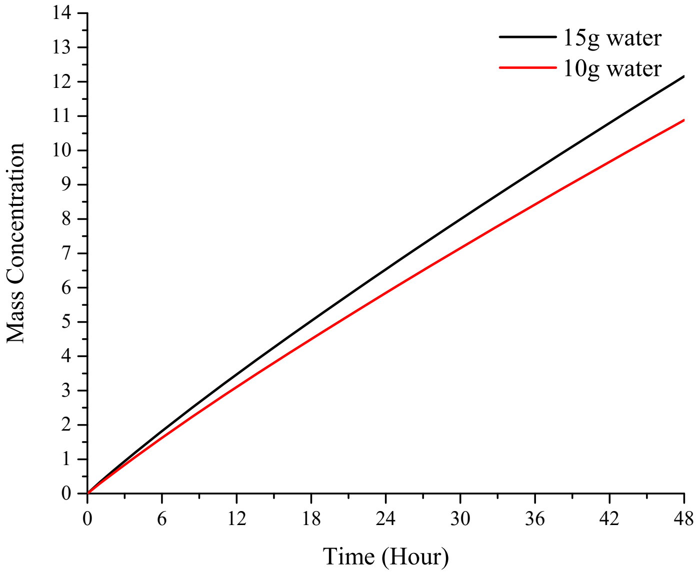

Figure 6.69: $CaCO_3$ mass concentrations ($\rho_8 \Big|_{10g}^{15g}$) comparison of on section $x_1 = 0$

From Figure 6.68 and 6.69, we got:

(1) Mass concentration $\left(\rho_8 \Big|_{10g}^{15g}\right)$ increased monotonically with time.

(2) Mass concentration $\left(\rho_8\Big|_{10\text{g}}^{15\text{g}}\right)$ decreased monotonically along x_1 direction.

(3) Mass concentrations $\left(\rho_8\Big|_{10\text{g}}^{15\text{g}}\right)$ equaled to zero initially. When $t>0$, Sample 1 mass concentration ($\rho_8\big|_{15\text{g}}$) is larger than Sample 2 value ($\rho_8\big|_{10\text{g}}$), and $\rho_8\big|_{15\text{g}}>\rho_8\big|_{10\text{g}}$.

(4) At $t=48hr$, Sample 1 mass concentration gradient $\left(\rho_8\big|_{15\text{g}}\right)$ is larger than Sample 2 mass concentration gradient $\left(\rho_8\big|_{10\text{g}}\right)$, $\rho_8^{t=48(\text{h})}\Big|_{15\text{g}}>\rho_8^{t=48(\text{h})}\Big|_{10\text{g}}$.

(5) At section $x_1=0$, Sample 1 mass concentration gradient $\left(\dfrac{\partial\rho_8}{\partial t}\Big|_{15\text{g}}\right)$ is larger than Sample 2 mass concentration gradient $\left(\dfrac{\partial\rho_8}{\partial t}\Big|_{10\text{g}}\right)$.

(6) Sample 1 generates more CaCO_3 material than Sample 2.

$3\text{CaCO}_3\cdot 2\text{SiO}_2\cdot 3\text{H}_2\text{O}$ is a resultant in chemical reaction (6.19). So the mass concentration gradient can be written as:

$$\frac{\partial\rho_9}{\partial t}=\mu_9\xi_5 \tag{6.29}$$

Figure 6.70 and Figure 6.71 show the distributions of $3\text{CaCO}_3\cdot 2\text{SiO}_2\cdot 3\text{H}_2\text{O}$ mass concentration over time and space. Figure 6.72 shows the comparison of mass concentrations ($\rho_9\Big|_{10\text{g}}^{15\text{g}}$) at $t=48hr$. Figure 6.73 shows the comparison of mass concentrations ($\rho_9\Big|_{10\text{g}}^{15\text{g}}$) at section $x_1=0$.

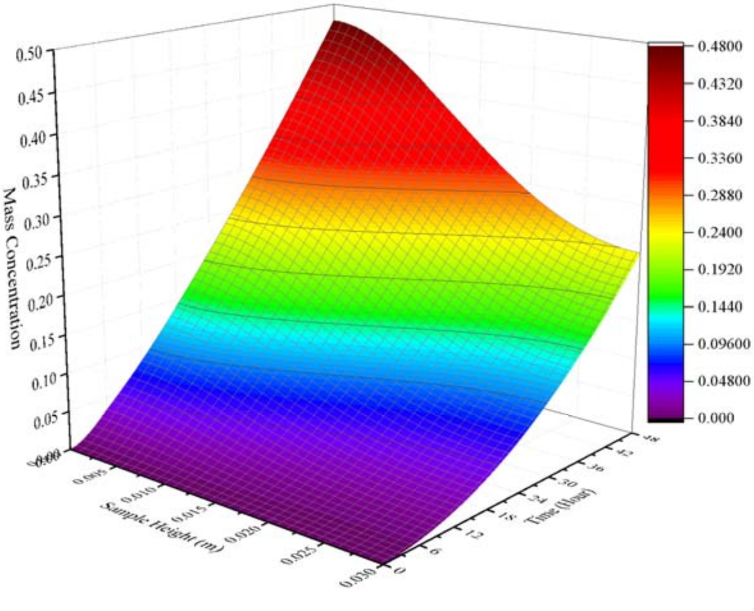

Figure 6.70: $3CaCO_3\cdot 2SiO_2\cdot 3H_2O$ mass concentration ($\rho_9\big|_{15g}$) time-space distribution

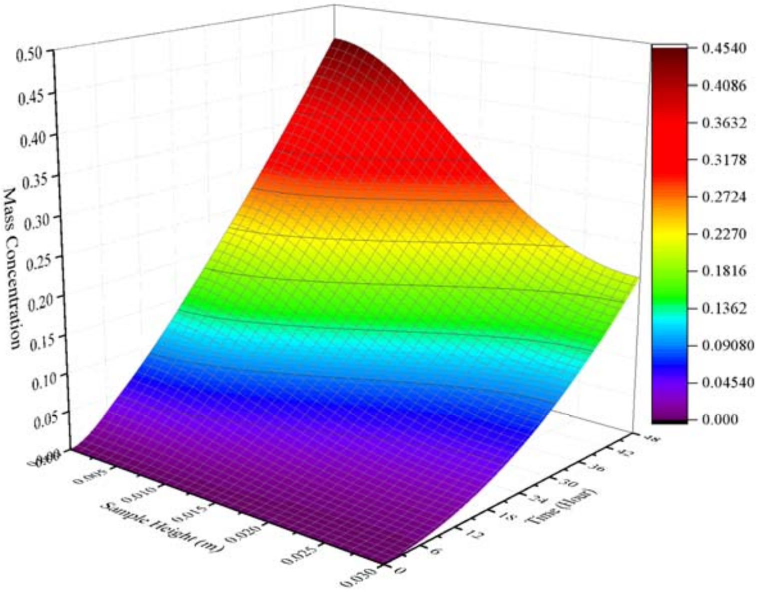

Figure 6.71: $3CaCO_3\cdot 2SiO_2\cdot 3H_2O$ mass concentration ($\rho_9\big|_{10g}$) time-space distribution

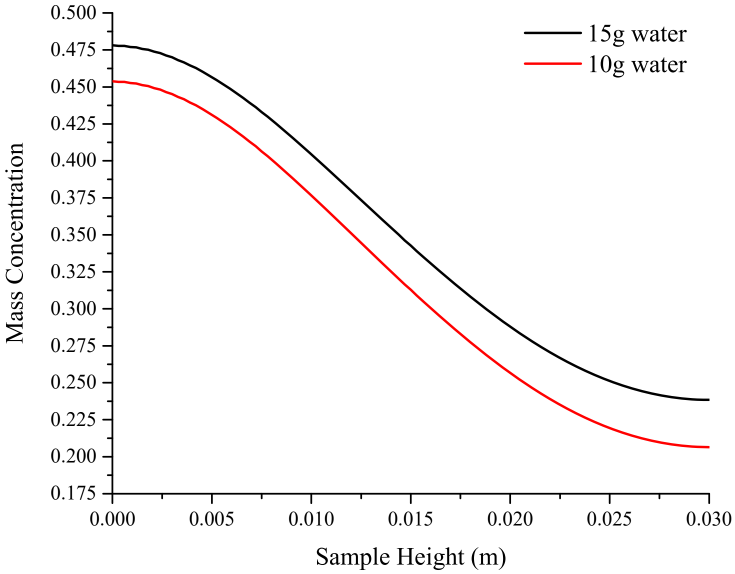

Figure 6.72: $3CaCO_3 \cdot 2SiO_2 \cdot 3H_2O$ mass concentrations ($\rho_9 \Big|_{10g}^{15g}$) comparison at $t = 48hr$

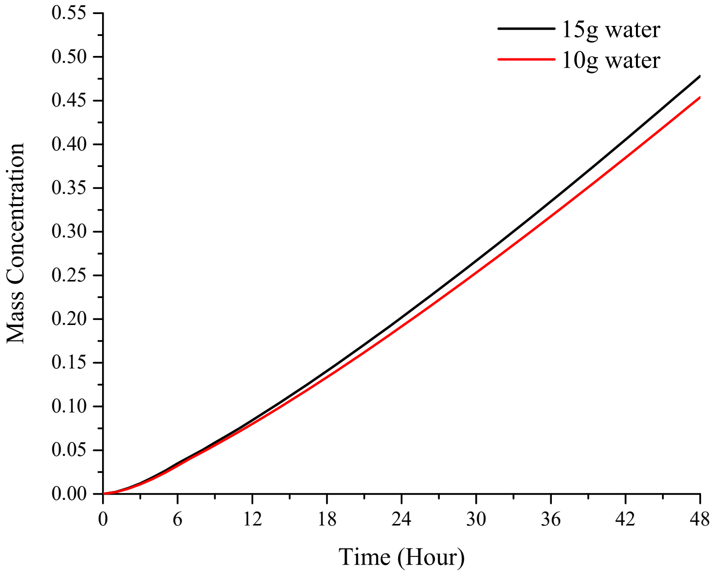

Figure 6.73: $3CaCO_3 \cdot 2SiO_2 \cdot 3H_2O$ mass concentrations ($\rho_9 \Big|_{10g}^{15g}$) comparison on section $x_1 = 0$

From Figure 6.72 and Figure 6.73, we got:

(1) Mass concentration $\left(\rho_9 \Big|_{10g}^{15g} \right)$ increased monotonically with time.

(2) Mass concentration $\left(\rho_9\left|_{10\text{g}}^{15\text{g}}\right.\right)$ decreased monotonically along x_1 direction.

(3) Mass concentrations $\left(\rho_9\left|_{10\text{g}}^{15\text{g}}\right.\right)$ are equal to zero initially. When $t>0$, Sample 1 mass concentration ($\rho_9\left|_{15\text{g}}\right.$) is larger than in Sample 2 ($\rho_9\left|_{10\text{g}}\right.$), $\rho_9\big|_{15\text{g}}>\rho_9\big|_{10\text{g}}$.

(4) At $t=48hr$, Sample 1 mass concentration gradient $\left(\rho_9\left|_{15\text{g}}\right.\right)$ is larger than Sample 2 mass concentration gradient $\left(\rho_9\left|_{10\text{g}}\right.\right)$, $\rho_9^{t=48(\text{h})}\Big|_{15\text{g}}>\rho_9^{t=48(\text{h})}\Big|_{10\text{g}}$.

(5) At section $x_1=0$, Sample 1 mass concentration gradient $\left(\frac{\partial\rho_9}{\partial t}\Big|_{15\text{g}}\right)$ is larger than Sample 2 mass concentration gradient $\left(\frac{\partial\rho_9}{\partial t}\Big|_{10\text{g}}\right)$, $\frac{\partial\rho_9}{\partial t}\Big|_{15\text{g}}>\frac{\partial\rho_9}{\partial t}\Big|_{10\text{g}}$.

(6) Sample 1 generates more $3\text{CaCO}_3\cdot2\text{SiO}_2\cdot3\text{H}_2\text{O}$ material than Sample 2.

$\text{SiO}_2\cdot\gamma\text{H}_2\text{O}$ is one of the resultants in chemical reactions (6.20) and (6.21). Its mass concentration gradient can be expressed as:

$$\frac{\partial\rho_{10}}{\partial t}=\mu_{10}\xi_6+\mu_{10}\xi_7 \tag{6.30}$$

Figure 6.74 and Figure 6.75 show the distributions of $\text{SiO}_2\cdot\gamma\text{H}_2\text{O}$ mass concentration over time and space. Figure 6.76 shows the comparison of mass concentrations ($\rho_{10}\left|_{10\text{g}}^{15\text{g}}\right.$) at $t=48hr$. Figure 6.77 shows the comparison of mass concentrations ($\rho_{10}\left|_{10\text{g}}^{15\text{g}}\right.$) at section $x_1=0$.

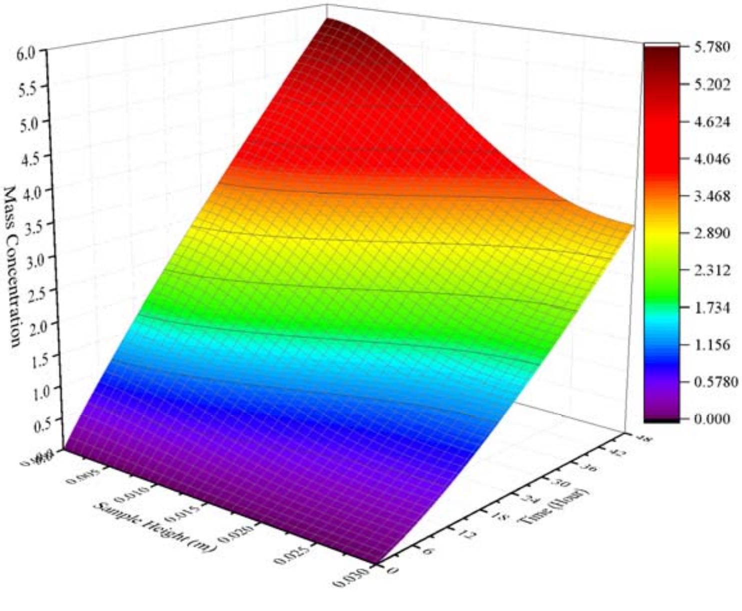

Figure 6.74: $SiO_2 \cdot \gamma H_2O$ mass concentration ($\rho_{10}\big|_{15g}$) time-space distribution

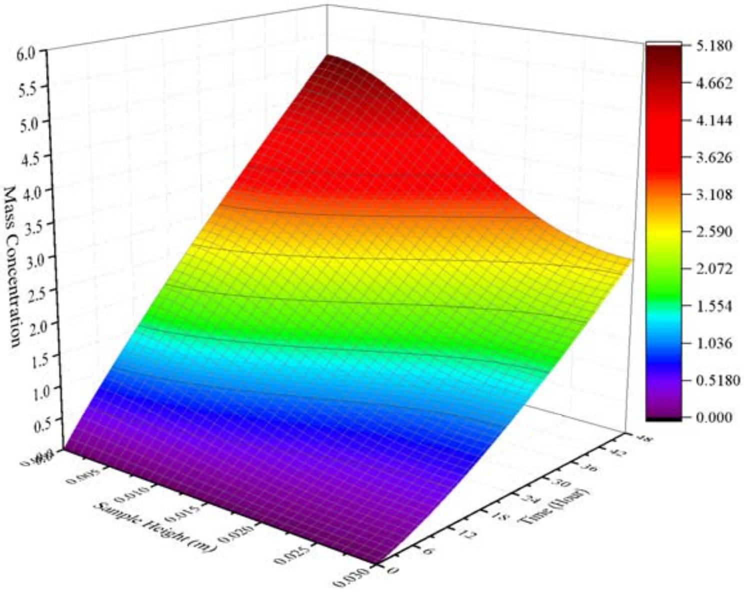

Figure 6.75: $SiO_2 \cdot \gamma H_2O$ mass concentration ($\rho_{10}\big|_{10g}$) time-space distribution

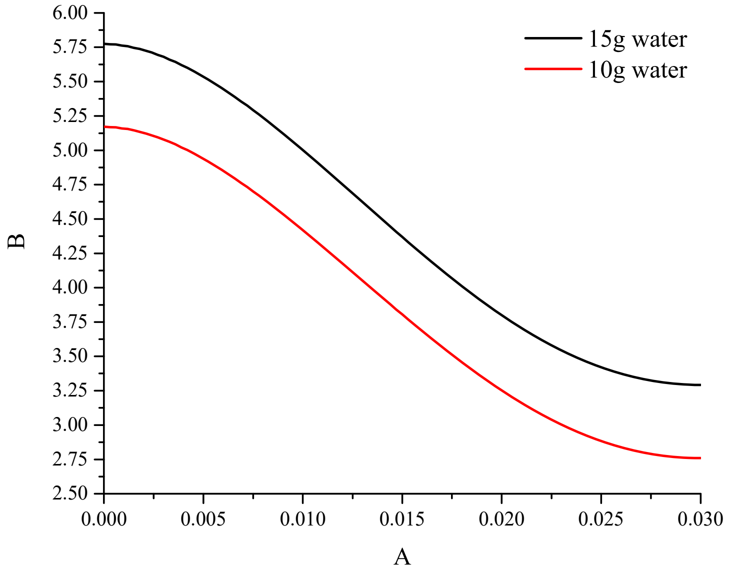

Figure 6.76: $SiO_2 \cdot \gamma H_2O$ mass concentrations ($\rho_{10}\Big|_{10g}^{15g}$) comparison at $t = 48hr$

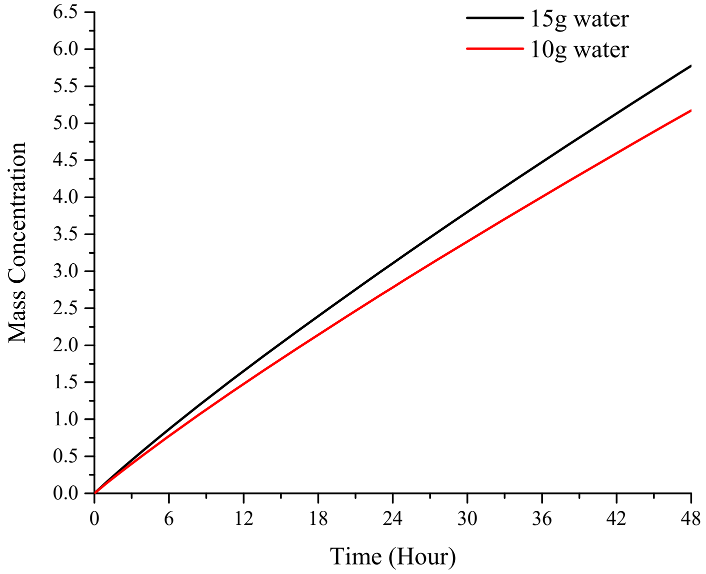

Figure 6.77: $SiO_2 \cdot \gamma H_2O$ mass concentrations ($\rho_{10}\Big|_{10g}^{15g}$) comparison of on section $x_1 = 0$

Figure 6.76 and Figure 6.77 conclude the following:

(1) Mass concentration $\left(\rho_{10}\Big|_{10g}^{15g}\right)$ is increased monotonically with time.

(2) Mass concentration $\left(\rho_{10}\Big|_{10\mathrm{g}}^{15\mathrm{g}}\right)$ decreased monotonically along x_1 direction.

(3) Mass concentrations $\left(\rho_{10}\Big|_{10\mathrm{g}}^{15\mathrm{g}}\right)$ are equal to zero initially. When $t > 0$, Sample 1 mass concentration ($\rho_{10}\big|_{15\mathrm{g}}$) is larger than its value in Sample 2 ($\rho_{10}\big|_{10\mathrm{g}}$), $\rho_{10}\big|_{15\mathrm{g}} > \rho_{10}\big|_{10\mathrm{g}}$.

(4) At $t = 48hr$, Sample 1 mass concentration gradient $\left(\rho_{10}\big|_{15\mathrm{g}}\right)$ is larger than Sample 2 mass concentration gradient $\left(\rho_{10}\big|_{10\mathrm{g}}\right)$, $\rho_{10}^{t=48(\mathrm{h})}\Big|_{15\mathrm{g}} > \rho_{10}^{t=48(\mathrm{h})}\Big|_{10\mathrm{g}}$.

(5) At section $x_1 = 0$, the mass concentration gradient $\left(\frac{\partial \rho_{10}}{\partial t}\Big|_{15\mathrm{g}}\right)$ is large than Sample 2 mass concentration gradient $\left(\frac{\partial \rho_{10}}{\partial t}\Big|_{10\mathrm{g}}\right)$, $\frac{\partial \rho_{10}}{\partial t}\bigg|_{15\mathrm{g}} > \frac{\partial \rho_{10}}{\partial t}\bigg|_{10\mathrm{g}}$.

(6) Sample 1 generates more $\mathrm{SiO_2 \cdot \gamma H_2O}$ material than Sample 2.

6.3 Initial Porosity Impact on CO$_2$ Diffusion and Chemical Reaction

The porosity of the sample can be controlled by varying the amount of aluminum powder in the sample. The initial porosity impact on CO$_2$ diffusion and chemical reaction under the same initial CO$_2$ pressure and initial water binder ratio is investigated. The initial conditions for Sample 3 and Sample 4 are defined in Table 6.2.

Table 6.2 Initial condition for Sample 3 and Sample 4

	Cement Weight	Water Weight	Aluminum Powder Weight	Sample Height	Initial Porosity	Initial CO$_2$ Pressure
Sample 3	30(g)	15(g)	0.5(g)	30(mm)	0.36	150(psi)
Sample 4	30(g)	15(g)	0.3(g)	30(mm)	0.22	150(psi)

In the numerical simulation, the sample period is set as 1 second. The steps of kinetic response of diffusion-chemical reaction (h_t) is also set as 1 second.

Based on the experiment and numerical simulation results, the cavity CO_2 pressure variation, the cavity CO_2 quality variation, the CO_2 mass concentration variation, the CO_2 chemical reaction consumption and the reaction rates under different initial porosity condition are studied.

6.3.1 Cavity CO_2 Pressure Variation

Figure 6.78 shows the experimental results of cavity CO_2 pressure variation.

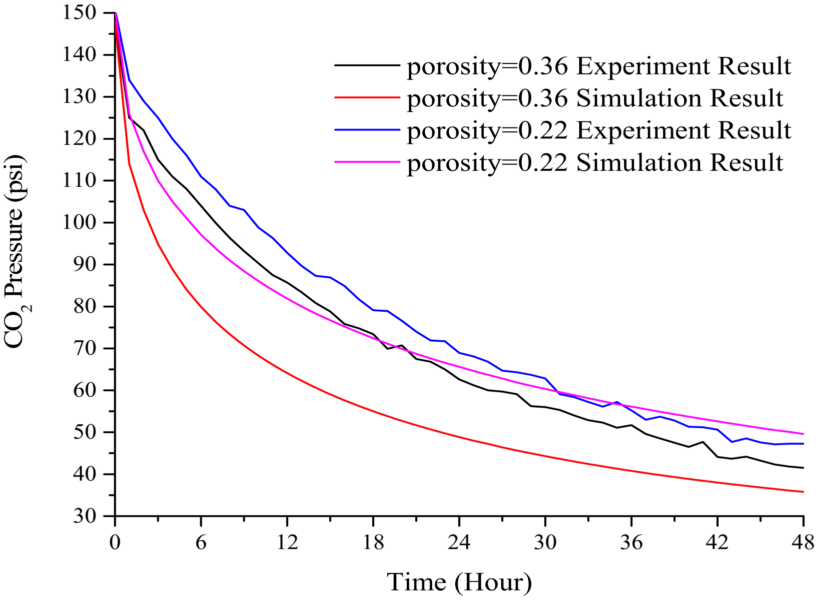

Figure 6.78: Experiment results of cavity CO_2 pressure variation

Sample 3 initial porosity is larger than of Sample 4, which implies that the diffusion coefficient of Sample 3 is larger than that of Sample 4. As a result, it is anticipated that more CO_2 migrated into Sample 3 than in Sample 4. Therefore, the cavity CO_2 pressure in Sample 3 is lower than in Sample 4. In addition, CO_2 drop rate in Sample 3 is higher than Sample 4. As shown in figure, after 48 hours, the cavity CO_2 pressure in Sample 3 reached 41psi and the cavity CO_2 pressure in Sample 4 reached to 53psi.

6.3.2 Cavum CO_2 Mass Loss

Denote the cavity CO$_2$ pressure as p_{chmb}^{0}, the CO$_2$ mass concentration can be written as $m_{\text{CO}_2}^{\text{atm}}\frac{p_{\text{chamb}}^{0}}{p_{\text{atm}}}$. The CO$_2$ weight in cavity can be calculated as:

$$M_{\text{CO}_2}^{0}=\pi a_{\text{s}}^{2}h_{\text{chamb}}m_{\text{CO}_2}^{\text{atm}}\frac{p_{\text{chamb}}^{0}}{p_{\text{atm}}} \tag{6.31}$$

CO$_2$ gas diffuses from cavity into the sample. After the pressure drop, CO$_2$ pressure is given as p_{chamb}. CO$_2$ mass concentration reduced to $m_{\text{CO}_2}^{\text{atm}}\frac{p_{\text{chamb}}}{p_{\text{atm}}}$. Hence, the CO$_2$ mass in cavity can be calculated as:

$$M_{\text{CO}_2}^{\text{diff}}=\pi a_{\text{s}}^{2}h_{\text{chamb}}m_{\text{CO}_2}^{\text{atm}}\frac{p_{\text{chamb}}^{0}\text{-}p_{\text{chamb}}}{p_{\text{atm}}} \tag{6.32}$$

Figure 6.79 shows the cavity CO$_2$ mass losses in Sample 3 and 4.

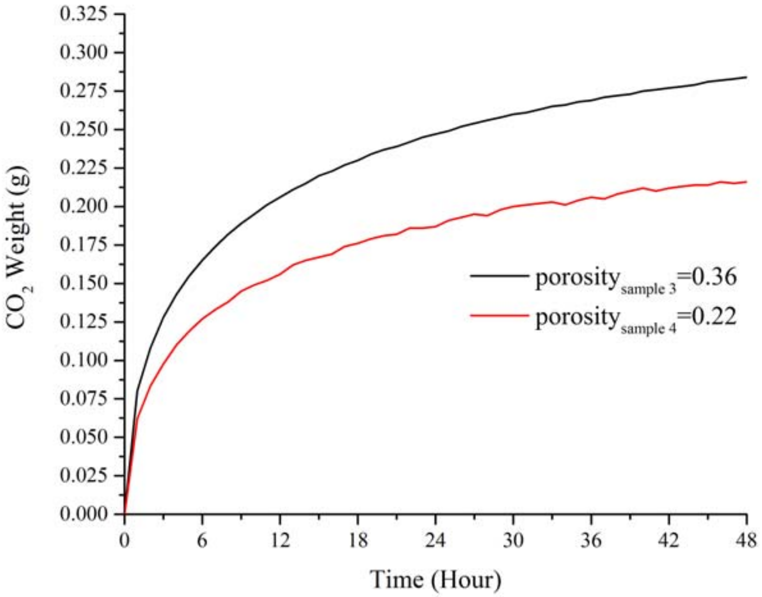

Figure 6.79: Numerical simulation results of cavity CO$_2$ mass loss

As shown in Figure 6.79, the different initial porosities have little influence on cavity CO$_2$ variation. At $t=1hr$, the cavity CO$_2$ consumptions are

$M_{\mathrm{CO_2}}^{\mathrm{diff}}\Big|_{\mathrm{t=1h}}^{\phi_0=0.36}=80.3(\mathrm{mg})$ and $M_{\mathrm{CO_2}}^{\mathrm{diff}}\Big|_{\mathrm{t=1h}}^{\phi_0=0.22}=62.2(\mathrm{mg})$. The ratio of those two values is $\mathrm{ratio}_1=M_{\mathrm{CO_2}}^{\mathrm{diff}}\Big|_{\mathrm{t=1h}}^{\phi_0=0.36}:M_{\mathrm{CO_2}}^{\mathrm{diff}}\Big|_{\mathrm{t=1h}}^{\phi_0=0.22}=1.29:1$. The ratio of those two porosities is $\mathrm{ratio}_0=0.36:0.22=1.64:1$.

At $t=48hr$, the cavity CO_2 consumptions are $M_{\mathrm{CO_2}}^{\mathrm{diff}}\Big|_{\mathrm{t=48h}}^{\phi_0=0.36}=284(\mathrm{mg})$ and $M_{\mathrm{CO_2}}^{\mathrm{diff}}\Big|_{\mathrm{t=48h}}^{\phi_0=0.22}=216(\mathrm{mg})$. The ratio of those two values is $\mathrm{ratio}_2=M_{\mathrm{CO_2}}^{\mathrm{diff}}\Big|_{\mathrm{t=48h}}^{\phi_0=0.36}:M_{\mathrm{CO_2}}^{\mathrm{diff}}\Big|_{\mathrm{t=48h}}^{\phi_0=0.22}=1.31:1$. After we compared ratio_1 and ratio_2 , we noticed that there are some differences between them. Hence, porosity can impact on the CO_2 sorption results.

6.3.3 Residual Amount of CO_2 in Sample

The residual amount of CO_2 can be defined as:

$$Q'_{\mathrm{CO_2}}=\pi a_{\mathrm{s}}^2\frac{\partial}{\partial t}\int_0^{h_s}\rho_7(t,x_1)dx_1 \tag{6.33}$$

Figure 6.80 shows the residual amount of CO_2 in Sample 3 and 4.

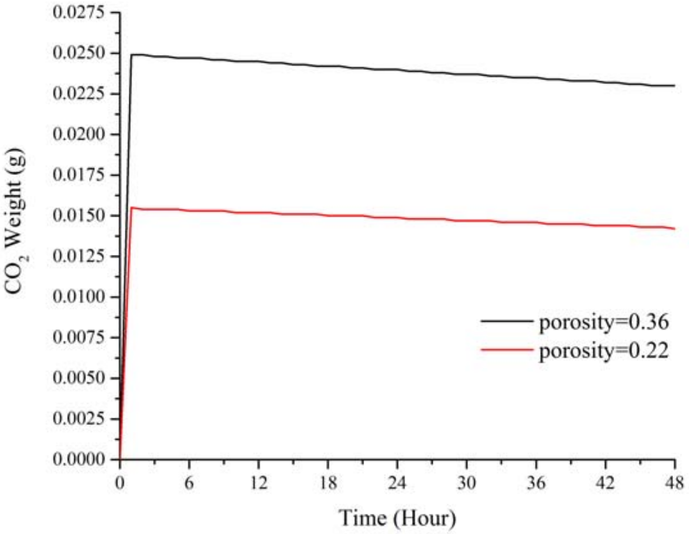

Figure 6.80: Numerical simulation results of residual amount of CO_2

As shown in Figure 6.80, the residual amount of CO_2 in Sample 3 ($Q'_{\mathrm{CO}_2}\big|_{\phi_0=0.36}$) is always larger than in Sample 4 ($Q'_{\mathrm{CO}_2}\big|_{\phi_0=0.22}$), hence, $Q'_{\mathrm{CO}_2}\big|_{\phi_0=0.36} > Q'_{\mathrm{CO}_2}\big|_{\phi_0=0.22}$.

6.3.4 CO_2 chemical reaction consumption amount

Figure 6.81 shows the amount of CO_2 consumptions for Sample 3 and 4.

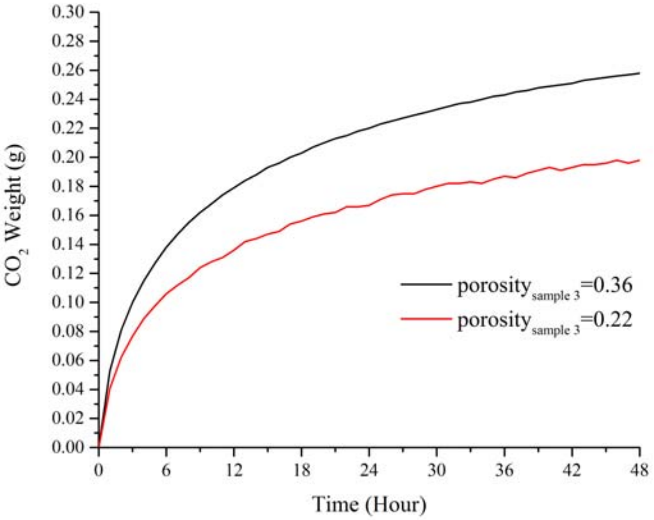

Figure 6.81: CO_2 chemical reaction consumption

As shown in Figure 6.81, the chemical reaction consumption of CO_2 in Sample 3 ($Q_{\text{consume}}\big|_{\phi_0=0.36}$) is larger than in Sample 4 ($Q_{\text{consume}}\big|_{\phi_0=0.22}$), hence, $Q_{\text{consume}}\big|_{\phi_0=0.36} > Q_{\text{consume}}\big|_{\phi_0=0.22}$.

6.3.5 Chemical Reaction Rate

The reaction rates ξ_i $(i=1,\cdots,7)$ are the decisive parameters of the concentration of reactants and resultants. The chemical reaction rate (ξ_4) represents the major carbonation procedure. Figure 6.82 shows us the distribution of ξ_4 variation on section $x_1 = 0$.

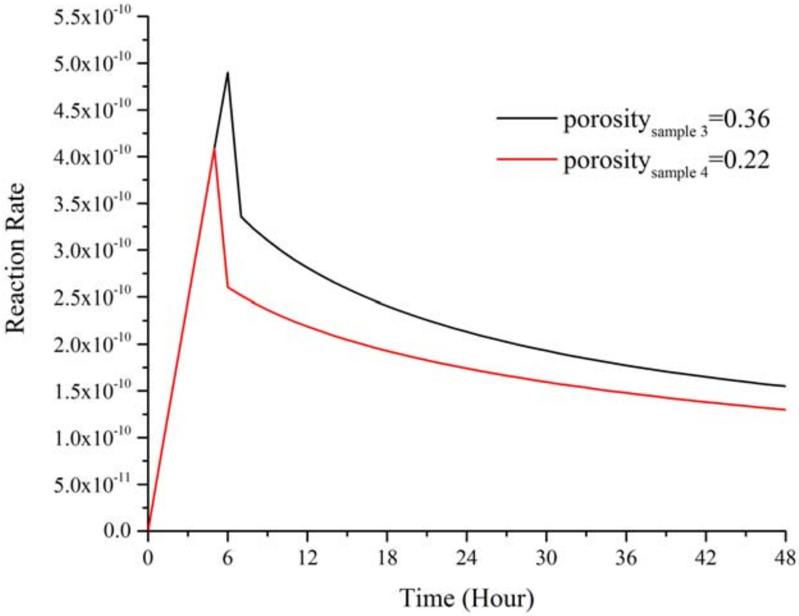

Figure 6.82: Reaction rate ($\xi_4\Big|_{\phi_0=0.22}^{\phi_0=0.36}$) distribution at section $x_1 = 0$

From the Figure 6.82, it is shown that the reaction rate ($\xi_4 \Big|_{\phi_0=0.36}^{\text{sample 3}}$) is larger than in Sample 4 ($\xi_4 \Big|_{\phi_0=0.22}^{\text{sample 4}}$) after 5 hours, which means Sample 3 generated more carbonated material.

6.3.6 Carbonated Material ($CaCO_3$) Mass Concentration

Mass concentration ρ_i $(i = 1, \cdots, 10)$ is the key parameter that determines the cement hydration process, and ρ_8 represents $CaCO_3$ mass concentration. Figure 6.83 shows the distribution of $CaCO_3$ mass concentration at section $x_1 = 0$, and Sample 3 $CaCO_3$ mass concentration ($\rho_8 \big|_{\phi_0=0.36}$) is shown to be larger than of Sample 4 mass concentration ($\rho_8 \big|_{\phi_0=0.22}$) at section $x_1 = 0$.

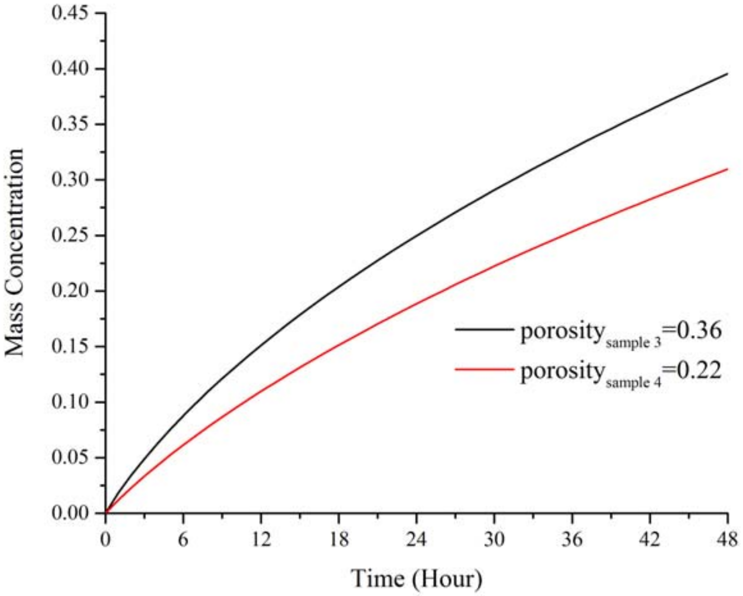

Figure 6.83: $CaCO_3$ mass concentration distribution on section $x_1 = 0$

Figure 6.84 and Figure 6.85 show the time-space distribution of CO_2 mass concentration ($\rho_7 \Big|_{\phi_0=0.22}^{\phi_0=0.36}$) for Sample 3 and Sample 4. The following can be concluded:

(1) The distributions of CO_2 mass concentration in both samples are very similar: CO_2 mass concentration decreased with time at the upper surface, but increased with time at the bottom surface.

(2) The general characteristics of mass concentration in both samples are very similar. Initially, the $\rho_7 \sim x_1$ curve has a maximum value of curvature, and then the curve gradually flattened over time.

(3) Initially, the CO_2 mass concentration for Sample 3 is $\rho_7 \Big|_{\phi_0=0.36}^{x_1=0} = 6.53\left(\mathrm{kg/m^3}\right)$ at section $x_1 = 0$, and Sample 4 CO_2 mass concentration is $\rho_7 \Big|_{\phi_0=0.22}^{x_1=0} = 4.06\left(\mathrm{kg/m^3}\right)$. The ratio of initial porosity is $0.36 : 0.22=1.64 : 1$, which is very close to the initial porosity ratio, indicating that the initial porosity has direct impact on the distribution of CO_2 mass concentration.

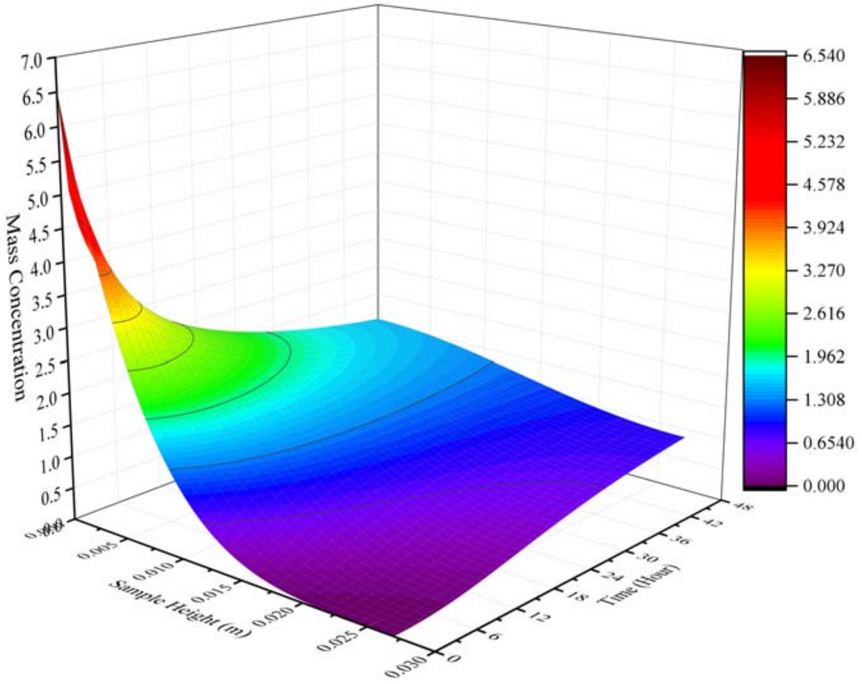

Figure 6.84: CO$_2$ mass concentration ($\rho_7 \big|_{\phi_0=0.36}$) time-space distribution

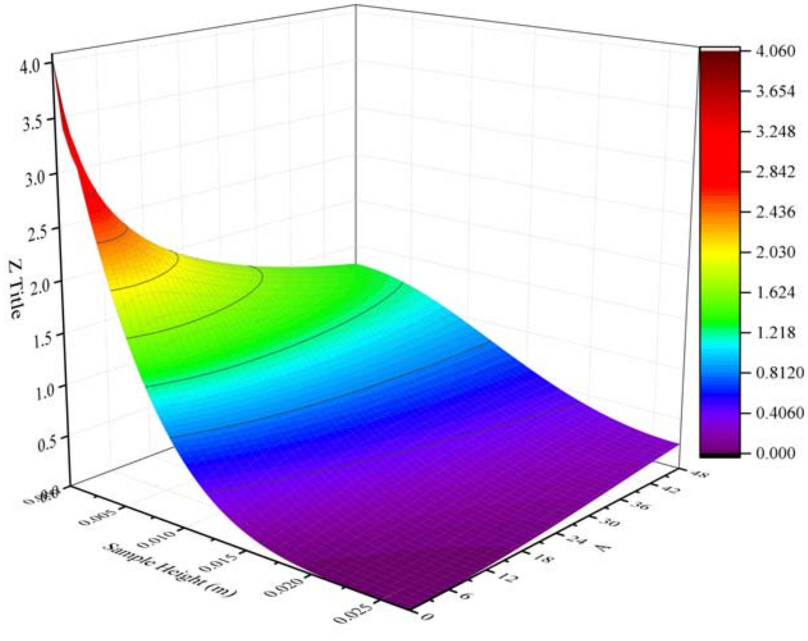

Figure 6.85: CO$_2$ mass concentration ($\rho_7 \big|_{\phi_0=0.22}$) time-space distribution

6.4 Initial Pressure Impact on CO_2 Diffusion and Chemical Reaction

The initial injected CO_2 pressure can be adjusted by using the pressure valve in the CTPRC experiment, which would allow study on how initial CO_2 pressure may impact on the diffusion and chemical reaction. The initial conditions for the Sample 5 and Sample 6 are shown in Table 6.3.

Table 6.3: Initial conditions for the Sample 5 and Sample 6

	Cement Weight	Water Weight	Aluminum Powder Weight	Sample Height	Initial Porosity	Initial CO_2 Pressure
Sample 5	30(g)	15(g)	0.5(g)	30(mm)	0.36	150(psi)
Sample 6	30(g)	15(g)	0.5(g)	30(mm)	0.36	100(psi)

In numerical simulation, the sample period was set as 1 second. The step of kinetic response of diffusion-chemical reaction (h_t) was also set as 1 second. Based on the experiment and numerical simulation results, the cavity CO_2 pressure variation, the cavity CO_2 quality variation, the CO_2 mass concentration variation, the CO_2 chemical reaction consumption and the reaction rates under different initial CO_2 injection pressure are studied.

6.4.1 Cavity CO_2 Pressure Variation

Figure 7.86 shows us the experiment results of cavity CO_2 pressure variation.

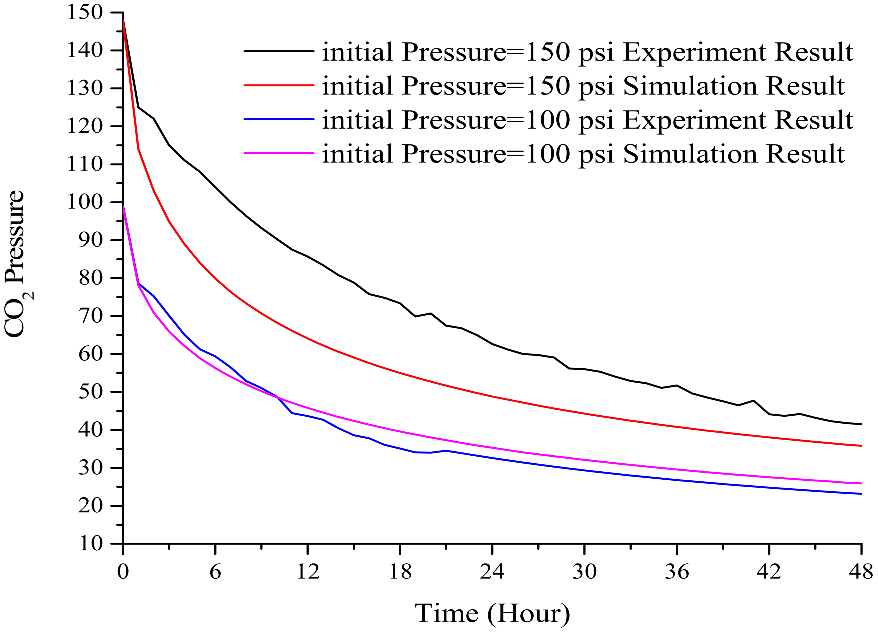

Figure 6.86: Experiment results of cavity CO_2 pressure variation

Sample 5 and Sample 6 have the same porosity, hence, the diffusion coefficient of Sample 5 should equal to Sample 6. The CO_2 diffusion rates in both samples are found to be very close. After 48 hours, the cavity CO_2 pressure in Sample 5 reached to 38psi and the cavity CO_2 pressure in Sample 6 reached to 26psi.

6.4.2 Cavity CO_2 Mass Loss

Denote the cavity CO_2 pressure as p_{chmb}^{0} and the CO_2 mass concentration as $m_{\text{CO}_2}^{\text{atm}} \frac{p_{\text{chamb}}^{0}}{p_{\text{atm}}}$, then, the CO_2 weight in cavity can be calculated as:

$$M_{\text{CO}_2}^{0} = \pi a_{\text{s}}^{2} h_{\text{chamb}} m_{\text{CO}_2}^{\text{atm}} \frac{p_{\text{chamb}}^{0}}{p_{\text{atm}}} \tag{6.34}$$

After the initial pressure drop, CO_2 pressure is p_{chamb} .and the CO_2 mass concentration is reduced to $m_{\text{CO}_2}^{\text{atm}} \frac{p_{\text{chamb}}}{p_{\text{atm}}}$.The CO_2 weight in cavum is:

$$M_{\mathrm{CO_2}}^{\mathrm{diff}} = \pi a_{\mathrm{s}}^{2} h_{\mathrm{chamb}} m_{\mathrm{CO_2}}^{\mathrm{atm}} \frac{p_{\mathrm{chamb}}^{0} - p_{\mathrm{chamb}}}{p_{\mathrm{atm}}} \tag{6.35}$$

Figure 6.87 shows the cavity CO_2 weight losses in Sample 5 and Sample 6.

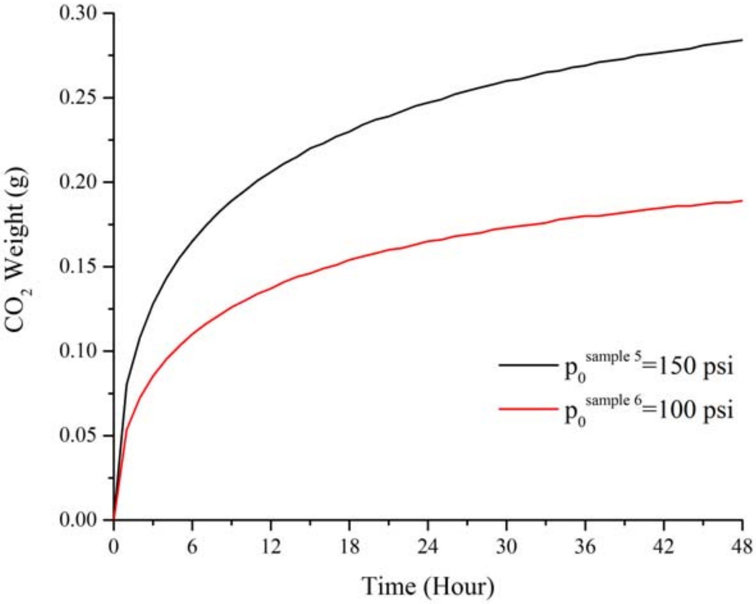

Figure 6.87: Numerical simulation results of cavity CO_2 weight loss

As shown in Figure 6.87, the initial porosities have limited influence on cavity CO_2 variation. At $t = 1hr$, the cavity CO_2 consumptions are $M_{\mathrm{CO_2}}^{\mathrm{diff}}\Big|_{\mathrm{t=1h}}^{p_0=150\mathrm{psi}} = 80.3(\mathrm{mg})$ and $M_{\mathrm{CO_2}}^{\mathrm{diff}}\Big|_{\mathrm{t=1h}}^{p_0=100\mathrm{psi}} = 53.6(\mathrm{mg})$. The ratio of those two values is $\mathrm{ratio}_1 = M_{\mathrm{CO_2}}^{\mathrm{diff}}\Big|_{\mathrm{t=1h}}^{p_0=150\mathrm{psi}} : M_{\mathrm{CO_2}}^{\mathrm{diff}}\Big|_{\mathrm{t=1h}}^{p_0=100\mathrm{psi}} = 1.49:1$. At $t = 48hr$, the cavity CO_2 consumptions are $M_{\mathrm{CO_2}}^{\mathrm{diff}}\Big|_{\mathrm{t=48h}}^{p_0=150\mathrm{psi}} = 284(\mathrm{mg})$ and $M_{\mathrm{CO_2}}^{\mathrm{diff}}\Big|_{\mathrm{t=48h}}^{p_0=100\mathrm{psi}} = 189(\mathrm{mg})$. The ratio of those two values is $\mathrm{ratio}_2 = M_{\mathrm{CO_2}}^{\mathrm{diff}}\Big|_{\mathrm{t=48h}}^{p_0=150\mathrm{psi}} : M_{\mathrm{CO_2}}^{\mathrm{diff}}\Big|_{\mathrm{t=48h}}^{p_0=100\mathrm{psi}} = 1.50:1$. Comparing ratio_1 and ratio_2, we notice that there is little difference between them, which means the impact caused by initial pressure is limited.

6.4.3 Residual Amount of CO_2 in Sample

The residual amount of CO_2 can be calculated by the following equation:

$$Q'_{\mathrm{CO_2}} = \pi a_{\mathrm{s}}^2 \frac{\partial}{\partial t}\int_0^{h_s} \rho_7(t,x_1)dx_1 \tag{6.36}$$

Figure 6.88 shows the residual CO_2 in Sample 5 and Sample 6.

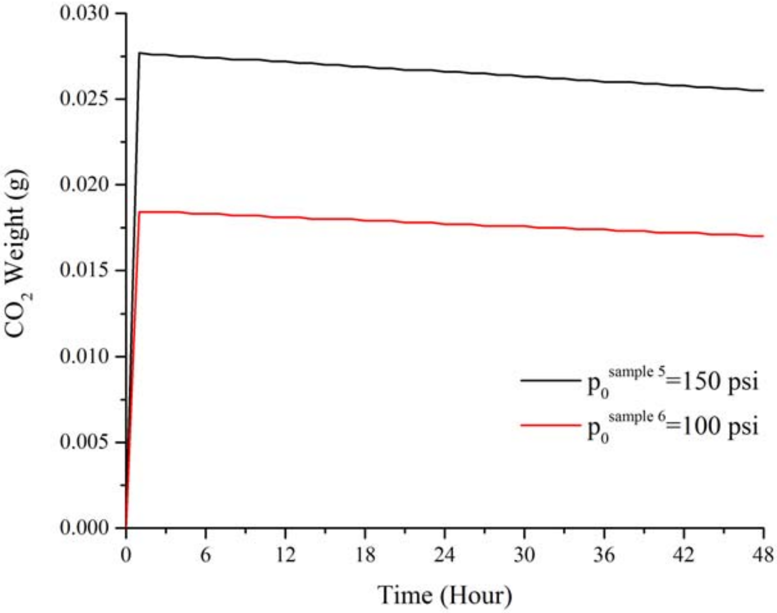

Figure 6.88: Numerical simulation results of residual amount of CO_2

As shown in Figure 6.88, the residual amount of CO_2 in Sample 5 ($Q'_{\mathrm{CO_2}}\big|_{p_0=150\mathrm{psi}}$) is always larger than in Sample 6 ($Q'_{\mathrm{CO_2}}\big|_{p_0=100\mathrm{psi}}$), and $Q'_{\mathrm{CO_2}}\big|_{p_0=150\mathrm{psi}} > Q'_{\mathrm{CO_2}}\big|_{p_0=100\mathrm{psi}}$.

6.4.4 CO_2 chemical reaction consumption amount

Figure 6.89 shows the amount of CO_2 consumption by chemical reaction.

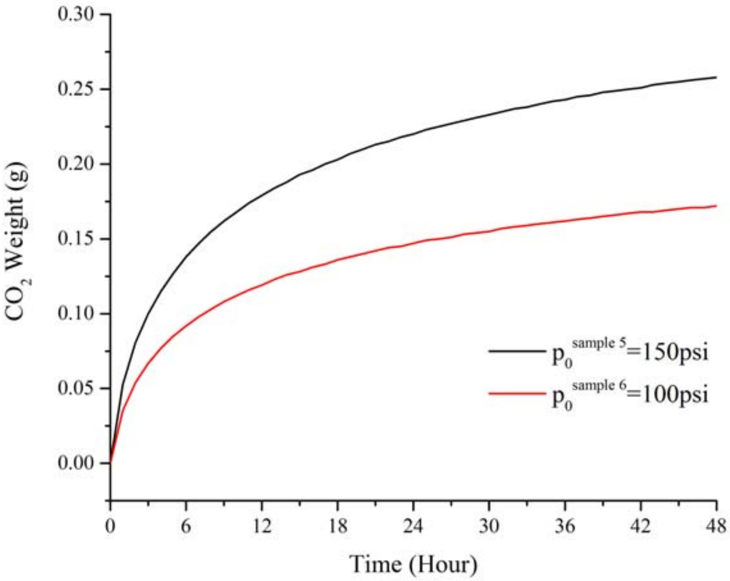

Figure 6.89: CO$_2$ chemical reaction consumption

As shown in Figure 6.89, the chemical reaction consumption of CO$_2$ in Sample 5 ($Q_{\text{consume}}\big|_{p_0=150\text{psi}}$) is always larger than in Sample 6 ($Q_{\text{consume}}\big|_{p_0=100\text{psi}}$), and $Q_{\text{consume}}\big|_{p_0=150\text{psi}} > Q_{\text{consume}}\big|_{p_0=100\text{psi}}$.

6.4.5 Chemical Reaction Rate

The chemical reaction rate (ξ_4) represents the major carbonation process. Figure 6.90 shows the distribution of ξ_4 variation at section $x_1 = 0$.

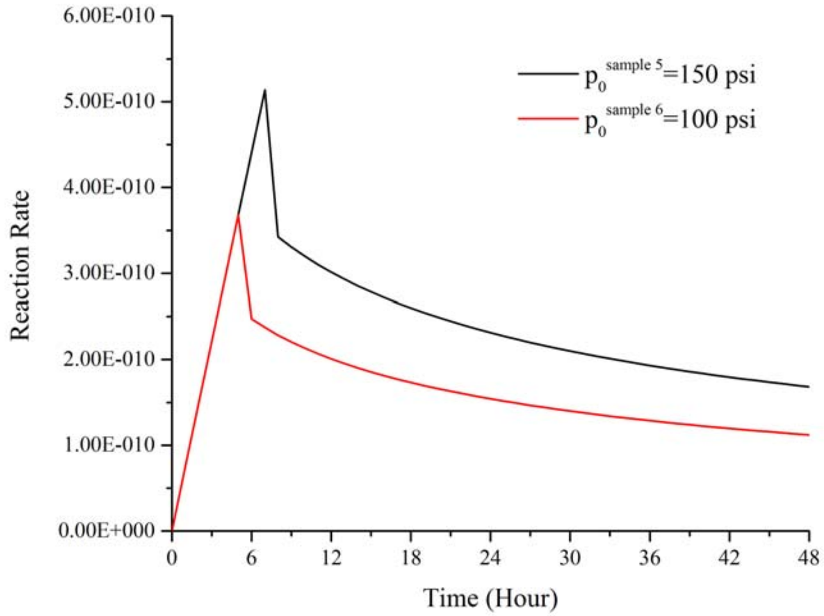

Figure 6.90: Reaction rate ($\xi_4 \Big|_{p_0=100\text{psi}}^{p_0=150\text{psi}}$) distribution of on section $x_1 = 0$

From the above figure, the reaction rate ($\xi_4 \Big|_{p_0=150\text{psi}}^{\text{sample 5}}$) of Sample 5 is larger than in Sample 6 ($\xi_4 \Big|_{p_0=100\text{psi}}^{\text{sample 6}}$) after 5 hours, which means Sample 5 generated more carbonated material than Sample 6.

6.4.6 Carbonated Material ($CaCO_3$) Mass Concentration

ρ_8 represents the $CaCO_3$ mass concentration. Figure 6.91 shows the distribution of $CaCO_3$ mass concentration ($\rho_8 \Big|_{p_0=150\text{psi}}^{p_0=100\text{psi}}$) at section $x_1 = 0$, which Sample 5 $CaCO_3$ mass concentration ($\rho_8 \Big|_{p_0=150\text{psi}}$) is always larger than in Sample 6 ($\rho_8 \Big|_{p_0=100\text{psi}}$) at section $x_1 = 0$.

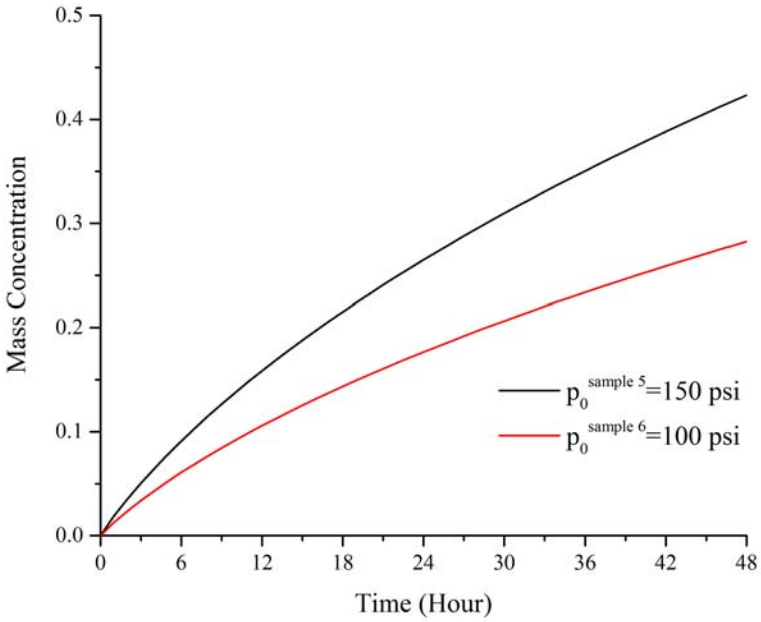

Figure 6.91: $CaCO_3$ mass concentration ($\rho_8 \Big|_{p_0=150\text{psi}}^{p_0=100\text{psi}}$) time-space distribution on section $x_1 = 0$

Figure 6.92 and Figure 6.93 show the time-space distribution of CO_2 mass concentration ($\rho_7 \Big|_{p_0=100\text{psi}}^{p_0=150\text{psi}}$) for Sample 5 and Sample 6, and conclude that:

(1) The distributions of CO_2 mass concentration for both samples are very similar. CO_2 mass concentrations decreased with time on the upper surface. And its value kept increasing with time on the lower surface.

(2) The general characteristics of mass concentrations in both samples are very similar. Initially, $\rho_7 \sim x_1$ curve has the maximum value of curvature, which gradually changed to flat.

(3) Initially, the CO_2 mass concentration of Sample 5 is $\rho_7 \Big|_{\phi_0=0.36}^{x_1=0} = 6.53\left(\text{kg/m}^3\right)$ at section $x_1 = 0$, Sample 6 CO_2 mass concentration is $\rho_7 \Big|_{\phi_0=0.22}^{x_1=0} = 4.36\left(\text{kg/m}^3\right)$ at section

$x_1 = 0$. The ratio of initial porosity is $0.36 : 0.36 = 1 : 1$. The CO_2 mass concentration ratio is slightly different to the initial porosity ratio, indicating that the initial porosity has no impact on the distribution of CO_2 mass concentration. The only difference is caused by the initial CO_2 pressure.

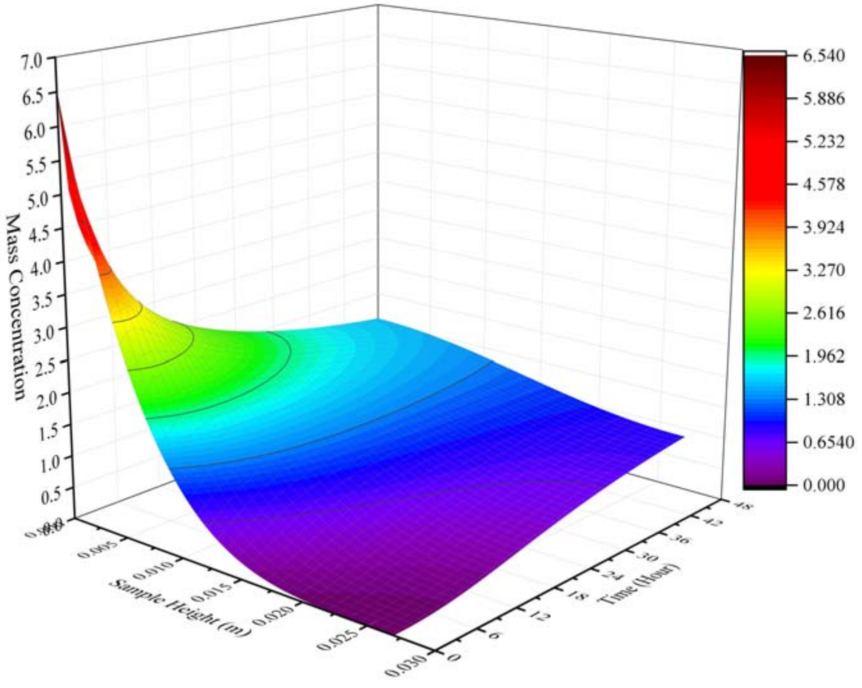

Figure 6.92: CO_2 mass concentration ($\rho_7 \Big|_{p_0=150\text{psi}}$) time-space distribution

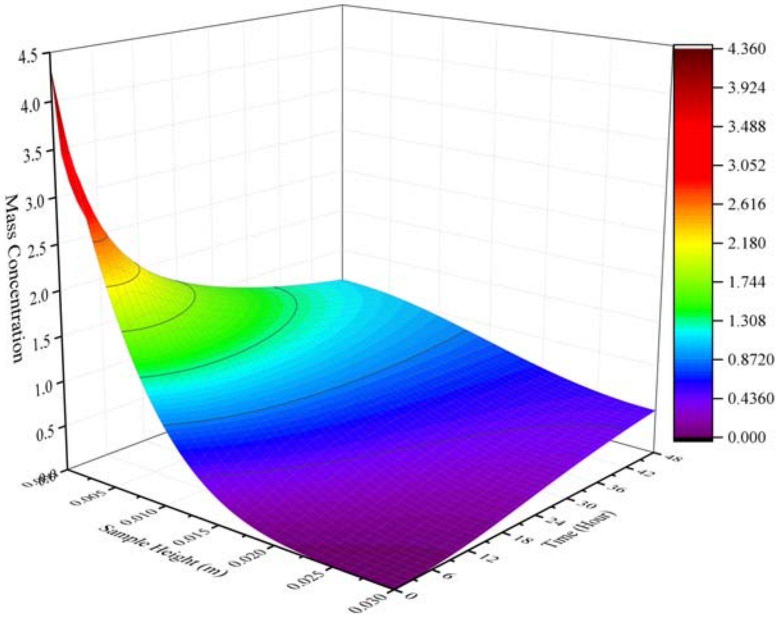

Figure 6.93: CO_2 mass concentration ($\rho_7 \big|_{p_0 = 100\text{psi}}$) time-space distribution

6.5 Summary

In this chapter, we analyzed the effect of different initial conditions on materials(C_3S , H_2O , $3CaO \cdot 2SiO_2 \cdot 3H_2O$, $Ca(OH)_2$, C_2S , CaO , CO_2 , $CaCO_3$, $3CaCO_3 \cdot 2SiO_2 \cdot 3H_2O$ and $SiO_2 \cdot \gamma H_2O$) including the mass concentration, the chemical reaction rate and the cavum CO_2 pressure. The emphases are placed on the initial water binder ratio and porosity condition (Section 6.2 and Section 6.3).

The conclusions from section 6.2 are:

(1) After 48 hours, with the same initial CO_2 injection pressure, Sample 1 (15g water) got more cavum CO_2 consumption than Sample 2 (10g water).

(2) Sample 1 has more residual CO_2 placed than Sample 2.

(3) Sample 1 has more chemical CO_2 consumption than Sample 2.

(4) The overall characteristics of CO_2 mass concentration distributions are very similar for both Samples. CO_2 mass concentration decreased over time on the top surface, but increased at end surface. CO_2 mass concentration first increased and then decreased at midsection.

(5) The different water-binder ratio has very limited effect on CO_2 mass concentration during the simulation. However, it has great impact on other chemical components mass concentration and chemical reaction rate.

The conclusions from section 6.3 are:

(1) In Sample 1 ($\phi_{\text{sample 1}} = 0.36$), the cavum CO_2 pressure dropped from 150 psi to 36 psi, and the cavum gas pressure for Sample 2 ($\phi_{\text{sample 1}} = 0.22$) decreased from 150 psi to 50 psi- indicating that the larger porosity sample has more cavum CO_2 consumption than the small porosity Sample.

(2) The larger porosity sample has more residual CO_2 than the smaller porosity Sample.

(3) The larger porosity sample has more chemical CO_2 consumption than the smaller porosity Sample.

(4) The chemical reaction rates for the larger porosity sample are bigger than the smaller porosity sample.

(5) CO_2 mass concentration in all sections would increase initially and then decrease, except the top surface, during the entire process. CO_2 mass concentration value in Sample 3 is always larger than in Sample 4 at any time on any section. However, CO_2 mass concentration difference between those two samples decreases with time increasing.

CHAPTER 7: DISCUSSION AND CONCLUSION

7.1 Discussion

The bulk of this work is on the CTPRC test and the modeling of the idealized process involved in the tests. There needs to be a measure of how accurate the numerical model actually represents the real process. Thus, this section presents an elaborated discussion on the comparisons between experimental and numerical simulation results.

Figures 7.1, 7.2 and 7.3 present the combined sorption pressure results for Sample 1 and 2, 3 and 4, 5 and 6, respectively. Unlike the rough experimental results, the numerical sorption pressure curves are smooth curves indicating idealized assumptions made in the models.

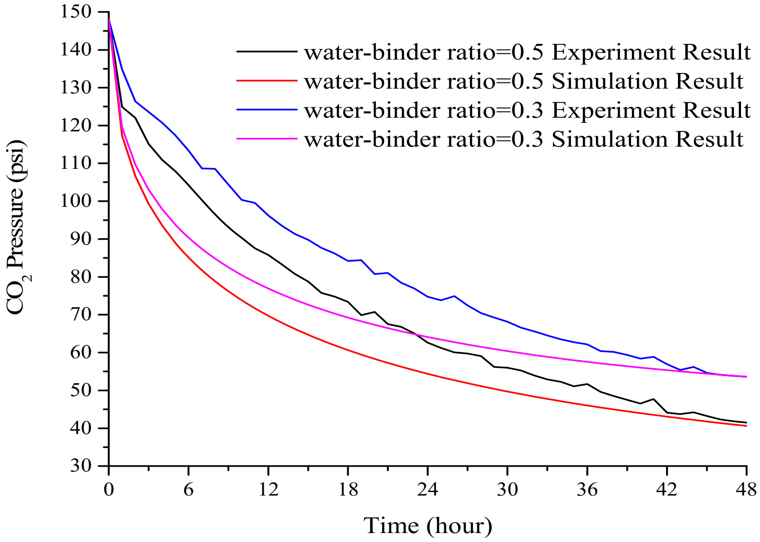

Figure 7.1: Experimental and numerical results of CO_2 cavum pressure variation in Sample 1 and Sample 2

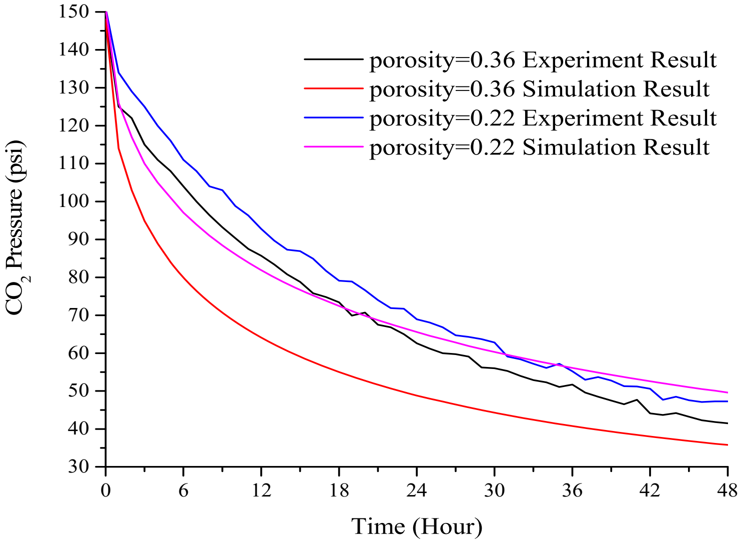

Figure 7.2: Experimental and numerical results of cavity CO_2 pressure variation in Sample 3 and Sample 4

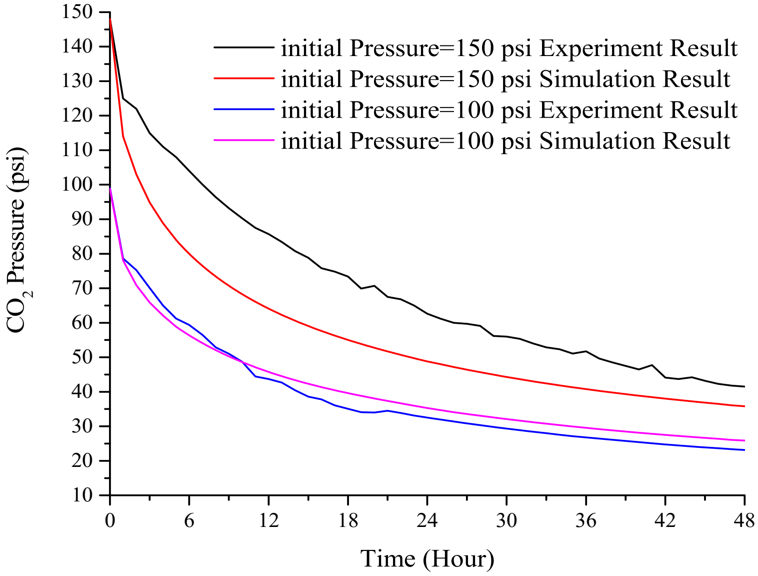

Figure 7.3: Experimental and numerical results of cavity CO_2 pressure variation in Sample 5 and Sample 6

To provide a quantitative measure to account for the differences between the experimental and numerical results, we introduce a simple, two-parameters indexing technique:

(1) The sorption process index (SPI) is defined as the maximum point to point difference between the experimental and numerical results.

$$\text{SPI=Max}\left(P_{\exp}(t)-P_{num}(t)\right) \tag{7.1}$$

where t is the particular time that the two curves have the largest difference.

(2) The sorption quantity index (SQI) is defined as the difference between the final sorption pressure from the experiment and the final sorption pressure from the numerical simulation.

$$\text{SQI=}P_{\exp}(t_n)-P_{num}(t_n) \tag{7.2}$$

where t_n is the last reading of the measured data and $P(t_n)$ represents the final sorption amounts.

SPI measures the largest numeric difference between the experimental and numerical CO_2 pressure curves and is dependent on the curve shapes and the maximum pressure difference. SQI is the final sorption quantity and is the main parameter to determine the sorption potential.

SPI and SQI combined can help determine the differences between the experimental results and the simulation results. Any improvement or modification to the test procedure or the numerical modeling scheme should result in changes to SPI and SQI. And a limit state may be introduced to define the accuracy in representation for the numerical modeling.

For the study of the three critical parameters (Chapter 6), the differences between experiment and numerical results are presented in Figure 7.4, 7.5, 7.6, 7.7, 7.8 and 7.9 for Sample 1, 2, 3, 4, 5 and 6, respectively. A summary of SPI and SQI values derived from these figures are presented in Table 7.1, which shows that the maximum SPI is 24.37 psi

(Sample 3) and maximum SQI is 5.74 psi (also Sample 3). This means that the deviation between experimental numerical results is largest for Sample 3.

In general, the SPI and SQI values are reasonably small when compared to the initial quantity of 150 psi, indicating that the numerical modeling is reasonably accurate for current study. However, the curves shown in Figure 7.1 to 7.3 indicate that these curves do not necessarily matching. The differences may be due to the fact that the porosity distributions in actual specimens are not uniformly distributed and may not be connected. Another reason for the difference may be because the numerical model did not account for all the chemical reactions involved in the carbonation process. Hence, the numerical model may need to be modified to account for the porosity distribution effect and a further consideration of the key chemical reactions may be necessary.

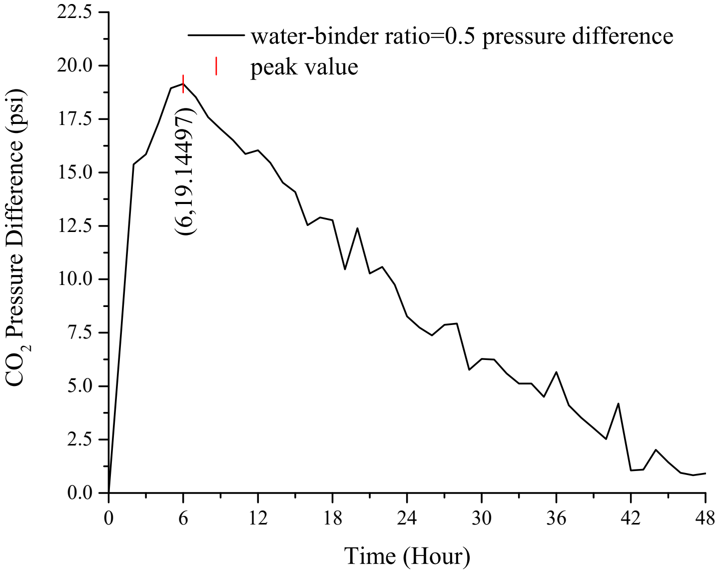

Figure 7.4: Pressure difference (water-binder ratio=0.5) between experiment and simulation result

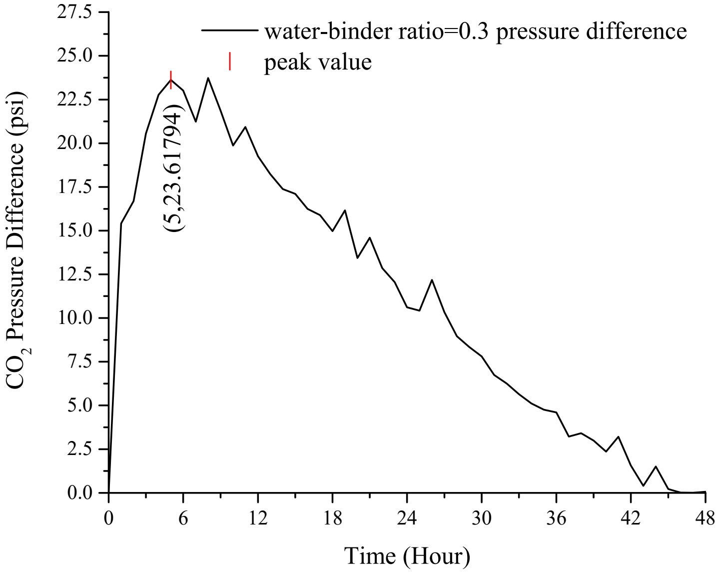

Figure 7.5: Pressure difference (water-binder ratio=0.3) between experiment and simulation result

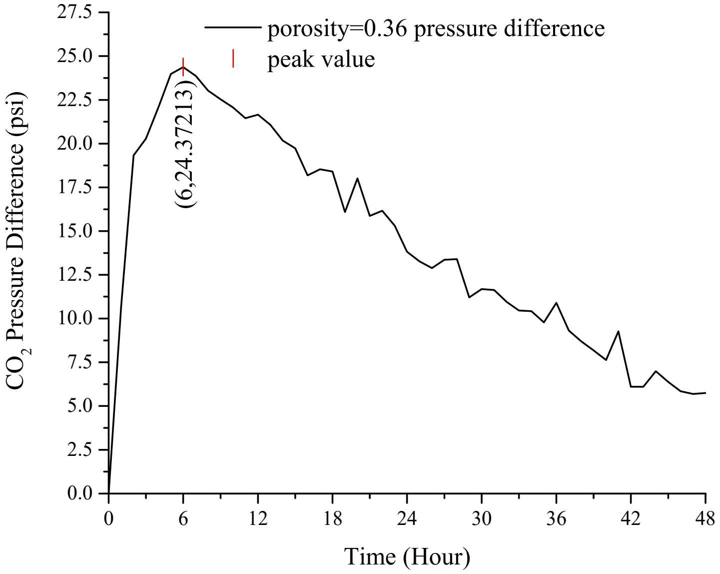

Figure 7.6: Pressure difference (porosity=0.36) between experiment and simulation result

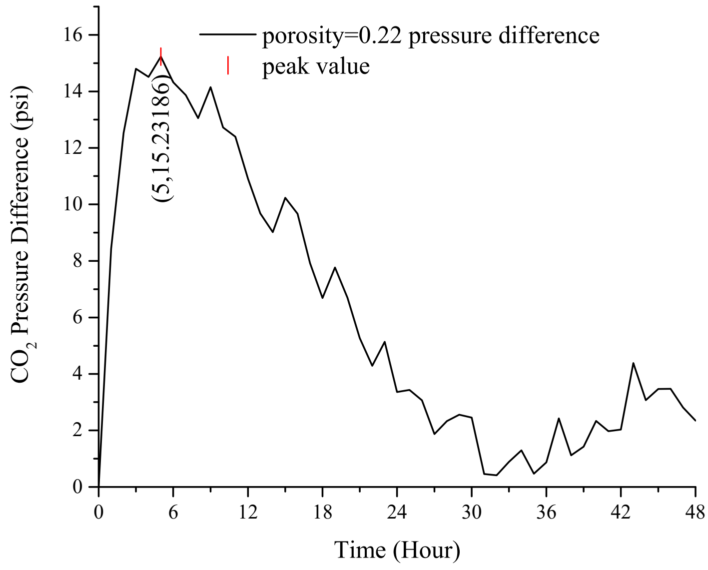

Figure 7.7: Pressure difference (porosity=0.22) between experiment and simulation result

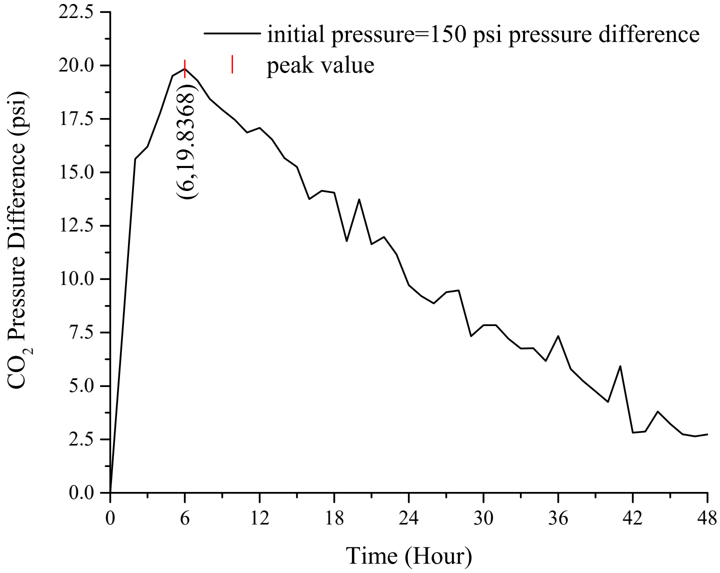

Figure 7.8: Pressure difference (initial pressure 150 psi) between experiment and simulation result

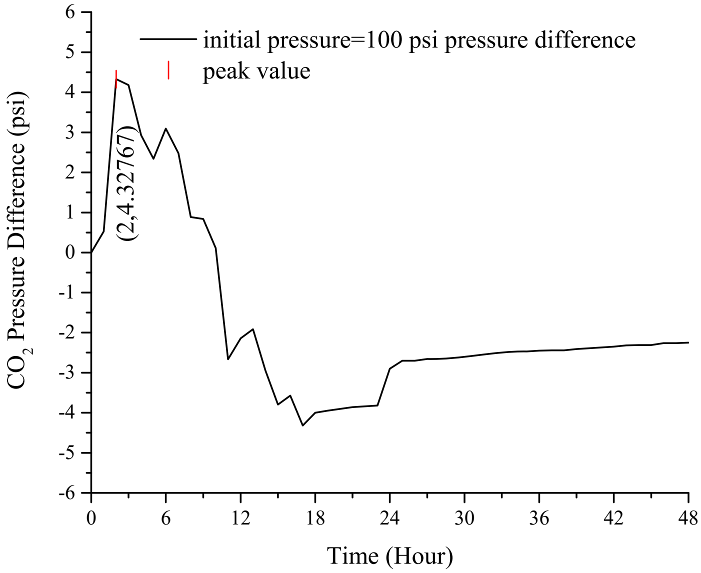

Figure 7.9: Pressure difference (initial pressure 100 psi) between experiment and simulation result

Table 7.1 SPI and SQI index

	Sorption process index (psi)	Sorption quantity index (psi)
Sample 1	19.14	0.91
Sample 2	23.73	0.07
Sample 3	24.37	5.74
Sample 4	15.23	2.35
Sample 5	19.84	2.73
Sample 6	4.33	2.25

7.2 Conclusion

Emission control and storage of carbon dioxide (CO_2) from fossil fuel combustion is an emerging and frontier research area to counter likely global climate changes. Although the carbon dioxide separation techniques are quite maturity, there is still an issue of excessive carbon dioxide being emitted into the atmosphere. Carbon sequestration as mineral carbonates is an attractive and novel method with the potential to be implemented with acceptable economics to dispose carbon dioxide in large scale. This study suggests innovative research in using building materials (cement and concrete) for CO_2 storage and presents two new tools for the development of this technology.

The CTPRC testing technique allows mineral sequestration and assumed to embed CO_2 within a highly porous, calcium rich material, which would then allow high diffusion and maximize the chemical sorption. A numerical model is developed to help understand the sorption process. This dissertation summarized the hazards of carbon dioxide to the environment and society, the source of carbon dioxide in atmosphere and the current control technologies in the world. Laboratory experiments were conducted to demonstrate the proposed CTPRC testing technique and the sorption potential. The theory behind the mineral carbonation mechanism is investigated including the complicated dynamic behavior about porous material deformation, carbon dioxide gas diffusion and chemical reactions. The coupled system involved in the laboratory study is then simulated with the multi-physical model. The main contributions and results are as follows:

(1) An experimental technique, CTPRC (Constant Temperature Pressurized Reaction Chamber) is developed to quantify the carbon dioxide mineral carbonation and a series of six experiments were reported to determine critical factors involved in the sorption process. These factors influenced the rate of carbonation reaction, such as initial gas pressure, initial sample porosity and initial sample water-binder ratio.

(2) The hydration and carbonation reactions involved in the cement based porous material were reasonably simplified in the numerical simulation and each component quantity changes were analyzed. According to mass conservation involved in the process of chemical reaction and diffusion, the reaction rate equations were established and were

summarized into seven reaction rates. Ten kinds of component concentration field and CO_2 gas diffusion velocity field with different water-binder ratios, initial CO_2 pressure and initial sample porosities were simulated by the numerical modeling. The impact of the three factors on the component concentration field was investigated.

(3) A two parameter index technique is proposed to quantify the differences between the experiment (actual sorption) and the numerical simulation (idealized sorption). The SPI and SQI for the six experiments presented are reasonably close, indicating that the theoretical model can be used to simulate the actual sorption process within the CTPRC system.

(4) The results involving the carbon dioxide sorption process using both physical and chemical sorption of the porous cement material conclusively indicate a hopeful sequester of a maximum 50% of the injected CO_2 within initial 48 hours.

7.3 Proposed Future Studies

The results presented in Chapter 5, 6 and 7 of this dissertation sustained a confidence that CTPRC tests can encourage CO_2 sorption within the porous, cement based material and the multi-physics model can be used to rationalize the sorption processes.

However, there are still rooms to improve on the numerical modeling and the experimental techniques. The following are suggested potential future tasks to prolong current research that can lead to the development of functional carbon storage building materials that can be used to combat excessive CO_2 emissions:

(1) CTPRC test with pH and temperature measurements;

(2) Numerical modeling that can include inhomogeneous porosity distributions.

(3) Extend current study to beyond 48 hours and include material phase transformation.

The ultimate goal of current study is to be able to establish a functional sorption material that can be "engineered" to optimize its applications to civil structure construction and mine void and other geotechnical systems stabilization, while at the same time, encourage CO_2 removal from our living environment.

REFERENCES

Bachu, S. (2000). Sequestration of CO_2 in geological media: criteria and approach for site selection in response to climate change. *Energy Conversion and Management, 41*(9), 953-970.

Bamford, C., & Tipper, C. F. H. (1973). *Chemical kinetics*: Elsevier Scientific.

Benson, S., Bennaceur, K., Cook, P., Davison, J., Coninck, H. d., Farhat, K., *et al.* (2012). Carbon capture and storage.

Benson, S. M., & Cole, D. R. (2008). CO_2 sequestration in deep sedimentary formations. *Elements, 4*(5), 325-331.

Biot, M. (1972). Theory of finite deformations of porous solids. *Indiana University Mathematics Journal, 21*(7), 597-620.

Blunt, M., Fayers, F. J., & Orr, F. M. (1993). Carbon dioxide in enhanced oil recovery. *Energy Conversion and Management, 34*(9), 1197-1204.

Bonen, D., & Sarkar, S. L. (1995). The effects of simulated environmental attack on immobilization of heavy metals doped in cement-based materials. *Journal of Hazardous Materials, 40*(3), 321-335.

Boresi, A. P., Schmidt, R. J., & Sidebottom, O. M. (1993). *Advanced mechanics of materials* (Vol. 6): Wiley New York.

Bukowski, J., & Berger, R. L. (1979). Reactivity and strength development of CO_2 activated non-hydraulic calcium silicates. *Cement and Concrete Research, 9*(1), 57-68.

Bye, G. C. (1999). *Portland cement: composition, production and properties*: Thomas Telford.

Carcione, J. M., Picotti, S., Gei, D., & Rossi, G. (2006). Physics and seismic modeling for monitoring CO_2 storage. *Pure and Applied Geophysics, 163*(1), 175-207.

Chen, Q., Tyrer, M., Hills, C. D., Yang, X., & Carey, P. (2009). Immobilisation of heavy metal in cement-based solidification/stabilisation: a review. *Waste Management, 29*(1), 390-403.

Connors, K. A. (1990). *Chemical kinetics: the study of reaction rates in solution*: John Wiley & Sons.

Cowin, S. C., & Nunziato, J. W. (1983). Linear elastic materials with voids. *Journal of Elasticity, 13*(2), 125-147.

Cussler, E. L. (2009). *Diffusion: mass transfer in fluid systems*: Cambridge university press.

Dagan, G. (1984). Solute transport in heterogeneous porous formations. *Journal of Fluid Mechanics, 145*, 151-177.

Damen, K., Faaij, A., & Turkenburg, W. (2006). Health, safety and environmental risks of underground CO_2 storage–overview of mechanisms and current knowledge. *Climatic Change, 74*(1-3), 289-318.

Day, S., Fry, R., & Sakurovs, R. (2012). Swelling of coal in carbon dioxide, methane and their mixtures. *International Journal of Coal Geology, 93*, 40-48.

Evans III, R., Watson, G., & Mason, E. (1961). Gaseous diffusion in porous media at uniform pressure. *The journal of chemical physics, 35*(6), 2076-2083.

Finley, R. J., Greenberg, S. E., Frailey, S. M., Krapac, I. G., Leetaru, H. E., & Marsteller, S. (2011). The path to a successful one-million tonne demonstration of geological sequestration: Characterization, cooperation, and collaboration. *Energy Procedia, 4*, 4770-4776.

Fischedick, M. (2007). *CO_2-capture and geological storage as a climate policy option: Technologies, concepts, perspectives*: Wuppertal Spezial, Wuppertal Institut für Klima, Umwelt und Energie.

Fitzgerald, J., Pan, Z., Sudibandriyo, M., Robinson Jr, R., Gasem, K., & Reeves, S. (2005). Adsorption of methane, nitrogen, carbon dioxide and their mixtures on wet Tiffany coal. *Fuel, 84*(18), 2351-2363.

Fujiwara, D., & Morimoto, H. (1977). An L_r-theorem of the Helmholtz decomposition of vector fields.

Gale, J., Christensen, N. P., Cutler, A., & Torp, T. A. (2001). Demonstrating the potential for geological storage of CO_2: the Sleipner and GESTCO projects. *Environmental Geosciences, 8*(3), 160-165.

GaO, X., Sun, G., Zhang, Y., & Sun, W. (2012). Relationship between porosity and chloride diffusivity in cement-based composite materials. *Journal of Chongqing University, 11*, 010.

Gasem, K., Sudibandriyo, M., Fitzgerald, J., Pan, Z., & Robinson Jr, R. (2002). *Measurement and modelling of gas adsorption on selected coals.* Paper presented at the Proceesings of the AICHE Spring National Meeting, New Orleans, Lousiana.

Gensterblum, Y., Van Hemert, P., Billemont, P., Battistutta, E., Busch, A., Krooss, *et al.* (2010). European inter-laboratory comparison of high pressure CO_2 sorption isotherms II: natural coals. *International Journal of Coal Geology, 84*(2), 115-

124.

Gillespie, D. T. (2007). Stochastic simulation of chemical kinetics. *Annu. Rev. Phys. Chem., 58*, 35-55.

Gozalpour, F., Ren, S., & Tohidi, B. (2005). CO_2 EOR and storage in oil reservoir. *Oil & gas science and technology, 60*(3), 537-546.

Gunter, W. D., Bachu, S., & Benson, S. (2004). The role of hydrogeological and geochemical trapping in sedimentary basins for secure geological storage of carbon dioxide. *Geological Society, London, Special Publications, 233*(1), 129-145.

Hills, C. (1999). Hazardous waste treatment: Patents.

Hills, C. D., & Macleod, C. L. (2001). Silicate/aluminate materials: Patents.

Huijgen, W. J. J., & Comans, R. N. J. (2003). *Carbon dioxide sequestration by mineral carbonation. Literature Review*.

James, R. (2014). X-ray Diffraction. *A with Honors Projects*, Page 115.

Jaynes, D., & Rogowski, A. (1983). Applicability of Fick's law to gas diffusion. *Soil Science Society of America Journal, 47*(3), 425-430.

Johnson, J. W., Nitao, J. J., & Knauss, K. G. (2004). Reactive transport modeling of CO_2 storage in saline aquifers to elucidate fundamental processes, trapping mechanisms and sequestration partitioning. *Geological storage of carbon dioxide, 233*, 107-128.

Juanes, R., Spiteri, E., Orr, F., & Blunt, M. (2006). Impact of relative permeability hysteresis on geological CO_2 storage. *Water Resources Research, 42*(12).

Karayannis, V., Charalampides, G., & Lakioti, E. (2014). Socio-economic Aspects of CCS Technologies. *Procedia Economics and Finance, 14*, 295-302.

Kärger, J., & Valiullin, R. (2011). Diffusion in porous media. *eMagRes*.

Keller, J. U., & Staudt, R. (2005). *Gas adsorption equilibria: experimental methods and adsorptive isotherms*: Springer Science & Business Media.

Kondrat'Ev, V. N. (2013). *Chemical kinetics of gas reactions*: Elsevier.

Kovscek, A. (2002). Screening criteria for CO_2 storage in oil reservoirs. *Petroleum Science and Technology, 20*(7-8), 841-866.

Kovscek, A., & Cakici, M. (2005). Geologic storage of carbon dioxide and enhanced oil recovery. II. Cooptimization of storage and recovery. *Energy Conversion and Management, 46*(11), 1941-1956.

Krevor, S., Pini, R., Li, B., & Benson, S. M. (2011). Capillary heterogeneity trapping of CO_2 in a sandstone rock at reservoir conditions. *Geophysical Research Letters, 38*(15).

Krooss, B., Van Bergen, F., Gensterblum, Y., Siemons, N., Pagnier, H., *et al*. (2002). High-pressure methane and carbon dioxide adsorption on dry and moisture-equilibrated Pennsylvanian coals. *International Journal of Coal Geology, 51*(2), 69-92.

Kunz, O., Klimeck, R., Wagner, W., & Jaeschke, M. (2006). The GERG-2004 Wide-Range Reference Equation of State for Natural Gases and Other Mixtures. Fortschr. *Ber. VDI, VDI-Verlag, Düsseldorf.*

Lange, L. C. (1997). *Carbonation of cement: solidified hazardous waste.* Queen Mary, University of London.

Levenspiel, O. (1999). Chemical reaction engineering. *Industrial & engineering chemistry research, 38*(11), 4140-4143.

Li, Q., & Liu, G. (1999). The influence of porosity of catalyst pellet on the gas effective diffusion. *NATURAL GAS CHEMICAL INDUSTRY, 24*(2), 16-20.

Loitsyanskiy, L. G., & Nunn, R. H. (1995). *Mechanics of liquids and gases*: Begell House New York.

Macias, A., Kindness, A., & Glasser, F. (1997). Impact of carbon dioxide on the immobilization potential of cemented wastes: chromium. *Cement and Concrete Research, 27*(2), 215-225.

MacMinn, C., Szulczewski, M., & Juanes, R. (2011). CO_2 migration in saline aquifers. Part 2. Capillary and solubility trapping. *Journal of Fluid Mechanics, 688*, 321-351.

McCarty, R., & Arp, V. (1990). A new wide range equation of state for helium. *Adv. Cryog. Eng, 35*, 1465-1475.

Mead, A., Hull, T., Dawson, J., Laskaris, G., & Dawson, C. (2013). Carbon capture and storage. *National Grid.*

Metz, B., Davidson, O., de Coninck, H., Loos, M., & Meyer, L. (2005). Carbon dioxide capture and storage. *UNT Digital Libiary*, NY, USA.

Michels, A., Wouters, H., & De Boer, J. (1936). Isotherms of nitrogen between 200 and 3000 atm. and 0° and 150°. *Physica, 3*(7), 585-589.

Millington, R. (1959). Gas diffusion in porous media. *Science, 130*(3367), 100-102.

Ming, Z., Shaojie, O., Yingjie, Z., & Hui, S. (2014). CCS technology development in

China: Status, problems and countermeasures—Based on SWOT analysis. *Renewable and Sustainable Energy Reviews, 39*, 604-616.

Nataly Echevarria Huaman, R., & Xiu Jun, T. (2014). Energy related CO_2 emissions and the progress on CCS projects: A review. *Renewable and Sustainable Energy Reviews, 31*, 368-385.

Nield, D. A., & Bejan, A. (2013). *Mechanics of Fluid Flow Through a Porous Medium*: Springer.

Nodzeński, A. (1998). Sorption and desorption of gases (CH_4, CO_2) on hard coal and active carbon at elevated pressures. *Fuel, 77*(11), 1243-1246.

Nur, A., & Byerlee, J. D. (1971). An exact effective stress law for elastic deformation of rock with fluids. *Journal of Geophysical Research, 76*(26), 6414-6419.

O'Connor, W. K., Dahlin, D. C., Rush, G., Dahlin, C. L., & Collins, W. K. (2002). Carbon dioxide sequestration by direct mineral carbonation: process mineralogy of feed and products. *Minerals & metallurgical processing, 19*(DOE/ARC-2002-006).

Oelkers, E. H., Gislason, S. R., & Matter, J. (2008). Mineral carbonation of CO_2. *Elements, 4*(5), 333-337.

Okwen, R. T., Stewart, M. T., & Cunningham, J. A. (2010). Analytical solution for estimating storage efficiency of geologic sequestration of CO_2. *International Journal of Greenhouse Gas Control, 4*(1), 102-107.

Ozdemir, E., Morsi, B. I., & Schroeder, K. (2003). Importance of volume effects to adsorption isotherms of carbon dioxide on coals. *Langmuir, 19*(23), 9764-9773.

Peng, D.Y., & Robinson, D. B. (1976). A new two-constant equation of state. *Industrial & Engineering Chemistry Fundamentals, 15*(1), 59-64.

Ping, Z., Benelli, G., Jiutian, Z., Lin, G., Shujuan, W., *et al.* (2014). The Application of CCS Technology in China: Lesson from the Sino-Italy Collaboration on Coal Fired Power Plants. *Energy Procedia, 63*, 8116-8133.

Pires, J., Martins, F., Alvim-Ferraz, M., & Simões, M. (2011). Recent developments on carbon capture and storage: an overview. *Chemical Engineering Research and Design, 89*(9), 1446-1460.

Rackley, S. (2009). *Carbon capture and storage*: Gulf Professional Publishing.

Reeves, S., Gonzalez, R., Gasem, K. A., Fitzgerald, J. E., Pan, Z., *et al.* (2005). *Measurement and prediction of single-and multi-component methane, carbon dioxide and nitrogen isotherms for US coals.* Paper presented at the 2005 International Coalbed Methane Symposium, Paper.

Reeves, S. R. (2001). *Geological Sequestration of CO_2 in Deep, Unmineable Coalbeds: An Integrated Research and Commerical-Scale Field Demonstration Project.* Paper presented at the SPE annual technical conference and exhibition.

Reeves, S. R. (2003). *Assessment of CO_2 sequestration and ECBM potential of US coalbeds*: United States. Department of Energy.

Romanov, V., Soong, Y., & Schroeder, K. (2006). Volumetric effects in coal sorption capacity measurements. *Chemical engineering & technology, 29*(3), 368-374.

Rubin, E. S. (2006). Summary of the IPCC special report on carbon dioxide capture and storage. *Proceedings of International Workshop on CO_2 Geological Storage, Japan*, 35-41

Rubin, E. S. (2008). CO_2 capture and transport. *Elements, 4*(5), 311-317.

Rutqvist, J., & Tsang, C. F. (2002). A study of caprock hydromechanical changes associated with CO_2-injection into a brine formation. *Environmental Geology, 42*(2-3), 296-305.

Saadatpoor, E., Bryant, S. L., & Sepehrnoori, K. (2010). New trapping mechanism in carbon sequestration. *Transport in Porous Media, 82*(1), 3-17.

Semenov, N. N. (1935). Chemical kinetics and chain reactions.

Setzmann, U., & Wagner, W. (1991). A new equation of state and tables of thermodynamic properties for methane covering the range from the melting line to 625 K at pressures up to 100 MPa. *Journal of Physical and Chemical Reference Data, 20*(6), 1061-1155.

Shao, Y., Mirza, M. S., & Wu, X. (2006). CO_2 sequestration using calcium-silicate concrete. *Canadian Journal of Civil Engineering, 33*(6), 776-784.

Shaw, J., & Bachu, S. (2002). Screening, evaluation, and ranking of oil reservoirs suitable for CO_2-flood EOR and carbon dioxide sequestration. *Journal of Canadian Petroleum Technology, 41*(09).

Shtepani, E. (2006). *CO_2 sequestration in depleted gas/condensate reservoirs.* Paper presented at the SPE Annual Technical Conference and Exhibition.

Siemons, N., & Busch, A. (2007). Measurement and interpretation of supercritical CO_2 sorption on various coals. *International Journal of Coal Geology, 69*(4), 229-242.

Sorochkin, M., Shchurov, A., & Safonov, I. (1975). Study of possibility of using carbon-dioxide for accelerating hardening of products made from portland-cement. *Journal of Applied Chemistry of the USSR, 48*(6), 1271-1274.

Suekane, T., Nobuso, T., Hirai, S., & Kiyota, M. (2008). Geological storage of carbon dioxide by residual gas and solubility trapping. *International Journal of Greenhouse Gas Control, 2*(1), 58-64.

Szulczewski, M., Hesse, M., & Juanes, R. (2013). Carbon dioxide dissolution in structural and stratigraphic traps. *Journal of Fluid Mechanics, 736*, 287-315.

Taylor, P. (2010). Energy Technology Perspectives 2010. *Scenarios & Strategies to, 2050.*

Thomas, D. C., & Benson, S. M. (2015). *Carbon Dioxide Capture for Storage in Deep Geologic Formations-Results from the CO_2 Capture Project: Vol 2-Geologic Storage of Carbon Dioxide with Monitoring and Verification*: Elsevier.

Thommes, M. (2010). Physical adsorption characterization of nanoporous materials. *Chem. Ing. Tech, 82*(7), 1059-1073.

Valls, S., & Vazquez, E. (2001). Accelerated carbonatation of sewage sludge–cement–sand mortars and its environmental impact. *Cement and Concrete Research, 31*(9), 1271-1276.

Venhuis, M. A., & Reardon, E. J. (2001). Vacuum method for carbonation of cementitious wasteforms. *Environmental Science & Technology, 35*(20), 4120-4125.

Verbeck, G. (1958). Carbonation of hydrated portland cement. *Cement and Concrete*, 17-36.

Walton, J. C., Bin-Shafique, S., Smith, R. W., Gutierrez, N., & Tarquin, A. (1997). Role of carbonation in transient leaching of cementitious wasteforms. *Environmental Science & Technology, 31*(8), 2345-2349.

Warren, B. E. (1969). *X-ray Diffraction*: Courier Corporation.

Warwick, P. D., Verma, M. K., Freeman, P. A., Corum, M. D., & Hickman, S. H. (2014). U.S. Geological Survey Carbon Sequestration – Geologic Research and Assessments. *Energy Procedia, 63*, 5305-5309.

Webb, S. W., & Pruess, K. (2003). The use of Fick's law for modeling trace gas diffusion in porous media. *Transport in Porous Media, 51*(3), 327-341.

Weissberg, H. L. (1963). Effective diffusion coefficient in porous media. *Journal of applied physics, 34*(9), 2636-2639.

White, C. M., Strazisar, B. R., Granite, E. J., Hoffman, J. S., & Pennline, H. W. (2003). Separation and capture of CO_2 from large stationary sources and sequestration in geological formations—coalbeds and deep saline aquifers. *Journal of the Air & Waste Management Association, 53*(6), 645-715.

Xu, T., Apps, J. A., & Pruess, K. (2003). Reactive geochemical transport simulation to study mineral trapping for CO_2 disposal in deep arenaceous formations. *Journal of Geophysical Research: Solid Earth (1978–2012), 108*(B2).

Ye, G., Hu, J., Van Breugel, K., & Stroeven, P. (2002). Characterization of the development of microstructure and porosity of cement-based materials by numerical simulation and ESEM image analysis. *Materials and Structures, 35*(10), 603-613.

Young, J., Berger, R., & Breese, J. (1974). Accelerated curing of compacted calcium silicate mortars on exposure to CO_2. *Journal of the american ceramic society, 57*(9), 394-397.

Zakkour, P., & Haines, M. (2007). Permitting issues for CO_2 capture, transport and geological storage: a review of Europe, USA, Canada and Australia. *International Journal of Greenhouse Gas Control, 1*(1), 94-100.

Zhang, D., & Song, J. (2014). Mechanisms for Geological Carbon Sequestration. *Procedia IUTAM, 10*, 319-327.

Zhu, L., Duan, H.-B., & Fan, Y. (2015). CO_2 mitigation potential of CCS in China – an evaluation based on an integrated assessment model. *Journal of Cleaner Production, 103*, 934-947.

APPENDIX A: ALGORITHM PROGRAMMING

A.1 Algorithm Programming Design

Fast Lagrangian Analysis of Continua (FLAC) is frequently-used in geotechnical engineering field. Similar to all discrete modeling, this method uses the interactive computing between node quantity and unit quantity for a physical problem. The basic consider action is to divide the computational domain by N_e number of units, i_e ($i_e = 1,2,\cdots,N_e$), and to generate N_n number of nodes, i_n ($i_n = 1,2,\cdots,N_n$) ($N_n = N_e + 1$). Based on the physical quantity $u_{i_n}^{i}$ at i_n node at the time step, t_i ($i =,2,\cdots,N_t$), FLAC uses difference quotient to substitute the derivative, and then computes the physical quantity in the unit by $\left.\frac{\partial u}{\partial X_1}\right|_{i_e}^{t_i}$. Integration is then carried out on the specific zone around node i_n. Finally, the physical quantity $u_{i_n}^{i+1}$ at t_{i+1} moment is determined. The interactive computing between node quantity and unit quantity can help determine any derived unknown physical quantities for the time series t_i ($i =,2,\cdots,N_t$).

A.1.1 Node Quantity and Unit Quantity Formulation for CTPRC Experiment

For the CTPRC experiment, we first divide the sample into N_e numbers of equal units. The identifier of the units is i_e $(i_e = 1,2,\cdots,N_e)$. Each unit has one node on each of the upper and lower sides. Each adjacent unit will have one shared node. As shown in Figure A.1, the total nodes will be $N_n = N_e + 1$. Set the coordinate of the nodes as $x_1^{i_n}(i_n = 1,2,\cdots,N_n)$, and then configure the unit i $(i = 1,2,\cdots,N)$ for points between the interval $\left[x_1^{i_n}, x_1^{i_n+1}\right]$.

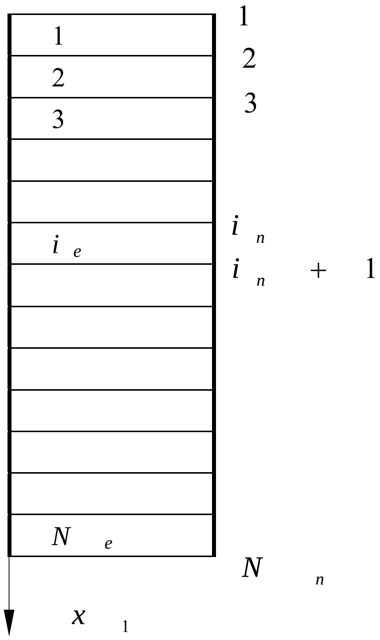

Figure A.1: Identify of node and unit

We can identify the displacement, velocity, stress, strain, strain rate, pressure and component concentrations for node i_n as $u_{i_n}^i$ 、 $v_{i_n}^i$ 、 $\sigma_{i_n}^i$ 、 $\varepsilon_{i_n}^i$ 、 $\dot{\varepsilon}_{i_n}^i$ 、 $p_{i_n}^i$ 、 $\left(\rho_i\right)_{i_n}^i$, for each time step, t_i . And the pressure gradient, diffusion flux and diffusion flux gradient of unit i_e can be written as $\left.\frac{\partial p}{\partial x_1}\right|_{i_e}^{t_i}$ 、 $J_{i_e}^{t_i}=D\left.\frac{\partial \rho_6}{\partial x_1}\right|_{i_e}^{t_i}$ 、 $\left.\frac{\partial J}{\partial x_1}\right|_{i_e}^{t_i}$ for each time step t_i .

A.1.2 Unit Quantity Calculation

The response of the computing system starts at $t_0=0$. The time step is set as h_t . So the pressure gradient of unit i_e （$i_e=1,2,\cdots,N_e$）can be calculated by difference method at time, $t_i=ih_t$.

$$\left.\frac{\partial p}{\partial X_1}\right|_{i_e}^{i}=\frac{p_{i_e+1}^i-p_{i_e}^i}{x_1^{i_e+1}-x_1^{i_e}},\ (i_e=1,2,\cdots,N_e) \tag{A.1}$$

The difference scheme for strain rate $B_{11}=\frac{\partial v_1}{\partial X_1}$ is given as

$$\left(B_{11}\right)_{i_e}^{i} = \left.\frac{\partial v_1}{\partial X_1}\right|_{i_e}^{i} = \frac{\left(v_1\right)_{i_e+1}^{i} - \left(v_1\right)_{i_e}^{i}}{x_1^{i_e+1} - x_1^{i_e}}, \quad (i_e = 1,2,\cdots,N_e) \tag{A.2}$$

where super script i refers to mode I and subscript i_e refers to the specific time. Then we can calculate the unit strain by kinematics consideration

$$\left(\varepsilon_{11}\right)_{i_e}^{i} = \left(\varepsilon_{11}\right)_{i_e}^{i} + B_{11}h_t, \quad \left(i_e = 1,2,\cdots,N_e\right) \tag{A.3}$$

Then we can use elastic constitutive relation to calculate the unit stress

$$\left(\sigma_{11}\right)_{i_e}^{i} = \left(\lambda + 2G\right)\left(\varepsilon_{11}\right)_{i_e}^{i}, \quad \left(i_e = 1,2,\cdots,N_e\right) \tag{A.4}$$

The difference scheme for the diffusion flux $J = D\frac{\partial \rho_{\text{gas}}}{\partial X_1}$ on unit i_e can be given as:

$$J\Big|_{i_e}^{i} = -D_{i_e}^{i}\frac{\left(\rho_{\text{gas}}\right)_{i_e+1}^{i} - \left(\rho_{\text{gas}}\right)_{i_e}^{i}}{x_1^{i_e+1} - x_1^{i_e}}, \quad \left(i_e = 1,2,\cdots,N_e\right) \tag{A.5}$$

In the above equation, $D_{i_e}^{i}$ represents the effective diffusion coefficient on unit i_e $\left(i_e = 1,2,\cdots,N_e\right)$ at times t_i .

A.1.3 Node Quantity Calculation

A.1.3.1 Node Velocity and Node Displacement Calculation

(1) Internal Node

We can integrate equation (4.1) on interval $[\frac{x_1^{i_n} + x_1^{i_n-1}}{2}, \frac{x_1^{i_n+1} + x_1^{i_n}}{2}]$ and get the following equation:

$$\begin{aligned} &\left(m_c\frac{\partial v}{\partial t}\right)_{i_n}^{i}\frac{x_1^{i_n+1} - x_1^{i_n-1}}{2} \\ &= \sigma_{i_n}^{\text{eff}} - \sigma_{i_n-1}^{\text{eff}} - \left(\alpha p\right)_{i_n} + \left(\alpha p\right)_{i_n-1} + b\frac{x_1^{i_n+1} - x_1^{i_n}}{2}, \quad \left(i_n = 2,3,\cdots,N_n - 1\right) \end{aligned} \tag{A.6}$$

or

$$\left(\frac{\partial v}{\partial t}\right)_{i_n}^{i} = \frac{1}{m_c}\left\{\frac{2}{x_1^{i_n+1} - x_1^{i_n-1}}\left[\sigma_{i_n}^{\text{eff}} - \sigma_{i_n-1}^{\text{eff}} - (\alpha p)_{i_n} + (\alpha p)_{i_n-1}\right] + b\right\}, \quad \left(i_n = 2,3,\cdots,N_n - 1\right) \tag{A.7}$$

By time integration, we get

$$\left(v_1\right)_{i_n}^{i+1} = \left(v_1\right)_{i_n}^{i} + \frac{1}{m_c}\left\{\frac{2}{x_1^{i_n+1} - x_1^{i_n-1}}\left[\sigma_{i_n}^{\text{eff}} - \sigma_{i_n-1}^{\text{eff}} - (\alpha p)_{i_n} + (\alpha p)_{i_n-1}\right] + b\right\} h_t, \quad \left(i_n = 2,3,\cdots,N_n - 1\right) \tag{A.8}$$

Based on kinematic principle, the equation for the node displacement is

$$\left(u_1\right)_{i_n}^{i+1} = \left(u_1\right)_{i_n}^{i} + \left(v_1\right)_{i_n}^{i} h_t, \left(i_n = 2,3,\cdots,N_n - 1\right) \tag{A.9}$$

(2) Boundary Node

By integrating equation (4.1) between the interval $\left[0, \frac{x_1^1 + x_1^2}{2}\right]$, and set the boundary condition $\sigma^{\text{eff}}\big|_{X_1 = H} = -p_{\text{co}_2}$, $p\big|_{X_1 = H} = p_{\text{co}_2}$, we get:

$$\left(m_c \frac{\partial v}{\partial t}\right)_1^{i} \frac{x_1^1 + x_1^2}{2} = \sigma_1^{\text{eff}} + p_{\text{co}_2} - (\alpha p)_1 + \alpha p_{\text{co}_2} + b\frac{x_1^1 + x_1^2}{2} \tag{A.10}$$

or

$$\left(\frac{\partial v}{\partial t}\right)_1^{i} = \frac{1}{m_c}\left\{\frac{2}{x_1^1 + x_1^2}\left[\sigma_1^{\text{eff}} + p_{\text{co}_2} - (\alpha p)_1 + \alpha p_{\text{co}_2}\right] + b\right\} \tag{A.11}$$

By time integration, we then get

$$\left(v_1\right)_1^{i+1} = \left(v_1\right)_1^{i} + \frac{1}{m_c}\left\{\frac{2}{x_1^1 + x_1^2}\left[\sigma_1^{\text{eff}} + p_{\text{co}_2} - (\alpha p)_1 + \alpha p_{\text{co}_2}\right] + b\right\} h_t \tag{A.12}$$

Again based on kinematics, we get the equation for node displacement

$$\left(u_1\right)_1^{i+1} = \left(u_1\right)_1^{i} + \left(v_1\right)_1^{i} h_t \tag{A.13}$$

Use boundary condition, we get

$$\begin{cases} \left(v_1\right)_{N_n}^{i+1} = 0 \\ \left(u_1\right)_{N_n}^{i+1} = 0 \end{cases} \tag{A.14}$$

A.1.3.2 CO$_2$ Concentration at Node

(1) Internal Node

Equation (4.41) can be modified for the interval $\left[\frac{x_1^{i_n} + x_1^{i_n - 1}}{2}, \frac{x_1^{i_n + 1} + x_1^{i_n}}{2}\right]$,

$$\left.\frac{\partial \rho_7}{\partial t}\right|_{i_n}^{i} = -\left(\mu_7 \xi_4 + 3\mu_7 \xi_5 + 3\mu_7 \xi_6 + 2\mu_7 \xi_7\right) - \frac{2}{x_1^{i_n+1} - x_1^{i_n}}\left(J_1^{i_n} - J_1^{i_n - 1}\right) \tag{A.15}$$

Through integration, we get:

$$\begin{aligned} \rho_7\Big|^{i+1} = \rho_7\Big|^{i} &- \left(\mu_7 \xi_4 + 3\mu_7 \xi_5 + 3\mu_7 \xi_6 + 2\mu_7 \xi_7\right) ht \\ &- \frac{2}{x_1^{i_n+1} - x_1^{i_n}}\left(J_1^{i_n} - J_1^{i_n - 1}\right) h_t \end{aligned} \tag{A.16}$$

(2) Boundary Node

Equation (4.41) within the interval $\left[x_1^1, \frac{x_1^1 + x_1^2}{2}\right]$ and include $J_1\big|_{X_1 = 0} = J_{CO_2}^{\text{int}}$,

$$\left.\frac{\partial \rho_7}{\partial t}\right|_{1}^{i} = -\left(\mu_7 \xi_4 + 3\mu_7 \xi_5 + 3\mu_7 \xi_6 + 2\mu_7 \xi_7\right) - \frac{2}{x_1^2 - x_1^1}\left(J_1^1 - J_{CO_2}^{\text{int}}\right) \tag{A.17}$$

Through integration, we get:

$$\rho_7\Big|_1^{i+1} = \rho_7\Big|_1^{i} - \left[\left(\mu_7 \xi_4 + 3\mu_7 \xi_5 + 3\mu_7 \xi_6 + 2\mu_7 \xi_7\right) + \frac{2}{x_1^2 - x_1^1}\left(J_1^1 - J_{\text{CO}_2}^{\text{cav}}\right)\right] h_t \tag{A.18}$$

Define equation (4.41) for the interval $\left[\dfrac{x_1^{N_n-1}+x_1^{N_n}}{2},x_1^{N_n}\right]$ and $J_1\big|_{X_1=h_s}=0$, we get:

$$\left.\frac{\partial\rho_7}{\partial t}\right|_{N_n}^{i}=-\left(\mu_7\xi_4+3\mu_7\xi_5+3\mu_7\xi_6+2\mu_7\xi_7\right)-\frac{2}{x_1^{N_n}-x_1^{N_n-1}}\left(0-J_{N_n-1}^{i}\right)\quad\text{(A.19)}$$

Do the time integration for the above equation and get

$$\rho_7\Big|_{N_n}^{i+1}=\rho_7\Big|_{N_n}^{i}-\left[\left(\mu_7\xi_4+3\mu_7\xi_5+3\mu_7\xi_6+2\mu_7\xi_7\right)+\frac{2}{x_1^2-x_1^1}J_{N_n-1}^{i}\right]h_t\quad\text{(A.20)}$$

A.1.3.3 Other Component Concentration in Node Calculation

The mass conservation equation is,

$$\frac{\partial\rho_k}{\partial t}=\sum_{j=1}^{7}m_{jk}\mu_k\xi_j,\ \left(i=1,2,\cdots,10,i\neq 7\right)\quad\text{(A.21)}$$

Through integration, the equation for every other component concentration becomes

$$\rho_k\Big|_{i_n}^{i+1}=\rho_k\Big|_{i_n}^{i}+\sum_{j=1}^{7}m_{jk}\mu_k\xi_j h_t,\ \left(i=1,2,\cdots,10,i\neq 7\right)\quad\text{(A.22)}$$

A.1.3.4 Porosity and Diffusion Coefficient in Node Calculation

Since the velocity of sample deformation is slow, we can assume substantial derivative is similar to local derivative, $\dfrac{D\phi}{Dt}=\dfrac{\partial\phi}{\partial t}$, and the deformation equation can be simplified to

$$\frac{\partial\phi}{\partial t}=\frac{\partial v_1}{\partial X_1}-\frac{1}{m_c}\sum_{i=1}^{10}\frac{\partial\rho_i}{\partial t}\quad\text{(A.23)}$$

(1) Internal Node Porosity

Define equation (A.23) between the interval $\left[\dfrac{x_1^{i_n}+x_1^{i_n-1}}{2},\dfrac{x_1^{i_n+1}+x_1^{i_n}}{2}\right]$, we get:

$$\left.\frac{\partial\phi}{\partial t}\right|_{i_n}^{i}=\frac{x_1^{i_n}-x_1^{i_n-1}}{x_1^{i_n+1}-x_1^{i_n-1}}\left(\frac{\partial v_1}{\partial x_1}\right)_{i_n-1}^{i}+\frac{x_1^{i_n+1}-x_1^{i_n}}{x_1^{i_n+1}-x_1^{i_n-1}}\left(\frac{\partial v_1}{\partial X_1}\right)_{i_n}^{i}-\frac{1}{m_c}\sum_{k=1}^{10}\left(\frac{\partial\rho_k}{\partial t}\right)_{i_n}^{i}, \quad \text{(A.24)}$$

$$\left(i_n=2,3,\cdots,N_n-1\right)$$

Integrate (A.24) and we get:

$$\phi_{i_n}^{i+1}=\phi_{i_n}^{i}+\left[\frac{x_1^{i_n}-x_1^{i_n-1}}{x_1^{i_n+1}-x_1^{i_n-1}}\left(\frac{\partial v_1}{\partial X_1}\right)_{i_n-1}^{i}+\frac{x_1^{i_n+1}-x_1^{i_n}}{x_1^{i_n+1}-x_1^{i_n-1}}\left(\frac{\partial v_1}{\partial X_1}\right)_{i_n}^{i}-\frac{1}{m_c}\sum_{k=1}^{10}\left(\frac{\partial\rho_k}{\partial t}\right)_{i_n}^{i}\right]h_t, \quad \text{(A.25)}$$

$$\left(i_n=2,3,\cdots,N_n-1\right)$$

(2) Boundary Node Porosity

Define equation (A.23) between the interval $\left[0,\frac{x_1^1+x_1^2}{2}\right]$,

$$\left.\frac{\partial\phi}{\partial t}\right|_{1}^{i}=\left(\frac{\partial v_1}{\partial x_1}\right)_{1}^{i}-\frac{1}{m_c}\sum_{k=1}^{9}\left(\frac{\partial\rho_k}{\partial t}\right)_{1}^{i} \quad \text{(A.26)}$$

Through time integration, we get:

$$\phi_1^{i+1}=\phi_1^{i}+\left[\left(\frac{\partial v_1}{\partial X_1}\right)_{1}^{i}-\frac{1}{m_c}\sum_{k=1}^{9}\left(\frac{\partial\rho_k}{\partial t}\right)_{1}^{i}\right]h_t, \ \left(i_n=2,3,\cdots,N_n-1\right) \quad \text{(A.27)}$$

We integrate equation (A.23) between the interval $\left[\frac{X_1^{N_n-1}+X_1^{N_n}}{2},X_{N_n}^2\right]$,

$$\left.\frac{\partial\phi}{\partial t}\right|_{N_n}^{i}=\left(\frac{\partial v_1}{\partial X_1}\right)_{N_n-1}^{i}-\frac{1}{m_c}\sum_{k=1}^{9}\left(\frac{\partial\rho_k}{\partial t}\right)_{N_n}^{i} \quad \text{(A.28)}$$

and get

$$\phi_{N_n}^{i+1}=\phi_{N_n}^{i}+\left[\left(\frac{\partial v_1}{\partial x_1}\right)_{N_n-1}^{i}-\frac{1}{m_c}\sum_{k=1}^{9}\left(\frac{\partial\rho_k}{\partial t}\right)_{N_n}^{i}\right]h_t \quad \text{(A.29)}$$

(3) Diffusion Coefficient

The diffusion coefficient equation is defined similar to equation (A.23),

$$D_{i_n}^{i} = D_r \left(\frac{\phi_{i_n}^{i}}{\phi_r} \right)^{p_d}, \quad \left(i_n = 1,2,\cdots,N_n \right) \tag{A.30}$$

A.1.3.5 Free Space CO2 Pressure and Mass Density Calculation

CO_2 flux at gas-solid interface is equal to the top surface CO_2 flux,

$$J_{CO_2}^{\text{int}} = J_1 \Big|_{x_1=0} \tag{A.31}$$

Then,

$$\left. \frac{\partial p_{\text{chamb}}}{\partial t} \right|^{i} = \frac{p_{\text{atam}}}{h_c m_{\text{CO}_2}^{\text{atam}}} J_1^i \tag{A.32}$$

where subscripts "chamb" means the reaction chamber and "atam" means standard atmosphere. Do the integration for the above equation, we get,

$$p_{\text{chamb}}^{i+1} = p_{\text{chamb}}^{i} + \frac{p_{\text{atam}}}{h_c m_{\text{CO}_2}^{\text{atam}}} J_1^i h_t \tag{A.33}$$

CO_2 mass density equation can be defined following equation (4.48),

$$m_{\text{CO}_2}^{i} = m_{\text{CO}_2}^{\text{atm}} \frac{p_{\text{chamb}}^{i}}{p_{\text{atm}}} \tag{A.34}$$

A.1.4 Diffusion Coefficient and Rate Coefficient Estimation Using Genetic Algorithm

Before we start to calculate diffusion and reaction kinetics responses, we need to provide the initial estimated values for the reference diffusion coefficient D_r, power exponent p_d and rate coefficient of reaction $k_i \, (i = 1,2,\cdots,7)$. However, consider the number of possible values and the perturbations, there is need for a rational approach to determine the optimal values. Here we use a genetic algorithm program to do those parameters estimation. The following describes our approach:

(1) Based on CTPRC experiment pressure results the time history of CO_2 pressure

$p_{\text{test}}^{i}(i=1,2,\cdots,N_t)$ in the CTPRC system is established;

(2) Coding and decoding;

$k_1, k_2, \cdots, k_7$, D_r and p_d are mapped to the character string which is composed of 0 and 1. Table A.1 defines the coefficients and the lengths of the character string are $l_1, l_2, \cdots, l_9$. The decoding formula for each code is also listed.

Table A.1: $k_1, k_2, \cdots, k_7$, D_r and p_d coding and decoding

	Code	Search Range		Decoding Formula
		Left	Right	
k_1	$I_{11}I_{12}\cdots I_{1l_1}$	k_1^{left}	k_1^{right}	$k_1^j = k_1^{\text{left}}\left[1+\frac{j}{2^{l_1}-1}\frac{k_1^{\text{right}}-k_1^{\text{left}}}{k_1^{\text{left}}}\right], j=\sum_{i=1}^{l_1} 2^{l_1-i} I_{1i}$
k_2	$I_{21}I_{22}\cdots I_{2l_2}$	k_2^{left}	k_2^{right}	$k_2^j = k_2^{\text{left}}\left[1+\frac{j}{2^{l_2}-1}\frac{k_2^{\text{right}}-k_2^{\text{left}}}{k_2^{\text{left}}}\right], j=\sum_{i=1}^{l_1} 2^{l_2-i} I_{2i}$
k_3	$I_{31}I_{32}\cdots I_{3l3}$	k_3^{left}	k_3^{right}	$k_3^j = k_3^{\text{left}}\left[1+\frac{j}{2^{l_3}-1}\frac{k_1^{right}-k_3^{\text{left}}}{k_3^{\text{left}}}\right], j=\sum_{i=1}^{l_1} 2^{l_3-i} I_{3i}$
k_4	$I_{41}I_{42}\cdots I_{4l_4}$	k_4^{left}	k_4^{right}	$k_4^j = k_4^{\text{left}}\left[1+\frac{j}{2^{l_4}-1}\frac{k_4^{\text{right}}-k_4^{\text{left}}}{k_4^{\text{left}}}\right], j=\sum_{i=1}^{l_1} 2^{l_4-i} I_{4i}$
k_5	$I_{51}I_{52}\cdots I_{5l_5}$	k_5^{left}	k_5^{right}	$k_5^j = k_5^{\text{left}}\left[1+\frac{j}{2^{l_5}-1}\frac{k_5^{\text{right}}-k_5^{\text{left}}}{k_5^{\text{left}}}\right], j=\sum_{i=1}^{l_5} 2^{l_5-i} I_{5i}$
k_6	$I_{61}I_{62}\cdots I_{6l_6}$	k_6^{left}	k_6^{right}	$k_6^j = k_6^{\text{left}}\left[1+\frac{j}{2^{l_6}-1}\frac{k_6^{\text{right}}-k_6^{\text{left}}}{k_6^{\text{left}}}\right], j=\sum_{i=1}^{l_6} 2^{l_6-i} I_{6i}$
k_7	$I_{71}I_{72}\cdots I_{7l_7}$	k_7^{left}	k_7^{right}	$k_7^j = k_7^{\text{left}}\left[1+\frac{j}{2^{l_7}-1}\frac{k_1^{\text{right}}-k_1^{\text{left}}}{k_7^{\text{left}}}\right], j=\sum_{i=1}^{l_1} 2^{l_7-i} I_{7i}$
D_r	$I_{81}I_{82}\cdots I_8$	D_r^{left}	D_r^{right}	$D_r^j = D_r^{\text{left}}\left[1+\frac{j}{2^{l_1}-1}\frac{D_r^{\text{right}}-D_r^{\text{left}}}{D_r^{\text{left}}}\right], j=\sum_{i=1}^{l_8} 2^{l_8-i} I_{8i}$
p_d	$I_{91}I_{92}\cdots I_9$	p_d^{left}	p_d^{right}	$p_d^j = p_d^{\text{left}}\left[1+\frac{j}{2^{l_9}-1}\frac{p_d^{\text{right}}-p_d^{\text{left}}}{p_d^{\text{left}}}\right], j=\sum_{i=1}^{l_9} 2^{l_9-i} I_{9i}$

(3) Generate Random Population

A FORTRAN program is used to generate random numbers, z_i , in $m = \sum_{i=1}^{9} l_i$ data between the interval $[0,1]$. The random numbers are then assigned as character variables by the following rules:

$$I_i = \begin{cases} 1 & \text{if } z_i \geq 0.5 \\ 0 & \text{if } z_i < 0.5 \end{cases}, i = 1, 2, \cdots, m \tag{A.35}$$

After this, we can get the unit gene $I_1 I_2 \cdots I_m$. This process can be repeat k_{group} times and then we could get the initial population:

$$\text{initial\_pop} = \left\{ I_1^i I_2^i \cdots I_m^i \middle| i = 1, 2, \cdots, k_{\text{group}} \right\} \tag{A.36}$$

By decoding those values, we get the phenotypic gene for each unit.

(4) Calculate the fitness value

For the individual $I_1^i, I_2^i, \cdots, I_m^i \ \left(i = 1, 2, \cdots, k_{\text{group}} \right)$ in the population, genetic phenotype values are assigned respectively to k_1 , k_2 , k_3 , k_4 , k_5 , k_6 , k_7 , D_r and p_d . Use Fast Lagrangian Analysis of Continuum (FLAC) to calculate the CO_2 diffusion and reaction kinetics responses. Then the computed value sequence for the free space CO_2 pressure, $p_{\text{calc}}^i (i = 1, 2, \cdots, N_t)$, can be established. Fitness value can be calculated by,

$$\text{fitn}(i) = \frac{1}{\frac{1}{N_t} \sum_{k=1}^{N_t} \left(1 - \frac{p_{\text{calc}}^i}{p_{\text{test}}^i} \right)^2}, \quad \left(i = 1, 2, \cdots, k_{\text{group}} \right) \tag{A.37}$$

(5) Operation Selection

The random covering path method is used to pick up k_{cop} data, which have the mating right in the initial population. The genotype for each unit can be described by the following:

$$\mathrm{P}_{\mathrm{cop}} = \left\{ \mathrm{chromosome}(i_1) \middle| \mathrm{chromosome}(i_1) = I_1^{i_1} I_2^{i_1} \cdots I_m^{i_1}, i_1 = 1, 2, \cdots, k_{\mathrm{cop}} \right\} \qquad \text{(A.38)}$$

(6) Crossover Operation

The random pair for each gene unit in $\mathrm{P}_{\mathrm{cop}}$ data can be established through randomly generating crossover. After the crossover operation on a certain crossover rate p_c is performed, a new group of gene unit is generated, which can be called $\mathrm{P}_{\mathrm{cop}}^{*}$ data.

(7) Mutation Operation

The mutation operation is performed on each gene unit in $\mathrm{P}_{\mathrm{cop}}^{*}$ data group. The mutation is then followed by a certain mutation rate p_m and thus a new population is established:

$$\mathrm{New\_pop} = \left\{ I_1^i I_2^i \cdots I_m^i \middle| i = 1, 2, \cdots, k_{\mathrm{cop}} \right\} \qquad \text{(A.39)}$$

(8) Reproduction Operation Termination

To terminate the reproduction process, a criterion should be satisfied. A fitness value $\mathrm{fitn}(i)$ $i = 1, 2, \cdots, k_{\mathrm{cop}}$, is defined for each gene unit in the new population. If the maximum fitness value, ($\mathrm{fitn\_max}$), is greater than the preset value s,

$$\mathrm{fitn\_max} \geq s \qquad \text{(A.40)}$$

or if the reproduction generation is equal to a preset number N_g, the reproduction procedure will be terminated. Otherwise, the reproduction will keep going until the condition fits equation (A.40). After this step, the selected gene unit will be need to determine the optimal values for k_1^{best}, k_2^{best}, k_3^{best}, k_4^{best}, k_5^{best}, k_6^{best}, k_7^{best}, D_r^{best}, p_d^{best} for k_1, k_2, k_3, k_4, k_5, k_6, k_7, D_r and p_d.

A.2 FORTRAN Program Calculation Procedure

The above procedure is coded into a FORTRAN program. The flow chart for the program is summarized in Figure A.2. For housekeeping purpose, the following sections describe the constants, coordinates, integer variables, and units in the program.

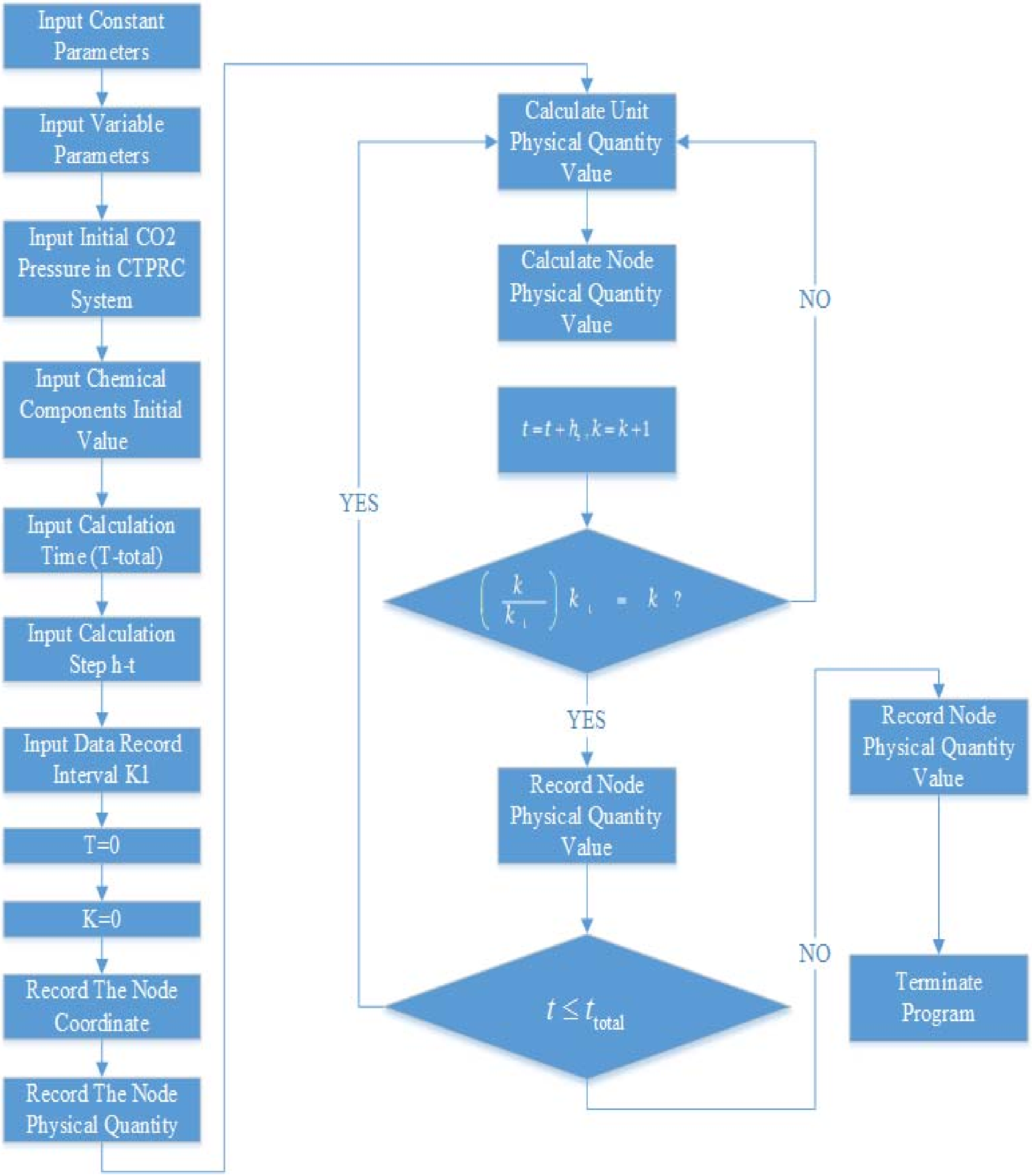

Figure A.2: Computer program flow chart

(1) Constants

The constants used in the program included the sample diameter a_s, height h_s, ideal gas constant R, standard atmospheric pressure p_a, the mass densities of cement components, $m_i, (i=1,2,\cdots,10)$, stoichiometric coefficients, $m_{ij} (i=1,2,\cdots,7; j=1,2,\cdots,10)$, molecular weights, $\mu_i, (i=1,2,\cdots,10)$, reaction rate constant, $k_i\ (i=1,2,\cdots,7)$, diffusion coefficient reference value, D_r, and power exponent p_d.

(2) Variables

The variables in the program included the mass of cement component $M_i, (i=1,2,\cdots,10)$, the initial porosity ϕ_0 and the initial height of CO_2 (h_c) in the reaction chamber.

(3) Initial mass concentration

The Initial mass concentration, $\rho_i, (i=1,2,\cdots,10)$, is calculated as:

$$\rho_i = \frac{Y_i \sum_{j=1}^{10} M_j}{\pi a_s^2 h_s} \tag{A.41}$$

where, $\pi a_s^2 h_s$ represents the total volume occupied by 10 material components. Y_i represents the mass fraction for each component i.

For illustration purpose, we introduce volume fraction to explain the relationship between mass concentration and mass density.

$$Z_j = \frac{\text{the volume taken by j component}}{\text{the total volume taken by 10 component}}, (j=1,2,\cdots,10) \tag{A.42}$$

So, the initial mass density $\rho_i, (i=1,2,\cdots,10)$ can be described by the following equation.

$$\rho_i = \frac{M_j}{\pi a_s^2 h_s} = Z_j \left(\frac{M_j}{Z_j \pi a_s^2 h_s} \right) = Z_j m_j \tag{A.43}$$

And it is obvious that the mass concentration is less than the mass density.

We can assume initial mass concentration for the components is uniformly distributed in the sample. The CO_2 mass concentration can be described by the following equation:

$$\rho_7 \Big|_{t=0} = \phi_0 \, m_7 \Big|_{t=0} \left(\frac{h_s - x_1}{h_s} \right)^3 \tag{A.44}$$

where, ϕ_0 represents the initial porosity of the sample. The initial CO_2 mass density $m_7\big|_{t=0}$ can be calculated by the ideal gas law equation,

$$m_7 \Big|_{t=0} = \frac{p_{\text{chamb}}\big|_{t=0}}{p_{\text{atm}}} m_7 \Big|_{p=p_a} \tag{A.45}$$

where, p_{atm} refers to the standard atmosphere pressure, $p_{\text{chamb}}\big|_{t=0}$ represents the initial pressure in the reaction chamber.

(4) Record node coordinate

The node coordinate is selected such that a 3D surface plot can be easily generated.

(5) Integer variable

An integer variable k_1 is needed to reduce the data storage content. The integer variable can also be used to control the length of category axis and series axis. In FORTRAN language, $\left(\frac{k}{k_1} \right) k_1$ can only equal to k when k is an integer multiple of k_1.

For example, $\frac{12}{10} \times 10 = 10 \neq 12$, $\frac{40}{10} \times 10 = 40$.

(6) Physical quantity of unit

The physical quantities of unit include diffusion velocity, and pressure gradient, etc. are described in Chapter 2.

(7) Physical quantity of node

As described in Chapter 2, the physical quantities of node include concentration of each material component, diffusion coefficient, and displacement, etc.

APPENDIX B: ADDITIONAL TESTS

This paper is published at Advanced Characterization of Asphalt and Concrete Materials, GSP 255, ASCE 2014

Concrete Carbonation Quantification Using Constant Temperature Pressure Chamber (CTPRC)

Peng Wang[1], Shen-En Chen[2], Xianbiao Mao[3], Qiyan Feng[4], Qianlin Zhu[4]

[1]Ph.D Candidate, Department of Civil & Environmental Engineering, University of North Carolina at Charlotte, NC 28262;
[2]Professor, Department of Civil & Environmental Engineering, University of North Carolina at Charlotte,NC 28262;
[3]Professor, State Key Laboratory for Geo-mechanics & Deep Underground Engineering, China University of Mining & Technology, Xuzhou, Jiangsu, 221116, China;
[4]Professor, Department of Environment & Spatial Engineering, China University of Mining & Technology, Xuzhou, Jiangsu, 221116, China;
[4]Researcher, Research Institute of Low Carbon Energy, China University of Mining & Technology, Xuzhou, Jiangsu, 221116, China;

ABSTRACT

The goal of this research is to develop an experimental method for evaluating the physical and chemical CO_2 sorption capacity of solid waste from the coal energy and cement industries with a new material called Ash Carbonated Concrete (ACC). The proposed ACC material is a highly porous cementitious material intended to rapidly sequester CO_2 and reduce other coal energy waste. ACC relies on the bonding of ash with cement to physically stabilize ash material, and calcium carbonation to chemically fixate CO_2. To accurately quantify the CO_2 absorption process, a new testing technique is proposed. The constant temperature pressurized reaction chamber (CTPRC) isolates temperature effects and measures gas absorption volumes through pressure change measurements. Results from different blends of ash, aluminum, water, and cement indicate that the CTPRC can accurately differentiate chemical and physical sorption and quantify the amount of consumed CO_2.

INTRODUCTION

Motivated by concerns about global warming, there has been a resurgence of proposed technical solutions to minimize the harmful consequences of greenhouse gas. Fossil fuels account 85% of world’s energy requirements in the current system. The use of fossil fuels will likely continue through the coming decades due to its low cost and availability(Stewart and Hessami 2005). A viable alternative for reducing CO_2 emissions, without changing the energy consumption system, is the sequestration of carbon dioxide in stable deep geological reservoirs. However, geological sequestration and ocean sequestration cannot reach the same level as the amount of CO_2 emission. For this reason, there is room for additional sequestration with other techniques(Huijgen and Comans 2003). The carbonation sequestration technique suggested is mineral carbonation in cementitious materials. This paper describes an experimental technique that quantifies the sorption process of CO_2 flow into the material matrix.

CTPRC TEST METHOD & MATERIAL SORPTION

In the CTPRC experimental setup, both reference and sample cells are placed into constant temperature water baths to balance the CTPRC system under isothermal conditions. The AAC sample is then placed in the sample chamber. Pressure sensors are affixed to the reference cell and reaction cell, and monitored by an NI data acquisition system. First, the CTPRC system will be vacuumed. Then the total volume of system free space will be determined by injecting helium as a non-absorbing gas, helium. The reference chamber's volume ($V_{\text{reference cell}}$) is fixed at 200ml. By injecting helium at certain pressure ($P_{\text{helium initial}}$) into the reference cell we can calculated the initial condition by the following equation:

$$P_{\text{helium initial}} V_{\text{reference cell}} = \frac{N}{M} RT \tag{1.1}$$

In the above equations, T is constant system temperature, M is the mass of gas, N is the molar mass of CO_2 and R is the universal gas constant. An equilibrium pressure ($P_{\text{helium eq}}$) is achieved by opening the balance valve between the reference cell and reaction chamber. The equilibrium stage of the system can be described by:

$$P_{\text{helium eq}} \left(V_{\text{reference cell}} + V_{\text{free space}} \right) = \frac{N}{M} RT \tag{1.2}$$

By equating Eq(1.1) and Eq(1.2), the total free volume in the system can be described in the following form:

$$V_{\text{free space}} = \frac{P_{\text{helium initial}} V_{\text{reference cell}}}{p_{\text{helium left}}} - V_{\text{reference cell}} \tag{1.3}$$

Before CO_2 is injected into the system, the helium is removed by vacuum. After CO_2 is injected into the CTPRC system and the initial gas pressure ($P_{CO_2 \text{ initial pressure}}$) is balanced, the volume of CO_2 pumped into the system can be calculated by the following equation:

$$M_{CO_2}^{\text{initial}} = \frac{P_{CO_2 \text{ inital pressure}} \times \left(V_{\text{reference cell}} + V_{\text{free space}} \right) \times N}{RT} \tag{1.4}$$

After 48 hours, the final CO_2 pressure ($P_{CO_2 \text{ eq}}$) can be utilized to calculate the CO_2 in the system free space by the following equation:

$$M_{CO_2}^{\text{final}} = \frac{P_{CO_2 \text{ final}} \times \left(V_{\text{reference cell}} + V_{\text{free space}} \right) \times N}{RT} \tag{1.5}$$

Based on Eq(1.4) and Eq(1.5), the CO_2 mass consumed in the CTPRC system by chemisorption and physisorption procedures can be isolated:

$$M_{CO_2}^{\text{consumed}} = M_{CO_2}^{\text{initial}} - M_{CO_2}^{\text{final}} \tag{1.6}$$

Adsorbate material (Ash Carbonated Concrete)

For a solid to be suitable for accelerated carbonation, it must have certain chemical and physical properties that make it eligible for treatment. The following steps describe the sequential mechanisms that take place during the carbonation of cementitious materials.

1) Permeation of CO_2 through the solid.

2) Solution of $CO_{2(g)}$ to $CO_{2(aq)}$. Boundary layer transfer is favored by a high internal surface area of solid (Fritz, Clement et al. 2013).

3) Hydration of $CO_{2(aq)}$ to H_2CO_3. This is a slow, rate-determining. Step during multiphase transition.

4) Ionization of H_2CO_3 to H^+, HCO_3^-, CO_3^{2-}. This occurs almost instantaneously, making the pH fall by approximately 3 units, typically from 11 to 8 during CTPRC experiment.

5) Dissolution of cementitious phases C_3S and C_2S. Because the process is cyclic, this step is rapid and extensive, and generates considerable exothermal output (Constantinides and Ulm 2004, Fernández Bertos, Simons et al. 2004, Fabbri, Corvisier et al. 2009). The calcium silicate grains are covered by a loose layer of calcium silicate hydrate gel, which is quickly dissolved, releasing Ca^{2+} and SiO_4^{-4} ions.

6) Nucleation of $CaCO_3$.

Experimental Setup

ACC is a man-made material and therefore goes through a process of maturation. Traditional sorption tests cannot address the multi-phase change. The CTPRC test technique isolates temperature effects and can measure the gas absorption volume through pressure change measurements, as described earlier. Fig.1 shows a schematic of the CTPRC experimental setup.

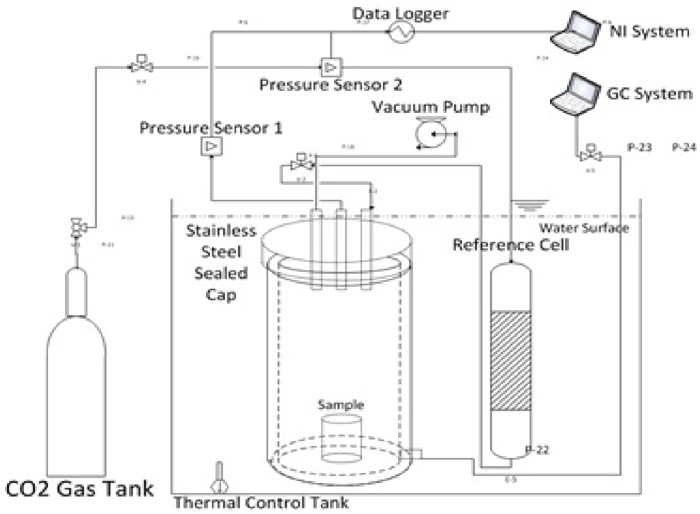

FIG.1. Schematic diagram of CTPRC setup

EXPERIMENT RESULTS

The following is a report on experiments conducted to determine the performance of the CTPRC to quantify the CO_2 sorption of ACC. Material blends submitted for testing are shown in Table 1.

Table 1: CTPRC experiment initial condition

Sample	Cement	Ash	Water	Aluminum powder
1	30(g)	0(g)	14(ml)	0(g)
2	30(g)	0(g)	14(ml)	0.5(g)
3	30(g)	0(g)	14(ml)	0.5(g)
4	3(g)	27(g)	14(ml)	0.5(g)
5	30g	0g	14ml (pH=2.2)	0.5g

During experimentation, all specimens were espoused to a pressure of 150 psi. Figure 3 shows the monitored volumetric pressure, of different specimens, over the 48-hour test period. A decrease in volumetric pressure directly correlated to the volume of absorbed CO_2. The characteristics of the ACC impose physical and chemical constraints on CO_2 diffusion. Carbonation is physically encouraged by enhanced CO_2 penetration through increased gas-permeability. Figure 3(c) shows that physical CO_2 penetration is partially a function of the materials porosity and surface area. Porosity can be augmented to impede or enhance CO_2 penetration by controlling material permeability by adjusting aluminum content (Figure 3(a)). The chemical carbonation is influenced by the free water content, pH, and calcium concentration of the ACC host. In the closed CTPRC method, optimal water content and pH values are required to allow the reaction from mechanisms 5 and 6 to occur.

Excess water diminishes the rate of concrete carbonation by limiting CO_2 concentration in the surface water and restricts proper CO_2 penetration. The acidic pH tendencies of fresh concrete enhance carbonation by encouraging CO_2 diffusion into saturated pores in the ACC material (Figure 3(d)). The directly proportional relationships shared between calcium content and carbonation rates are shown in Figure 3(b); samples with higher concentrations of calcium garner increased levels of carbonation. Use equation (1.4) to (1.6), we can calculate the consumed CO_2 as shown in Table 2.

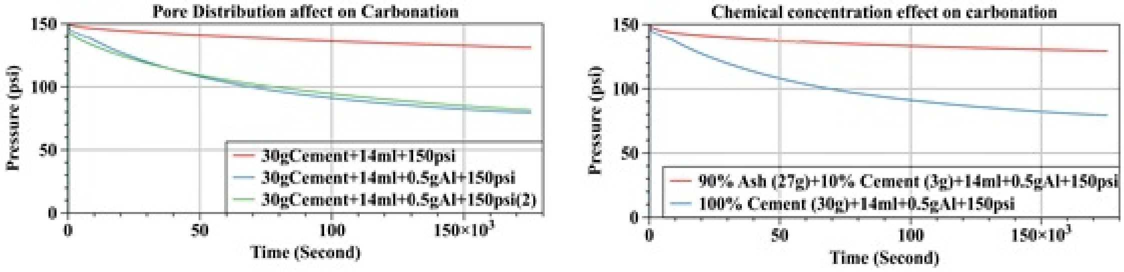

(a) Pore distribution affect on carbonation (b) Chemical content affect on carbonation

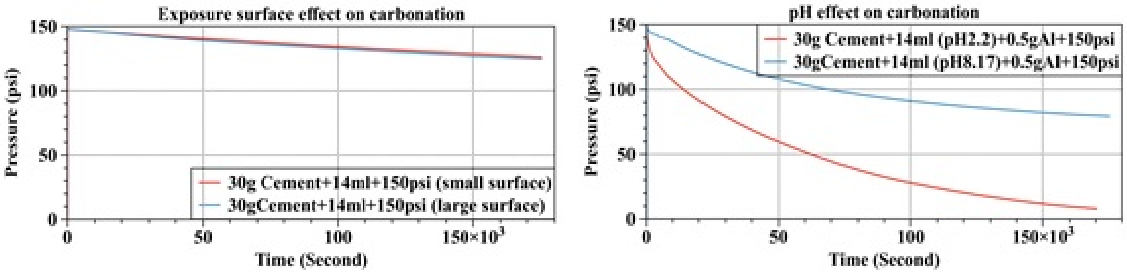

(c) Exposure surface affect on carbonation (d) pH affect on carbonation

FIG.3. CO_2 **pressure variation in 48 hours**

Table 2: Carbonation Results

Sample Name	**Consumed** CO_2
30gCement+14ml	2.26(g)
30gCement+14ml+0.5gAl	3.80(g)
90%Ash (27g)+10%Cement (3g) +14ml+0.5gAl	1.1(g)
30gCement+14ml(pH=2.2) +0.5gAl	15.25(g)

Microstructure analysis

The morphology of the ACC before and after carbonation was examined using a high resolution Scanning Electron Microscope (SEM). The SEM output from analysis of the sample with 90% fly ash and 10% cement is presented in Figure 4. The microstructure is spacious in this sample because of weak chemical bonds between the fly ash and cement particles. The original fly ash showed sheet morphology (Figure 4(a)), whereas carbonation caused the sheet to become irregular in shape. Some crystalline reaction products can be identified (Figure 4(b)).

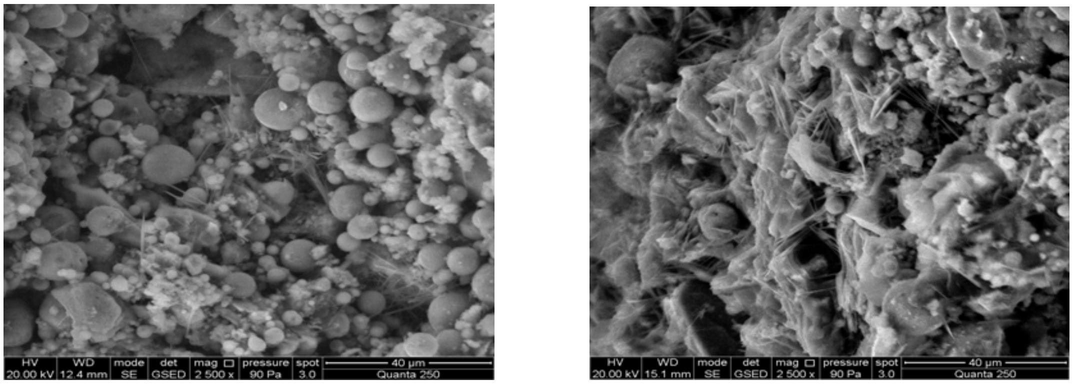

(a) 90% Ash+10% Cement+0gAl(no carbonation) (b) 90% Ash+10% Cement+0gAl (carbonation)

FIG. 4. SEM Results (90%Ash (27g) +10%Cement (3g))

Following the introduction of an air entrainment agent (aluminum powder). Large-scale porous structures were generated as shown in Figure 5. These large-scale porous structures showed potential to function as gas diffuse channels, which can will increase the gas-solid interaction surface and make the calcium based carbonation reaction faster and more completely. As shown in Figure 5(b), most of the micro-porous structures showed that there is very limited conductivity due to the closed formation. Based on the above SEM evidences, the material structure can be characterized as dual-porosity form.

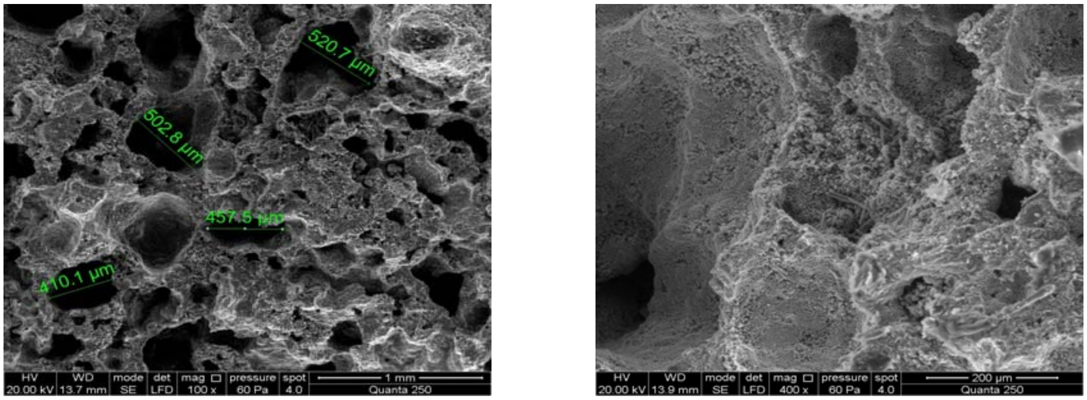

(a) Large-scale porous (b) small-scale porous

FIG. 5. SEM Result (100% Cement (30g) +5gAl with carbonation)

CONCLUSIONS

The following can be conducted from the experimental results: To have sufficient carbonation potential, the materials must be inorganic in nature, containing calcium and/or silicon salts. They may be hydraulic, lime-bearing or other CO_2 reactive calcium rich material with heavy metal. Greater carbonation is achieved when the solid has high concentration of CaO, and presents a large surface area. The carbonation is optimum when the CO_2 pressure is maintained during exposure. Beneficial carbonation affects microelement mobility in cement based systems. After the treatment the heavy metals in the containment may be absorbed, insolubilized, or physically encapsulated.

ACKNOWLEDGMENTS

The State Key Laboratory of Geo-mechanics and Deep Underground Engineering at China University of Mining & Technology support this work. We also acknowledge Professors Xiexing Miao, Zhengfu Bian, and Lai Zhou of the China University of Mining Technology for facilitating our study in China.

REFERENCES

Constantinides, G. and F.-J. Ulm (2004). "The effect of two types of C-S-H on the elasticity of cement-based materials: Results from nanoindentation and micromechanical modeling." Cement and Concrete Research 34(1): 67-80.
Fabbri, A., et al. (2009). "Effect of carbonation on the hydro-mechanical properties of Portland cements." Cement and Concrete Research 39(12): 1156-1163.
Fernández Bertos, M., et al. (2004). "A review of accelerated carbonation technology in the treatment of cement-based materials and sequestration of CO2." Journal of Hazardous Materials 112(3): 193-205.
Fritz, B., et al. (2013). "Calcite formation by hydrothermal carbonation of portlandite: complementary insights from experiment and simulation." Crystengcomm 15(17): 3392-3401.
Huijgen, W. J. J. and R. N. J. Comans (2003). Carbon dioxide sequestration by mineral carbonation: Literature review, Energy research Centre of the Netherlands ECN.
Stewart, C. and M.-A. Hessami (2005). "A study of methods of carbon dioxide capture and sequestration—the sustainability of a photosynthetic bioreactor approach." Energy Conversion and Management 46(3): 403-420.

APPENDIX C: FORTRAN PROGRAM SAMPLE

```
implicit double precision (A-H,o-z)
dimension sc(7,10),weight(10),dens(10)
dimension ptest0(172801),ptest(49),pcal(49)
dimension irc(8),rc(8),rcl(8),rcr(8),csi(7)
dimension
ichrom(48),igroup0(100,48),icop(60),iseq(60)
dimension igroup(60,48),ngroup(60,48)
dimension fitn(100),fit1(100),fit2(60),fit3(60)
dimension x1(101),u1(101),v1(101),dvdx(101)
dimension stress(101),strain(101)
dimension
press(101),roun(10,101),rou(10),rout(10,101)
dimension diff(101),gd(101),dcoe(101),fy(101)
character ss4*9,ss5*9,ss6*9,ss7*9,ss8*9,ss9*9
character ss10*9,ss11*9,ss12*9,ss13*9,ss14*9
character
ss15*9,ss16*9,ss17*9,ss18*9,ss19*9,ss20*9
character ss21*9,ss22*9,ss23*9,ss24*9
character chapit
common /c0/h1,hc,hs,ht,tmass,cmass,aera,bulk
common /c1/sc,weight,dens,ptest
common /c2/patm,dens_atm,dr,pd,fyr,fy0
common /c3/rcl,rcr
writE(*,8)
8       format(1x,'input file name of output
data,ss5')
read(*,*) ss5
writE(*,18)
18       format(1x,'input file name of output
data,ss4')
read(*,*) ss4
chapit='1'
ss6=chapit//'06'
ss7=chapit//'07'
ss8=chapit//'08'
ss9=chapit//'09'
ss10=chapit//'10'
ss11=chapit//'11'
ss12=chapit//'12'
ss13=chapit//'13'
ss14=chapit//'14'
ss15=chapit//'15'
ss16=chapit//'16'
ss17=chapit//'17'
ss18=chapit//'18'
ss19=chapit//'19'
ss20=chapit//'20'
ss21=chapit//'21'
ss22=chapit//'22'
ss23=chapit//'23'
ss24=chapit//'24'
OPEN(5,FILE=ss5,status='old')
```

```
OPEN(6,FILE=ss6,status='new')
OPEN(7,FILE=ss7,status='new')
OPEN(8,FILE=ss8,status='new')
OPEN(9,FILE=ss9,status='new')
OPEN(10,FILE=ss10,status='new')
OPEN(11,FILE=ss11,status='new')
OPEN(12,FILE=ss12,status='new')
OPEN(13,FILE=ss13,status='new')
OPEN(14,FILE=ss14,status='new')
OPEN(15,FILE=ss15,status='new')
OPEN(16,FILE=ss16,status='new')
OPEN(17,FILE=ss17,status='new')
OPEN(18,FILE=ss18,status='new')
OPEN(19,FILE=ss19,status='new')
OPEN(20,FILE=ss20,status='new')
OPEN(21,FILE=ss21,status='new')
OPEN(22,FILE=ss22,status='new')
OPEN(23,FILE=ss23,status='new')
OPEN(24,FILE=ss24,status='new')
OPEN(4,FILE=ss4,status='old')
ktime=172801
kdraw=1+ktime/3600
m1=kdraw
fyr=0.1d+00
fy0=0.36d+00
pd=0.14d+01
kgrp=100
kcop=60
pc=0.8d+00
pm=0.2d+00
mmut=6
mcross=4
n1=6
n2=6
n3=6
n4=6
n5=6
n6=6
n7=6
n8=6
nt=n1+n2+n3+n4+n5+n6+n7+n8
rcl(1)=0.1d-09
rcr(1)=0.1d-07
rcl(2)=0.1d-09
rcr(2)=0.1d-07
rcl(3)=0.1d-07
rcr(3)=0.3d-06
rcl(4)=0.1d-09
rcr(4)=0.1d-07
rcl(5)=0.1d-09
rcr(5)=0.1d-07
rcl(6)=0.1d-09
```

```
rcr(6)=0.1d-07
rcl(7)=0.1d-09
rcr(7)=0.1d-07
rcl(8)=0.1d-10
rcr(8)=0.1d-09
do i=1,7
read(5,*) (sc(i,j),j=1,10)
end do
do i=1,ktime
read(4,*)ptest0(i)
end do
do k=1,m1
ptest(k)=ptest0(3600*(k-
1)+1)*0.1d+07/0.145d+03
end do
temp=0.295d+03
rcap=0.6022d+24
pco2=ptest(1)
patm=0.1d+06
dens_atm=0.44d+00/0.32d+00*0.12d+02
weight(1)=0.228d+03
weight(2)=0.18d+02
weight(3)=0.342d+03
weight(4)=0.74d+02
weight(5)=0.172d+03
weight(6)=0.56d+02
weight(7)=0.44d+02
weight(8)=0.1d+03
weight(9)=0.474d+03
weight(10)=0.114d+03
hc=0.17d+00
hs=0.3d-01
area=0.785d+00*0.2d-01**2
bulk=hs*area
tmass=0.455d-01
cmass=0.30d-01
dens(1)=3.25d+03
dens(2)=1.0d+03
dens(3)=2.33d+03
dens(4)=1.65d+03
dens(5)=3.28d+03
dens(6)=3.3d+03
dens(7)=dens_atm*pco2/patm
dens(8)=2.71d+03
dens(9)=2.5d+03
dens(10)=2.4d+03
em=0.2d+10
poiss=0.26d+00
algha=0.3d+00
m2=101
m3=100
h1=hs/dble(m3)
ht=0.1d+01
time=dble(ktime)*ht
ig=0
write(22,11) ig
```

```
write(23,12) rcl(8),rcr(8),pd,fy0
11      format('generation',i6)
12      format(4e16.3)
write(*,371)ig
371     format(3x,i6,'th generation population')
call chromosome(nt,kgrp,igroup0)
do 2100 i=1,kgrp
do j=1,nt
ichrom(j)=igroup0(i,j)
end do
call
decode(n1,n2,n3,n4,n5,n6,n7,n8,nt,ichrom,irc,rc)
15      format(3x,'i=',i3,12x,d16.6)
125     format(16x,8e16.6)
call fitness(m1,m2,time,rc,afit)
fitn(i)=afit
fit1(i)=afit
2100    continue
call bubble_sort(fit1,kgrp,kbest)
best=fit1(kgrp)
best1=fitn(kbest)
write(*,171)best,best1
171
        format(3x,'fit1(kgrp)=',d16.6,'fitn(kbest)
=',d16.6)
if(best.gt.0.1d+01) goto 888
call select0(kgrp,fitn,kcop,icop,iseq)
do 201 i=1,kcop
i1=iseq(i)
fit2(i)=fitn(i1)
do 201 j=1,nt
igroup(i,j)=igroup0(i1,j)
201     continue
ig=1
999     write(22,11) ig
call crossover(nt,mcross,kcop,pc,igroup,ngroup)
call mutation(kcop,nt,mmut,pm,igroup,ngroup)
do 300 i=1,kcop
do j=1,nt
ichrom(j)=igroup(i,j)
end do
call
decode(n1,n2,n3,n4,n5,n6,n7,n8,nt,ichrom,irc,rc)
call fitness(m1,m2,time,rc,afit)
fit2(i)=afit
fit3(i)=afit
300     continue
call bubble_sort(fit3,kcop,kbest)
best=fit3(kcop)
best1=fit2(kbest)
write(*,171)best,best1
write(22,272)kbest,rc,best
ig=ig+1
if(best.lt.0.5d+01.and.ig.lt.11) goto 999
888     do j=1,nt
if(kbest.gt.kcop) then
```

```
ichrom(j)=igroup0(kbest,j)
else
ichrom(j)=igroup(kbest,j)
end if
end do
call
decode(n1,n2,n3,n4,n5,n6,n7,n8,nt,ichrom,irc,rc)
write(21,271)kbest,irc,ichrom
write(22,272)kbest,rc,best
271       format(i12,8i6,48i1)
272       format(i16,8e16.6,16x,e16.6)
do j=1,m2
x1(j)=dble(j-1)*h1
press(j)=pco2
stress(j)=-pco2
strain(j)=stress(j)/em
u1(j)=dble(m2-j)/dble(m3)*strain(j)
v1(j)=0.0d+01
dvdx(j)=0.0d+00
fy(j)=fy0
roun(1,j)=0.6d+00*cmass/bulk
roun(2,j)=(tmass-cmass)/bulk
roun(3,j)=0.1d-09
roun(4,j)=0.1d-09
roun(5,j)=0.30d+00*cmass/bulk
roun(6,j)=0.10d+00*cmass/bulk
roun(7,j)=fy(j)*dens(7)*(dble(m2-j)/dble(m2-
1))**4
roun(8,j)=0.1d-09
roun(9,j)=0.1d-09
roun(10,j)=0.1d-09
if(fy(j).ge.0.20d+00) then
dcoe(j)=rc(8)*(fy(j)/fyr)**pd
else
dcoe(j)=rc(8)*(fy(j)/fyr)**pd/0.1d+01
end if
end do
diff(1)=-dcoe(1)*(roun(7,2)-roun(7,1))/h1
do i=2,m3
diff(i)=-0.5d+01*dcoe(i)*(roun(7,i+1)-roun(7,i-
1))/h1
end do
diff(m2)=0.0d+00
t=0.0d+00
k1=0
k2=3600
k3=1
pcal(1)=ptest(1)
time=dble(ktime)*ht
write(7,47) (x1(j),j=1,m2)
write(8,47) (x1(j),j=1,m2)
write(9,47) (x1(j),j=1,m2)
write(10,47) (x1(j),j=1,m2)
write(11,47) (x1(j),j=1,m2)
write(12,47) (x1(j),j=1,m2)
write(13,47) (x1(j),j=1,m2)
write(14,47) (x1(j),j=1,m2)
write(15,47) (x1(j),j=1,m2)
write(16,47) (x1(j),j=1,m2)
write(17,47) (x1(j),j=1,m2)
write(18,47) (x1(j),j=1,m2)
write(19,47) (x1(j),j=1,m2)
write(20,47) (x1(j),j=1,m2)
47        format(16x,101e16.5)
write(6,37)t/dble(3600),pco2*0.145e-
3,(csi(j),j=1,7)
write(7,27)t/dble(3600),(fy(j),j=1,m2)
write(8,27)t/dble(3600),(dcoe(j),j=1,m2)
write(9,27)t/dble(3600),(diff(j),j=1,m2)
write(10,27)t/dble(3600),(strain(j),j=1,m2)
write(11,27)t/dble(3600),(roun(1,j),j=1,m2)
write(12,27)t/dble(3600),(roun(2,j),j=1,m2)
write(13,27)t/dble(3600),(roun(3,j),j=1,m2)
write(14,27)t/dble(3600),(roun(4,j),j=1,m2)
write(15,27)t/dble(3600),(roun(5,j),j=1,m2)
write(16,27)t/dble(3600),(roun(6,j),j=1,m2)
write(17,27)t/dble(3600),(roun(7,j),j=1,m2)
write(18,27)t/dble(3600),(roun(8,j),j=1,m2)
write(19,27)t/dble(3600),(roun(9,j),j=1,m2)
write(20,27)t/dble(3600),(roun(10,j),j=1,m2)
do j=1,m2
dcoe(j)=rc(8)*(fy(j)/fyr)**pd
end do
800       pt=dcoe(1)*(roun(7,1)-
roun(7,2))/h1/hc*patm/dens_atm
diff(1)=hc*dens_atm/patm*pt
diff(m2)=0.0d+00
do i=2,m3
diff(i)=-0.5d+01*dcoe(i)*(roun(7,i+1)-roun(7,i-
1))/h1
end do
gd(1)=-(diff(2)-diff(1))/h1
gd(m2)=-(diff(m2)-diff(m2-1))/h1
do i=2,m3
gd(i)=-0.5d+00*(diff(i+1)-diff(i-1))/h1
end do
do 10 j=1,m2
do k=1,10
rou(k)=roun(k,j)
end do
call rate(rc,rou,csi)
rout(1,j)=sc(1,1)*csi(1)+csi(6)*sc(6,1)
rout(2,j)=sc(1,2)*csi(1)+csi(2)*sc(2,2)+csi(3)*sc
(3,2)
*    +csi(4)*sc(4,2)+csi(6)*sc(6,2)+csi(7)*sc(7,2)
rout(3,j)=sc(1,3)*csi(1)+sc(2,3)*csi(2)+sc(5,3)*c
si(5)
rout(4,j)=sc(1,4)*csi(1)+sc(2,4)*csi(2)+sc(3,4)*c
si(3)
*    +sc(4,4)*csi(4)
rout(5,j)=sc(2,5)*csi(2)+sc(7,5)*csi(7)
rout(6,j)=sc(3,6)*csi(3)
```

```
rout(7,j)=sc(4,7)*csi(4)+sc(5,7)*csi(5)+sc(6,7)*c
si(6)
*    +sc(7,7)*csi(7)
rout(8,j)=sc(4,8)*csi(4)+sc(6,8)*csi(6)+sc(7,8)*c
si(7)
rout(9,j)=sc(5,9)*csi(5)
rout(10,j)=sc(6,10)*csi(6)+sc(7,10)*csi(7)
do k=1,10
rout(k,j)=rout(k,j)*weight(k)
end do
rout(7,j)=rout(7,j)+gd(j)
do k=1,10
roun(k,j)=roun(k,j)+rout(k,j)*ht
end do
zz=0.0d+00
do k=1,10
zz=zz-rout(k,j)/dens(k)
end do
zz=zz+rout(7,j)/dens(7)
fy(j)=fy(j)+zz*ht
dcoe(j)=rc(8)*(fy(j)/fyr)**pd
10         continue
pco2=patm*roun(7,1)/fy(1)/dens_atm
t=t+ht
k1=k1+1
if(k1/k2*k2.eq.k1) then
k3=k3+1
pcal(k3)=pco2
do j=1,m2
press(j)=pco2
 stress(j)=-pco2
strain(j)=stress(j)/em/(0.1d+01-poiss)
*    *(0.1d+01+poiss)/(0.1d+01-0.2d+00*poiss)
u1(j)=dble(m2-j)/dble(m3)*strain(j)
v1(j)=0.0d+01
dvdx(j)=0.0d+00
end do
write(6,37)t/dble(3600),pco2*0.145e-
3,(csi(j),j=1,7)
write(7,27)t/dble(3600),(fy(j),j=1,m2)
write(8,27)t/dble(3600),(dcoe(j),j=1,m2)
write(9,27)t/dble(3600),(diff(j),j=1,m2)
write(10,27)t/dble(3600),(strain(j),j=1,m2)
write(11,27)t/dble(3600),(roun(1,j),j=1,m2)
write(12,27)t/dble(3600),(roun(2,j),j=1,m2)
write(13,27)t/dble(3600),(roun(3,j),j=1,m2)
write(14,27)t/dble(3600),(roun(4,j),j=1,m2)
write(15,27)t/dble(3600),(roun(5,j),j=1,m2)
write(16,27)t/dble(3600),(roun(6,j),j=1,m2)
write(17,27)t/dble(3600),(roun(7,j),j=1,m2)
write(18,27)t/dble(3600),(roun(8,j),j=1,m2)
write(19,27)t/dble(3600),(roun(9,j),j=1,m2)
write(20,27)t/dble(3600),(roun(10,j),j=1,m2)
17         format(3x,'t=',3x,8d16.5)
27         format(102e16.5)
37         format(9e16.5)
end if
if(t.le.time) goto 800
do k=1,m1
tdraw=dble(k-1)
write(24,77)
tdraw,ptest(k),pcal(k),ptest(k)*0.145e-03,
*    pcal(k)*0.145e-03
end do
77         format(5e16.3)
close(4)
close(5)
close(6)
close(7)
close(8)
close(9)
close(10)
close(11)
close(12)
close(13)
close(14)
close(15)
close(16)
close(17)
close(18)
close(19)
close(20)
close(21)
close(22)
close(23)
close(24)
stop
end
subroutine fitness(m1,m2,time,rc,fitn)
implicit double precision (A-H,o-z)
dimension x1(101)
dimension roun(10,101),rou(10),rout(10,101)
dimension diff(101),gd(101),dcoe(101),fy(101)
dimension
rc(8),csi(7),dens(10),sc(7,10),weight(10)
dimension ptest(49),pcal(m1),x(m1)
common /c0/h1,hc,hs,ht,tmass,cmass,aera,bulk
common /c1/sc,weight,dens,ptest
common /c2/patm,dens_atm,dr,pd,fyr,fy0
m3=m2-1
pco2=ptest(1)
do j=1,m2
x1(j)=dble(j-1)*h1
fy(j)=fy0
roun(1,j)=0.60d+00*cmass/bulk
roun(2,j)=(tmass-cmass)/bulk
roun(3,j)=0.1d-09
roun(4,j)=0.1d-09
roun(5,j)=0.30d+00*cmass/bulk
roun(6,j)=0.10d+00*cmass/bulk
roun(7,j)=fy(j)*dens(7)*(dble(m2-j)/dble(m2-
1))**4
```

```
roun(8,j)=0.1d-09
roun(9,j)=0.1d-09
roun(10,j)=0.1d-09
dcoe(j)=rc(8)*(fy(j)/fyr)**pd
end do
diff(1)=-dcoe(1)*(roun(7,2)-roun(7,1))/h1
do i=2,m3
diff(i)=-0.5d+01*dcoe(i)*(roun(7,i+1)-roun(7,i-1))/h1
end do
diff(m2)=0.0d+00
t=0.0d+00
k1=0
k2=3600/10
k3=1
pcal(k3)=pco2
do j=1,m2
dcoe(j)=dr*(fy(j)/fyr)**pd
end do
800       pt=dcoe(1)*(roun(7,1)-roun(7,2))/h1/hc*patm/dens_atm
diff(1)=hc*dens_atm/patm*pt
diff(m2)=0.0d+00
do i=2,m3
diff(i)=-0.5d+01*dcoe(i)*(roun(7,i+1)-roun(7,i-1))/h1
end do
gd(1)=-(diff(2)-diff(1))/h1
gd(m2)=-(diff(m2)-diff(m2-1))/h1
do i=2,m3
gd(i)=-0.5d+00*(diff(i+1)-diff(i-1))/h1
end do
do 10 j=1,m2
do k=1,10
rou(k)=roun(k,j)
end do
call rate(rc,rou,csi)
rout(1,j)=sc(1,1)*csi(1)+csi(6)*sc(6,1)
rout(2,j)=sc(1,2)*csi(1)+csi(2)*sc(2,2)+csi(3)*sc(3,2)
*    +csi(4)*sc(4,2)+csi(6)*sc(6,2)+csi(7)*sc(7,2)
rout(3,j)=sc(1,3)*csi(1)+sc(2,3)*csi(2)+sc(5,3)*csi(5)
rout(4,j)=sc(1,4)*csi(1)+sc(2,4)*csi(2)+sc(3,4)*csi(3)
*    +sc(4,4)*csi(4)
rout(5,j)=sc(2,5)*csi(2)+sc(7,5)*csi(7)
rout(6,j)=sc(3,6)*csi(3)
rout(7,j)=sc(4,7)*csi(4)+sc(5,7)*csi(5)+sc(6,7)*csi(6)
*    +sc(7,7)*csi(7)
rout(8,j)=sc(4,8)*csi(4)+sc(6,8)*csi(6)+sc(7,8)*csi(7)
rout(9,j)=sc(5,9)*csi(5)
rout(10,j)=sc(6,10)*csi(6)+sc(7,10)*csi(7)
do k=1,10
rout(k,j)=rout(k,j)*weight(k)
end do
rout(7,j)=rout(7,j)+gd(j)
do k=1,10
roun(k,j)=roun(k,j)+rout(k,j)*ht*0.1d+02
end do
zz=0.0d+00
do k=1,10
zz=zz-rout(k,j)/dens(k)
end do
zz=zz+rout(7,j)/dens(7)
fy(j)=fy(j)+zz*ht*0.1d+02
dcoe(j)=dr*(fy(j)/fyr)**pd
10        continue
pco2=patm*roun(7,1)/fy(1)/dens_atm
t=t+ht*0.1d+02
k1=k1+1
if(k1/k2*k2.eq.k1) then
k3=k3+1
pcal(k3)=pco2
end if
if(t.le.time) goto 800
pcal(m1)=pco2
do k=1,m1
x(k)=dabs(ptest(k)-pcal(k))/ptest(k)
end do
sum=0.0d+00
do k=1,m1
sum=sum+x(k)**2
end do
fitn=0.1d+01/dsqrt(sum)
return
end
subroutine select0(kgrp,fitn,kcop,icop,iseq)
implicit double precision (A-H,p-y)
implicit character(o,z)
dimension fitn(kgrp),fitt(kgrp),pfit(kgrp)
dimension prob(kgrp),icop(kcop),iseq(kcop)
fitt(1)=fitn(1)
do 20 i=2,kgrp
20        fitt(i)=fitt(i-1)+fitn(i)
tot=fitt(kgrp)
do 30 i=1,kgrp
30        pfit(i)=fitn(i)/tot
call random_number(t)
prob(1)=t/dble(kcop)
do i=2,kcop
prob(i)=prob(1)+dble(i-1)/dble(kcop)
end do
do 50 i=1,kcop
a=prob(i)
call minim(kgrp,i1,a,pfit)
iseq(i)=i1
icop(i)=i1
50        continue
call bubble(iseq,kcop)
```

```
end
subroutine
crossover(m,mcross,kcop,pc,igroup,ngroup)
implicit double precision (A-H,o-z)
dimension n1(m),n2(m)
dimension rd(kcop),ith(kcop)
dimension
igroup(kcop,m),ngroup(kcop,m),icross(kcop/2)
pc1=(0.1d+01-pc)/0.2d+01
pc2=pc1+pc
call init_random_seed()
do k=1,kcop/2
call random_number(x)
if (x.gt.pc2.or.x.lt.pc1) then
icross(k)=0
else
icross(k)=1
end if
end do
do i=1,kcop
ith(i)=i
end do
call random_seed()
call random_number(rd)
do i=1,kcop-1
do j=i+1,kcop
if (rd(i).gt.rd(j)) then
itemp=ith(i)
ith(i)=ith(j)
ith(j)=itemp
end if
end do
end do
do 100 i=1,kcop/2
i1=ith(i)
i2=ith(kcop+1-i)
do j=1,m
n1(j)=igroup(i1,j)
n2(j)=igroup(i2,j)
end do
do j=3,m,5
if (icross(i).eq.1) then
ngroup(i1,j)=n2(j)
ngroup(i2,j)=n1(j)
else
ngroup(i1,j)=n1(j)
ngroup(i2,j)=n2(j)
end if
end do
100       continue
return
end
subroutine
mutation(kcop,m,mmut,pm,igroup,ngroup)
implicit double precision (A-H,o-z)
dimension igroup(kcop,m),ngroup(kcop,m)
```

```
pm1=(0.1d+01-pm)/0.2d+01
pm2=pm1+pm
call init_random_seed()
do i=1,kcop
call random_number(x)
call random_number(x1)
k1=int(dble(m)*x)
k2=max(k1,1)
do j=1,m
igroup(i,j)=ngroup(i,j)
end do
if(x1.lt.pm1.or.x1.gt.pm2) then
if(ngroup(i,k2).eq.0) then
igroup(i,k2)=1
else
igroup(i,k2)=1
end if
end if
end do
return
end
subroutine init_random_seed()
integer clock
integer, dimension(:), allocatable :: seed
call random_seed(size = n)
allocate(seed(n))
call system_clock(count=clock)
seed = clock + 37 * (/ (i - 1, i = 1, n) /)
call random_seed(put = seed)
deallocate(seed)
end subroutine init_random_seed
implicit double precision (a-h,o-z)
dimension a(n)
y=a(1)
kbest=1
do i=2,n
if(a(i).gt.y) then
y=a(i)
kbest=i
end if
end do
do i=n-1,1,-1
do j=1,i
if (a(j).gt.a(j+1)) then
temp=a(j)
a(j)=a(j+1)
a(j+1)=temp
end if
end do
end do
return
end subroutine
subroutine bubble(ia,n)
dimension ia(n)
do i=n-1,1,-1
do j=1,i
```

```
if (ia(j).gt.ia(j+1)) then
itemp=ia(j)
ia(j)=ia(j+1)
ia(j+1)=itemp
end if
end do
end do
return
end subroutine
subroutine minim(n,i1,a,x)
implicit double precision (A-H,o-z)
dimension x(n)
i1=1
dminim=x(1)
do 10 i=2,n
if(dabs(x(i)-a).lt.dminim) then
dminim=x(i)
i1=i
end if
10      continue
return
end
subroutine chromosome(m,kgrp,igroup)
implicit double precision (A-H,o-z)
dimension igroup(kgrp,m)
call init_random_seed()
do i=1,kgrp
do k=1,m
call random_number(t)
if(t.lt.0.5d+00) then
igroup(i,k)=0
else
igroup(i,k)=1
end if
end do
end do
return
end
subroutine decode(n1,n2,n3,n4,n5,n6,n7,n8,nt,ichrom,irc,rc)
implicit double precision (A-H,o-z)
dimension ichrom(nt),irc(8),rc(8),nk(8),rcl(8),rcr(8)
common /c3/rcl,rcr
nk(1)=n1
nk(2)=n2
nk(3)=n3
nk(4)=n4
nk(5)=n5
nk(6)=n6
nk(7)=n7
nk(8)=n8
do k=1,8
irc(k)=0
rc(k)=0.0d+00
end do
do i=1,n1
irc(1)=irc(1)+ichrom(i)*2**(n1-i)
end do
do i=1,n2
irc(2)=irc(2)+ichrom(n1+i)*2**(n2-i)
end do
do i=1,n3
irc(3)=irc(3)+ichrom(n1+n2+i)*2**(n3-i)
end do
do i=1,n4
irc(4)=irc(4)+ichrom(n1+n2+n3+i)*2**(n4-i)
end do
do i=1,n5
irc(5)=irc(5)+ichrom(n1+n2+n3+n4+i)*2**(n5-i)
end do
do i=1,n6
irc(6)=irc(6)+ichrom(n1+n2+n3+n4+n5+i)*2**(n6-i)
end do
do i=1,n7
irc(7)=irc(7)+ichrom(n1+n2+n3+n4+n5+n6+i)*2**(n7-i)
end do
do i=1,n8
irc(8)=irc(8)+ichrom(n1+n2+n3+n4+n5+n6+n7+i)*2**(n8-i)
end do
do k=1,8
rc(k)=rcl(k)+(rcr(k)-rcl(k))*dble(irc(k))/dble(2**nk(k)-1)
end do
return
end
subroutine rate(rc,rou,csi)
implicit double precision (A-H,O-Z)
dimension rou(10),weight(10),dens(10)
dimension csi(7),sc(7,10),rc(8),ptest(49)
double precision lamd11,lamd21
double precision lamd52,lamd22
double precision lamd63,lamd23
double precision lamd44,lamd74
double precision lamd35,lamd75
double precision lamd16,lamd76,lamd26
double precision lamd57,lamd77,lamd27
common /c0/h1,hc,hs,ht,tmass,cmass,aera,bulk
common /c1/sc,weight,dens,ptest
common /c2/patm,dens_atm,dr,pd,fyr,fy0
z1=rou(1)+rou(2)
z2=weight(1)*dabs(sc(1,1))+weight(2)*dabs(sc(1,2))
x1=rou(1)/z1*z2/weight(1)/dabs(sc(1,1))
x2=rou(2)/z1*z2/weight(2)/dabs(sc(1,2))
if(x1.lt.x2) then
lamd11=1.0
else
```

```
lamd11=0.0
end if
lamd21=0.1d+01-lamd11
z1=rou(5)+rou(2)
z2=weight(5)*dabs(sc(2,5))+weight(2)*dabs(sc(
2,2))
x1=rou(5)/z1*z2/weight(5)/dabs(sc(2,5))
x2=rou(2)/z1*z2/weight(2)/dabs(sc(2,2))
if(x1.lt.x2) then
lamd52=1.0
else
lamd52=0.0
end if
lamd22=0.1d+01-lamd52
z1=rou(6)+rou(2)
z2=dabs(sc(3,6))*weight(6)+dabs(sc(3,2))*weig
ht(2)
x1=rou(6)/z1*z2/dabs(sc(3,6))/weight(6)
x2=rou(2)/z1*z2/dabs(sc(3,2))/weight(2)
if(x1.lt.x2) then
lamd63=1.0
else
lamd63=0.0
end if
lamd23=0.1d+01-lamd63
z1=rou(4)+rou(7)
z2=dabs(sc(4,4))*weight(4)+dabs(sc(4,7))*weig
ht(7)
x1=rou(4)/z1*z2/dabs(sc(4,4))/weight(4)
x2=rou(7)/z1*z2/dabs(sc(4,7))/weight(7)
if(x1.lt.x2) then
lamd44=1.0
else
lamd44=0.0
end if
lamd74=0.1d+01-lamd44
z1=rou(3)+rou(7)
z2=dabs(sc(5,3))*weight(3)+dabs(sc(5,7))*weig
ht(7)
x1=rou(3)/z1*z2/dabs(sc(5,3))/weight(3)
x2=rou(7)/z1*z2/dabs(sc(5,7))/weight(7)
z=min(x1,x2)
if(x1.eq.z) then
lamd35=1.0
else
lamd35=0.0
end if
lamd75=0.1d+01-lamd35
z1=rou(1)+rou(7)+rou(2)
z2=dabs(sc(6,1))*weight(1)+dabs(sc(6,7))*weig
ht(7)
*    +dabs(sc(6,2))*weight(2)
x1=rou(1)/z1*z2/dabs(sc(6,1))/weight(1)
x2=rou(7)/z1*z2/dabs(sc(6,7))/weight(7)
x3=rou(2)/z1*z2/dabs(sc(6,2))/weight(2)
z=min(x1,x2,x3)
if(x1.eq.z) then
lamd16=1.0
lamd76=0.0
lamd26=0.0
else if(x2.eq.z) then
lamd16=0.0
lamd76=1.0
lamd26=0.0
else
lamd16=0.0
lamd76=0.0
lamd26=1.0
end if
z1=rou(5)+rou(7)+rou(2)
z2=dabs(sc(7,5))*weight(5)+dabs(sc(7,7))*weig
ht(7)
*    +dabs(sc(7,2))*weight(2)
x1=rou(5)/z1*z2/dabs(sc(7,5))/weight(5)
x2=rou(7)/z1*z2/dabs(sc(7,7))/weight(7)
x3=rou(2)/z1*z2/dabs(sc(7,2))/weight(2)
z=min(x1,x2,x3)
if(x1.eq.z) then
lamd57=1.0
lamd77=0.0
lamd27=0.0
else if(x2.eq.z) then
lamd57=0.0
lamd77=1.0
lamd27=0.0
else
lamd57=0.0
lamd77=0.0
lamd27=1.0
end if
csi(1)=rc(1)*rou(1)**lamd11*rou(2)**lamd21
csi(2)=rc(2)*rou(5)**lamd52*rou(2)**lamd22
csi(3)=rc(3)*rou(6)**lamd63*rou(2)**lamd23
csi(4)=rc(4)*rou(4)**lamd44*rou(7)**lamd74
csi(5)=rc(5)*rou(3)**lamd35*rou(7)**lamd75
csi(6)=rc(6)*rou(1)**lamd16*rou(7)**lamd76*r
ou(2)**lamd26
csi(7)=rc(7)*rou(5)**lamd57*rou(7)**lamd77*r
ou(2)**lamd27
return
end
```